REPORT DOCUMENTATION PAGE

1. REPORT DATE (DD-MM-YYYY)	2. REPORT TYPE	3. DATES COVERED (From - To)
12-09-2015	Final Technical Report	06/04/2010 - 09/30/2015

4. TITLE AND SUBTITLE

Planar Solid-Oxide Fuel Cell System Demonstration at UT SimCenter (Congressional)

5a. CONTRACT NUMBER

5b. GRANT NUMBER

N00014-10-1-0882

5c. PROGRAM ELEMENT NUMBER

6. AUTHOR(S)

Dr. Sagar Kapadia, Dr. James Newman III, Dr. Kyle Anderson

5d. PROJECT NUMBER

15PR20539-01

5e. TASK NUMBER

5f. WORK UNIT NUMBER

7. PERFORMING ORGANIZATION NAME(S) AND ADDRESS(ES)

The University of Tennessee at Chattanooga
615 McCallie Avenue
Chattanooga, TN 37403-2504

8. PERFORMING ORGANIZATION REPORT NUMBER

9. SPONSORING/MONITORING AGENCY NAME(S) AND ADDRESS(ES)

Office of Naval Research
875 North Randolph Street
Arlington, VA 22203-1995

10. SPONSOR/MONITOR'S ACRONYM(S)

11. SPONSOR/MONITOR'S REPORT NUMBER(S)

12. DISTRIBUTION/AVAILABILITY STATEMENT

Distribution Statement A: Approved for Public Release; distribution is unlimited

13. SUPPLEMENTARY NOTES

14. ABSTRACT

See attached report.

15. SUBJECT TERMS

16. SECURITY CLASSIFICATION OF:			17. LIMITATION OF ABSTRACT	18. NUMBER OF PAGES	19a. NAME OF RESPONSIBLE PERSON
a. REPORT	b. ABSTRACT	c. THIS PAGE			Sagar Kapadia
					19b. TELEPHONE NUMBER (Include area code)
				135	423-425-5552

20151214437

INSTRUCTIONS FOR COMPLETING SF 298

1. REPORT DATE. Full publication date, including day, month, if available. Must cite at least the year and be Year 2000 compliant, e.g. 30-06-1998; xx-06-1998; xx-xx-1998.

2. REPORT TYPE. State the type of report, such as final, technical, interim, memorandum, master's thesis, progress, quarterly, research, special, group study, etc.

3. DATE COVERED. Indicate the time during which the work was performed and the report was written, e.g., Jun 1997 - Jun 1998; 1-10 Jun 1996; May - Nov 1998; Nov 1998.

4. TITLE. Enter title and subtitle with volume number and part number, if applicable. On classified documents, enter the title classification in parentheses.

5a. CONTRACT NUMBER. Enter all contract numbers as they appear in the report, e.g. F33315-86-C-5169.

5b. GRANT NUMBER. Enter all grant numbers as they appear in the report. e.g. AFOSR-82-1234.

5c. PROGRAM ELEMENT NUMBER. Enter all program element numbers as they appear in the report, e.g. 61101A.

5e. TASK NUMBER. Enter all task numbers as they appear in the report, e.g. 05; RF0330201; T4112.

5f. WORK UNIT NUMBER. Enter all work unit numbers as they appear in the report, e.g. 001; AFAPL30480105.

6. AUTHOR(S). Enter name(s) of person(s) responsible for writing the report, performing the research, or credited with the content of the report. The form of entry is the last name, first name, middle initial, and additional qualifiers separated by commas, e.g. Smith, Richard, J, Jr.

7. PERFORMING ORGANIZATION NAME(S) AND ADDRESS(ES). Self-explanatory.

8. PERFORMING ORGANIZATION REPORT NUMBER. Enter all unique alphanumeric report numbers assigned by the performing organization, e.g. BRL-1234; AFWL-TR-85-4017-Vol-21-PT-2.

9. SPONSORING/MONITORING AGENCY NAME(S) AND ADDRESS(ES). Enter the name and address of the organization(s) financially responsible for and monitoring the work.

10. SPONSOR/MONITOR'S ACRONYM(S). Enter, if available, e.g. BRL, ARDEC, NADC.

11. SPONSOR/MONITOR'S REPORT NUMBER(S). Enter report number as assigned by the sponsoring/ monitoring agency, if available, e.g. BRL-TR-829; -215.

12. DISTRIBUTION/AVAILABILITY STATEMENT. Use agency-mandated availability statements to indicate the public availability or distribution limitations of the report. If additional limitations/ restrictions or special markings are indicated, follow agency authorization procedures, e.g. RD/FRD, PROPIN, ITAR, etc. Include copyright information.

13. SUPPLEMENTARY NOTES. Enter information not included elsewhere such as: prepared in cooperation with; translation of; report supersedes; old edition number, etc.

14. ABSTRACT. A brief (approximately 200 words) factual summary of the most significant information.

15. SUBJECT TERMS. Key words or phrases identifying major concepts in the report.

16. SECURITY CLASSIFICATION. Enter security classification in accordance with security classification regulations, e.g. U, C, S, etc. If this form contains classified information, stamp classification level on the top and bottom of this page.

17. LIMITATION OF ABSTRACT. This block must be completed to assign a distribution limitation to the abstract. Enter UU (Unclassified Unlimited) or SAR (Same as Report). An entry in this block is necessary if the abstract is to be limited.

Planar Solid-Oxide Fuel Cell System Demonstration at UT SimCenter

S. Kapadia, J. C. Newman III, W. K. Anderson

University of Tennessee SimCenter at Chattanooga,
701, East M.L. King Boulevard, Chattanooga, TN – 37403, U.S.A.

Abstract

A three-dimensional, unstructured, multi-species reacting flow solver is developed to model solid oxide fuel cells (SOFCs) as well as catalytic reactors. The finite volume based solver utilizes density-based method to solve the coupled system of governing equations. Numerical results for both SOFC and reactor obtained using the in-house code are compared with the experimental results from the literature for validation purposes. Effects of mass flow rates of incoming species on performance of SOFC as well as catalytic reactor are investigated. Two different methods namely direct differentiation and discrete adjoint method are implemented in the code to compute sensitivity derivatives for computational design. The catalytic partial oxidation of methane over both platinum and rhodium catalysts is studied using the in-house solver. Eight gas-phase species (CH_4, CO_2, H_2O, N_2, O_2, CO, OH and H_2) are considered for the simulation. The surface chemistry is modeled using detailed reaction mechanisms including 24 heterogeneous reactions with 11 surface-adsorbed species for Pt catalyst and 38 heterogeneous reactions with 20 surface-adsorbed species for Rh catalyst. The numerical results are compared with the experimental data and good agreement is observed. The effects of the design variables of inlet velocity, methane/oxygen ratio, catalytic wall temperature and catalyst loading on the cost functions representing methane conversion and hydrogen production are numerically investigated. The design cycle is performed using two gradeint-based optimization algorithms to improve the value of the implemented cost function and optimize the reactor performance. A capability to perform thermo-mechanical analysis is developed by coupling the multispecies solver with the structures code. Results obtained using this capability are shown for the planar SOFC. Also, sensitivity derivatives of stress are computed using the direct differentiation method in the reacting flow and structures codes. A novel method to perform shape optimization using CAD based parameters has been collaboratively developed. This method is also effective in generating curved elements for high-order finite element meshes. A robust mesh movement algorithm is implemented to ensure grid quality during shape design and high-order element creation. Examples using this technique are presented for a tubular SOFC, three-dimensional body of revolution and NACA 4412.

1. Introduction

Energy efficiency has been one of the most important research areas of recent times. Improving efficiency of existing systems as well as developing new technologies

for energy production and storage has captured a lot of attention lately due in part to reducing reliance on fossil fuels as well as their environmental impacts. Systems that are capable of operating with variety of fuels while producing energy at higher efficiency are very desirable. Solid oxide fuel cells (SOFCs) can be classified as one of such technologies due to its capability of producing efficient energy using various hydrocarbon fuel types. SOFCs are high temperature fuel cells capable of producing electrical energy at high efficiency. As the name suggests, the SOFC contains a solid electrolyte that is capable of transporting oxygen ions from the cathode-electrolyte interface to the anode-electrolyte interface.

Fuel reformer is one of the most important components of the SOFC system. The purpose of the fuel reformer is to convert the chemical composition of primary fuel into the species that systems like SOFC can be operated with. Fuel reforming can be broadly classified into three categories including, steam reforming (SR), partial oxidation (POX) and autothermal reforming (ATR). The reactors used in reforming process can have many different structures such as pack bed and monolith depending on application and other parameters. These reactors are categorized as the catalytic reactors. The catalytic reactor can be distinguished from the conventional reactor by considering fundamental differences between homogeneous (conventional) combustion and catalytic combustion. The main differences can be summarized as [1] following.

- Conventional combustion occurs in the presence of a flame, while catalytic combustion is a flameless process.
- Catalytic combustion generally proceeds at a lower temperature than conventional combustion.
- Catalytic combustion results in lower emission of oxides of nitrogen.
- Conventional combustion can only exist within well-defined fuel to air ratios. Catalytic combustion is not constrained by such condition.
- Catalytic combustion can offer fewer constraints on reactor design.

Numerical simulation techniques have become matured enough to be utilized in performing design and optimization in vast variety of fields. Some of the advantages of the numerical simulations over the experiments are the cost effectiveness and the fact that the simulations provide a wealth of data that is difficult or impossible to obtain experimentally and can be used to perform in-depth analysis of the system. Numerical design is an iterative process starting with baseline solution, followed by sensitivity computation and parameter optimization. Each of the steps mentioned can be performed with different methods from high-fidelity to low-fidelity as well as in one-dimension to multi-dimensions. As expected, high-fidelity simulations provide detailed information about the flowfield, but comes with a burden of higher computational cost compared to the simplified models. Even though SOFCs are still in the developmental stage, numerical techniques can be effectively utilized to find solutions to many of the design hurdles affecting the commercial application of the technology. Numerical simulations can contribute greatly toward the development of better designs that can produce more power, increased efficiency, and extended life expectancy of various SOFCs and reformers.

Behavior of SOFCs has been studied by different researchers using both simulation models as well as experiments [2-9]. Primary focus of numerical simulations is on analysis of fuel cells without putting much emphasis on formal optimization procedures or sensitivity computation. Most of the design studies are performed by simply changing the parameter of interest, re-running the simulation, and comparing the results with those from the original simulation [2,6,7,9]. While this approach can be used to determine the effects of parameter variations on fuel cell performance, a more rigorous approach toward optimization would likely lead to better designs, and can also provide improved insight into the parameters affecting the performance of the fuel cell. For SOFC problems, example cost functions that can be used for improving performance include minimizing temperature variations, obtaining equal distribution of fuel in each of the channels, minimizing stress inside different components or maximizing power. Design variables may be related to the shape/size of the fuel channels, electrodes, electrolyte, and interconnect, but may also be coupled to the stoichiometric composition of fuel or material properties such as the porosity or tortuosity of the electrodes. In references [10] and [11], optimization algorithms have been used to improve the performance of a polymer-electrolyte-membrane fuel cell (PEM) using four design variables, where the sensitivity derivatives used for the optimization algorithm have been obtained using a finite-difference approach. While finite differences are often a viable means for computing sensitivity derivatives, this method can be computationally restrictive when a sufficiently large number of design variables are present. In addition, accurate derivatives can sometimes be difficult to obtain using finite differences because of subtractive cancellation errors [12], which occur when the function evaluations in the numerator become computationally indistinguishable [13] when very small perturbations are used. By using a direct differentiation or discrete adjoint method [14-25], sensitivity derivatives that are consistent with the flow solver may be obtained for use in a design optimization environment. The code utilized in this report is capable of computing sensitivity derivatives of a cost function with respect to desired parameters using both direct differentiation and discrete adjoint methods. In different design studies performed at the SimCenter, sensitivity derivatives were also utilized in a design environment to optimize cost functions representing uniform fuel distribution [26,27], temperature distribution [28] and cell voltage [27].

Due to the presence of various thermal mechanisms inside SOFC, temperature distribution exhibits non-uniformity throughout the domain. This coupled with the mismatch in coefficients of thermal expansion of different SOFC components makes stress analysis an interesting avenue to explore. Recently, few studies have been performed [29-35] to analyze stress components inside different components of SOFC. Lin et al. [29] analyzed effects of clamping load on the thermal stress distribution in a planar SOFC. Five different compressible loads were applied to investigate effects on stress distribution. Gulfam et al. [32] analyzed thermal stress inside PEN region of SOFC for co-flow, counter-flow and cross-flow configurations using commercial software, ABAQUS [36]. Maximum stress inside anode layer was found at high-temperature regions located on the anode-electrolyte interface for all configurations. Jiang et al. [33] performed thermal stress analysis of SOFC with the bonded compliant seal design. Stress analysis performed using commercial software, FLUENT [37] and ANSYS [38]

3

investigated effects of temperature non-uniformity and cell voltage on thermal stress distribution. Weil and Koeppel [34] also analyzed effects of different seal designs on stress-strain state. They used glass-ceramic, brazed joints and foil-based seals in this study. Chiang et al. [35] analyzed effects of anode porosity on thermal stress in anode-supported SOFC using commercial software, STAR-CD [39] and MARC [40]. The study indicated presence of higher principal stress at low cell voltages due to high local current density and steep temperature gradients. None of these studies attempted to compute sensitivity derivatives of a cost function involving thermal stress components using formal procedures such as direct differentiation or discrete adjoint methods. Such capability is required if optimization of principal stress components or strain rates with respect to geometrical or material parameters is desired. One of the cases described in this report demonstrates such capability, where stress sensitivities are computed with respect to the cathode porosity using direct differentiation method. Implementation of this method is not trivial, as it requires computation of sensitivity derivatives of flowfield variables in the multispecies Navier-Stokes code and coupling them with the structures solver to compute stress sensitivities with respect to the design parameters.

The monolith or honeycomb reactor is a commonly used configuration in catalytic combustion. It consists of a number of parallel passageways through which the gas flows, with the catalyst being coated on its walls. Catalytic monolithic reactors are generally characterized by the complex interaction of various physical and chemical processes that include transport of momentum, energy, and chemical species. Modeling of monolithic reactors can be broadly divided into two categories: single-channel modeling that considers one channel of the monolith and full-scale modeling that considers the whole reactor comprised of several hundred channels [41]. Single-channel models can be one-dimensional, two-dimensional or three-dimensional. One-dimensional (1D) models ignore radial and angular gradients in temperature, concentration, and velocity, and consider only axial variations. These models with lumped heat and mass coefficients were widely used because of their simplicity and easy implementation. A simplifying assumption of plug flow is frequently made in 1D models. Inside the monolith channel, the catalytic reactions occur in the washcoat on the channel wall. There are two choices for incorporating these catalyst reactions in numerical model.

- The pseudo-homogeneous model: The wall temperature and concentrations are assumed to be the same as fluid, and the reaction rate is incorporated directly into the conservation equations.
- The heterogeneous model: The gas-solid interface at the wall is assumed to be discontinuous and separate mole and energy balance equations are solved for the solid. These equations are coupled to the fluid equations through mass and heat transfer coefficients. Catalytic reactor results presented in this report utilizes heterogeneous model for surface chemistry.

Catalytic combustion of hydrogen was investigated by Cerkanowicz et al. [42] with simplified chemistry and by Kramer et al. [43] with detailed kinetics. Multi-dimensional models of catalytic reactors can be developed based on either boundary-layer equations or full Navier-Stokes equations. In boundary-layer approximation, axial

(streamwise) diffusive transport is neglected, but detailed transport to and from the channel walls is retained. Raja et al. [44] investigated the efficiency and validity range of the Navier–Stokes, boundary layer and plug-flow models in a catalytic monolithic channel. Their research showed that the boundary-layer models provide accurate results with relatively low computational cost [44]. Deutschmann et al. [45] and Dogwiler et al. [46] used two-dimensional Navier-Stokes models with detailed heterogeneous and homogeneous chemistry for simulation of catalytic combustion. Catalytic combustion of methane-air was studied by Markatou et al. [47] using two-dimensional boundary layer model. Kumar [41] developed a coupled implicit solver to solve species conservation equations and investigated the flowfield in a full-scale 3D catalytic converter. Catalytic combustion of iso-octane over rhodium catalysts was studied by Hartmann et al. [48]. They used detailed surface chemistry including 17 surface species and 58 surface reactions for this simulation. Maestri and Cuoci [49] used OpenFOAM to simulate heterogeneous catalytic systems in three-dimensions with detailed kinetics schemes. Catalytic partial oxidation (CPOX) of methane over a honeycomb reactor was numerically studied by Hettel et al. [50]. They coupled OpenFOAM [51] and DETCHEM [52] to model a large-scale COPX reactor. Minh [53] developed numerical methods for the simulation and optimization of complex processes in catalytic monoliths for two practical applications: catalytic combustion of methane and conversion of ethane to ethylene. In this study, [54] optimization of the oxidative dehydrogenation of ethane to ethylene over platinum was investigated using a two-dimensional model to simulate a single monolith channel. In the work presented in this report, an in-house three-dimensional multispecies solver is coupled with Cantera [55] to solve for the heterogeneous reactions present in catalytic reactors. The solver is also coupled with the DAKOTA [56] toolkit to perform optimization of the reactor.

Computational fluid dynamics (CFD) methods are generally classified as two distinct families of schemes: pressure-based and density-based methods. The pressure-based algorithm solves the momentum and pressure correction equations separately. The density-based solver solves the governing equations of continuity, momentum, energy and species transport simultaneously. In density-based approach, velocity field is obtained from the momentum equations and the continuity equation is used to obtain the density field. Pressure field is determined from the equation of state using computed flowfield variables. In pressure-based methods, since there is no independent equation for pressure, a special treatment is required in order to achieve velocity-pressure coupling and enforcing mass conservation. Originally, pressure-based approach was developed for low-speed incompressible flows, while density-based approach was mainly used for high-speed compressible flows. However, this distinction has been blurred in recent times as both methods have been extended and reformulated to solve for a wide range of flow conditions beyond their original intent. As majority of work involving simulation of the catalytic combustion uses pressure-based schemes, relatively less research has been performed in this field using fully coupled density-based methods. In the study presented in this report, potential of using the density-based approach for solving chemically reacting flow inside a catalytic reactor and SOFC is investigated. Since all governing equations including species, momentum and energy are solved simultaneously, very accurate solution is obtained. One of the drawbacks of the density-based methods is that

the system of equations becomes very stiff at low velocity. This problem is usually fixed by using appropriate preconditioners.

An in-house three-dimensional, multispecies solver is developed to obtain different simulation results described in this report. Two validation cases are included in this report. The first validation case compares polarization curve for a planar SOFC with the experimental results [57]. The second validation case involves catalytic oxidation of methane. In the reacting flow, mass flow rate of incoming species is considered an important parameter. Effect of different mass flow rates of incoming species on performance of SOFC as well as catalytic reactor is investigated. Another goal is implementation of formal methods to accurately and efficiently compute sensitivity derivatives. Sensitivity derivatives for different cost functions involving SOFC and catalytic reactor are computed using discrete adjoint method and direct differentiation and compared with each other for validation purposes. Effects of different design parameters on reactor performance are also investigated. The catalytic reactor is numerically optimized using two different gradient-based algorithms. One of the goals of this project is development of fluid-structure interaction capability to analyze thermal stress distribution and stress sensitivities. Application of this capability is shown for different components of SOFC in this report. Finally, results are shown for obtaining surface derivatives with respect to CAD based design parameters. This method has been developed in collaboration with the Aerospace Computational Design Laboratory of Massachusetts Institute of Technology (MIT). The surface derivatives obtained using this method are fed into a finite element mesh movement solver to modify the shape of the tubular SOFC. Application of this capability is also shown to accurately generate high-order grids when underlying CAD model has curvatures.

2. Governing Equations and Computational Methodology

2.1 Multispecies Navier-Stokes and Electric Potential Equations

The three-dimensional code utilized to perform various simulations in this project solves multi-species Navier-Stokes equations. For SOFC simulations, this model is combined with an electric potential equation that governs the distribution of electric potential and current density in the field. To solve for the surface chemistry in reforming simulations, an interface with Cantera is developed. For reforming simulations, solution of electric potential is not required, thus it is ignored. The three-dimensional model accounts for all components of the SOFC, including the anode, cathode, electrolyte, interconnects, and the fuel and air channels as well as different components of a reformer. Note that the model is not limited to any particular type of SOFC, i.e. planar as well as tubular type SOFC can be simulated using this model. The code is general enough to solve for different kind of reacting flows as well as surface chemistry reactions.

The governing equations for mass, momentum and energy conservation are solved simultaneously with the equation governing the electric potential in the numerical model. The system of equations utilized in the SOFC model is given by equations (1) - (6), which represent the conservation statements for the species concentrations,

6

momentum (x, y and z), energy and current, respectively. Equation (6) is ignored in catalytic reactor simulations.

Equations (1) – (5) are modified Navier-Stokes equations valid for both porous and fluid regions. Detailed discussion on flux formulation for these equations can be found in previous work [26]. Equation (6) represents the electric potential equation. As solid regions (interconnect and electrolyte) are considered zero-velocity regions, only energy and electric potential equations are solved inside them. Electric/ionic conductivity, σ, in equation (6) is a strong function of the temperature. Expressions describing the relationships between the electric/ionic resistivity (reciprocal of conductivity) and the temperature for various components of SOFC are presented in Table 1 [57,58] along with thermal conductivities and other material properties of different components of the SOFC.

$$\frac{\partial(\varepsilon\rho_i)}{\partial t}+\nabla\bullet(\varepsilon\rho_i\vec{V})+\nabla\bullet(\vec{J}_i)=s_i \tag{1}$$

$$\frac{\partial(\varepsilon\rho u)}{\partial t}+\nabla\bullet(\varepsilon\rho u\vec{V})=-\varepsilon\frac{\partial P}{\partial x}+\nabla\bullet(\varepsilon\tau_x)-\frac{\varepsilon^2 u\mu}{B} \tag{2}$$

$$\frac{\partial(\varepsilon\rho v)}{\partial t}+\nabla\bullet(\varepsilon\rho v\vec{V})=-\varepsilon\frac{\partial P}{\partial y}+\nabla\bullet(\varepsilon\tau_y)-\frac{\varepsilon^2 v\mu}{B} \tag{3}$$

$$\frac{\partial(\varepsilon\rho w)}{\partial t}+\nabla\bullet(\varepsilon\rho w\vec{V})=-\varepsilon\frac{\partial P}{\partial z}+\nabla\bullet(\varepsilon\tau_z)-\frac{\varepsilon^2 w\mu}{B} \tag{4}$$

$$\frac{\partial(\varepsilon E_t)}{\partial t}+\nabla\bullet(\varepsilon(E_t+P)\vec{V})+\nabla\bullet(\sum_{ns}\vec{J}_i H_i)=\nabla\bullet(\varepsilon\mu\tau\vec{V})-\nabla\bullet q^{\textit{eff}}+\nabla\phi.(\sigma\nabla\phi) \tag{5}$$

$$\nabla\bullet(\sigma\nabla\phi)=0 \tag{6}$$

As presented, equation (6) is an elliptic equation contrary to the rest of the governing equations, which are hyperbolic-parabolic equations. Equation (6) is solved in the entire domain except for the fuel and air channels, which are pure fluid regions.

Several transport processes take place at the anode-electrolyte and the cathode-electrolyte interfaces that strongly affect the overall behavior of the SOFC. The electrochemical reactions taking place at the cathode-electrolyte and anode-electrolyte interfaces can be described by equations (7) and (8), respectively.

$$0.5O_2+2e^- \rightarrow O^{2-} \tag{7}$$

$$H_2+O^{2-} \rightarrow H_2O+2e^- \tag{8}$$
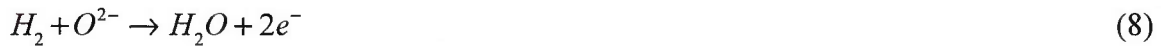
The effect of the aforementioned electrochemical reactions is modeled by applying mass flux conditions at the cathode-electrolyte (equation (9)) and anode-electrolyte (equations (10)-(11)) interfaces using Faraday's law.

$$J_{O_2} = -\frac{i}{4F} M_{O_2}$$

(9)

$$J_{H_2} = -\frac{i}{2F} M_{H_2}$$

(10)

$$J_{H_2O} = \frac{i}{2F} M_{H_2O}$$

(11)

In above equations, i is the local current density and F is Faraday's constant. A negative sign implies that the flux is leaving the interface.

Table 1. Material properties of various components of SOFC [57,58]	
Electric resistivity of anode (Ωm)	$2.98 \times 10^{-5} \exp(-1392/T)$
Electric resistivity of cathode (Ωm)	$8.11 \times 10^{-5} \exp(600/T)$
Electric resistivity of interconnect (Ωm)	6.41×10^{-8}
Ionic resistivity of electrolyte (Ωm)	$2.94 \times 10^{-5} \exp(10350/T)$
Thermal conductivity of anode $(W m^{-1} K^{-1})$	6.23
Thermal conductivity of cathode $(W m^{-1} K^{-1})$	9.6
Thermal conductivity of interconnect $(W m^{-1} K^{-1})$	9.6
Thermal conductivity of electrolyte $(W m^{-1} K^{-1})$	2.7
Porosity of anode	0.38
Porosity of cathode	0.5
Tortuosity of anode	1.5
Tortuosity of cathode	1.5
Permeability of anode (m^2)	1.0×10^{-10}
Permeability of cathode (m^2)	1.0×10^{-10}
Pore diameter of anode (m)	2.0×10^{-6}
Pore diameter of cathode (m)	2.0×10^{-6}

To account for the heat generated due to electrochemistry, heat flux proportional to the entropy change associated with the electrochemical reaction is applied at the anode-electrolyte and cathode-electrolyte interfaces. This heat flux is proportional to the molar formation rate, $(i / n_e F)$, where n_e is the number of electrons participating in the electrochemical reaction.

In addition to the electrochemical reactions, two chemical reactions, methane reforming (12.1) and water gas shift (12.2) reactions are also available when methane is used as a fuel and internal reforming is allowed.

8

$$CH_4 + H_2O \underset{kb_r}{\overset{kf_r}{\rightleftarrows}} CO + 3H_2 \tag{12.1}$$

$$CO + H_2O \underset{kb_s}{\overset{kf_s}{\rightleftarrows}} CO_2 + H_2 \tag{12.2}$$

Reaction rates for various species have been computed using the following equations.

$$Rate_r = kf_r p_{CH4} p_{H2O} - kb_r p_{CO} p_{H2}^3 \tag{13.1}$$

$$Rate_s = kf_s p_{CO} p_{H2O} - kb_s p_{CO2} p_{H2} \tag{13.2}$$

Subscripts "r" and "s" stand for reforming and shift reactions, respectively. Reaction rate constants, kf and kb, are computed using the methodology outlined in reference [28].

The voltage output of the SOFC strongly depends on several irreversibilities or losses encountered in the flowfield including activation polarization, concentration polarization and Ohmic polarization. Noren and Hoffman [59] have provided extensive discussion on accurately modeling the activation polarization. The SOFC model used in this work employs the Butler-Volmer equation to compute activation polarization [59].

The Butler-Volmer equation can be written as,

$$i = i_0 \left[\exp\left(\alpha \frac{n_e F}{R_u T} \eta_{act} \right) - \exp\left((1-\alpha) \frac{n_e F}{R_u T} \eta_{act} \right) \right] \tag{14}$$

The activation polarization is denoted by η_{act}.
α is the charge transfer coefficient and assumed to be 0.5 in the current work.
n_e represents the number of electrons involved in the electrochemical reaction, which is 2 (equations (7) and (8)) in the current simulation.
i_0 is the exchange current density and is computed using equations (15) and (16) for the anode and cathode [60], respectively.

$$i_{0,a} = \zeta_a \left(\frac{P_{H_2}}{P_{ref}} \right) \left(\frac{P_{H_2O}}{P_{ref}} \right) \exp\left(-\frac{E_{act,a}}{R_u T} \right) \tag{15}$$

$$i_{0,c} = \zeta_c \left(\frac{P_{O_2}}{P_{ref}} \right)^{0.25} \exp\left(-\frac{E_{act,c}}{R_u T} \right) \tag{16}$$

Various constants in the above equations are given in Table 2 [60]. Once the values of α and n_e are inserted in equation (14), the activation polarization can be computed using the following expression.

$$\eta_{act} = \left(\frac{R_u T}{F}\right) \sinh^{-1}\left(\frac{i}{2i_0}\right) \tag{17}$$

Ohmic polarization is a direct consequence of the resistance offered to the flow of electrons/ions inside various components of the SOFC. Voltage drop due to Ohmic resistance is directly proportional to the current and the resistance. The effect of Ohmic polarization on the voltage loss is directly included in the potential equation, equation (6), through the electric conductivity, σ, which is the reciprocal of the electric resistivity.

Table 2. Constants used to compute activation polarization [60]	
α	0.5
n_e	2
$\zeta_a (A\ m^{-2})$	5.5×10^8
$\zeta_c (A\ m^{-2})$	7.0×10^8
$E_{act,a}(J\ kmol^{-1})$	1.0×10^8
$E_{act,c}(J\ kmol^{-1})$	1.2×10^8
$P_{ref}(N\ m^{-2})$	101325

Concentration polarization is caused by reductions in the concentrations of the reacting species at the interface between the electrodes and the electrolyte. The effect of the reduction in concentrations can be seen from the well-known Nernst potential equation, given by equation (18). Also, exchange current densities at the anode-electrolyte interface and the cathode-electrolyte interface, represented by equations (15) and (16), respectively, are strongly affected by the concentration polarization.

Equation (18) computes the electromotive force (EMF) or electric potential under reversible conditions, i.e. in the absence of activation, Ohmic or any other losses.

$$EMF = EMF^0 + \frac{RT}{2F}\ln\left(\frac{\bar{P}_{H_2}\bar{P}_{O_2}^{0.5}}{\bar{P}_{H_2O}}\right), \text{ where } \bar{P}_i = \frac{P_i}{P_{ref}} \tag{18}$$

The electromotive force at standard pressure, EMF^0, is computed using polynomial thermodynamic relationship between Gibbs free energy and temperature of different species participating in the electrochemical reactions. The value of P_{ref} is taken as one atmosphere in the above equation.

The electrochemical reaction reduces the concentration of the reactants and increases the concentration of the products at the electrode-electrolyte interface. Thus, the partial pressures of the reactants and products are affected in the same manner. This will reduce the value of the second term on the right-hand side of the equation (18) thereby affecting the EMF of the cell adversely. Concentration polarization strongly

depends on the material properties of the electrodes that are responsible for the transport (diffusion and convection) of the reactants and products, to and from the electrode-electrolyte interface.

2.2 Surface Chemistry

The heterogeneous and homogeneous chemical reaction mechanisms are key components of the reacting flow modeling. The mechanism of heterogeneously catalyzed gas-phase reactions can be described by the sequence of elementary reaction steps including adsorption, surface diffusion, chemical transformations of adsorbed species, and desorption. Several modeling approaches are available to compute the reaction rates of heterogeneous reactions. Different approaches such as, Ab-initio calculation, density function theory (DFT) and kinetic Monte Carlo modeling are used to include the molecular aspects of heterogeneous catalysis. In power-law kinetic approach, rate of the catalytic reaction is calculated by fitting empirical equations to the experimental data. In the last two decades, the mean-field approximation (MF) has been used as a work-around in order to overcome the much simpler Langmuir-Hinshelwood or even power-law approaches and to include some of the elementary aspects of catalysis into models suitable for numerical simulation of catalytic reactors [61]. In the mean-field approximation, the rate equations similar to homogeneous reactions are used to model heterogeneous reactions.

In the MF model, the source term, $\dot{s}_i$, of gas-phase species due to adsorption/desorption and surface species (adsorbed species) are given by,

$$\dot{s}_i = \sum_{k=1}^{K_s} v_{ik} k_{f_k} \prod_{j=1}^{N_g+N_s} [X_j]^{v_{jk}'} \quad (i = 1, \dots, N_g + N_s) \tag{19}$$

Where K_s is the number of elementary surface reactions (including adsorption and desorption), N_s is the number of species adsorbed and N_g is the number of gaseous species. The heterogeneous flux on the surface is obtained by equation (20).

$$Flux_{het} = MW_i \dot{s}_i \tag{20}$$

Since the catalyst is dispersed as small particles in the reactor support, the active catalyst area is usually much greater than the geometric surface area. The ratio of catalyst and geometric area is defined as,

$$F_{cat/geo} = \frac{A_{catalyst}}{A_{geometric}} \tag{21}$$

To account for pore diffusion within the catalyst coating layer, the effectiveness factor, η, is defined. $F_{cat/geo}$ and η are experimentally determined. Therefore, the heterogeneous flux formula can be modified as,

$$Flux_{het} = F_{cat/geo} \eta MW_i \dot{s}_i \tag{22}$$

11

The temperature dependence of the rate coefficients in equation (19) is described by a modified Arrhenius expression shown in equation (23).

$$k_{f_k} = A_k T^{\beta_k} exp\left[\frac{-E_{a_k}}{RT}\right] \prod_{i=1}^{N_s} \Theta_i^{\mu_{ik}} exp\left[\frac{\epsilon_{ik}\Theta_i}{RT}\right] \tag{23}$$

In equation (23), Θ_i is surface coverage for species "i". For some simple surface reaction mechanisms, it is convenient to specify the surface reaction rate constant in terms of a "sticking coefficient" (probability) rather than the actual reaction rate. This approach is only allowed when there is exactly one gas-phase species reacting with the surface.

$$k_{f_k} = \frac{s_i^0}{\Gamma^\tau}\sqrt{\frac{RT}{2\pi M_i}}, \quad s_i^0 = \frac{\dot{s}_i}{1-\frac{\dot{s}_i}{2}} \tag{24}$$

In equation (24), s_i^0 is the initial (uncovered surface) sticking coefficient; τ is sum of surface reactants' stoichiometric coefficients and Γ is the surface site density (mol/m^2). Using equation (23), the equation (19) can be rewritten as,

$$\dot{s}_i = \sum_{k=1}^{K_s} v_{ik}\left(A_k T^{\beta_k} exp\left[\frac{-E_{a_k}}{RT}\right]\prod_{i=1}^{N_s}\Theta_i^{\mu_{ik}}exp\left[\frac{\epsilon_{ik}\Theta_i}{RT}\right]\right)\prod_{j=1}^{N_g+N_s}[X_j]^{v_{jk}'}$$
$$(i = 1, ..., N_g + N_s) \tag{25}$$

The surface molar concentration of a species is obtained by [62],

$$[X_i] = \Theta_i\Gamma \quad (i = N_g + 1, ..., N_g + N_s) \tag{26}$$

From equation above, $\dot{s}_i = \dfrac{\delta[X_i]}{\delta t} = \dfrac{\delta\Theta_i}{\delta t}\Gamma \tag{27}$

$$\frac{\delta\Theta_i}{\delta t} = \frac{\dot{s}_i}{\Gamma} \tag{28}$$

The surface site densities are of the order of 10^{-9} mol/cm^2 (approximately 10^{15} adsorption sites per cm^2) [63]. Equation (28) assumes that the total surface site density Γ is constant. The equation above is used for a transient simulation. In a steady-state calculation, surface species concentrations (or site fractions) remain constant with time [62], which gives,

$$\dot{s}_i = 0 \quad (i = N_g + 1, ..., N_g + N_s) \tag{29}$$

At steady state, surface species concentrations have to adjust themselves to be consistent with the adjacent gas-phase species concentrations such that the condition $\dot{s}_i = 0$ (equation (29)) is satisfied. The solution of equations (25) and (29) provide the surface coverages and the surface molar concentrations. Once these values are obtained, the source terms for the governing equations can be computed. The system of equations

generated by equations (25) and (29) is considered to be extremely stiff. C-language version of VODE, CVODE, which is included in the Sundials package, is chosen for solving these stiff equations. For coupling the flow solver with CVODE, an interface based on Cantera [55] is used. The structure of this interface is illustrated in figure 1. A Cantera input file is written based on the application including definition of gas and surface phases and detailed chemical reactions. This input file is read and used to create and allocate the Cantera gas, surface and interface objects at the beginning of the simulation. During simulation, flow solver gives the gas phase information including temperature, pressure and mole fractions of the species to Cantera. Then, Cantera sets the required parameters and sends to the CVODE solver. The surface coverages and reaction rates are computed and communicated back to the flow solver to use as the chemical source terms.
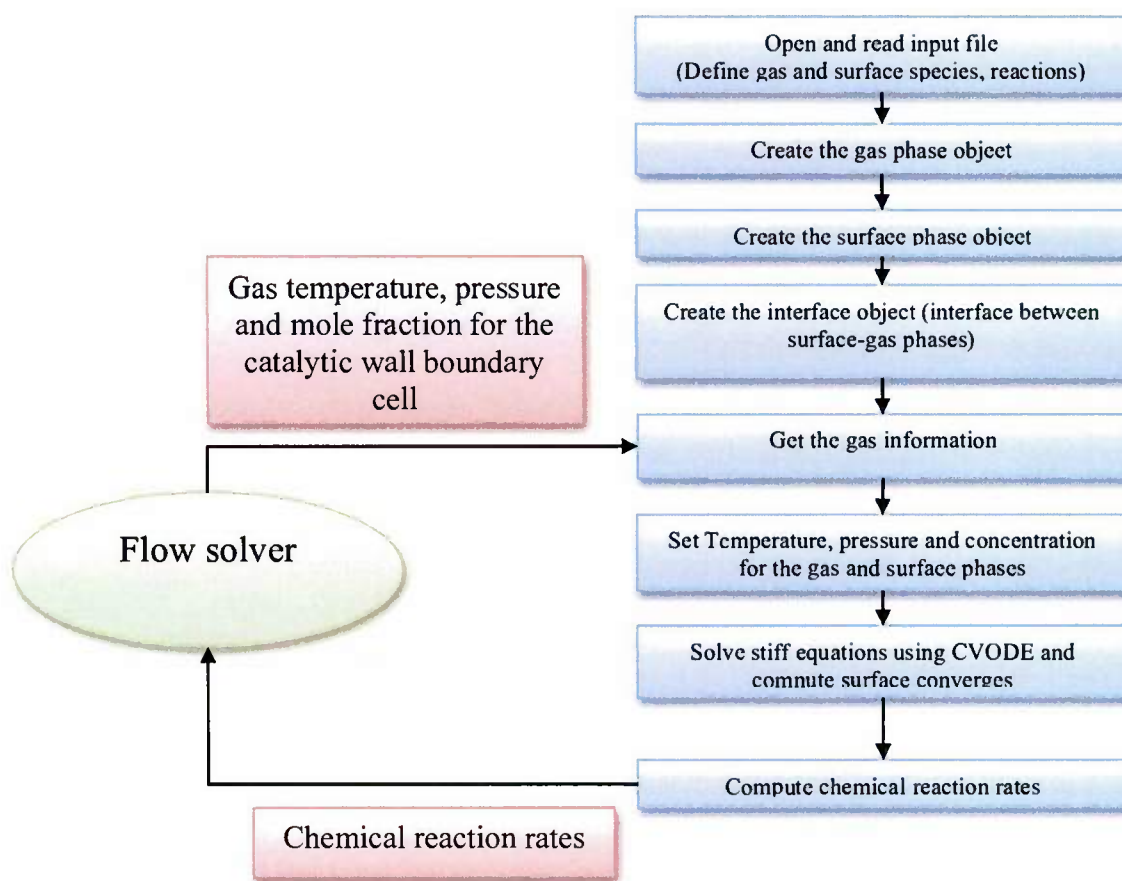
Figure1. Data exchange between the solver and Cantera through an interface

2.3 Boundary and Interface Conditions

To illustrate various boundary conditions implemented in the solver, an example of a planar SOFC is shown in figure 2. The geometry includes all relevant SOFC

components including air/fuel channels, anode, cathode, electrolyte and interconnects. No-slip, adiabatic wall boundary conditions are applied at the interfaces between the electrodes and the interconnect, as well as the side, top and bottom walls. Same boundary conditions are applied at the walls of reformers. No-slip, isothermal wall as well as catalytic wall boundary conditions are also implemented and utilized in catalytic reaction cases. Solid regions (interconnect and electrolyte) are considered zero-velocity regions and the only variables computed inside these regions are temperature and electric potential. A fixed potential ($\phi = 0$) boundary condition is applied at the bottom wall, whereas the top wall is treated by specifying average current density ($i = i_{applied}$) in SOFC simulations.

Inflow boundary conditions with specified mass flow rate and species mole fractions are applied at both fuel and air channel inlets. Specified back pressure outflow conditions are applied at both air and fuel channel outlets. Same inflow/outflow boundary conditions are applied in the reforming case. The code is capable of handling fluid, porous and solid regions as well as interfaces between them. Specific properties of different regions as well as surfaces are provided through input files.
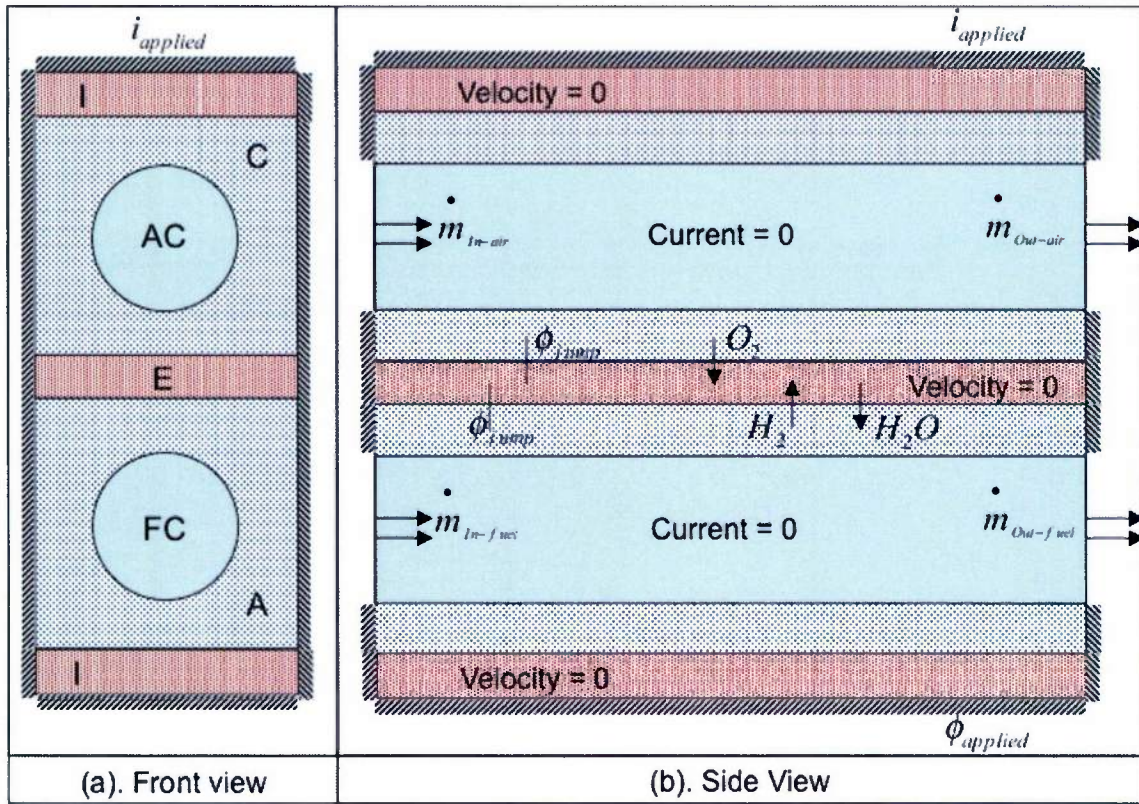
Figure 2. Boundary and interface conditions (I – Interconnect, C – Cathode, AC – Air Channel, E – Electrolyte, FC – Fuel Channel, A – Anode)

2.4 Structures

As mentioned earlier, capability to perform thermo-mechanical stress analysis has been developed to analyze stress inside different components of the SOFC and reformers. Thermo-mechanical stress analysis can be performed either fully coupled, or one-way coupled in which only one disciplinary response affects the other. Regardless of the formulation, the governing equation may be expressed as

$$\sigma_{ij,i} + b_j = \rho \frac{\partial^2 u_j}{\partial t^2} \tag{30}$$

where, σ represents the stress tensor, b the body force terms per unit mass, ρ the mass density, and u the displacement field. To cast the above equations in terms of displacements, the relationships between strain-displacement and stress-strain must be assumed. For small strains and displacements (i.e., geometric linearity), the strains are related to the deformation gradients as

$$\varepsilon_{ij} = \frac{1}{2}\left(u_{j,i} + u_{i,j}\right) \tag{31}$$

Additionally, under the assumption of linear elasticity (i.e. material linearity), the stress may be related to strain as

$$\sigma_{ij} = C_{ijkl}\left(\varepsilon_{ij} - \alpha \cdot \Delta T \cdot \delta_{kl}\right) \tag{32}$$

where, α is the coefficient of thermal expansion (which may in general be a function of temperature), ΔT the temperature difference from reference, and δ the Kronecker delta symbol. Here, the first term relates the stress to mechanical strain, and the second to the thermal strain. Assuming isotropic material behavior, the constitutive (elasticity) tensor may be conveniently written as

$$C_{ijkl} = \frac{E}{2(1+v)}\left(\delta_{il}\delta_{jk} + \delta_{ik}\delta_{jl}\right) + \frac{Ev}{(1+v)(1-2v)}\delta_{ij}\delta_{kl} \tag{33}$$

where, in general, the modulus of elasticity, E, and Poisson's ratio, v, may be functions of temperature. Currently, it is assumed that the mechanical response does not alter the temperature distribution, and therefore, a one-way coupling is utilized. Furthermore, a steady-state temperature field is applied to the structure and, hence, inertia may be neglected in the problem formulation.

The thermo-elastic structural analysis is performed using a standard displacement-based Galerkin formulation. With introduction of the stress-strain, and strain-displacement, relations into the equations of equilibrium, the Navier-displacement equations may be written (neglecting inertia) as

$$C_{ijkl}u_{k,li} + b_j = 0 \tag{34}$$

15

Integrating these equations over the volume of an element, using a standard Galerkin formulation, and assembling the element equations yields an algebraic system to be solved for the unknown nodal displacement vector {d} as

$$[K]\{d\} = \{F\} \tag{35}$$

where, the global stiffness matrix and load vector are

$$[K] = \sum \int [B]^T [C][B] dV \tag{36}$$

$$\{F\} = \sum \int [N]^T \{b\} dV + \sum \int [N]^T \{t\} dS + \sum \int [N]^T [C]\{\alpha \cdot \Delta T\} dV \tag{37}$$

Here, $[N]$ represents the element shape function matrix, which relates the displacement field to the element nodal displacements, and $[B]$ is the so-called strain-displacement matrix, which relates the element strains to the nodal displacements. The first term of the load vector represents body forces acting over the volume of the domain, the second term represents forces due to traction or stress ($t_i = \sigma_{ij}\eta_j$, where η_j are the components of the unit outward pointing normal) acting on the boundaries of the domain, whereas the last term are the loads resulting from the thermal strains.

The solution to the resulting system may be accomplished with either an iterative or direct method. Iterative solution algorithms can be beneficial for very large systems, which may prohibit direct solution methods, or for systems, which do not have symmetric, damping matrices. The direct method uses a sparse Cholesky decomposition based on skyline storage scheme. A preconditioned GMRES [64] is utilized to solve the system iteratively.

Once the nodal displacements have been determined, the strain and stress fields may be computed. In multidimensional problems, the individual components of the stress tensor do not provide adequate information in order to ascertain the proximity to failure or yielding of the material. In these regards, different stress measures are typically used. For brittle materials, the maximum in plane principal stress is typically used. The principal planes are those in which the shear stress vanishes and, therefore, are the planes that have maximum normal stress. Since brittle materials tend to fail due to normal stress, appropriate failure criteria are usually based on maximum principal stress. For ductile materials, which tend to fail in shear, typically either the von Mises or the Tresca yield criteria are used. The von Mises yield criterion uses the assumption that the onset of yield is based on the second deviatoric stress invariant. The Tresca yield surface is circumscribed by the von Mises yield surface, representing a more conservative criterion for prediction of plastic yielding.

3. Design and Sensitivity Analysis

The three-dimensional code developed is capable of computing sensitivity derivatives that can be utilized in optimization process for minimizing a specified cost

16

function, which is indicative of the performance of the system. The code is capable of computing sensitivity derivatives using either discrete adjoint method or direct differentiation method. Depending upon the design problem, one or other method provides higher efficiency. For example, discrete adjoint method is computationally efficient for design problems with large number of design variables.

A general optimization procedure begins by first defining a meaningful cost function and a desired set of design variables. A numerical analysis of the baseline system is then performed. The results of the analysis include the solution variables Q of the discretized partial differential equations, which are subsequently used to determine the initial cost. Because the numerical analysis involves discretization of the partial differential equations on a computational mesh, it should be noted that Q represents the vector of solution variables where each element of the vector is representative of one or more physical variables located at each mesh point, χ.

3.1 Discrete Adjoint Method

The cost function may have an explicit dependence on the vector of design variables, β, but will also have an implicit dependence because Q and χ may also depend on the design variables. Therefore, the cost function is typically written to indicate the implicit and explicit dependence on the design variables as,

$$f = f(Q(\beta), \chi(\beta), \beta) \tag{38}$$

If R represents the vector of discrete residuals at each mesh point, an augmented cost function L can be defined in terms of the original cost function and the vector of discrete residuals as,

$$L(Q(\beta), \chi(\beta), \beta, \Lambda) = f(Q(\beta), \chi(\beta), \beta) + \Lambda^T R(Q(\beta), \chi(\beta), \beta) \tag{39}$$

In equation (39), Λ is the vector of Lagrange multipliers (also known as costate variables). Note that the augmented cost function, L, is a scalar quantity that is identical to the original cost function f, when $R(Q)$ is zero, indicating that the steady-state solution is obtained. Differentiating the augmented cost function with respect to each of the design variables yields the following set of equations for $\dfrac{dL}{d\beta}$, which is a column vector where each element represents the derivative of the augmented cost function with respect to a particular design variable.

$$\frac{dL}{d\beta} = \left\{ \frac{\partial f}{\partial \beta} + \left[\frac{\partial \chi}{\partial \beta} \right]^T \frac{\partial f}{\partial \chi} \right\} + \left[\frac{\partial Q}{\partial \beta} \right]^T \left\{ \frac{\partial f}{\partial Q} + \left[\frac{\partial R}{\partial Q} \right]^T \Lambda \right\} + \left\{ \left[\frac{\partial R}{\partial \beta} \right]^T + \left[\frac{\partial \chi}{\partial \beta} \right]^T \left[\frac{\partial R}{\partial \chi} \right]^T \right\} \Lambda \tag{40}$$

Because the elements of Λ are arbitrary, the second term, which involves the derivatives of the dependent variables with respect to the design variables, can be

17

eliminated by solving a linear system of equations for the costate variables, also known as the adjoint equation.

$$\left[\frac{\partial R}{\partial Q}\right]^{T} \Lambda = -\left\{\frac{\partial f}{\partial Q}\right\} \tag{41}$$

Once the costate variables are obtained, the derivatives of the cost function with respect to all the design variables are obtained using a matrix-vector multiplication.

$$\frac{dL}{d\beta} = \left\{\frac{\partial f}{\partial \beta} + \left[\frac{\partial \chi}{\partial \beta}\right]^{T}\frac{\partial f}{\partial \chi}\right\} + \left\{\left[\frac{\partial R}{\partial \beta}\right]^{T} + \left[\frac{\partial \chi}{\partial \beta}\right]^{T}\left[\frac{\partial R}{\partial \chi}\right]^{T}\right\}\Lambda \tag{42}$$

In numerical simulations, the largest computational cost of computing sensitivity derivatives using the adjoint equations is due to the solution of the analysis and adjoint equations, both of which are independent of the number of design variables. The only dependency on the number of design variables is in the evaluation of equation (42), which is generally much cheaper to compute than either the analysis or adjoint solutions.

Note that the terms in equations (40) - (42) involve differentiation of the discrete residual R, the cost function f, and the computational mesh χ with respect to the dependent variables Q, the design variables β, and the location of the mesh points χ. Correct implementation of this procedure can be extremely tedious to accomplish by hand and the resulting code can be difficult to maintain. To overcome the difficulties associated with hand differentiation, the complex-variable technique of Burdyshaw et al. [16] and Nielsen et al. [24] has been used for evaluating all the terms in the matrices required for solving the adjoint equations and for evaluating equation (42) once the costate variables have been obtained. Although the original development of the complex-variable technique is described in the literature [14], a detailed derivation of complex variable technique is also given by Kapadia et al. [26] along with the detailed discussion on relative benefits and drawbacks of complex variable method in comparison to automatic differentiation and finite difference methods.

3.2 Direct Differentiation

Sensitivity derivatives can also be computed using the direct differentiation method. Derivation of this method using the chain rule is shown in equations (43) – (46).

$$\frac{df(Q(\beta),\chi(\beta),\beta)}{d\beta} = \frac{\partial f}{\partial \beta} + \frac{\partial f}{\partial Q}\frac{\partial Q}{\partial \beta} + \frac{\partial f}{\partial \chi}\frac{\partial \chi}{\partial \beta} \tag{43}$$

Now, $R(Q(\beta),\chi(\beta),\beta)=0$ \hfill (44)

$$\Rightarrow \frac{dR}{d\beta} = \frac{\partial R}{\partial \beta} + \frac{\partial R}{\partial Q}\frac{\partial Q}{\partial \beta} + \frac{\partial R}{\partial \chi}\frac{\partial \chi}{\partial \beta} = 0 \tag{45}$$

$$\Rightarrow \left[\frac{\partial R}{\partial Q}\right]\left\{\frac{\partial Q}{\partial \beta}\right\} = -\left\{\frac{\partial R}{\partial \beta}\right\} - \frac{\partial R}{\partial \chi}\frac{\partial \chi}{\partial \beta} \tag{46}$$

As seen, computation of $\partial Q/\partial \beta$ is an essential component of this method, which requires the solution of a linear system of equations for each design variable. This requirement makes direct differentiation methods computationally expensive for problems with many design variables. However, as derivatives of dependent variables with respect to the design variables are computed at each node in the flowfield, this method is particularly useful when there are many flowfield constraints. Direct differentiation method is utilized in this report for computing sensitivity derivatives in a case describing fluid-structure interaction capability for planar SOFC.

3.3 Mesh Sensitivity

Shape is one of the most important parameters in computational design of physical systems. The three-dimensional code is capable of computing sensitivity derivatives of desired cost function with respect to different shape parameters. Shape parameter can range from a single mesh point to the surface shape and size of different components of the system. A parameterization technique to represent the shape of the computational domain has been developed and described in Section 3.4. To maintain the quality of the mesh during a design cycle, a methodology is required to compute the displacements of the interior nodes when the underlying geometry is modified. The present simulations use the linear elasticity equations as applied in reference [64] to compute these displacements as shown in equation (47).

$$[\Gamma]\chi = \chi_{surface} \tag{47}$$

The matrix, $[\Gamma]$, is formed by applying a finite-volume method to the linear elasticity equations and $\chi_{surface}$ denotes the displacements applied to the surface nodes. Note that, $[\Gamma]$ does not depend on the vector of the design variables, β. Thus, by differentiating equation (47) with respect to β, mesh sensitivities, $\partial \chi/\partial \beta$ can be obtained.

$$[\Gamma]\frac{\partial \chi}{\partial \beta} = \frac{\partial \chi_{surface}}{\partial \beta} \tag{48}$$

Using equation (48), mesh sensitivities are computed separately for each shape parameter and are then used in equation (42) for determining the sensitivity derivatives of the overall cost function. Because this procedure is repeated for each design variable, it can be computationally prohibitive for three-dimensional design problems when many parameters are present. To overcome this difficulty, the method developed by Nielsen and Park [65] has been implemented in the current study. In this technique, satisfaction of the mesh equation given by equation (47) is included as a further constraint in the augmented cost function.

$$L(Q(\beta), \chi(\beta), \beta, \Lambda) = f(Q(\beta), \chi(\beta), \beta) + \Lambda^T R(Q(\beta), \chi(\beta), \beta)$$
$$+ \Lambda_g^T \left(\left[\Gamma \right] \chi - \chi_{surface} \right) \tag{49}$$

Here, Λ_g is the vector of co-state variables associated with the mesh displacements. The last term in equation (49) represents the residual of the linear system presented in equation (47), which is zero when the solution is converged. Thus, equation (49) maintains the original value of the desired cost function, f. Equation (50) is obtained by following the same procedure used in deriving equation (42).

$$\frac{dL}{d\beta} = \frac{\partial f}{\partial \beta} + \left[\frac{\partial R}{\partial \beta} \right]^T \Lambda + \left[\frac{\partial Q}{\partial \beta} \right]^T \left\{ \frac{\partial f}{\partial Q} + \left[\frac{\partial R}{\partial Q} \right]^T \Lambda \right\}$$
$$+ \left[\frac{\partial \chi}{\partial \beta} \right]^T \left\{ \frac{\partial f}{\partial \chi} + \left[\frac{\partial R}{\partial \chi} \right]^T \Lambda + \left[\Gamma \right]^T \Lambda_g \right\} - \Lambda_g^T \left[\frac{\partial \chi_{surface}}{\partial \beta} \right] \tag{50}$$

Finally, the grid adjoint problem, equation (51), is derived by solving for Λ_g to eliminate the mesh sensitivity term, $(\partial \chi / \partial \beta)^T$ in a similar manner as the first adjoint problem.

$$\left[\Gamma \right]^T \Lambda_g = - \frac{\partial f}{\partial \chi} - \left[\frac{\partial R}{\partial \chi} \right]^T \Lambda \tag{51}$$

Note that with this procedure, Λ is first obtained and subsequently used on the right-hand side of equation (51). Although equation (51) represents an additional linear system of equations, the effects of mesh sensitivities for each design variable are accounted for in a programming loop extending only over surface coordinates and eliminates the need for multiple solutions of equation (47). By combining equations (41), (50) and (51), sensitivity derivatives of an augmented cost function can be computed using equation (52).

$$\frac{dL}{d\beta} = \frac{\partial f}{\partial \beta} + \left[\frac{\partial R}{\partial \beta} \right]^T \Lambda - \Lambda_g^T \left[\frac{\partial \chi_{surface}}{\partial \beta} \right] \tag{52}$$

3.4 Parameterization

3.4.1 Control Grids

A parameterization method has been developed to improve the flexibility and speed in which a shape design problem can be defined. This method uses a construct called a control grid [66], which is associated with the surface mesh upon which shape modification is desired. Referring to Figure 3(a), design variables are defined on the boundaries of the control grid as perturbation sources, which are then propagated through

the domain via the solution of an elliptic PDE (Laplacian) over the control grid volume. The perturbations at the surface grid points are then obtained by interpolation from the surrounding nodes on the control grid. This procedure is applicable when disparate meshes have been generated for multidisciplinary analysis. Because the resulting surface displacements are linear functions of the design variables, the parameterization need only be computed for the original surface mesh. Subsequent shape deformations are then computed as a linear combination of the design variable values and their associated sensitivity derivatives, which are also computed only for original surface. This tool has been used to define a parameterization for a wide variety of shapes, including turbomachinery blades, wing/spar combinations, and an inlet s-duct. An example design case performed using this technique is shown in Figure 3(b) and 3(c). As seen in the figures, a surface for an aerodynamic analysis and an interior mesh representing the underlying structure are both represented. As the shape changes in response to adjustments in the design variables, both meshes deform in unison thereby maintaining a watertight geometry. This parameterization technique has been utilized to provide design variables to control the width of the 17 fuel channels of a manifold while treating the baffles as rigid bodies [27]. Same technique is applied for a single-channel SOFC, where design variables are located on the top and bottom walls of the fuel channel [27].

(a). Control grid

| (b). Initial design | (c). Final design |
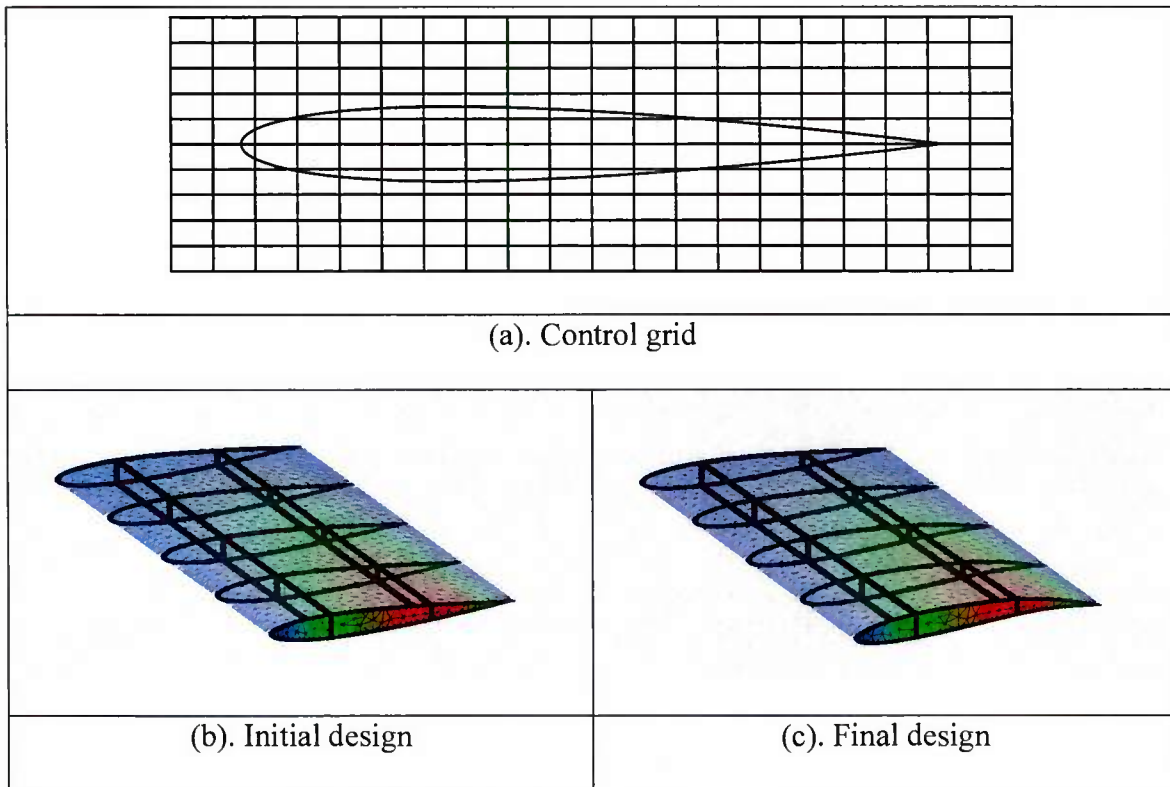
Figure 3. Parameterization

3.4.2 CAPRI

CAPRI [67] is a methodology developed by the Aerospace Computational Design Laboratory at the Massachusetts Institute of Technology (MIT). This technology provides

an Application Programming Interface (API) to allow vender neutral communication with CAD software. Through coordination with Dr. Bob Haimes at MIT (the developer of CAPRI), a framework has been developed for integrating CAPRI with the SimCenter's geometry libraries. With this capability, design variables used in the construction of the underlying geometry can be exposed through the API's, thereby allowing them to be used directly as design variables during an optimization process. The advantage of this approach is that after a simulation-based design improvement has been completed; the geometry is represented in CAD format so the new configuration can be manufactured without first having to "re-loft" the geometry.

Another important application of this capability lies in higher-order finite element simulations. While this interface had been originally developed for purposes of design optimization, it is also used for placing additional nodes or quadrature points onto the actual surface geometry as defined by the CAD definition. During this process, as boundary elements are curved to conform to the original geometry configuration, collapsed elements are likely to be generated, particularly when highly stretched elements are applied in the viscous boundary layer. In this context, a robust mesh movement strategy must be employed to accommodate the projection of the surface meshes for two or three-dimensional geometries. Here exclusive use is made of a modified linear elasticity theory, which assumes that the computational mesh obeys the isotropic linear elasticity relations. More information about this methodology is given in Section 3.5.

3.5 Mesh Movement

One of the most important steps in the shape design process is to utilize the surface derivatives and modified design parameters to perform volumetric mesh deformation. The volumetric shape deformation is computed by solving linear elasticity equations, (53) –(55). A finite volume linear elasticity solver is utilized to perform this task. A newly developed finite element method can also be used and supports higher-order spatial accuracy, which adds more flexibility and is compatible with future development plans at the SimCenter. This solver is utilized in results shown in Section 4.6.

$$\frac{\partial}{\partial x}\left[d_{11}\frac{\partial u}{\partial x} + d_{12}\frac{\partial v}{\partial y} + d_{13}\frac{\partial w}{\partial z}\right] + \frac{\partial}{\partial y}\left[d_{44}\left[\frac{\partial u}{\partial y} + \frac{\partial v}{\partial x}\right]\right] +$$
$$\frac{\partial}{\partial z}\left[d_{66}\left[\frac{\partial u}{\partial z} + \frac{\partial w}{\partial x}\right]\right] = 0 \tag{53}$$

$$\frac{\partial}{\partial x}\left[d_{44}\left[\frac{\partial u}{\partial y} + \frac{\partial v}{\partial x}\right]\right] + \frac{\partial}{\partial y}\left[d_{21}\frac{\partial u}{\partial x} + d_{22}\frac{\partial v}{\partial y} + d_{23}\frac{\partial w}{\partial z}\right] +$$
$$\frac{\partial}{\partial z}\left[d_{55}\left[\frac{\partial v}{\partial z} + \frac{\partial w}{\partial y}\right]\right] = 0 \tag{54}$$

22

$$\frac{\partial}{\partial x}\left[d_{66}\left[\frac{\partial u}{\partial z} + \frac{\partial w}{\partial x}\right]\right] + \frac{\partial}{\partial y}\left[d_{55}\left[\frac{\partial v}{\partial z} + \frac{\partial w}{\partial y}\right]\right] +$$
$$\frac{\partial}{\partial z}\left[d_{31}\frac{\partial u}{\partial x} + d_{32}\frac{\partial v}{\partial y} + d_{33}\frac{\partial w}{\partial z}\right] = 0 \tag{55}$$

where,
$$d_{11} = \frac{E(1-v)}{(1+v)(1-2v)} \qquad d_{12} = \frac{Ev}{(1+v)(1-2v)} \qquad d_{44} = \frac{E}{2(1+v)}$$
$$d_{11} = d_{22} = d_{33}, \qquad d_{12} = d_{13} = d_{21} = d_{23} = d_{31} = d_{32}, \qquad d_{44} = d_{55} = d_{66}$$

In equations (53) – (55), displacements in x, y and z directions are denoted by u, v and w, respectively. "E" and "v" denote modulus of elasticity and Poison's ratio, respectively. While utilizing CAPRI interface and linear elasticity solver to generate higher-order meshes, modulus of elasticity is set to be proportional to the inverse of wall distance, to enable the nodes closer to boundaries to present higher rigidity for maintaining the fidelity of the boundary-layer region. The value of Poison's ratio should be in the range of -1 and 0.5. For higher-order finite element work, a constant value of 0.25 is set and is found to be effective to transmit surface deformation into the interior while capable of producing valid high-aspect-ratio cells.

3.6 Optimization

Sensivity analysis can be used to choose the design parameters that have strong influence on objective function and ignore non-important parameters. This information is helpful prior to an optimization study. In addition, sensitivy derivitives are essential part of many optimization algoithms, especially gradeint-based methods. In gradient-based methods, gradients of the response functions are computed to find the direction of improvement. Gradient-based optimization is the search method that underlies many efficient local optimization methods. A drawback to this kind of methods is that computing gradients is expensive. However, by using methods like discrete ajoint and direct diffrention this cost can be decreased significantly when a large number of design parameters are present.

Optimization is the minimization or maximization of a cost function subjected to constrains on its variables. The optimization problem can be defined as,

$$\min f(x)_{x \in \mathbb{R}^n} \text{ subject to } g_i(x) \leq 0 \quad i \in I \tag{56}$$

where f is the objective function, a function of x that we want to optimize. x is a vector of design variables. There are several methods for solving an optimization problem. Table 3 summerizes some of these methods and their properites.

Several optimization software packages have been developed in the past. For this study, DAKOTA toolkit is used. The DAKOTA (Design Analysis Kit for Optimization and Terascale Applications) was developed by the engineers at the Sandia National Laboratories [56]. DAKOTA's optimization capabilities include a wide variety of gradient-based and nongradient-based optimization methods. It includes many

extenal optimization libraries such as the OPT++ library [68], CONMIN and DOT libraries [69].

Optimization method	Properties
Table 3. The optimzation methods and properties	
Gradient descent method	- Slow convergence (convergence rate is linear) - Zig-zag back and forth behavior
Newton's method	- Requires computation of Hessian - Quadratic convergence rate - Requires a good initial gauss - Can be unstable - Can be converged to maximum
Gauss-Newton method	- Can be unstable
Conjugate gradient method	- Requires line search - Does not need explicit second derivatives

An interface is created to link the flow solver to DAKOTA. Figure 4 shows the workflow involving an in-house solver and DAKOTA. The output file from DAKOTA containing new values for the solver is "params.in". This file is created by DAKOTA during each design cycle.
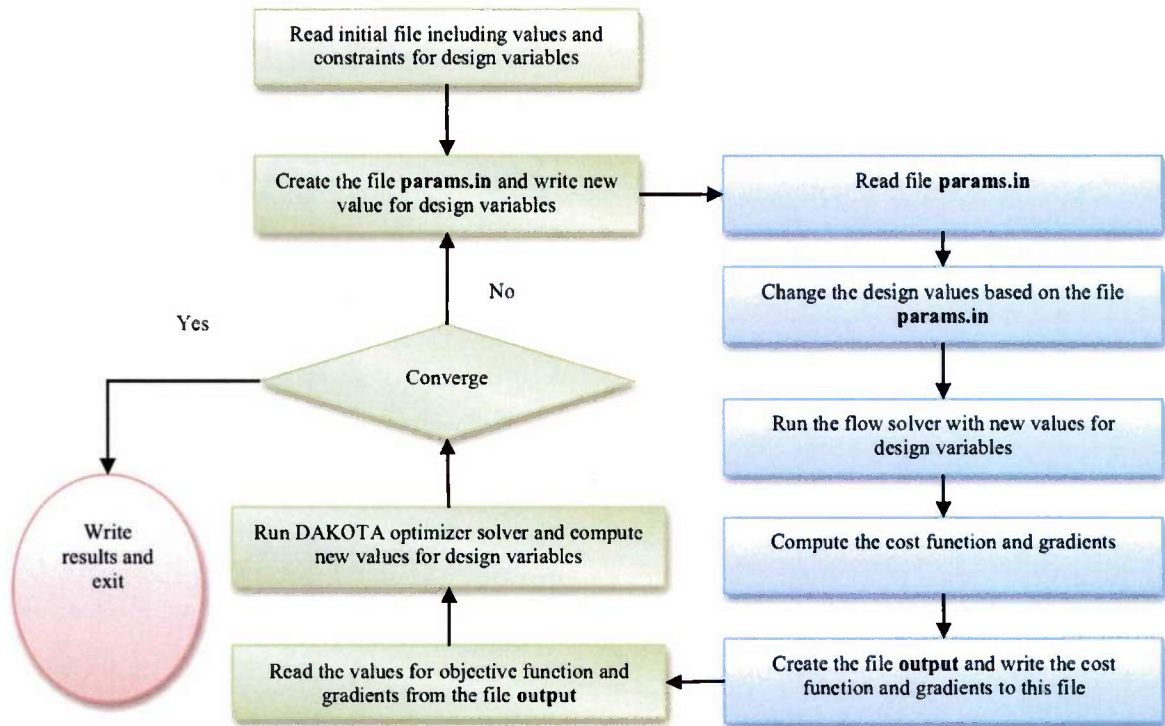
Figure 4. The data interchange and interface between the flow solver and DAKOTA

24

3.7 Solution Procedure

In the three-dimensional solver, flowfield variables are computed using an unstructured, implicit, finite-volume scheme. The solver is vertex centered and the discrete residual at each node is computed by integrating the governing equations, (1) – (6) over a median dual control volume. Because a steady-state solution is the primary goal of the current work, time accuracy of the solution is sacrificed by allowing local time-stepping to accelerate convergence.

To reduce computer time, the solution is obtained using multiple processors utilizing the message-passing interface (MPI) [70] and necessary grid decomposition is achieved using METIS [71]. Original grids are generated using the commercial software Pointwise [72].

An implicit Euler scheme is used to solve the non-linear system as given by equations (1) - (6). A flux-difference splitting scheme based on the ROE scheme [73,74] for a multi-component mixture is derived to model the convective fluxes. A central-difference formulation is used to compute all the second-order derivative terms. Linear systems encountered in both the flowfield and sensitivity solvers are solved using the GMRES [64] method with ILU-K preconditioner.

A domain decomposition tool has been developed to split computational domain into any number of subdomains. This tool is capable of generating internal interfaces, which are essential for multidisciplinary applications that contain domains with different properties. The tool is also capable of generating higher order grids using initial linear grid for higher-order finite element applications. Currently, this tool is being utilized for multidisciplinary simulation applications including, CFD, electromagnetics and batteries.

4. Results and Discussion

4.1 Code Validation

In this section, code validation results for baseline solution and sensitivity derivatives are presented for SOFC simulations. The geometry utilized in these simulations is the same as used by Wang et al. [57]. One of the main reasons for using this geometry is the availability of an experimental polarization curve [57] that can be used to validate the in-house, three-dimensional multi-species Navier-Stokes solver.

4.1.1 Baseline Solution

The fuel mixture is assumed to contain hydrogen and steam only, i.e. chemistry is not present in the validation case. Air is modeled as a mixture of oxygen and nitrogen. Species mole fractions of the fuel mixture and air entering the respective channels are given in Table 4. The operating pressure, temperature and mass flow rates of fuel and air are also given in Table 4. Wang et al. [57] has obtained the polarization curve under the same operating conditions as described in Table 4. Surface grid of the computational domain is shown in Figure 5.

Table 4. Operating conditions utilized in polarization curve							
X_{H_2}	X_{H_2O}	X_{O_2}	X_{N_2}	$T(K)$	$P(N/m^2)$	$\overset{g}{m}_{fuel}(kg/s)$	$\overset{g}{m}_{air}(kg/s)$
0.9578	0.0422	0.198	0.802	1273 K	101325	5.94×10^{-7}	2.15×10^{-5}

       A comparison between the experimental polarization curve [57] and the polarization curve obtained using the numerical model is shown in figure 6. As can be seen, the overall comparison is satisfactory. The numerical tool successfully predicts the shape of the polarization curve and obtains results that are within two percent of the experimental data at low current densities and are essentially identical to the experimental data at higher current densities. As expected, the cell voltage reduces with increasing current density due in part to Ohmic losses which are linearly proportional to the current density. Also, increase in current draws more hydrogen and oxygen from the anode-electrolyte and the cathode-electrolyte interfaces, respectively and produces more steam. This reduces the value of "EMF" in equation (18) i.e. concentration polarization increases. Thus, the cumulative effects of Ohmic polarization and concentration polarization are evident in Figure 6.
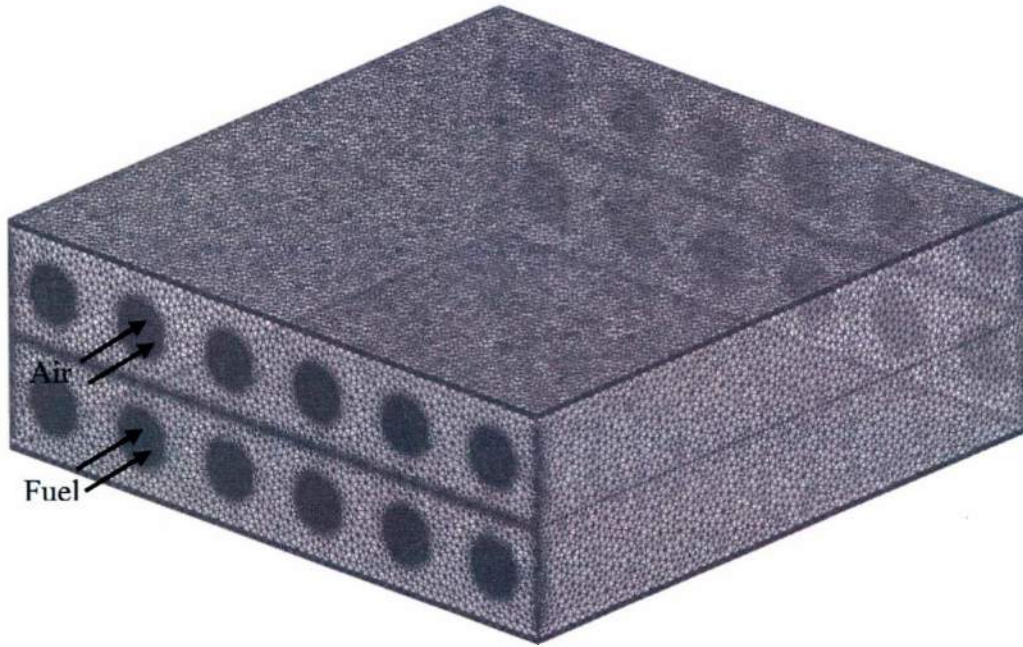
Figure 5. Surface Mesh
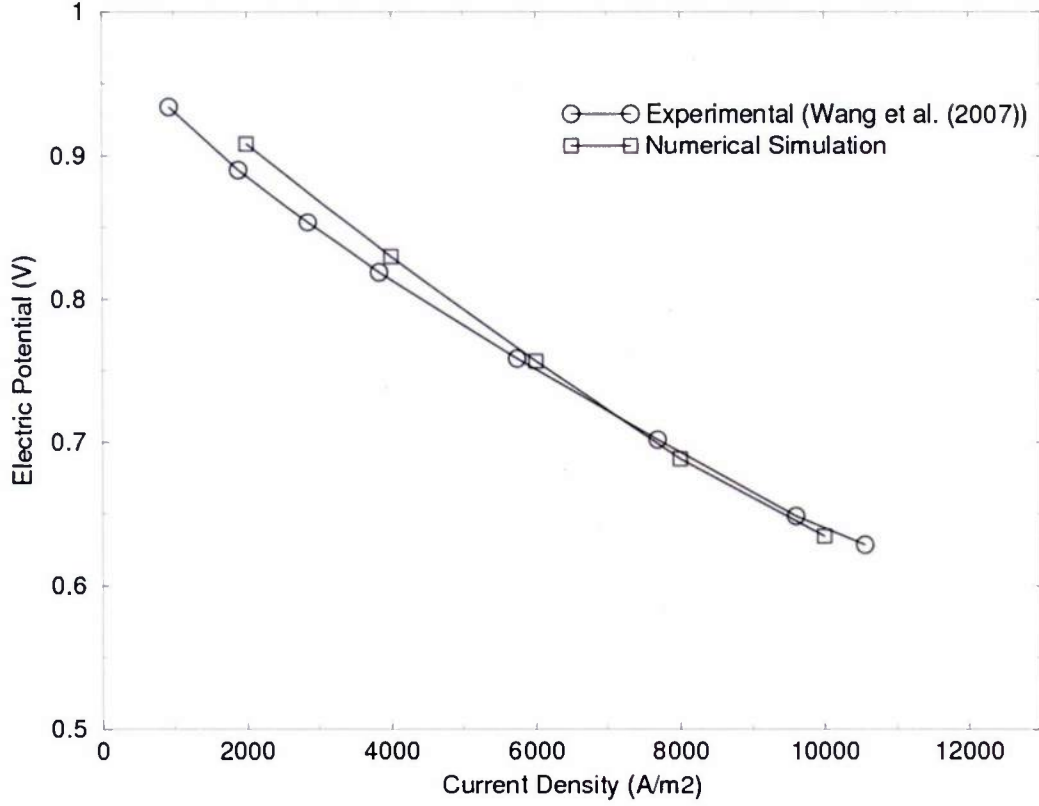
Figure 6. Polarization curve

4.1.2 Sensitivity Derivatives

In this study, the following two cost functions are considered.

Cost -1: Cell voltage – equation (57.1).

Cost -2: Term responsible for the concentration polarization at the anode-electrolyte interface – equation (57.2).

$$f_1 = \frac{1}{S_t} \iint_{S_t} \phi \, ds \quad S_t - \text{Surface area of the top surface} \tag{57.1}$$

$$f_2 = \frac{1}{S_e} \iint_{S_e} \frac{R_u T}{2F} \ln\left(\frac{P_{H_2}}{P_{H_2O}}\right) ds \quad S_e - \text{Surface area of the anode-electrolyte interface} \tag{57.2}$$

It should be noted that the sensitivity results described in this section assume H_2 / H_2O as the fuel mixture. The operating conditions are the same as described in Table 4 and the applied current density is $4000 \, A/m^2$.

Improving power output is the ultimate goal of the SOFC design. If current density is fixed, the power output can be improved by increasing the cell voltage. Thus, the first cost function chosen in this study is the cell voltage. Sensitivity derivatives of the cost function representing the cell voltage with respect to various design parameters can be extremely useful in the design cycle.

27

The second cost function represents the term responsible for the concentration polarization at the anode-electrolyte interface. As seen, equation (57.2) exhibits an interesting nature due to its explicit dependence on the species partial pressures and the temperature. Also, improvement in concentration polarization can increase the SOFC performance and thus, it is chosen as the second cost function in sensitivity studies.

Six design parameters are included to compute sensitivity derivatives of the aforementioned objective functions. The design parameters are comprised of the material properties of the anode and the cathode including porosity, tortuosity and mean pore radius.

To validate the implementation of the discrete adjoint method, sensitivity derivatives computed using the discrete adjoint method are compared with the same derivatives computed using the direct differentiation method and the finite difference method. Note that the sensitivity derivatives computed using central finite difference method require two flowfield solutions for each design variables. To reduce computational efforts, the comparison study is performed using a single channel geometry (original geometry contains six channels) and coarse grid. Relevant physics included for the original geometry is included in the comparison study.

Tables 5 and 6 show the comparisons amongst sensitivity derivatives computed using the different methods for the Cost-1 and Cost-2, respectively. As seen, sensitivity derivatives computed using the discrete adjoint method and direct differentiation method match up to 9 to 11 digits. This comparison is excellent. Also, matching significant digits between finite difference results and the discrete adjoint method results vary between 2 to 4. Due to subtractive cancellation errors, it is hard to find an optimum step size when the finite difference method is used to compute sensitivity derivatives. Thus, comparison between finite difference derivatives and the discrete adjoint derivatives are considered satisfactory.

Table 5. Validation of adjoint implementation (Cost 1)			
D.V.	Discrete Adjoint	Direct Differentiation	Finite Difference
ε_a	-1.4136629036e-02	-1.4136629036e-02	-1.411798953e-02
κ_a	-3.4924988954e-03	-3.4924988954e-03	-3.491000966e-03
$<r>_a$	8.7578106870e+02	8.7578106869e+02	8.754119812e+02
ε_c	2.7292696323e-03	2.7292696322e-03	2.761454211e-03
κ_c	-1.4976041763e-03	-1.4976041763e-03	-1.497321755e-03
$<r>_c$	1.8945315028e+02	1.8945315028e+02	1.894163071e+02

A run-time comparison between the discrete adjoint and direct differentiation method is shown in Table 7. Note that this comparison is made using the coarse mesh

utilized for Tables 5 and 6. As mentioned before, the direct differentiation method requires the solution of a linear system for each design variable. Thus, the run-time of a direct differentiation method is a linear function of the number of design variables. On the other hand, the discrete adjoint method only requires the solution of a single linear system and the dependency on the number of design variables is that a matrix-vector product must be computed for each design variable.

Table 6. Validation of adjoint implementation (Cost 2)			
D.V.	Discrete Adjoint	Direct Differentiation	Finite Difference
ε_a	-1.3870751906e-02	-1.3870751907e-02	-1.38668867e-02
κ_a	-3.5959382450e-03	-3.5959382450e-03	-3.59483888e-03
$<r>_a$	9.0264297426e+02	9.0264297426e+02	9.02379501e+02
ε_c	1.6938729757e-03	1.6938729757e-03	1.69193541e-03
κ_c	8.7332085595e-05	8.7332085595e-05	8.75493837e-05
$<r>_c$	-1.0164312515e+01	-1.0164312515e+01	-1.01922398e+01

Table 7. Run-time comparison between adjoint and direct differentiation methods		
	Adjoint	Direct Differentiation
Run-time (sec)	125	571

Once implementation of the discrete adjoint method is validated, the next step in the design process is to compute sensitivity derivatives for the actual geometry. Table 8 shows the sensitivity derivatives of both cost functions obtained using the discrete adjoint method for the original geometry.

Table 8. Sensitivity derivatives computed using discrete adjoint method		
D.V.	f_1	f_2
ε_a	-1.0110037400e-02	-1.0899218104e-02
κ_a	-5.0238174308e-03	-5.1098651595e-03
$<r>_a$	1.1323025342e+03	1.1549498370e+03
ε_c	3.3425032057e-03	2.3809517707e-04
κ_c	-1.6269401390e-03	-1.2959807450e-05
$<r>_c$	2.0610982993e+02	-7.5667688361e-01

4.2 Mass Flow Rate Effects

In this section, effects of mass flow rate variations on objective function are investigated for two different cases. The first case utilizes pure hydrogen as fuel and the second case utilizes fuel mixture containing methane. The second case also includes chemical reactions of steam reforming as well as shift reaction.

Mass flow enforcement is required to accurately model the physics of the given problem. Previously, continuous back pressure adjustment was required to achieve the desired mass flow rate. Recently, better control over mass flow rate enforcement has been achieved by re-formulating boundary conditions including, inlet, outlet and no-slip walls.

Figure 7 shows the relationship between the mass flow rate of fuel and the cell voltage. The fuel composition and operating conditions (temperature and pressure) are the same as shown in Table 4. The air mass flow rate is also constant at $\dot{m}_{air} = 1.76 \times 10^{-4} kg / \sec$ and the applied current density is specified as $4000\, A / m^2$. Fuel mass flow rate has been increased gradually to analyze its effect on output voltage. As can be seen, the cell voltage increases with increases in fuel mass flow rate. As described earlier, the three major contributors to the voltage loss in SOFC are Ohmic polarization, concentration polarization and activation polarization. For the particular case shown in Figure 7, concentration polarization plays a major role in deciding the variation in cell voltage with the fuel mass flow rate. Concentration polarization strongly depends on the partial pressures of hydrogen, steam and oxygen, as given by equation (18). The term responsible for the concentration polarization in equation (18) is $\ln\left(\dfrac{\overline{P}_{H_2} \overline{P}_{O_2}^{0.5}}{\overline{P}_{H_2O}} \right)$. The value of $\overline{P}_{O_2}^{0.5}$ can be assumed constant for different cases in Figure 7 as current density and air mass flow rate remain constant. Thus, the determining factor for the voltage loss is the ratio of partial pressures of hydrogen to steam, which becomes smaller as the mass flow rate of fuel is reduced and thus, affecting concentration polarization adversely. As seen in Figure 7, the effect of concentration polarization is weak for the cases with higher mass flow rate but becomes more prominent once the fuel mass flow rate reduces below $\dot{m}_{fuel} = 1.0 \times 10^{-6} kg / \sec$, which indicates that some part (near the fuel channel outlet) of the anode-electrolyte interface may be starving due to high fuel utilization. This eventually contributes towards a reduction in electrochemical activity in the affected regions.
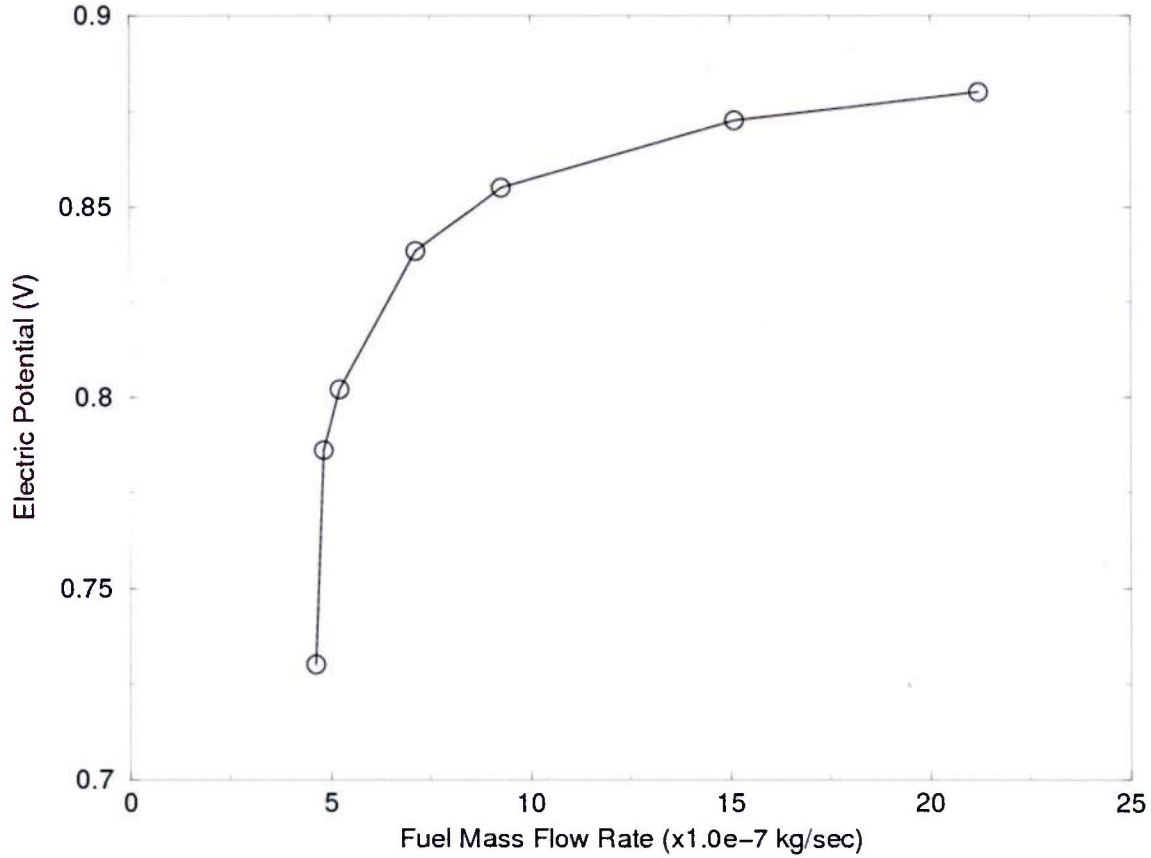
Figure 7. Voltage vs. Mass flow rate (Operating conditions: Table 4)

Results presented in Figure 7 utilize a H_2 / H_2O mixture as fuel and does not include chemistry inside the electrodes. To demonstrate the combined effect of chemistry/electrochemistry on SOFC performance, a fuel mixture containing H_2, H_2O, CO, CO_2 and CH_4 is used in the next case. Air is modeled as a mixture of O_2 / N_2. Mole fractions of various species and operating conditions utilized in this case are described in Table 7. Two chemical reactions, namely, methane reforming, equation (57.1) and water-gas shift reaction, equation (58.2) are present inside the anode.

$$CH_4 + H_2O \underset{kb_r}{\overset{kf_r}{\rightleftarrows}} CO + 3H_2 \qquad (58.1)$$

$$CO + H_2O \underset{kb_s}{\overset{kf_s}{\rightleftarrows}} CO_2 + H_2 \qquad (58.2)$$

Methane reforming is an endothermic reaction and tends to reduce the temperature of the system. The shift and electrochemical reactions are both exothermic and tend to increase the temperature of the system. Also, methane reforming is a fast reaction that finishes rapidly in the region located near the fuel channel inlet. The size of this region depends on the mass flow rate of the fuel.

31

Table 7. Operating conditions utilized in Figure 8								
X_{CO}	X_{H_2O}	X_{CO_2}	X_{H_2}	X_{CH_4}	$P(N/m^2)$	$T(K)$	X_{O_2}	X_{N_2}
0.029	0.493	0.044	0.263	0.171	101325	1273 K	0.198	0.802

To investigate the effect of fuel mass flow rate on the cell voltage, several cases were run using operating conditions described in Table 7 with a fixed air flow rate of $\dot{m}_{air} = 1.76 \times 10^{-4} kg/\sec$ and constant current density of $4000 \, A/m^2$. The fuel mass flow rate is reduced gradually and its effect on voltage output is plotted in figure 8. Even though the operating conditions utilized in the present case (figure 8) and the previous case (figure 7, H_2/H_2O mixture) are the same except for the fuel type, the nature of plots is opposite in figures 7 and 8.
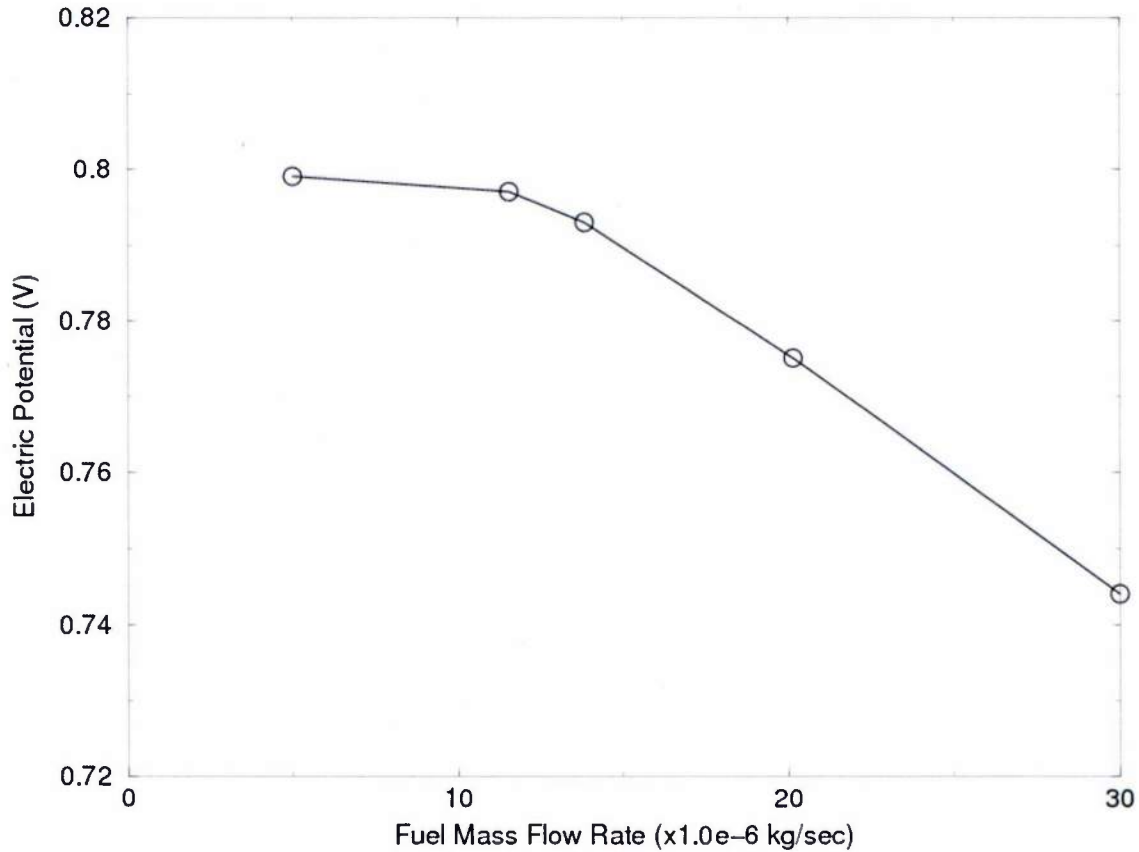
Figure 8. Voltage vs. Mass flow rate (Operating conditions: Table 7)

As seen in figure 8, cell voltage reduces with increases in the fuel mass flow rate, which is opposite to the trend found in figure 7. As described earlier, the reduction in flow rate of fuel increases concentration polarization, which is responsible for the voltage drop. In the previous case, as no chemical reactions were present (thus, no hydrogen source), the relationship between the fuel flow rate and the cell voltage is straightforward.

However, the same is not true for the current case and the reason is described in the next paragraph.

Concentration of H_2O increases at the anode-electrolyte interface due to the electrochemical reaction and additional H_2O diffuses inside the anode. This additional H_2O triggers methane reforming and shift reactions described by equations (58.1) and (58.2), respectively. In these reactions, H_2O participates as reactant and produces hydrogen and thus, increases the value of the term $\ln\left(\dfrac{\bar{P}_{H_2}\,\bar{P}_{O_2}^{0.5}}{\bar{P}_{H_2O}}\right)$. Due to these complicated interactions amongst chemical-electrochemical reactions, the concentration polarization does not necessarily increase with the reduction in fuel flow rate for the plot shown in figure 8. Thus, other modes of voltage losses or polarizations are required to be investigated to determine the reasons behind the nature of the plot shown in figure 8.

1273.0 1282.3 1291.7 1301.0 1310.3
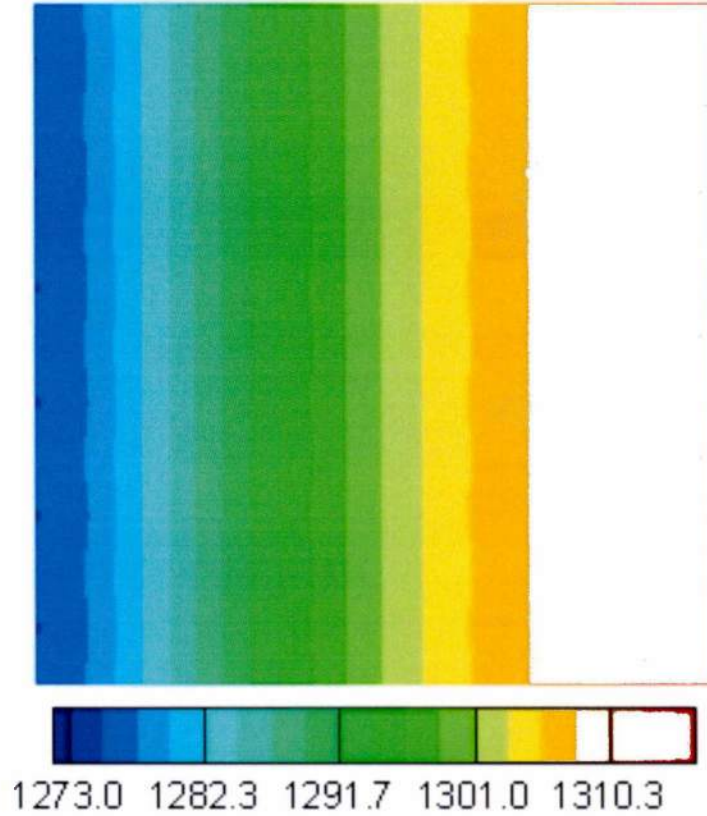
Figure 9. Temperature contours at the anode-electrolyte interface
$(\dot{m}_{fuel} = 4.98 \times 10^{-6}\,kg\,/\sec)$

Figures 9 and 10 show temperature contours plotted at the anode-electrolyte interface for two different points in figure 8. Figure 9 represents the location with the lowest mass flow rate of fuel $(\dot{m}_{fuel} = 4.98 \times 10^{-6}\,kg\,/\sec)$ and figure 10 represents the

location with the highest fuel flow rate $(\dot{m}_{fuel} = 30.02 \times 10^{-6} \, kg \, / \sec)$. The difference between the lowest and the highest temperature points in both figures is approximately 40 K. However, the average temperature in figure 9 is approximately 73 K higher than that in figure 10. Even though the electrochemical reaction produces the same amount of heat in both cases (due to the same current density), fluid that is flowing slower (figure 9) is heated more than the fluid that is flowing faster (figure 10). As described earlier, methane reforming is an extremely fast endothermic reaction and thus, the reduction in temperature caused by the reforming reaction remains similar in both cases. The next step is to determine the effect of temperature on Ohmic losses in both cases.

1200.0 1209.4 1218.8 1228.2 1237.6
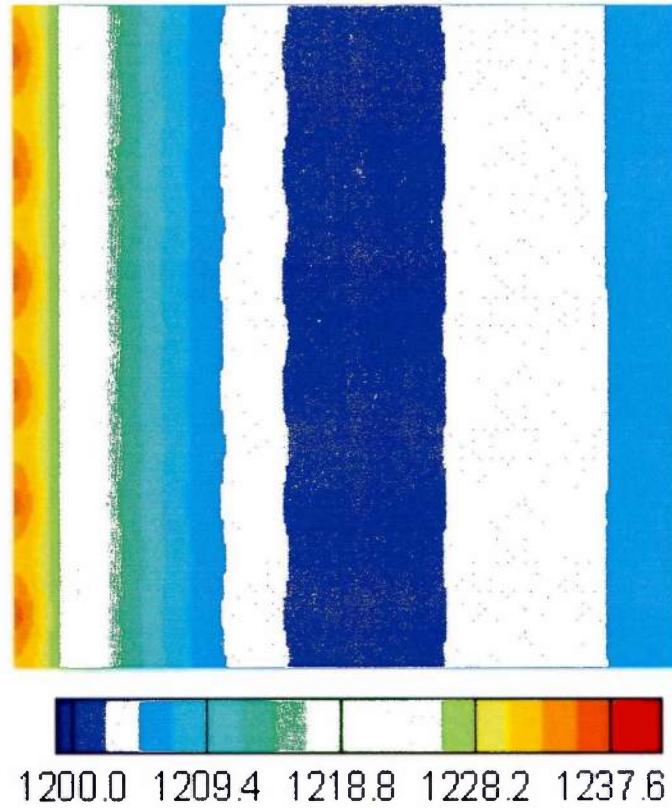
Figure 10. Temperature contours at the anode-electrolyte interface
$(\dot{m}_{fuel} = 30.02 \times 10^{-6} \, kg \, / \sec)$

Figures 11 and 12 show the electric potential distribution inside the electrolyte (z-plane) for the cases representing the lowest $(\dot{m}_{fuel} = 4.98 \times 10^{-6} \, kg \, / \sec)$ and the highest $(\dot{m}_{fuel} = 30.02 \times 10^{-6} \, kg \, / \sec)$ mass flow rates of fuel, respectively. The electrolyte thickness is 0.05 mm and acts as a main contributor in Ohmic losses. As seen, the voltage drop inside the electrolyte for the case with the highest fuel flow rate (figure 12) is almost twice the voltage drop for the case with the lowest fuel flow rate (figure 11).

Electric Potential (V)

0.891 0.894 0.897 0.9 0.903 0.906
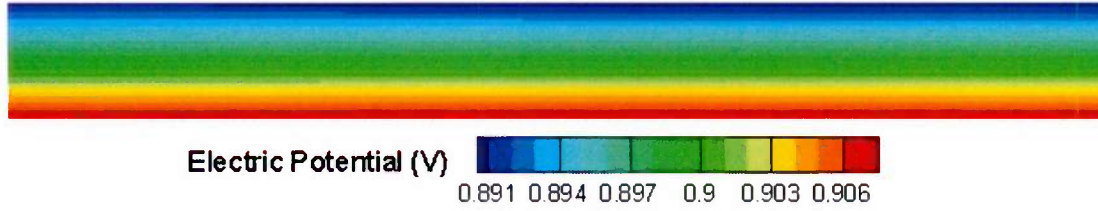
Figure 11. Ohmic losses inside the electrolyte $(\dot{m}_{fuel} = 4.98 \times 10^{-6} kg / \sec)$

Electric Potential (V)

0.868 0.877333 0.886667 0.896
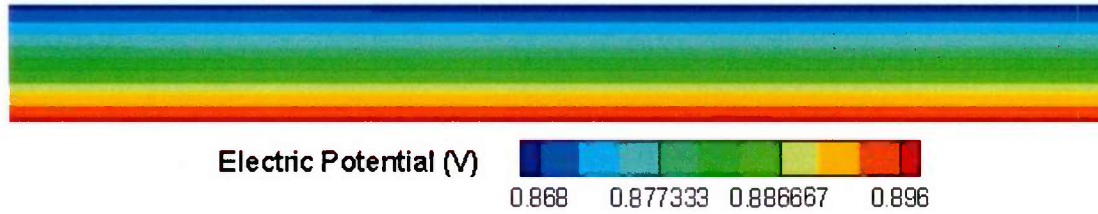
Figure 12. Ohmic losses inside the electrolyte $(\dot{m}_{fuel} = 30.02 \times 10^{-6} kg / \sec)$

As mentioned earlier, the electric/ionic resistivities of various components of the SOFC are strong functions of the temperature. To further investigate the effect of temperature, various values of electric/ionic resistivities for the anode, the cathode and the electrolyte are shown in Table 8 for a temperature range of 1100 K – 1300 K. As seen, the ionic resistivity of the electrolyte reduces by almost half when the temperature is raised from 1100 K to 1200 K. The same is true when the temperature is increased from 1200 K to 1300 K. This dependence can be correlated with the voltage drop found in figures 11 and 12 for the cases with the lowest fuel flow rate and the highest fuel flow rate, respectively. Note that the electric resistivity of the cathode is also reduced with increase in temperature but that the increase is not as significant as found for the electrolyte and also, the value of the resistivity is approximately three orders smaller than that in the electrolyte. Thus, the voltage drop due to the Ohmic polarization in the cathode can be assumed to be constant for both cases. Also, Ohmic polarization inside the anode can be ignored due to a very small size (compared to the electrolyte resistivity) of the electric resistivity of the anode.

Table 8. Relationship between electric/ionic resistivity and temperature			
Temperature (K)	Anode	Cathode	Electrolyte
1100	8.40691e-06	0.000139929	0.358644
1200	9.34189e-06	0.000133711	0.163733
1300	1.02138e-05	0.000128666	0.0843334

4.3 Catalytic Partial Oxidation of Methane

4.3.1 Baseline Solution and Validation

In this section, catalytic partial oxidation of methane over Rh/Al₂O₃ coated honeycomb is numerically investigated. The honeycomb-structured reactors are widely used in many engineering applications such as the fuel reformers, catalytic convertor and gas turbine combustors. For code validation purposes, experimental work conducted by Hettel et al. [50] is selected. The reactor is a 2 cm diameter cylinder with 260 channels and a channel density of 600 cpsi (channels per square inch). The initial and boundary conditions are summarized in Table 9. The simulations are performed with the detailed heterogeneous oxidation mechanism proposed by Deutschmann et al. [75]. It includes 38 heterogeneous reactions and 20 surface-adsorbed species. The site density is assumed to be 2.79×10^{-9} mol/cm^2. The kinetic data of the surface-reaction mechanisms are taken from the literature. Eight gas-phase species (CH_4, CO_2, H_2O, N_2, O_2, CO, OH and H_2) are considered for the simulation. The surface chemistry is modeled using the mean-field approximation. Homogenous combustion in the gas phase is ignored in this study since it has no the significant effect on the flow field for this test case and operating conditions [76]. Computational grid is comprised of 122208 tetrahedral cells. Figure 13 shows the surface grid of the computational domain representing one channel of the monolith. The grid is refined in the regions near catalytic wall to accurately resolve boundary layers. The "inflow" boundary condition is used at the channel inlet and a fully developed boundary condition is considered for the outlet. The no-slip boundary condition with catalytic reaction source term is applied at the channel walls. The temperature of the catalytic wall is assumed to be constant along the channel. The nonlinear system of equations obtained from the discretization is solved using Newton's method. The convergence history of the solution is shown in figure 14.

Table 9. Initial and boundary conditions for catalytic combustion of methane	
Gas inlet velocity	0.329 m/s
Gas inlet temperature	1000 K
Wall temperature	1000 K
Gas inlet compositions(mole fraction)	$x_{CH_4} = 0.133$ $x_{O_2} = 0.067$ $x_{N_2} = 0.8$
Working pressure	1 atm
Channel width	1 mm
Channel length	10 mm

Figure 13. Surface grid
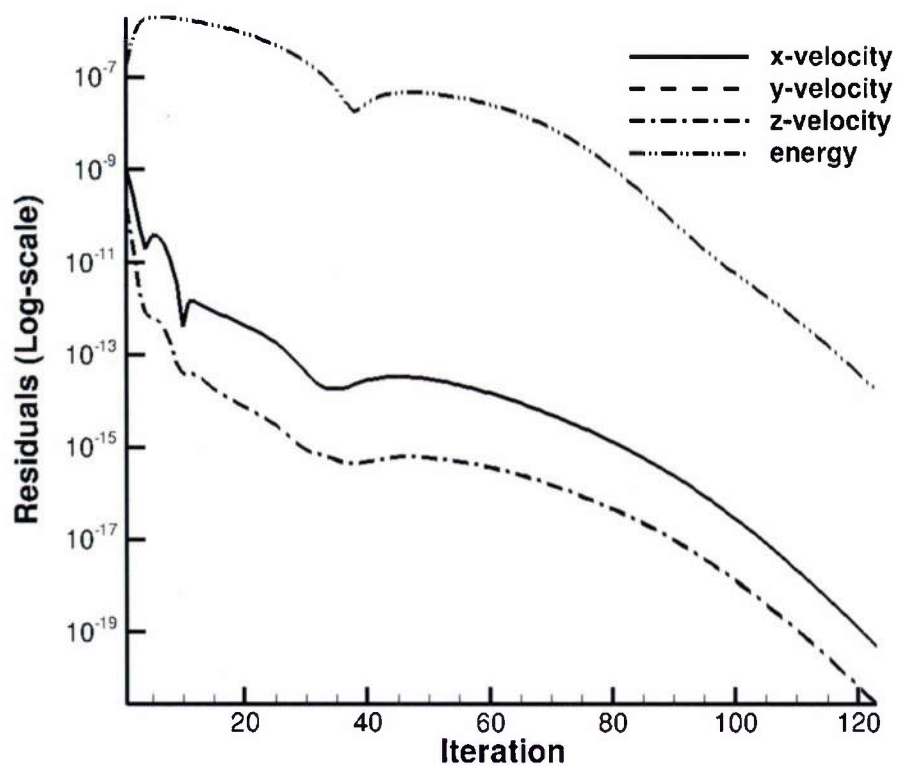
Figure 14. Convergence history

Figure 15 shows the comparison between the numerical results and experimental data for the species mole fractions as a function of position in the reactor. As indicated

in the figure 15, the good agreement is obtained. The methane oxidation starts instantly at the inlet of the reactor. As expected, oxygen is completely consumed in the first few millimeters of the reactor.
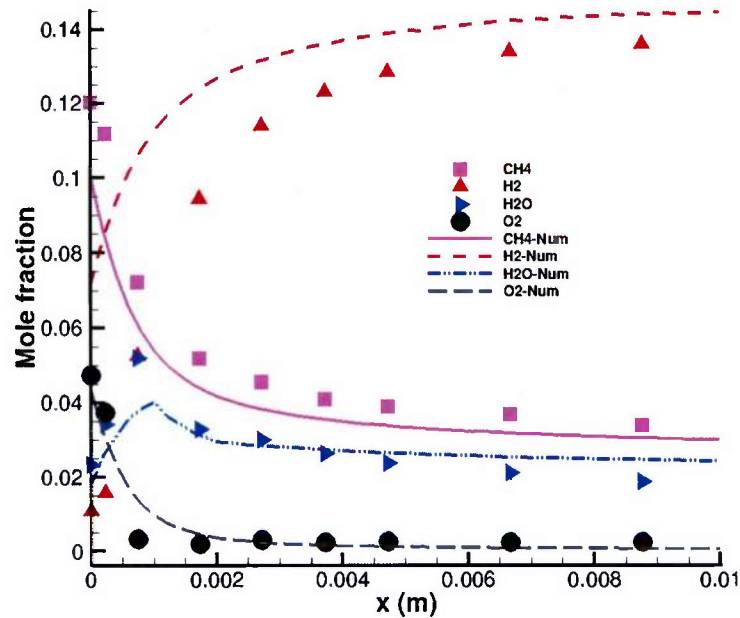
Figure 15. Comparison between the numerical results and experimental data for the partial oxidation of methane
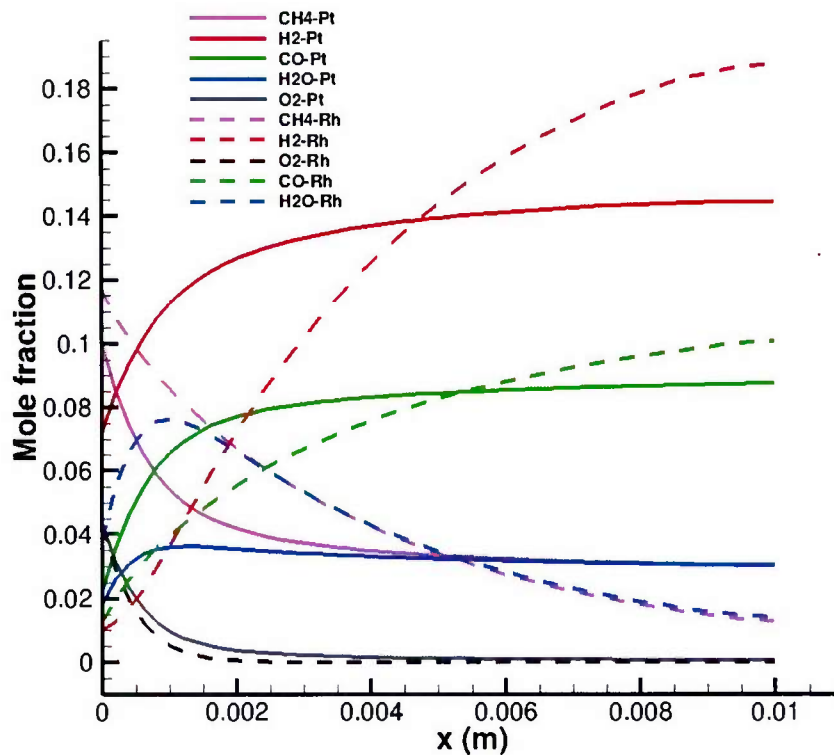
Figure 16. Species mole fraction along reformer symmetry axis for Rh and Pt catalyst

Rhodium and platinum are considered good catalysts in terms of stability and yields. They are widely used for partial oxidation and catalytic combustion of methane in fuel reformers, catalytic burners and catalytic gas turbines. To better understand the performance of methane reformer with these two catalysts, numerical simulations are performed. The detailed heterogeneous oxidation mechanisms developed by Deutschmann et al. [75] (24 heterogeneous reactions and 11 surface-adsorbed species) and Deutschmann et al. [77] (38 heterogeneous reactions and 20 surface-adsorbed species) are used to model surface chemistry for rhodium and platinum, respectively. The temperature of catalyst wall is fixed to 1070 K. The inlet velocity is considered to be 0.5 m/s. Figure 16 shows the mole fraction of species along symmetry axis of the reformer for both catalysts. As seen, oxygen is completely consumed (conversion of 99%) in both cases. Rhodium shows better performance for partial oxidation of methane (conversion of 90%) than platinum (conversion of 77%).

(a)

(b)

(c)

(d)

(e)

(f)
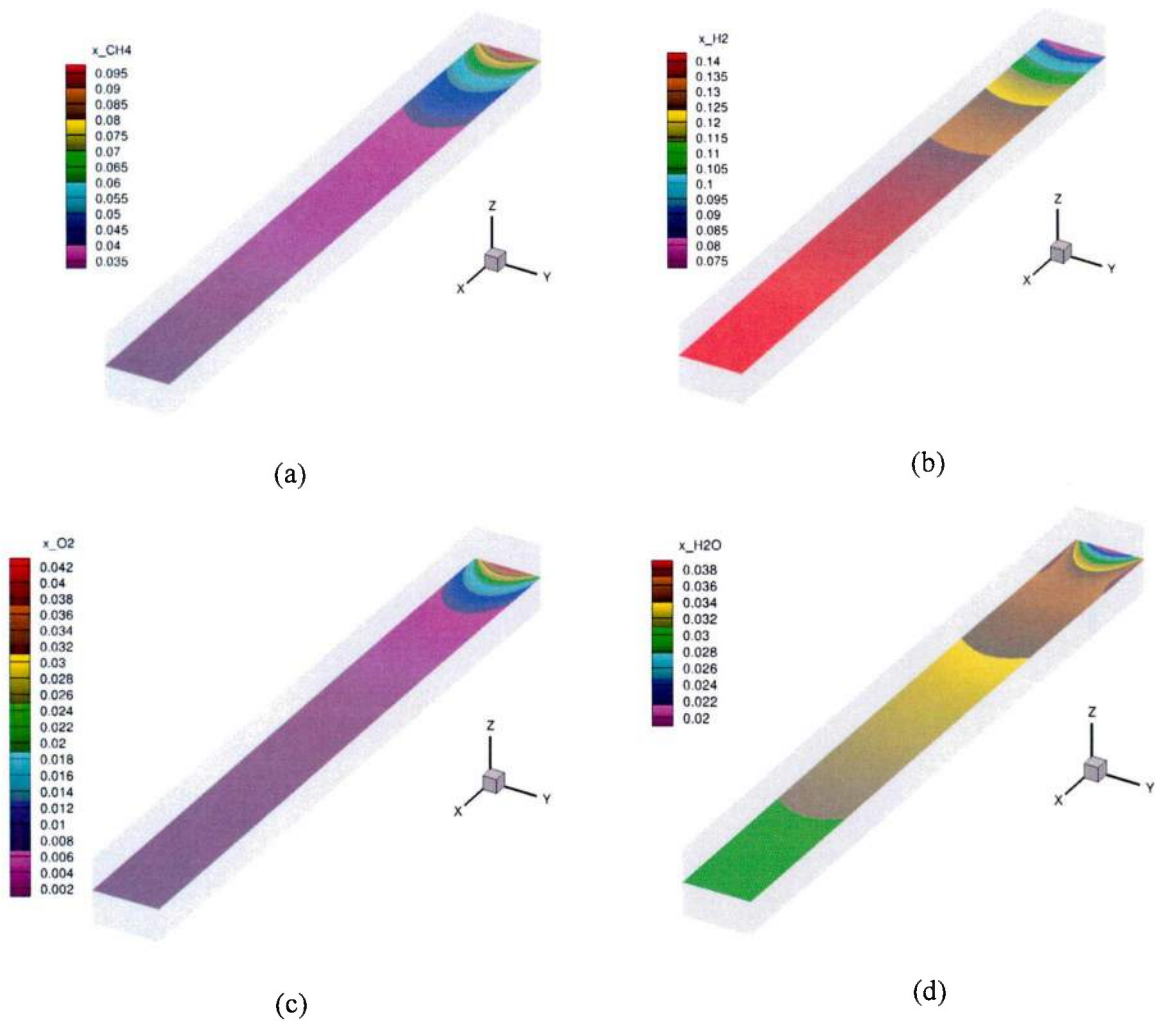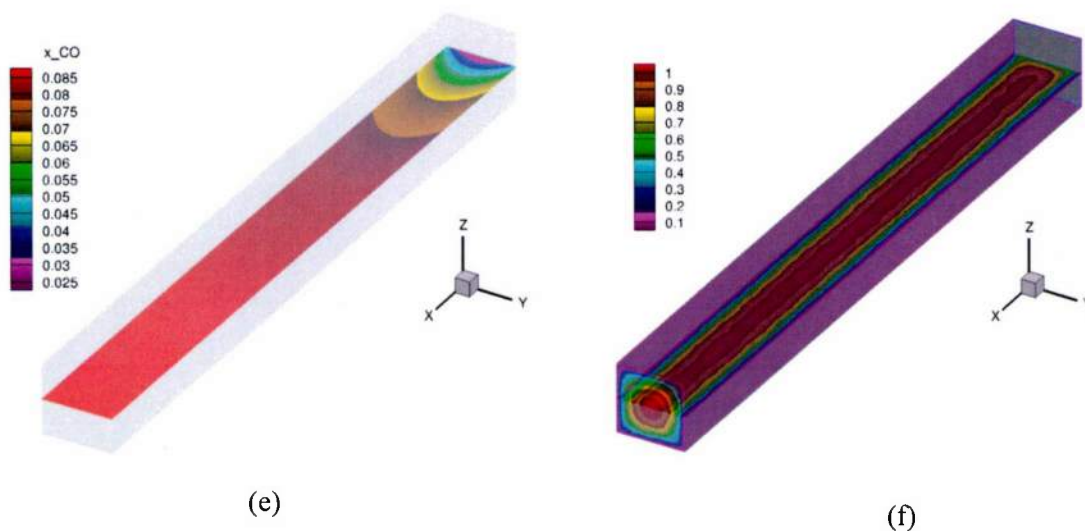
Figure 17. Species mole fractions and streamwise velocity (Pt catalyst)

Figures 17 and 18 show species mole fraction contours for reactors with platinum and fhodium, respectively. Streamwise velocity contours are also shown in figure 17(f). The gradient of hydrogen mole fraction is smaller across the cross section of the channel as hydrogen has higher diffusion coefficient relative to other species considered in this simulation. The maximum velocity in the channel is close to 1 m/s.

(a)

(b)

40

(c)

(d)

(e)
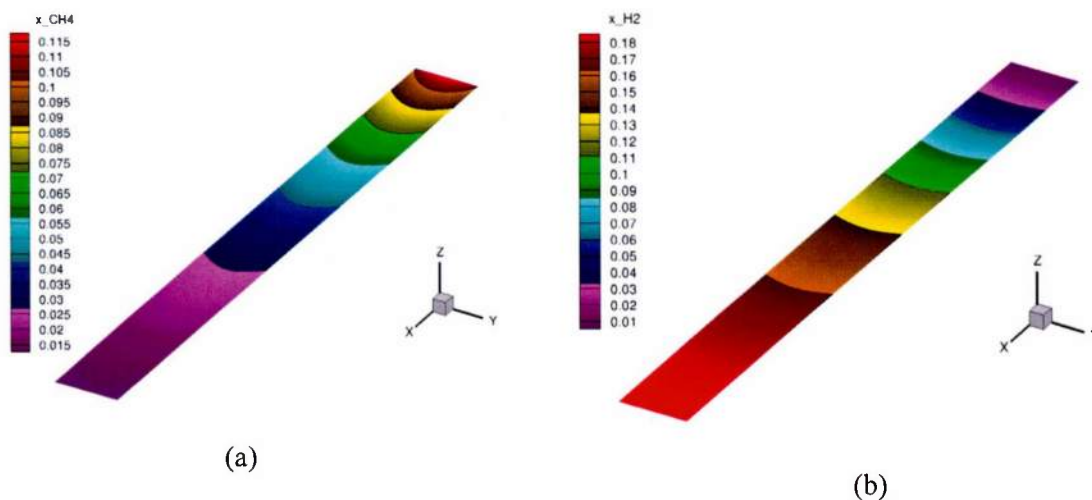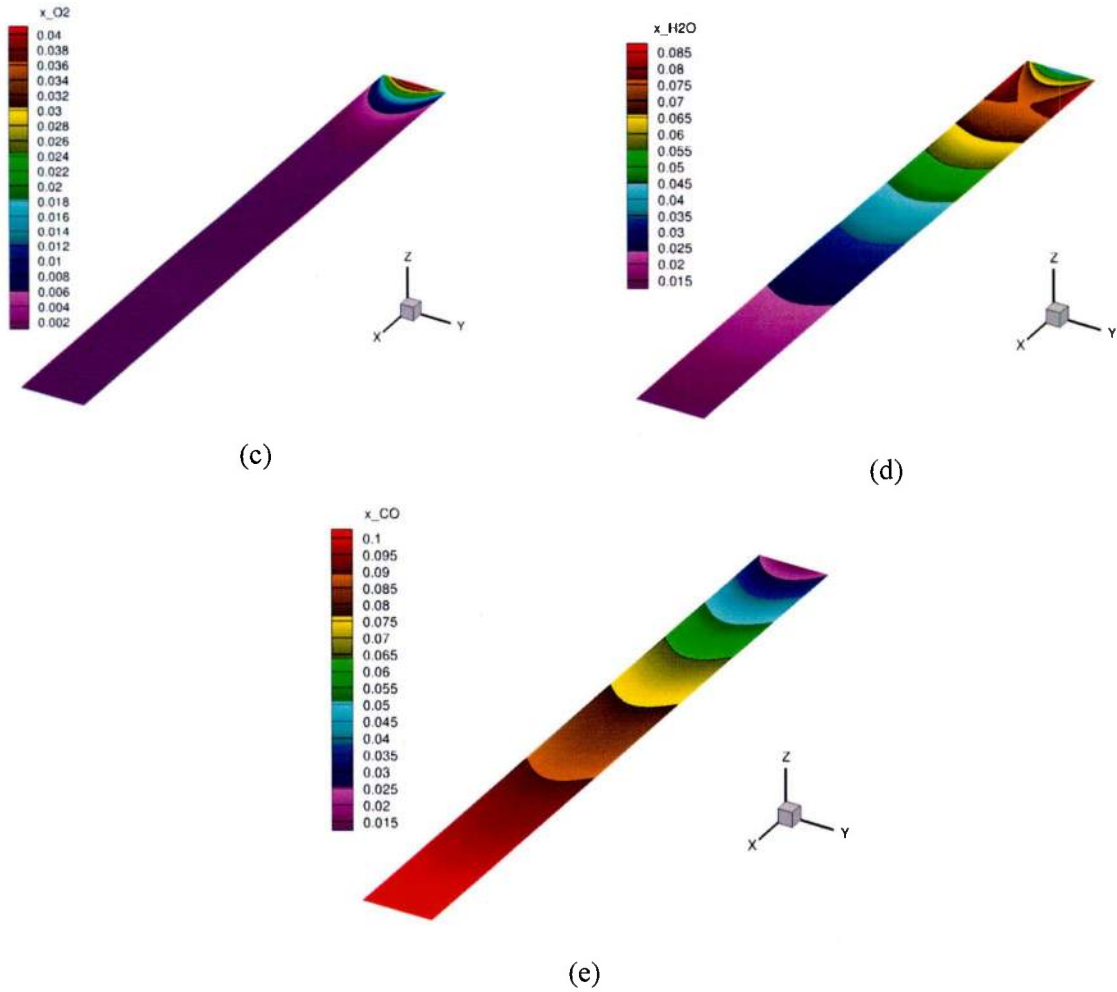
Figure 18. Species mole fractions (Rh catalyst)

4.3.2 Parameter study

In this section, effect of the different design parameters on the fuel reformer performance is investigated. There are many the design parameters affecting the reactor efficiency for fuel reforming. These design parameters can be related to the shape/size of the reformer as well as operating conditions and catalyst material. In this work, inlet methane/oxygen ratio, inlet velocity and catalytic wall temperature are considered as design variables. By using inlet velocity as one of the parameters, effect of different Reynolds numbers is also studied indirectly on reformer performance.
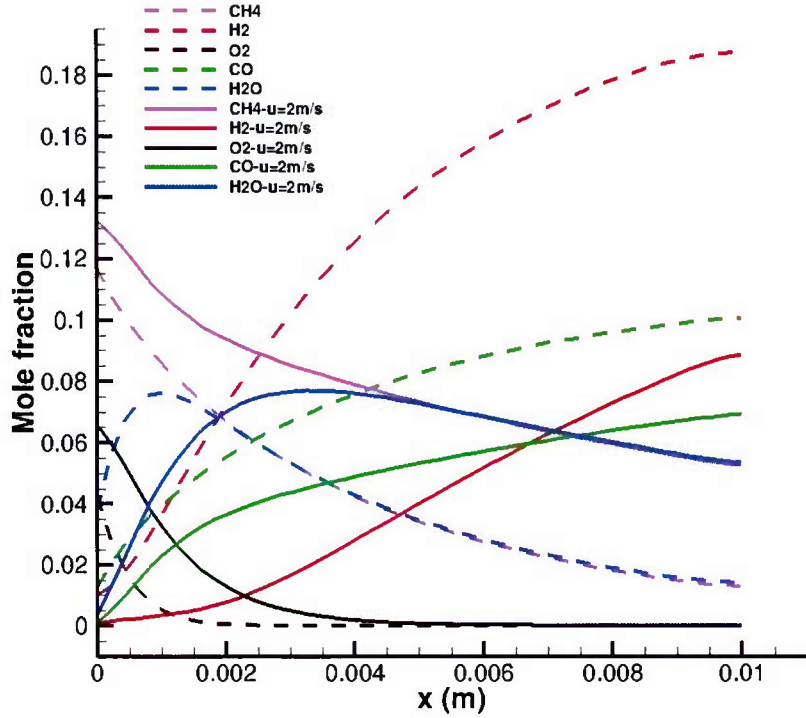
Figure 19. Comparison of the species mole fractions along reformer symmetry axis for inlet velocities 0.5m/s and 5 m/s

The baseline conditions for this study are shown in Table 10. Figure 19 shows the comparison of the mole fraction of species along the symmetry axis of the reformer with two different inlet velocities of 0.5 and 5 m/s. The conversion of methane is predicted to decrease with increase in inlet velocity. The rate of oxygen consumption along the reactor is also decreased and therefore the peak of H_2O concentration is shifted towards the middle of the channel for the case with higher inlet velocity. Mole fraction contours of different species for the reactor with inlet velocity of 5 m/s are presented in figure 20.

Table 10. Baseline conditions for catalytic combustion of methane	
Gas inlet velocity	0.5 m/s
Gas inlet temperature	1070 K
Wall temperature	1070 K
Gas inlet compositions (mole fraction)	$x_{CH_4} = 0.133$ $x_{O_2} = 0.067$ $x_{N_2} = 0.8$
Pressure	1 atm
Channel width	1 mm
Channel length	10 mm
Catalyst	Rh
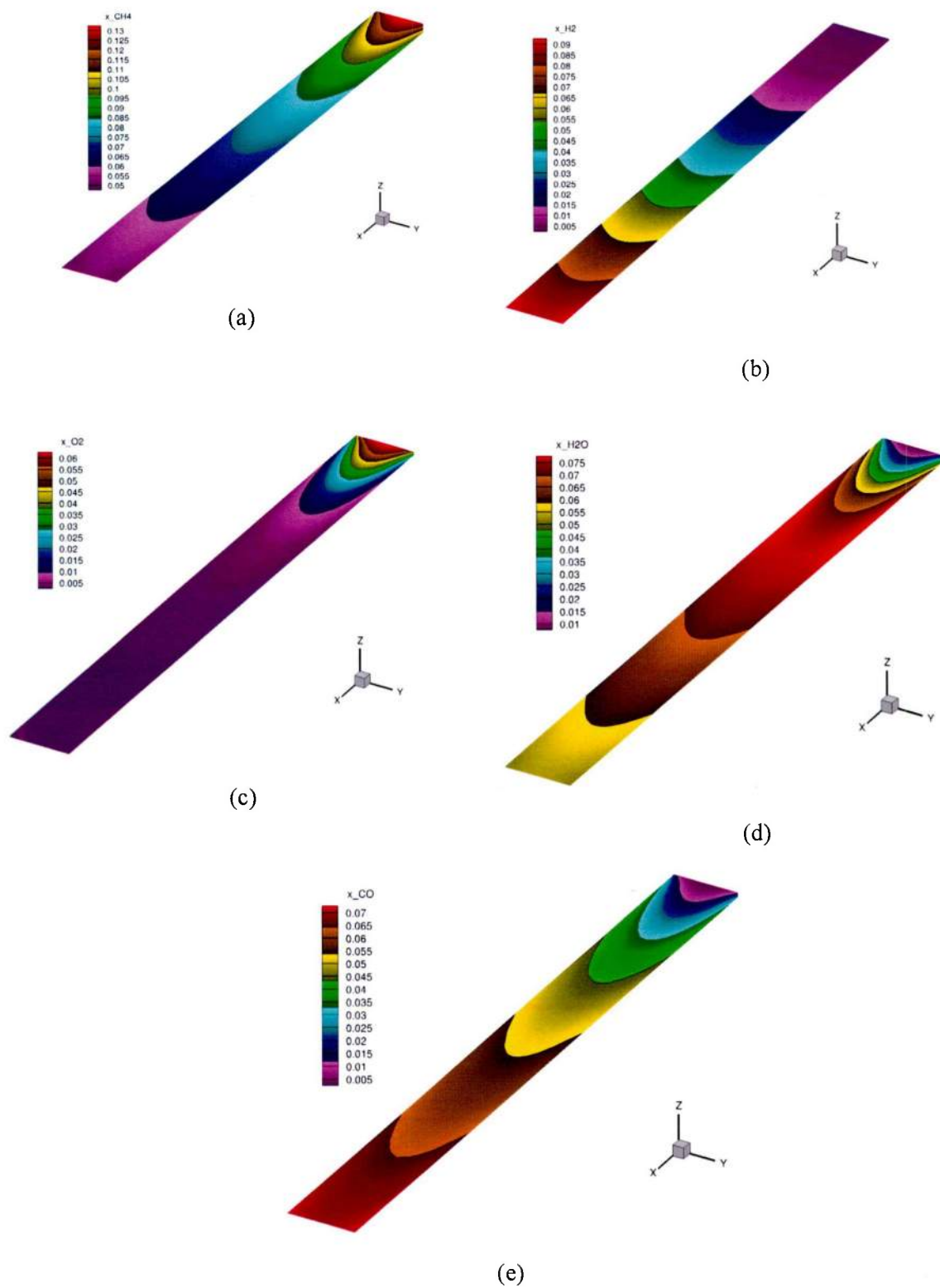
Figure 20. Species mole fractions (V = 5 m/s)

The influence of catalytic wall temperature variation on species conversion rates is shown in figure 21. The numerical result predicted the conversion of methane increases from 90% at 1070 K to 96% at 1170 K. The hydrogen production is also increased by about 10% at higher temperature.
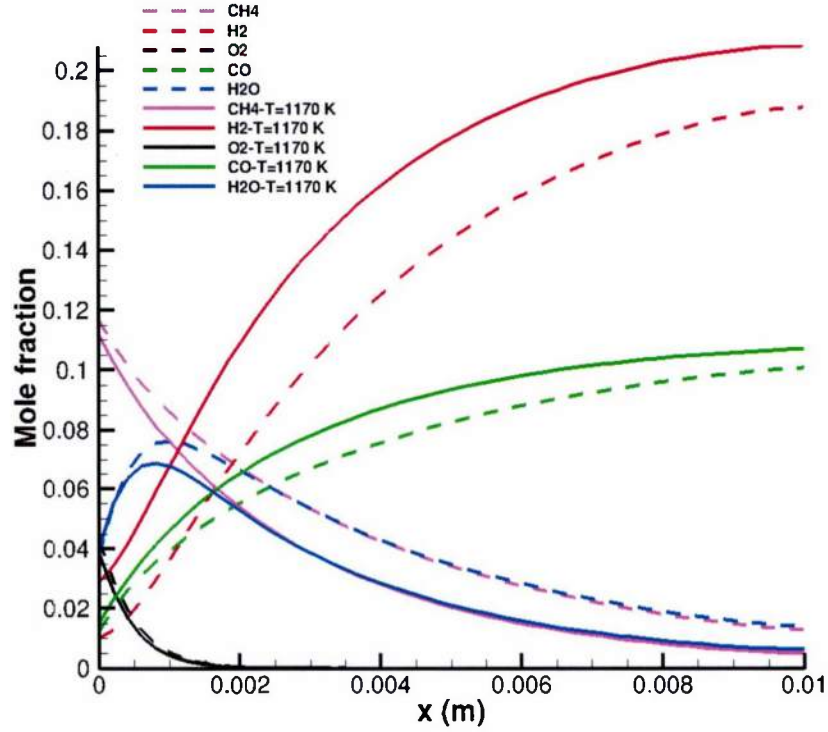
Figure 21. Comparison of the species mole fractions along reformer symmetry axis with different catalytic wall temperature

The inlet methane-oxygen ratio is another important design parameter. Two different cases with methane-oxygen ratios of 1 ($x_{CH4} = 0.1$ and $x_{O2} = 0.1$) and 1/3 ($x_{CH4} = 0.05$ and $x_{O2} = 0.15$) are numerically investigated. Results obtained are shown in figure 22, which compares the aforementioned cases with a baseline case of of $x_{CH4} = 0.133$ and $x_{O2} = 0.067$. Figure 22 shows the influence of variation in methane-oxygen ratio on reformer performance. As shown in figure 22, size of active methane conversion region increases with increasing methane-oxygen ratio at the inlet. The hydrogen production reaches the highest value for richer mixture (ratio of 2.0, baseline case). Hydrogen production for the mixture ratio of 1/3 is minimal and CO, CO_2 and H_2O are the main productions. The mole fraction contours for the reformer with the methane-oxygen ratio of 1/3 are shown in figure 23.

44
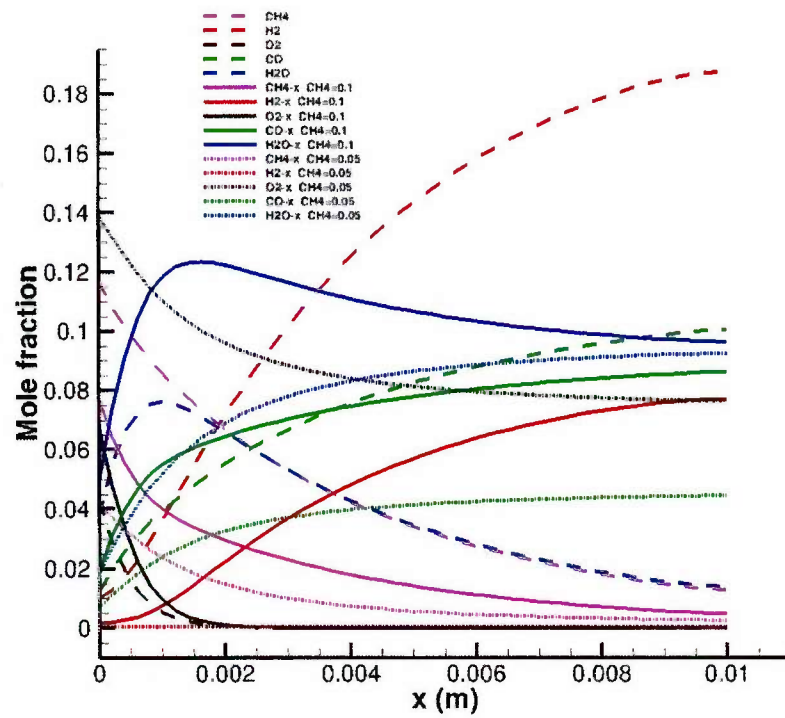
Figure 22. Effect of methane-oxygen ratio on reformer performance

(a)

(b)

(c)

(d)

(e)

(f)
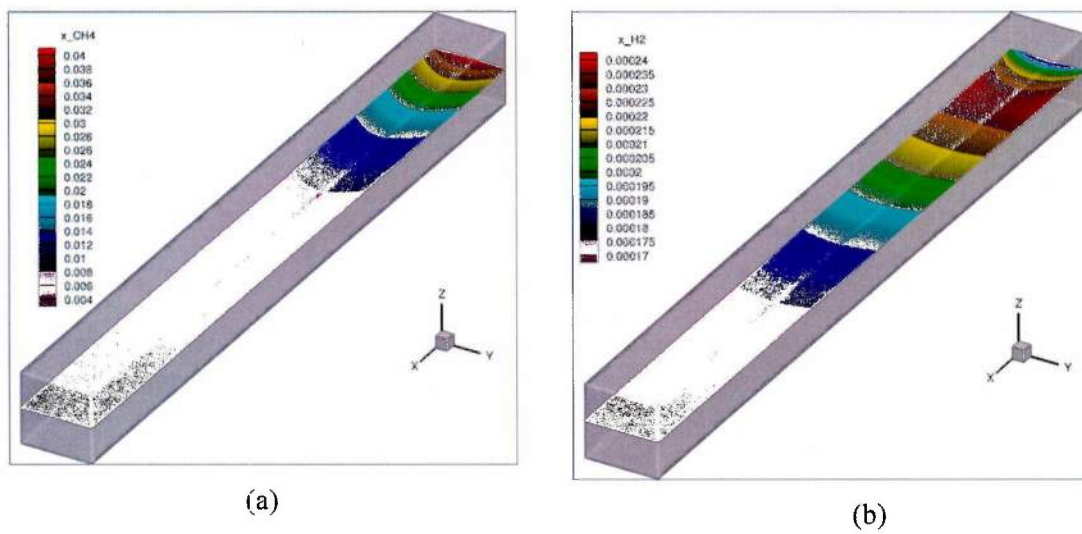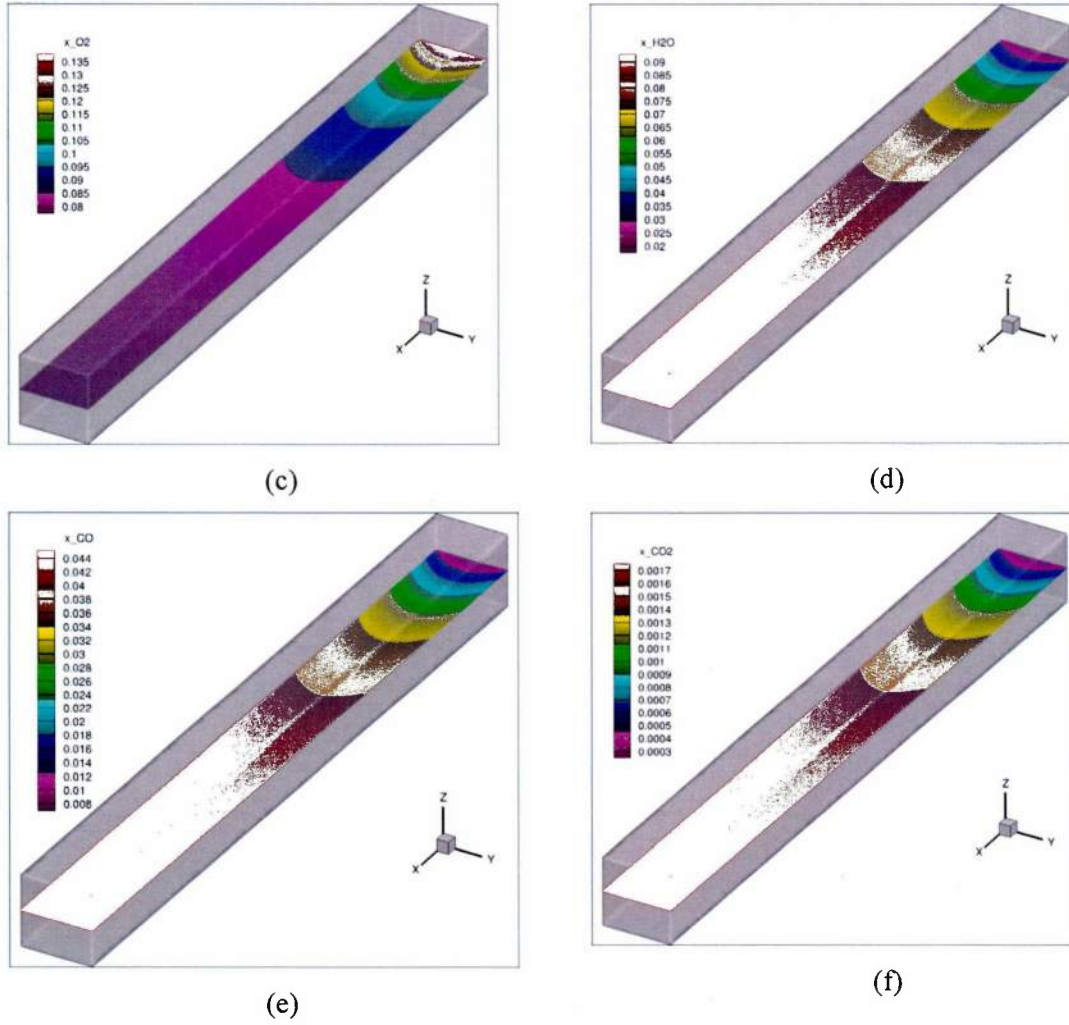
Figure 23. Species mole fractions (methane-oxygen ratio is 1:3)

The type of catalyst used significantly affects performance of the reformer. The reactor performance for two different catalysts, platinum and rhodium, was investigated earlier. In addition to the type of catalyst, catalyst loading is also an import factor in design and optimization of catalytic reactors. For considering the effect of catalyst loading, two parameters $F_{cat/geo}$ (ratio of catalytic surface area to geometric surface area) and η (effectiveness factor) are considered. As mentioned earlier, the heterogeneous flux with catalyst loading effects can be written as,

$$Flux_{het} = F_{cat/geo}\eta MW_i \dot{s}_i$$
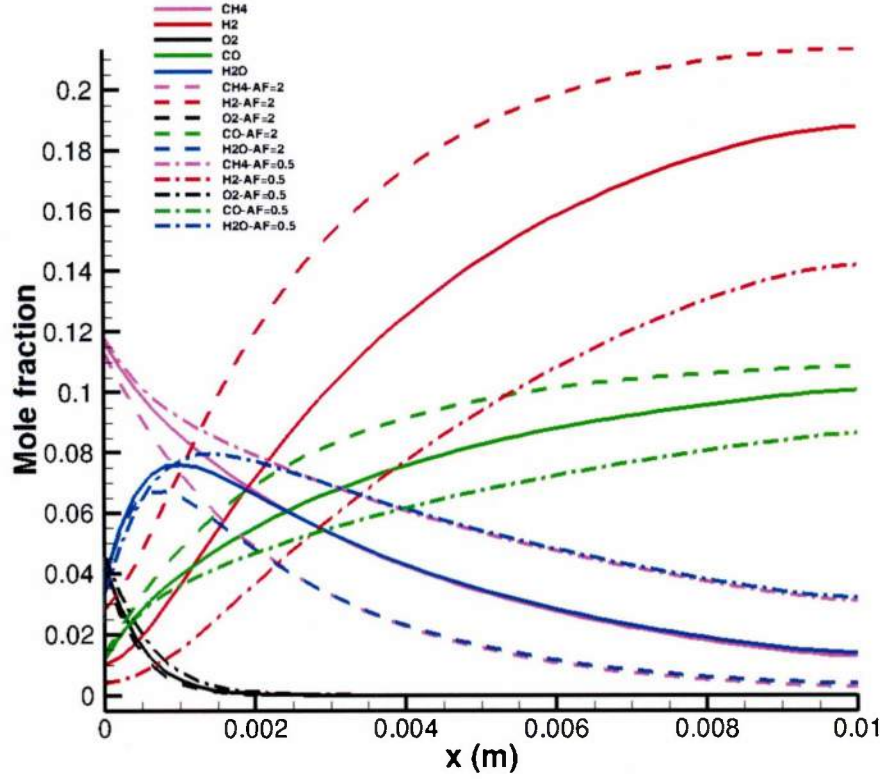
Figure 24. Effect of variation in catalyst loading on reformer performance

The effect of the catalyst loading factor ($F_{cat/geo}\eta$) on reformer performance is numerically investigated. As shown in figure 24, methane conversion increases at high catalyst loading. Oxygen is almost completely consumed by surface reactions in the first two-millimeter of the reactor length for all three cases. The methane conversion increases from 57 % at $F_{cat/geo}\eta = 0.5$ to 98 % at $F_{cat/geo}\eta = 2$. Hydrogen production at $F_{cat/geo}\eta = 2$ increases about 7% relative to the baseline case. Species mole fractions for the $F_{cat/geo}\eta = 0.5$ case are plotted in figure 25.

(a)

(b)

47

(c)

(d)

(e)
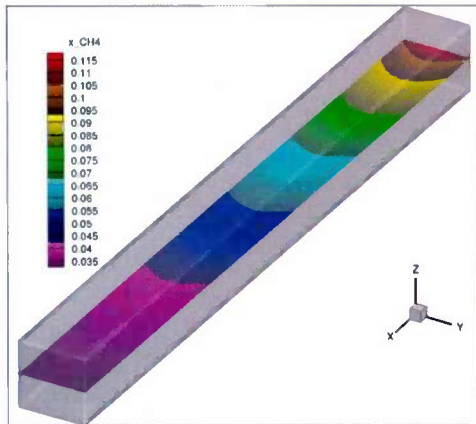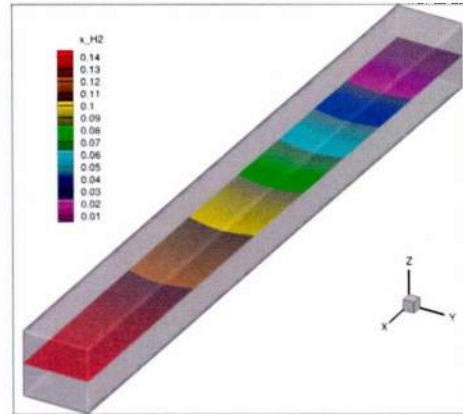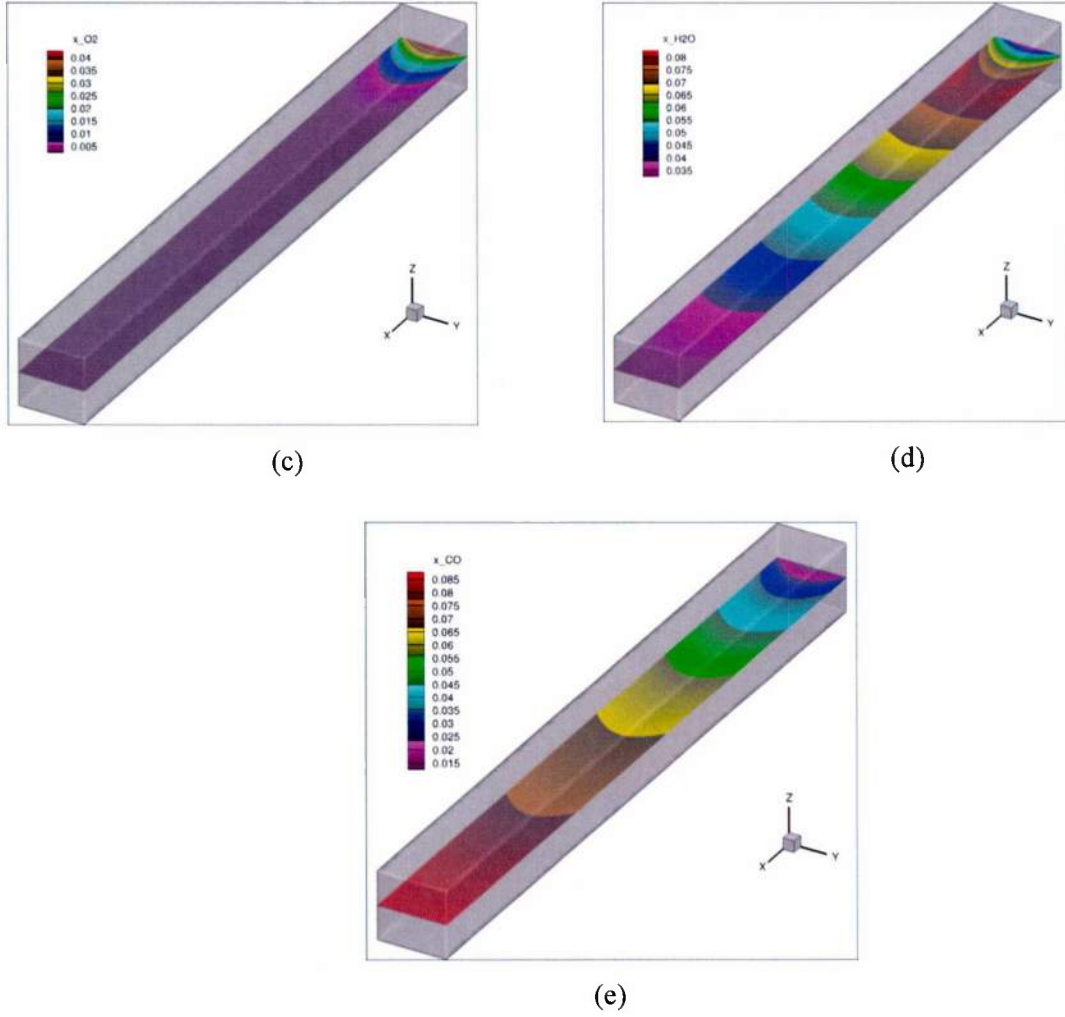
Figure 25. Species mole fractions ($F_{cat/geo}\eta = 0.5$)

4.3.3 Sensitivity Analysis

In the previous section, relationship between reformer performance and a design variable was obtained by running a baseline simulation, changing the parameter value and re-evaluating the change in the cost function. More sophisticated way for such analysis and computational design is using sensitivity analysis. In this method, the sensitivities are obtained by computing gradients or derivatives of the objective function with respect to design parameters of interest. There are several methods for computing sensitivity derivatives. In this work, the direction differentiation and adjoint methods are used to obtain the sensitivity derivatives. Implementation details of both these methods are given in earlier sections of this report.

The mean value of hydrogen concentration at the outlet boundary is considered as the cost function as increasing the value of this cost function improves the performance of the reformer. The design variables considered in this study include inlet

velocity, methane density, oxygen density, catalytic wall temperature and catalytic area ratio. For validation purposes, sensitivity derivatives are obtained using both adjoint and direct differentiation methods and provided in Table 11. The baseline conditions for this study are shown in Table 9. As ilustrated in the Table 11, the sensitivity derivatives obtained by direct differentiation and adjoint methods show good agreement.

Table 11. Comparison of sensitivity derivatives computed using different methods		
Design variable	**Direct Differentiation**	**Adjoint**
Inlet velocity	-0.00580817201	-0.005840817202
Inlet methane density	0.10718769820	0.107187698123
Inlet oxygen density	-0.07966058834	-0.07966058831
Catalytic wall temperature	0.00105843297	0.00105843127
Catalytic area ratio	0.00113610487	0.00113610454

Sensitivity derivatives are very useful for design and optimization purposes. With these derivatives, one can estimate how important a design parameter is for the given cost function. Thus, parameters that are not important can be ignored during optimization while concentrating on important variables. For example, in Table 11, inlet methane concentration is an important variable for the cost function of outlet hydrogen concentration.

4.3.4 Optimization

As mentioned earlier, an interface is created to link the flow solver code to DAKOTA to perform optimization. In the first case, numerical optimization based on only one design variable is studied. The mean value of CH_4 concentration at the outlet boundary is considered as the cost function. The inlet velocity is chosen as the design variable. The initial and boundary conditions shown in Table 9 are used for the baseline solution. The initial value for the design variable is 1.2 m/s and lower and upper thresholds (design constrains) are 0.3 and 2 m/s respectively. The optimization is performed by two methods: the Fletcher-Reeves conjugate gradient method (DAKOTA's conmin frcg method) and quasi-Newton method (DAKOTA's optpp q newton method). Both these methods are gradient-based optimizers that are best suited for efficient navigation to a local minimum in the vicinity of the initial point.
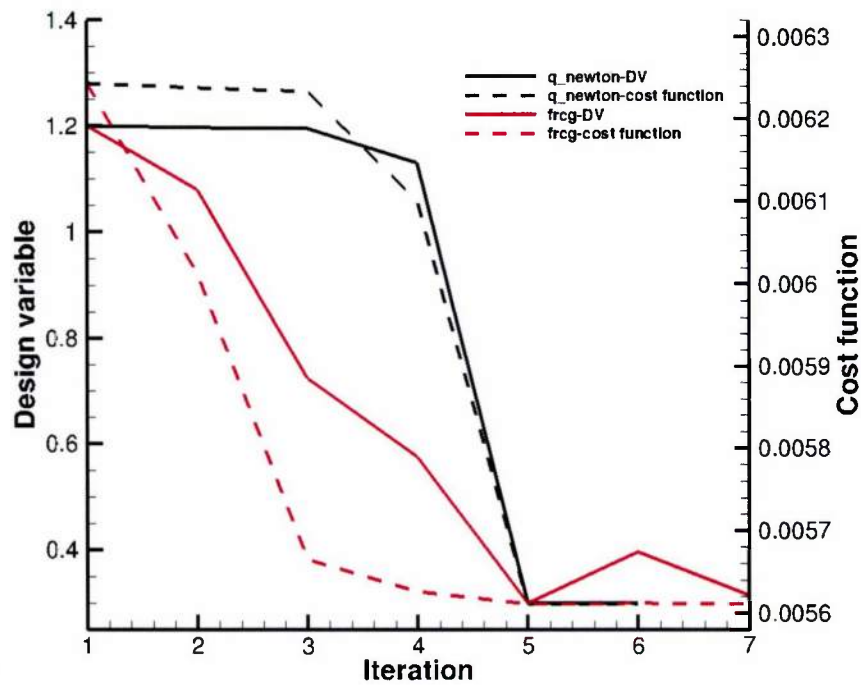
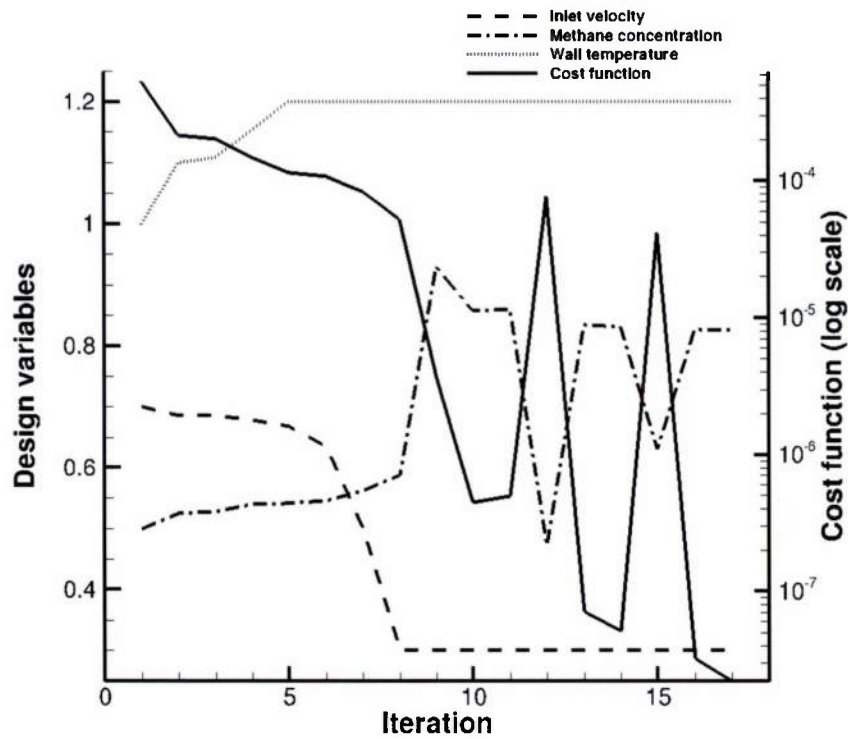Figure 26. Convergence history of the optimization problem with one design variable

Figure 27. Convergence behavior of the optimization problem with three design variables using Fletcher-Reeves conjugate gradient method

Figure 26 shows the convergence behavior of frcg and quasi-Nexton methods for solving this optimization problem. As expected, inlet velocity of 0.3 m/s is obtained as the optimum value for the design varible. The quasi-Newton method shows the quadratic convergence rate. In the frcg method, 7 cost function evaluations and 4 gradient evaluations are performed. The quasi-Newton used 6 cost function evaluations and 5 gradient evaluations.

The design problem with three parameters including, inlet velocity, inlet methane concentration and catalytic wall temperature is attempted as the second test case. Since the values of design variables are spread across different orders of magnitude, the normalized values are used for the optimization cycle. Constraints imposed in this optimization problem are listed in Table 12.

Table 12. Initial values and design constraints used in optimization			
	Inlet velocity	Methane concentration at inlet (Normalized by multiplying with 10)	Catalytic wall temperature (Normalized by dividing by 1000)
Lower bound	0.3	0.3	0.8
Upper bound	1.5	1.3	1.2
Initial values	0.7	0.5	1.0
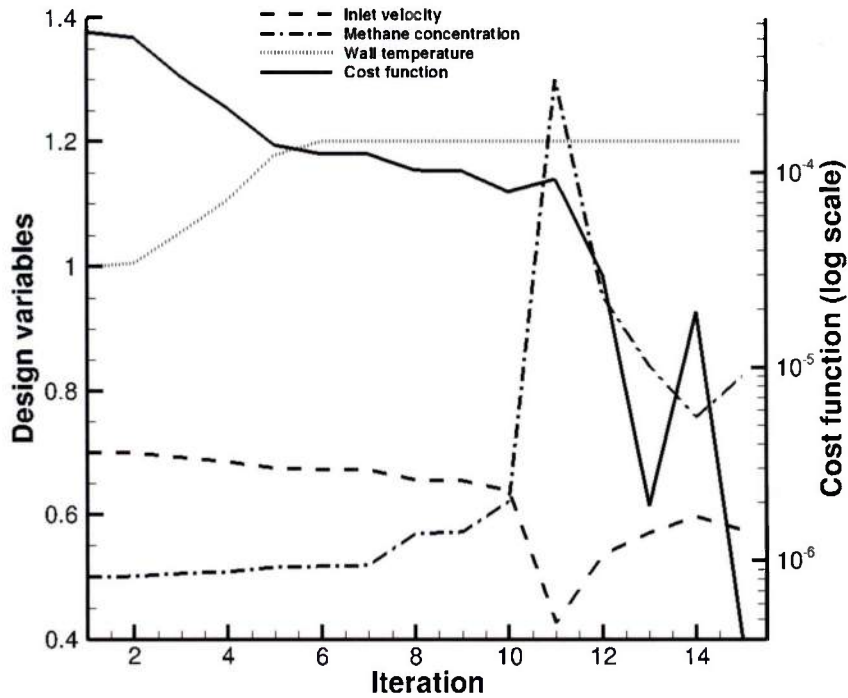
Figure 28. Convergence behavior for the optimization problem with three design variables using the quasi-Newton method

51

The cost function is defined as the mean value of CH_4 concentration at the outlet boundary. The initial and boundary conditions shown in Table 9 are applied. Again, two methods including Fletcher-Reeves conjugate gradient and quasi-Newton are used in this problem. Figures 27 (frcg) and 28 (quasi-Newton) show convergence behavior of both these optimization algorithms. In the Fletcher-Reeves conjugate gradient method, the cost function decreases from 5.34e-04 to 2.21e-08 for the local optimum point of (0.3, 0.825, 1.2). The cost function decreases from 5.34e-04 to 3.93e-07 using quasi-Newton method with the local optimum point of (0.575, 0.825, 1.2).

As shown in figures 27 and 28, both methods have a zig-zag convergence behavior. The comparison of the plots showing methane concentartion along the centerline of the reactor using baseline and both optimized conditions is illustrated in figure 29. The Fletcher-Reeves conjugate gradient method is a better optimization algorithm in this particular problem.
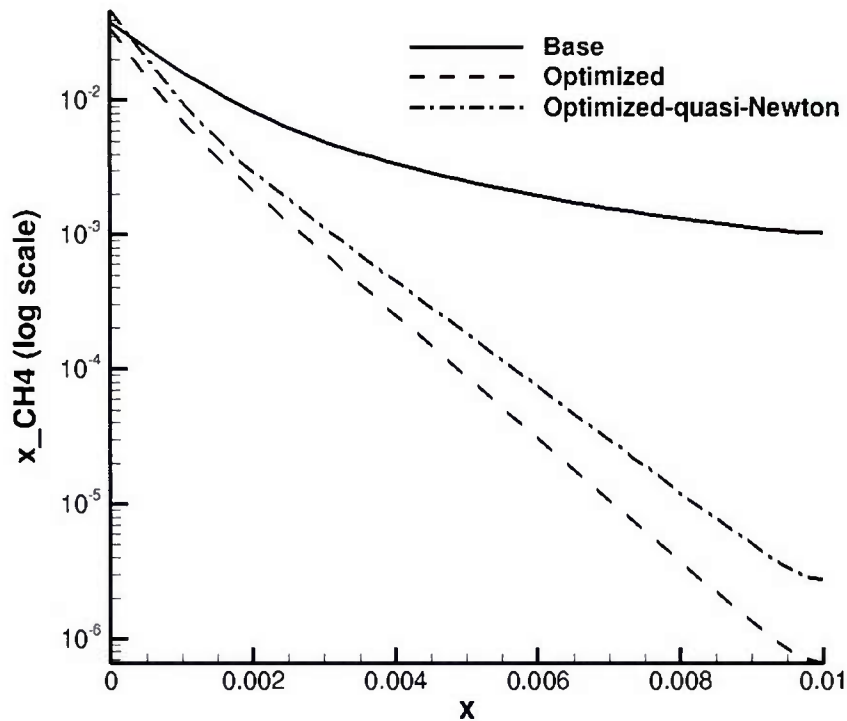
Figure 29. Comparison of methane concentartion along reactor length
using baseline and optimized conditions

Table 13. Number of solver and gradient calls for the optimization algorithms		
Method	Number of objective function evaluation (solver calls)	Number of objective gradient calculation (gradient calls)
Fletcher-Reeves conjugate gradient method	17	7
quasi-Newton algorithm	15	13

Table 13 shows the number of solver and gradient calls required for both optimization algorithms. Each gradient calculation step involves computing three derivatives for this problem. Therefore, the gradient calculation is the most expensive part of the optimization process and make up about 55% and 72% of the computational cost of the simulation in frcg and quasi-Newton algorithms, respectively. Since the number of design variables are small in this case, there is no significat advantage of using the adjoint method relative to the direct differentition.

While previous two caeses optimized the methane conversion, the main goal of the reformer design is to maximize the hydrogen production. In some cases, although methane is almost compeletly consumed for the given conditions, main products of the chemistry are species other than hydrogen. For this reason, another cost function representing hydrogen concentration at the outlet boundary is defined as following.

$$cost\ function = \frac{1 - \iint_{Outlet\ BC} \rho_{H_2}\, dA}{0.09} \tag{59}$$
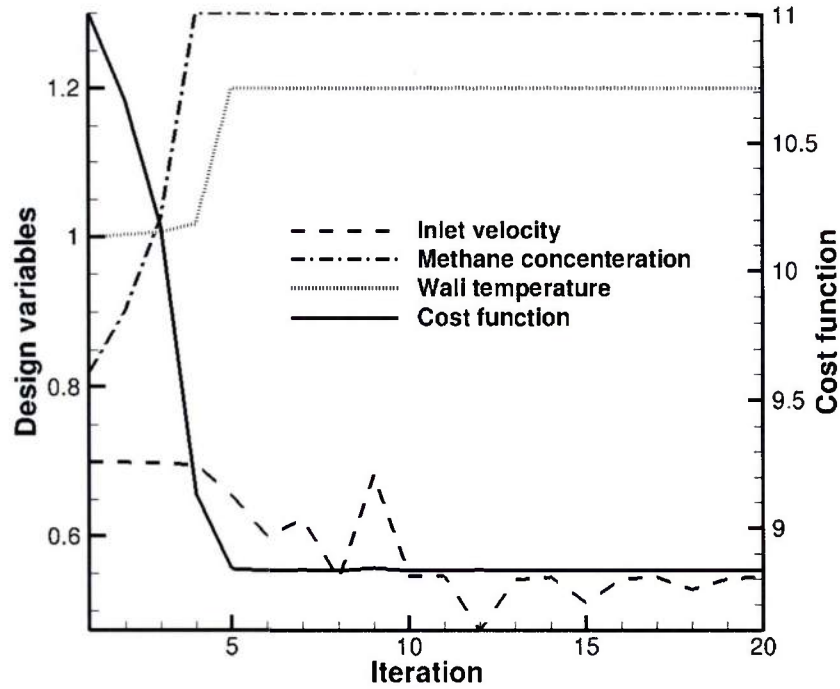
Figure 30. Convergence behavior for the optimization problem with three design variables and cost function representing hydrogen concentration at the outlet boundary

Based on the previous experience, the Fletcher-Reeves conjugate gradient method is selected for this problem. Initial and boundary conditions described in Table 9 are used for the baseline case. Design variables are same as the previous case including inlet velocity, wall temperature and inlet methane concentration. The initial values for inlet velocity and wall temperature are same as the previous test case. The value of 0.082 is chosen as the initial methane concentration at the inlet. Figure 30 shows the convergence

behavior for solving this optimization problem. Number of objective function evaluations and gradient calculations are 20 and 5, respectively to reach to the local minimum point. The comparison plot of hydrogen concentartion along the centerline of the reactor using baseline and optimized conditions is shown in figure 31.
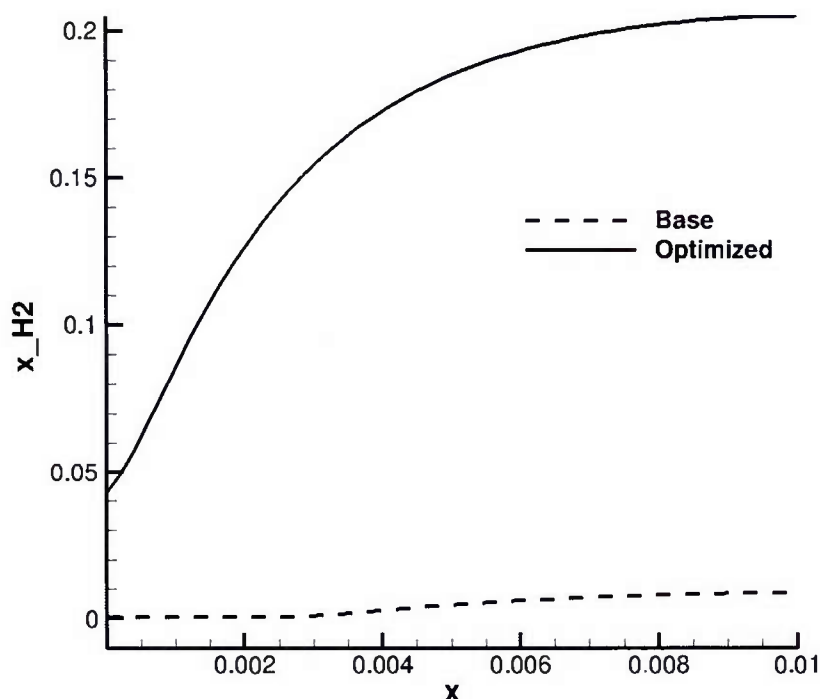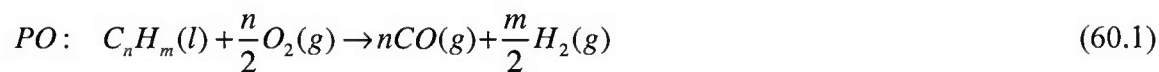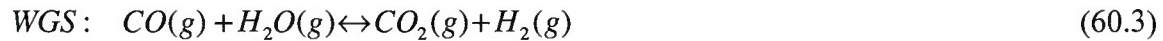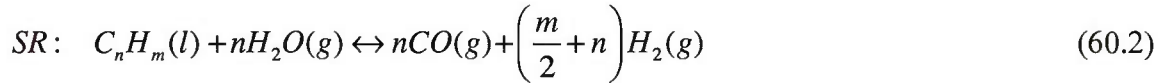

Figure 31. Comparison of hydrogen concentartion along reactor length using baseline and optimized conditions

4.4 Iso-Octane Reforming

In this section, steam reforming results of iso-octane using model described by Shi et al. [78] are presented. On-board hydrogen production is preferred due to lack of infrastructure for hydrogen production, storage and transportation. Different methods such as, partial oxidation (PO), steam reforming (SR) or autothermal reforming (ATR) can be utilized for on-board production of hydrogen using commonly used liquid fuels such as diesel or gasoline.

Partial oxidation is exothermic reaction and does not require external heat. Steam reforming is endothermic reaction and requires external heat to complete the reaction. Autothermal reforming is a combination of partial oxidation and autothermal reforming and is self-sustaining. Global reaction mechanism describing partial oxidation, steam reforming and water-gas shift reaction (WGS) for a general hydrocarbon can be written as following.

$$PO: \quad C_nH_m(l) + \frac{n}{2}O_2(g) \rightarrow nCO(g) + \frac{m}{2}H_2(g) \tag{60.1}$$

$$SR: \quad C_nH_m(l) + nH_2O(g) \leftrightarrow nCO(g) + \left(\frac{m}{2} + n\right)H_2(g) \tag{60.2}$$

$$WGS: \quad CO(g) + H_2O(g) \leftrightarrow CO_2(g) + H_2(g) \tag{60.3}$$

Most kinetic models available in literature employ methane (CH_4) as fuel. Very few models have been reported for heavy hydrocarbons such as, gasoline or diesel in literature [78,79]. These models generally use surrogates to represent actual hydrocarbons. For example,

(1) Diesel: n-hexadecane ($C_{16}H_{34}$)
(2) Gasoline: iso-octane (C_8H_{18})

Shi et al. [78] utilized global reaction model for n-hexadecane and iso-octane to simulate chemistry inside the reactor. Thormann et al. [79] presented a detailed kinetic model for n-hexadecane. Model developed by Thormann et al. includes 45 elementary reactions, 8 gaseous species and 13 adsorbed species. Transport properties (Lenard-Jones parameters) for the hydrocarbons utilized in simulations can be computed using relationships given in a paper by Tee et al [80].

A steam reforming model of iso-octane comprising of three global reactions and 6 species (C_8H_{18}, H_2, CO, CO_2, H_2O, N_2) is presented by Shi et al. [78]. This model is implemented in the in-house multispecies Navier-Stokes solver at the SimCenter. Few simulations have been run using iso-octane reforming model for different values of mass flow rates and results are shown in this report. Reactions used in iso-octane reforming model are given below. Details regarding reaction rate coefficients and reaction rate computation can be found in the paper by Shi et al. [78].

Iso-octane reforming:

$$R1: \quad C_8H_{18}(l) + 8H_2O(g) \leftrightarrow 8CO(g) + 17H_2(g)$$

$$R2: \quad CO(g) + H_2O(g) \leftrightarrow CO_2(g) + H_2(g)$$

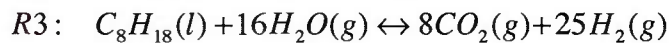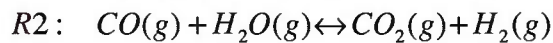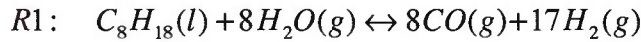$$R3: \quad C_8H_{18}(l) + 16H_2O(g) \leftrightarrow 8CO_2(g) + 25H_2(g)$$

Figure 32 shows the geometry utilized in the simulation along with different boundary conditions applied in the problem. Dimensions of the model are given in Table 14. Operating conditions used in the simulation are given in Table 15.

Table 14. Model dimensions (Shi et al. [78])		
Length (mm)	Width (mm)	Height (mm)
200.3	1.7308	1.2167

Table 15. Operating Conditions							
X_{H2O}	X_{H2O}	X_{CO2}	X_{H2}	X_{C8H18}	X_{N2}	T(K)	P(N/m2)

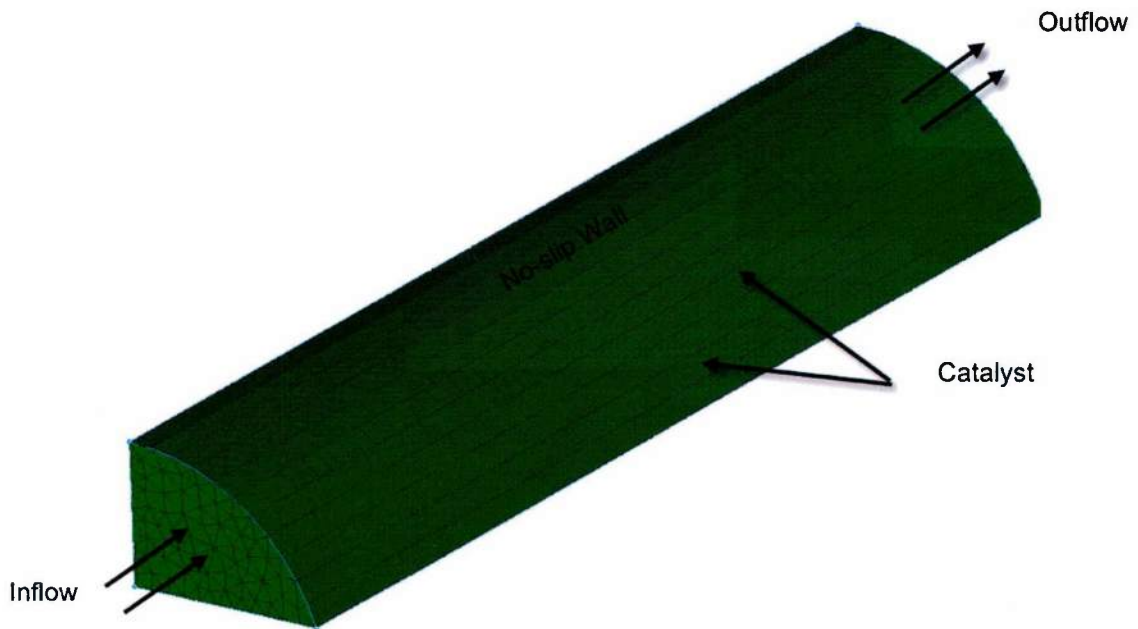| 0.005	0.39	0.005	0.005	0.016	0.579	898	303975

Figure 32. Reformer Model (Shi et al. [78])

To investigate the effect of fuel mass flow rate on temperature distribution, few cases have been run with varying fuel velocities while keeping the rest of the operating parameters constant. As seen, overall reaction mechanism is endothermic and thus, reduction in temperature is evident in figures 33 and 34. However, extent of such reduction is less for the case with higher velocity (Figure 33) by approximately 30° K. Such behavior is related to the extent of chemical activity taking place inside the reformer. When fuel is moving at slower velocity (figure 34), it spends more time inside the reformer and thus, has more time to participate in chemical reactions. As overall mechanism is endothermic, more reactions amount for higher temperature drop, which justifies the trends shown in figure 33 and 34.
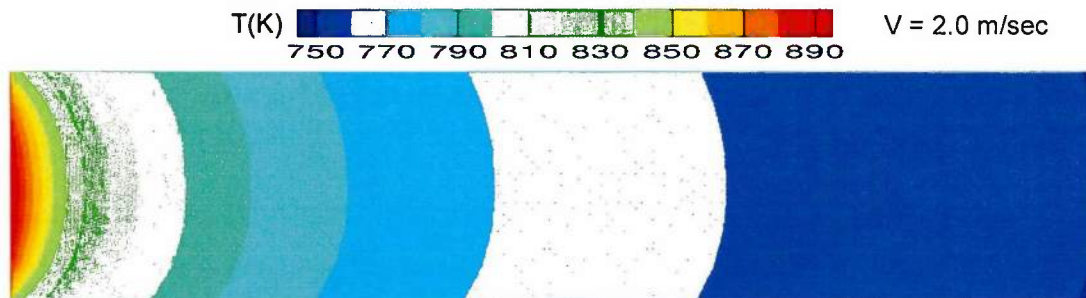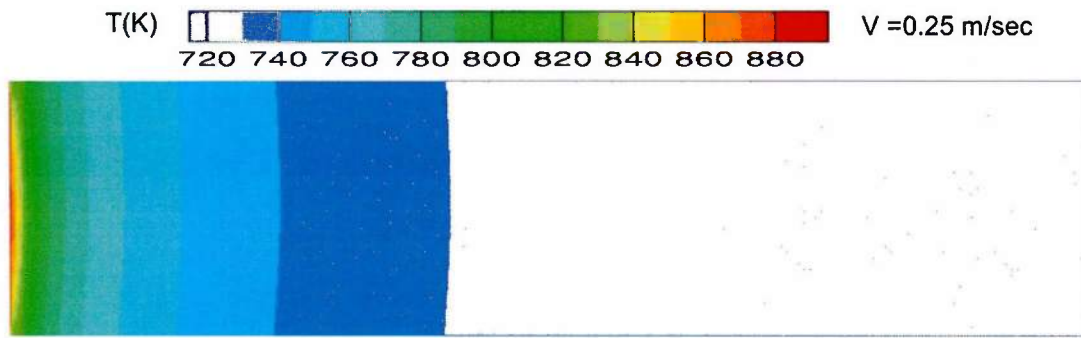

Figure 33. Temperature contours for V = 2 m/sec

Figure 34. Temperature contours for V = 0.25 m/sec

4.5 Fluid-Structure Interaction in SOFC

4.5.1 Analysis

The fluid-structure interaction capability has been developed and applied for the SOFC case described in this section. The geometry of the cell utilized in this case is shown in figure 35. As seen, computational model includes all relevant SOFC components including fuel/air manifolds, electrodes/electrolyte (PEN), seals and interconnects. The number of channels for both air and fuel manifolds is chosen to be twelve to make the geometry mimic realistic planar SOFC. Various geometric dimensions of the cell are listed in Table 16.
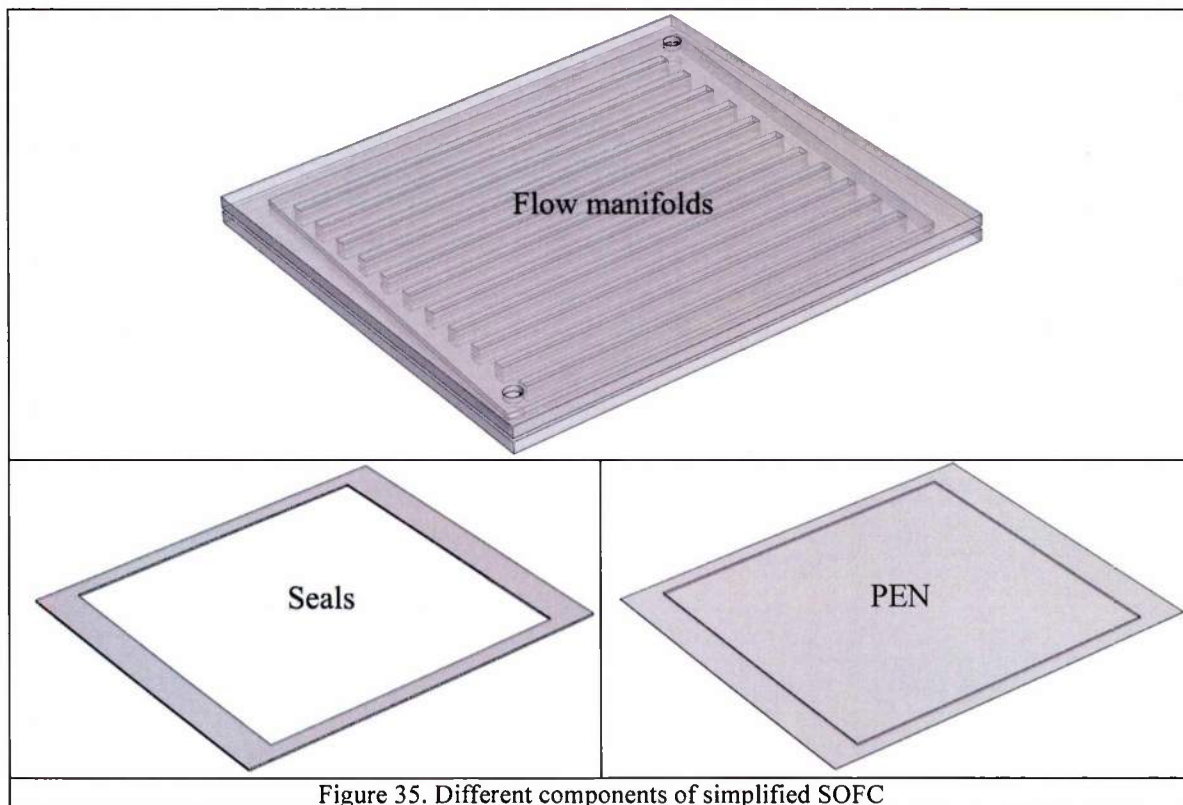

Figure 35. Different components of simplified SOFC

Table 16. Geometrical dimensions of simplified SOFC	
Length	43.0 mm
Width	39.0 mm
Height	0.23 mm
Anode thickness	0.1 mm
Cathode thickness	0.1 mm
Seal thickness	0.1 mm
Electrolyte thickness	0.1 mm
Interconnect thickness	0.5 mm
Channel thickness	0.5 mm

No-slip, adiabatic wall boundary conditions are applied at the top wall, bottom wall and side walls of the computational geometry shown in figure 35. Fixed potential ($\phi = 0$) boundary condition is applied at the bottom wall, while the top wall is treated by specifying average current density ($i = i_{applied}$). Inflow boundary conditions with specified mass flow rate and species mole fractions are applied at both fuel and air channel inlets. The temperature of the air and fuel mixture entering from their respective inlet ports is 1073 K. Also, both fluids are operating at atmospheric pressure. Specified back pressure outflow conditions are applied at both air and fuel outlet ports. Initial species mole fractions and thermodynamic conditions utilized in this simulation are given in Table 17. As seen in Table 17, partially reformed fuel has been utilized and thus, methane reforming and water gas shift reactions have been considered inside the anode. Material properties of different components of SOFC are shown in Table 18. Current density of 5500 Am^{-2} is applied at the top wall of the computational geometry shown in figure 35.

Table 17. Mole fractions and thermodynamic conditions								
X_{CO}	X_{H_2O}	X_{CO_2}	X_{H_2}	X_{CH_4}	X_{O_2}	X_{N_2}	$T(K)$	$P(N\ m^{-2})$
0.029	0.493	0.044	0.263	0.171	0.198	0.802	1073 K	101325

Table 18. Material properties of various components of SOFC	
Electric resistivity of anode (Ωm)	$2.98 \times 10^{-5} \exp(-1392 / T)$
Electric resistivity of cathode (Ωm)	$8.11 \times 10^{-5} \exp(600 / T)$
Electric resistivity of interconnect (Ωm)	6.41×10^{-8}
Ionic resistivity of electrolyte (Ωm)	$2.94 \times 10^{-5} \exp(10350 / T)$
Thermal conductivity of anode $(W\ m^{-1}K^{-1})$	40.0

Thermal conductivity of anode current collector $(W\,m^{-1}K^{-1})$	11.0
Thermal conductivity of cathode $(W\,m^{-1}K^{-1})$	10.0
Thermal conductivity of cathode current collector $(W\,m^{-1}K^{-1})$	11.0
Thermal conductivity of interconnect $(W\,m^{-1}K^{-1})$	25.0
Thermal conductivity of electrolyte $(W\,m^{-1}K^{-1})$	2.0
Thermal conductivity of seals $(W\,m^{-1}K^{-1})$	1.5
Porosity of anode	0.6
Porosity of cathode	0.6
Tortuosity of anode	6.0
Tortuosity of cathode	6.0
Porosity of anode current collector	0.9
Porosity of cathode collector	0.9
Tortuosity of anode collector	1.5
Tortuosity of cathode collector	1.5

Two different configurations of co-flow and counter-flow are analyzed in this case. Figures 36(a) and (b) show temperature contours plotted over outer surface of the cell for co-flow and counter-flow configurations, respectively. Figures also show flow directions of both air and fuel. As expected, in co-flow case, there is a gradual rise in temperature as both fuel and air move through the flow domain. Heat generated due to the electrochemical reaction is the main factor affecting the increase in temperature. In counter-flow case, regions showing maximum temperature are present in the middle of the computational domain. Also, maximum temperature found in the co-flow case is higher than the same found in the counter-flow case.

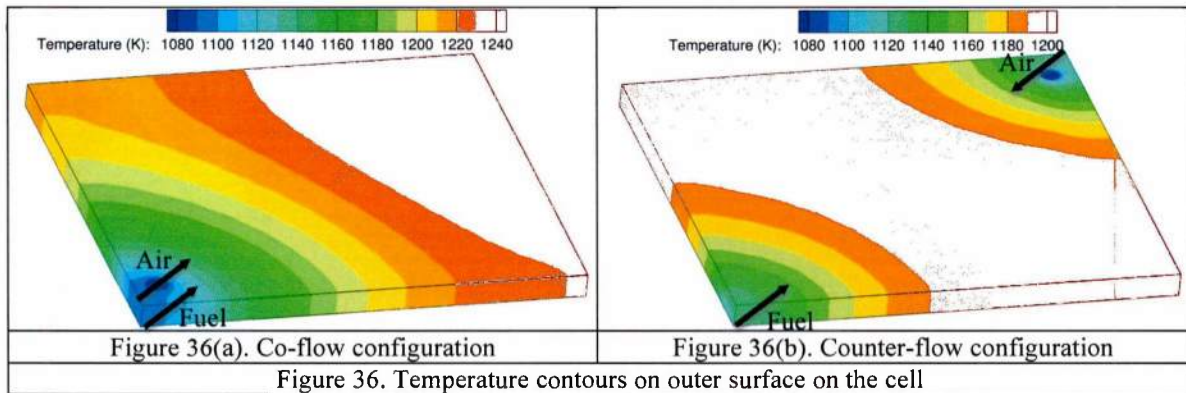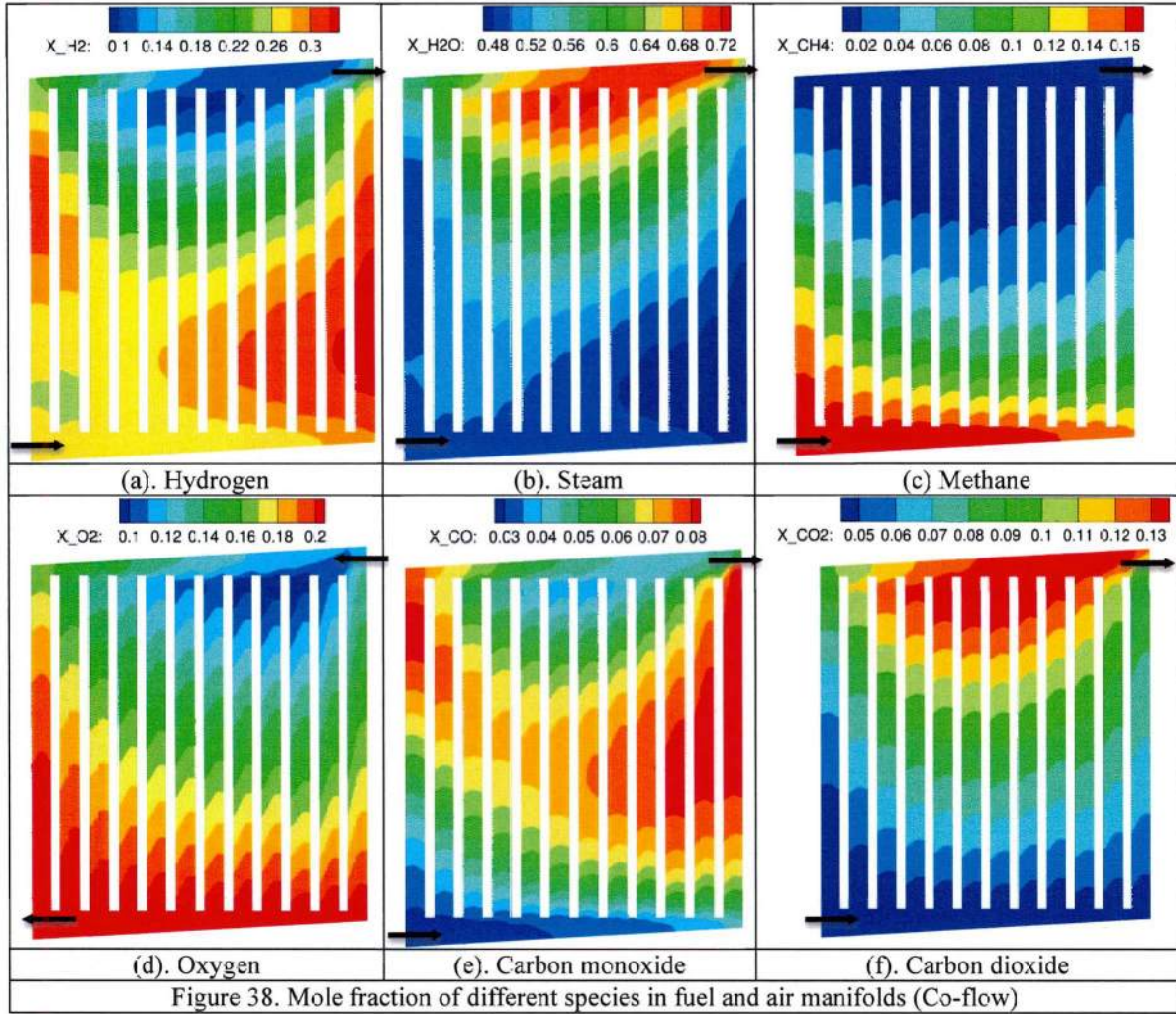| Figure 36(a). Co-flow configuration	Figure 36(b). Counter-flow configuration
Figure 36. Temperature contours on outer surface on the cell	

Figure 37 shows polarization curves plotted for both co-flow and counter-flow cases operating under the same conditions described in Table 17. As expected, cell voltage reduces with increase in current density due to the effects of several irreversibilities present inside the cell. Both cases exhibit similar performance for low

59

current densities. However, as current density increases, co-flow configuration performs better than the counter-flow configuration.

Figure 37. Polarization curve comparison
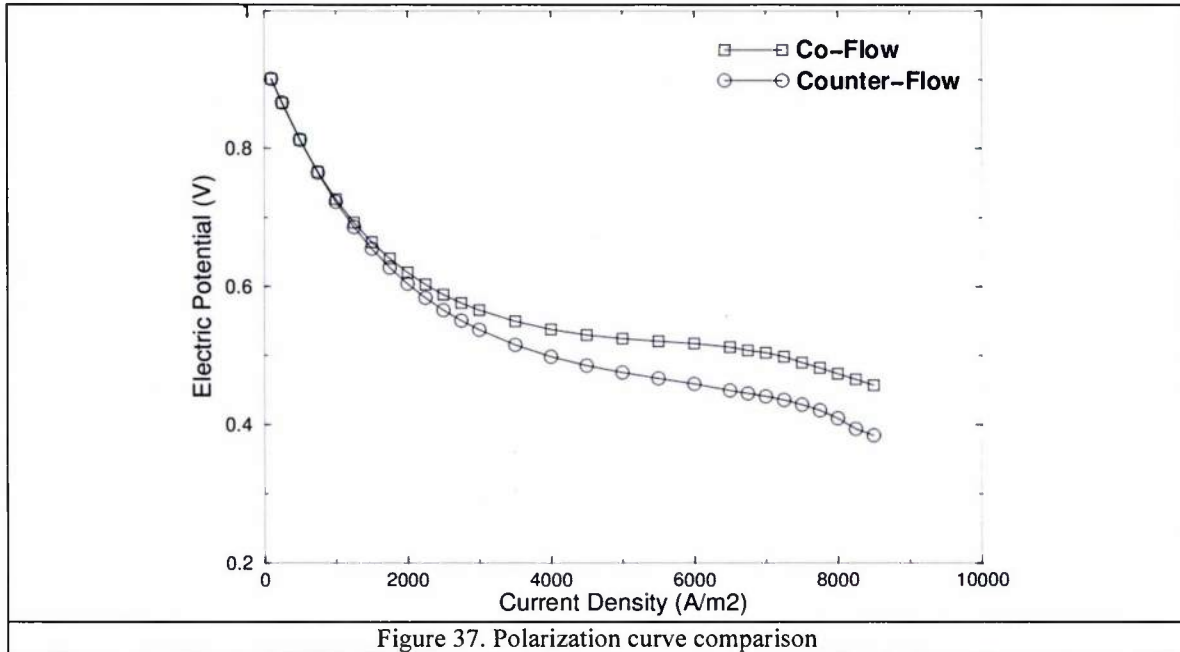
Figures 38 (a) – (f) show mole fractions of different species plotted on planes passing through fuel and air manifolds for the co-flow case. As mentioned earlier, two chemical reactions namely, methane reforming and water-gas shift reactions are considered inside the anode electrode. Also, electrochemical reaction, which is responsible for the production of steam and consumption of hydrogen and oxygen, affects species distribution in the flowfield. In figure 38(a), there is an overall reduction in hydrogen concentration as it moves through the flowfield. A region located near bottom right corner of the plane shows rise in hydrogen mole fraction. This behavior is caused by hydrogen production due to methane reforming reaction. In figure 38(b), gradual rise in steam concentration due to electrochemical reaction is evident as fuel moves from the inlet to the outlet of the manifold. Methane mole fraction is plotted in figure 38(c). As methane reforming is a fast reaction, most of the methane can be seen consumed in the first half of the flowfield. Figure 38(d) shows oxygen mole fraction plotted on a plane extracted from the air manifold. As oxygen is a reactant of the electrochemical reaction, there is gradual reduction in its mole fraction as air moves through the flowfield. Contours of carbon monoxide (CO) mole fraction plotted in figure 38(e) exhibit non-uniformity in the flowfield. As CO acts as a reactant in shift reaction and as a product in reforming reaction, their combined effect produces non-uniformity in the contours shown in figure 38(e). Finally, contours of carbon dioxide mole fraction are plotted in figure 38(f). As the only reaction involving carbon dioxide (as a product) is a shift reaction, gradual rise in carbon dioxide concentration is evident in figure 38(f).

Figure 38. Mole fraction of different species in fuel and air manifolds (Co-flow)

Figures 39(a) – (f) show stress contours plotted on planes extracted through different solid and porous components of the cell for co-flow configuration. Figures 39(a) and (b) show contours of maximum tresca equivalent stress (MTES) plotted on streamwise planes passing through seals located on both fuel and air sides, respectively. As seen, maximum stress is present near fuel inlet port in both figures. Figure 39(c) – (e) show contours of mean principal stress (MPS) plotted on planes passing through the anode, electrolyte and cathode, respectively. Some characteristics of these contours such as location of the maximum stress region are similar in all three plots. This region is located near fuel inlet port in the computational domain. Figure 39(f) shows contours of MTES plotted on a vertical plane passing through the interconnect and inlet ports. As expected, maximum stress is found near fuel inlet port. Regions near air inlet port also indicate high values of MTES. Overall, maximum stress values are found in a plane extracted through the anode electrode in figure 39(c).

61

(a). Anode seal	(b). Cathode seal
(c). Anode	(d). Electrolyte	(e). Cathode

MTES (MPa):   30   50   70   90   110   130
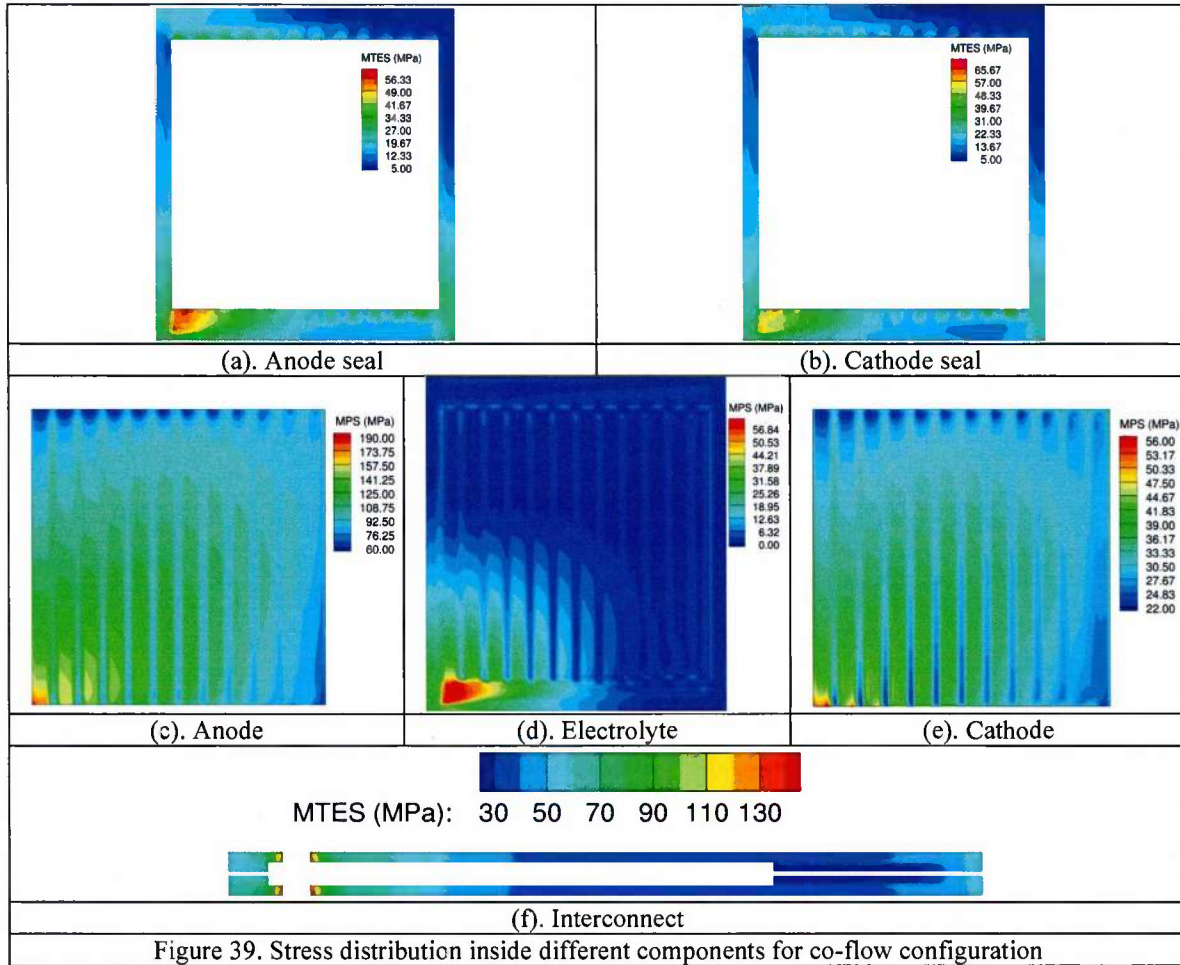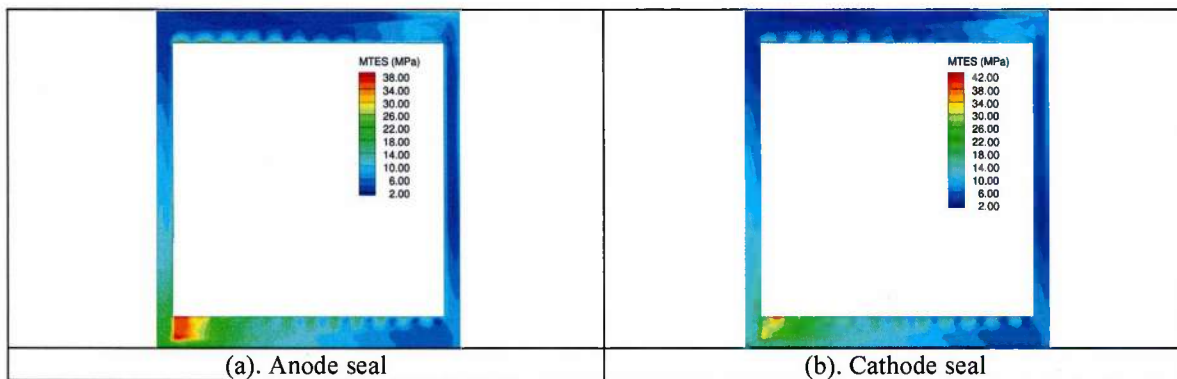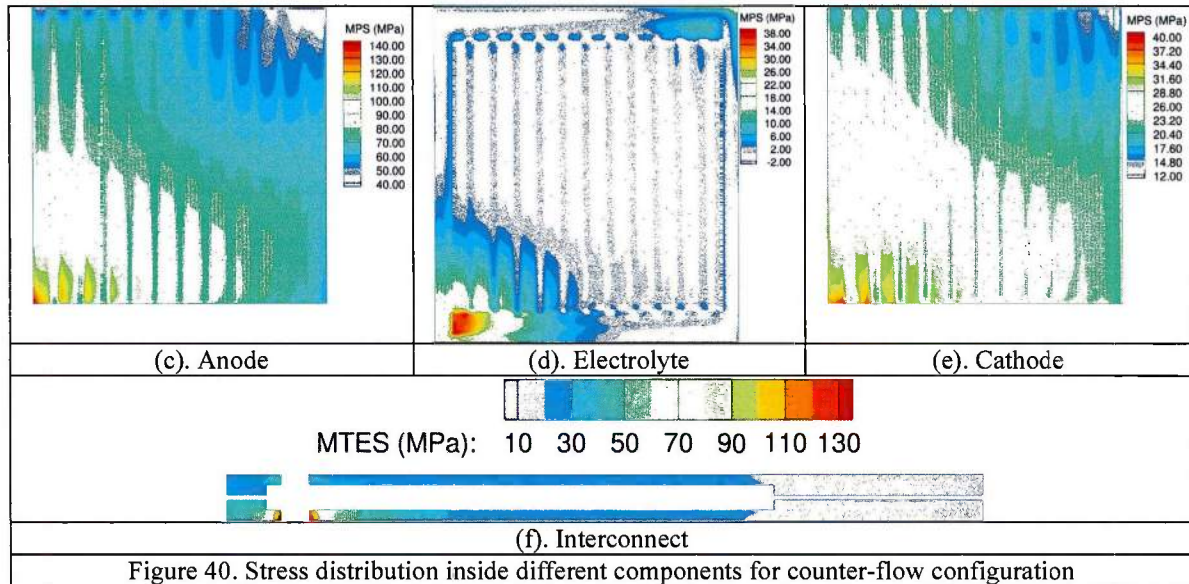
(f). Interconnect

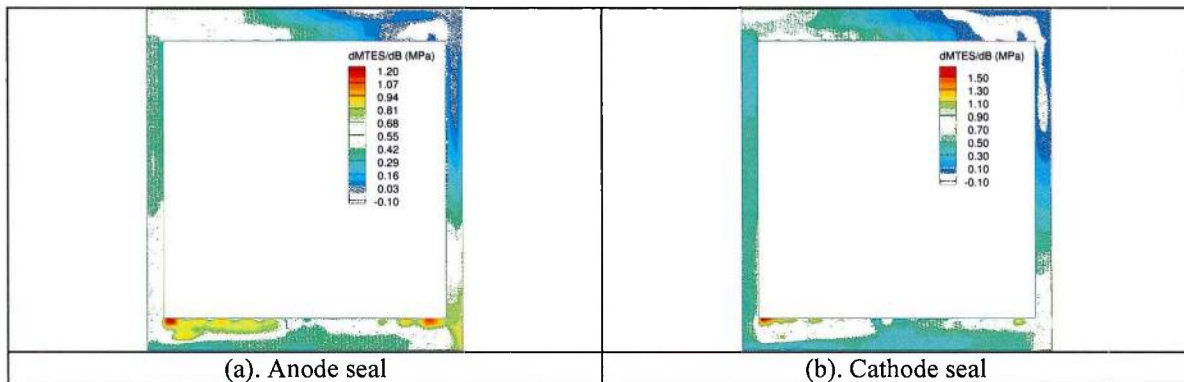Figure 39. Stress distribution inside different components for co-flow configuration

Figures 40(a) – (f) show stress contours plotted on planes extracted through different components of the cell for counter-flow configuration. Even though air is flowing in the opposite direction in this case compared to the previous case (figure 39), stress contours in different components show similar characteristics in both cases. Regions with maximum stress are located near fuel inlet port in different cell components. Overall, stress values for the counter-flow case are smaller than the co-flow case.

(a). Anode seal	(b). Cathode seal

(c). Anode	(d). Electrolyte	(e). Cathode

MTES (MPa):   10   30   50   70   90   110   130

(f). Interconnect

Figure 40. Stress distribution inside different components for counter-flow configuration
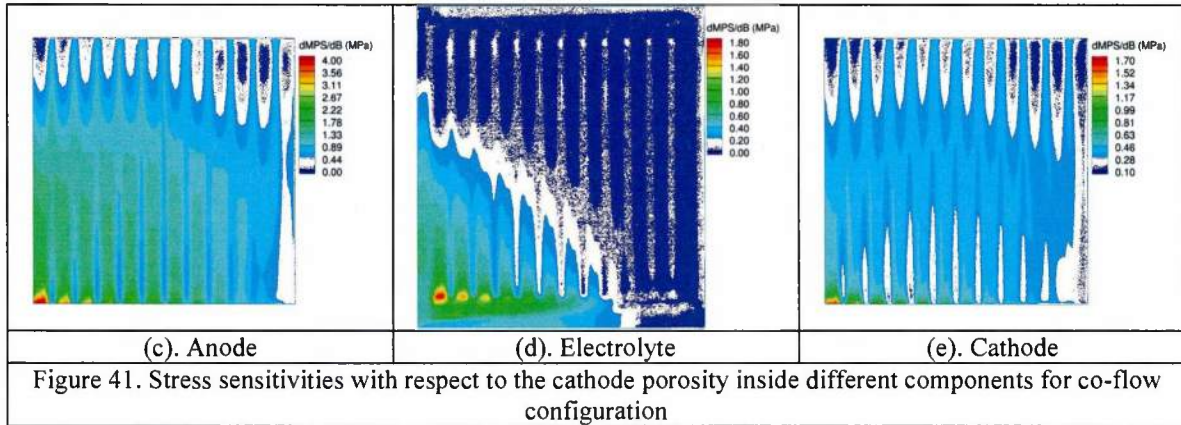
4.5.2 Stress Sensitivity

As mentioned earlier, both fuel cell and structures code are capable of performing sensitivity analysis. To demonstrate this capability, stress sensitivity contours are plotted on planes extracted through different components of the cell in figures 41(a) – (e). The co-flow configuration is utilized in figure 41. Design variable in this study is cathode porosity. The method utilized to compute sensitivity derivatives is direct differentiation in both fuel cell and structures code. Structures code requires values of flowfield variables and sensitivities of flowfield variables from the fuel cell code to compute stress sensitivities. The characteristics of stress sensitivity contours in figure 41 are similar to those shown for the stress contours in figure 39; especially regions with highest sensitivity values are located near fuel inlet port for all components.

(a). Anode seal	(b). Cathode seal

(c). Anode	(d). Electrolyte	(e). Cathode

Figure 41. Stress sensitivities with respect to the cathode porosity inside different components for co-flow configuration

4.6 CAD Integration and Mesh Movement

As described in section 3.4.2, a framework has been developed for integrating CAPRI [67] with the SimCenter geometry libraries so that CAD-based design variables can be utilized. In this section, three different examples demonstrating use of CAPRI interface and modified linear elasticity mesh movement solver are provided.

First example involves modifying the shape of the air channel for the tubular SOFC depicted in figure 42. Here, the geometry has been constructed in a CAD program (Solid Works) and the air channel is described as a simple ellipse, where the dimensions of the vertical and horizontal axes are exposed as design variables. The original design, as shown in the upper left portion of figure 43, has an air channel with a circular cross section. Sensitivity derivatives describing the changes in the surface coordinates with each design variable are shown in the right portion of this figure, whereas the result of a simple design problem is shown in the lower left. As seen in the final design, the circular cross section has become elliptical after one design cycle and the fidelity of the mesh is maintained after repositioning the coordinates of the air channel.
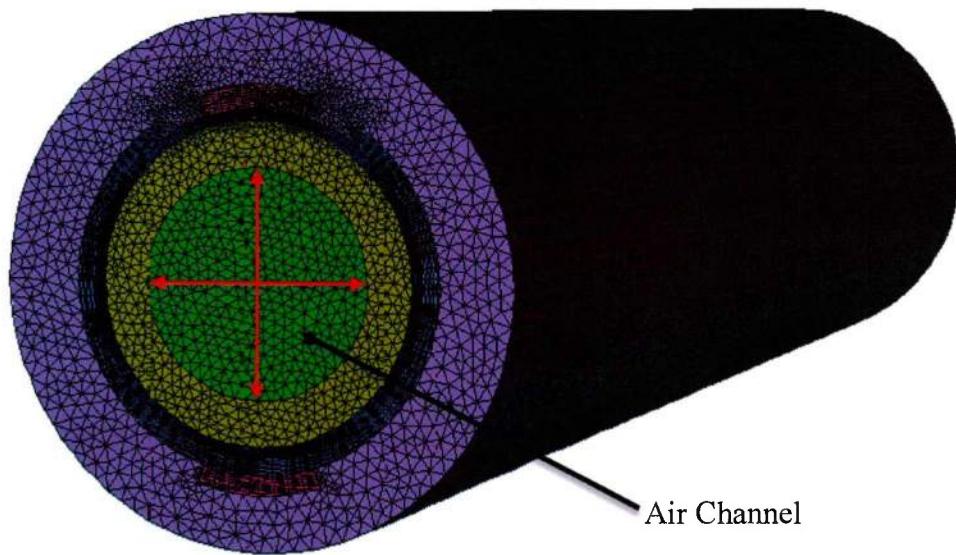
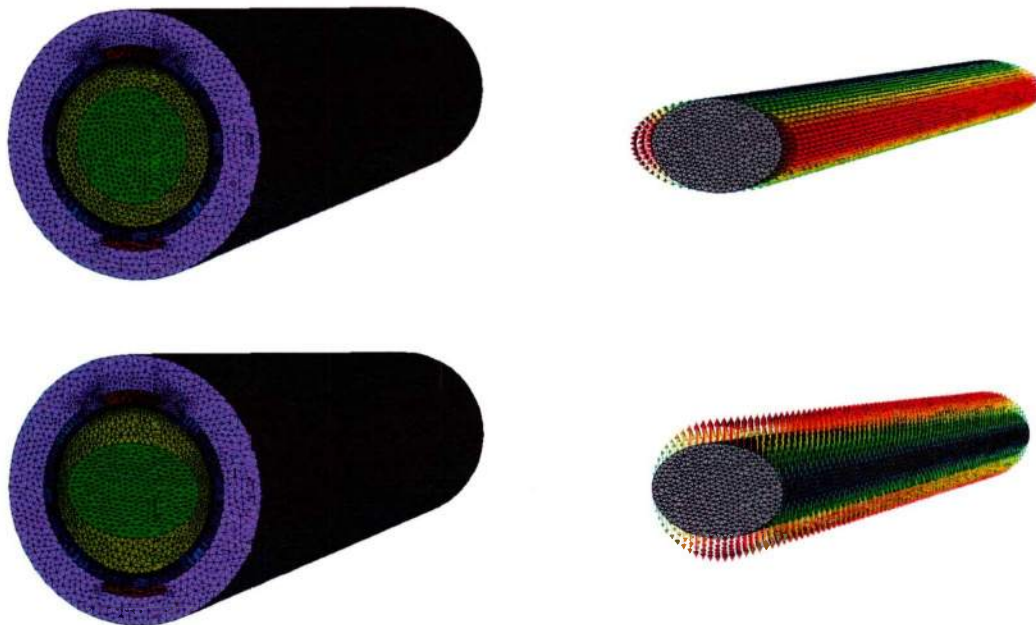Figure 42. Shape design of tubular SOFC

Figure 43. Shape design and sensitivity contours of tubular SOFC

Second example [81] is demonstrated in figure 44 showing capability to produce quadratic grids using CAPRI and linear elasticity solver. Shape shown in figure 44 is an analytically defined three-dimensional body of revolution [82]. Figure 44(a) shows the high-order mesh generated without getting original definition of the CAD model. The

linear surface representation shown in figure 44(a) is clearly inaccurate and using it for higher-order schemes would not allow accurate definition for the geometry. In contrast, figure 44(b) shows a surface mesh for the same geometry where quadratic elements are used. After adding additional surface quadrature points using the CAPRI interface to the elements, the fidelity of the surface is clearly improved.
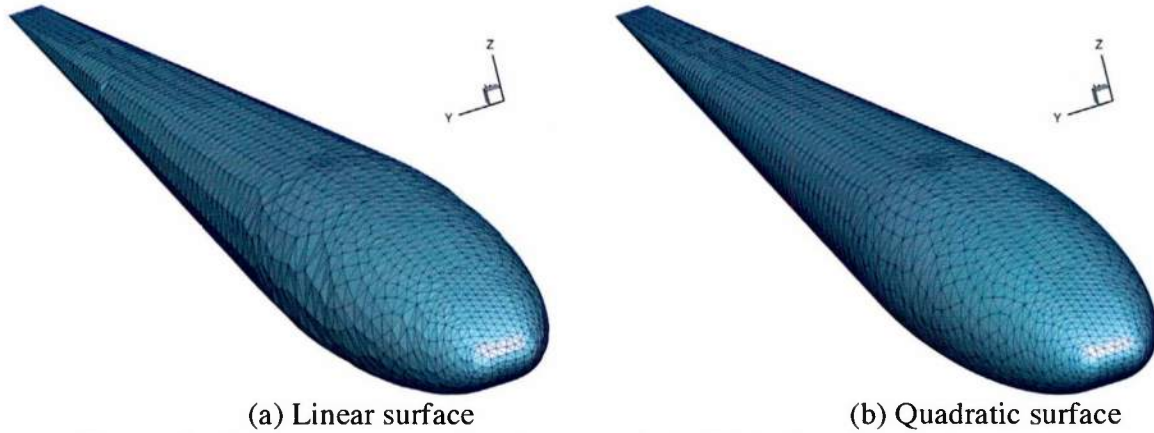

(a) Linear surface   (b) Quadratic surface

Figure 44. Surface representation for an analytic 3D body of revolution [81,82]

Third example illustrates the mesh movement strategy for a NACA 4412 mesh shown in figure 45(a) [81]. The mesh is generated with a viscous spacing of 1e-03 normal to the wall. Figure 45(b) plots contours of the perturbation magnitude obtained using linear elasticity solver described in Section 3.5. As expected, most perturbations are concentrated on the airfoil upper surface because of the presence of relatively larger curvatures, and the perturbation magnitude quickly decays as the distance to the airfoil increases. Figures 45(c) and (d) depict a close-up view of the viscous layer near 0.4 chord of length on the upper airfoil surface for linear and higher-order mesh, respectively. As shown in figure 45(d), the mesh movement strategy effectively produces sufficient deformations for the interior mesh points and quadrature points to prevent negative volumes or Jacobians. The mesh movement strategy employed in the current work is capable of obtaining valid finite-element meshes with high-aspect ratio elements for high Reynolds number flows.
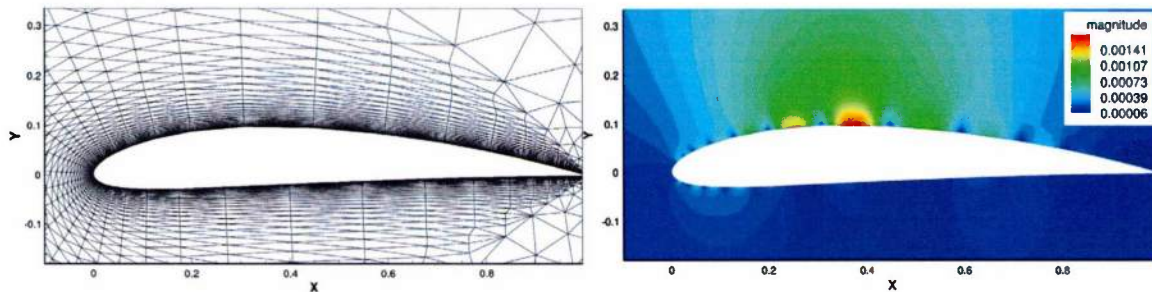
(a) NACA 4412 mesh   (b) Displacements obtained using LE solver
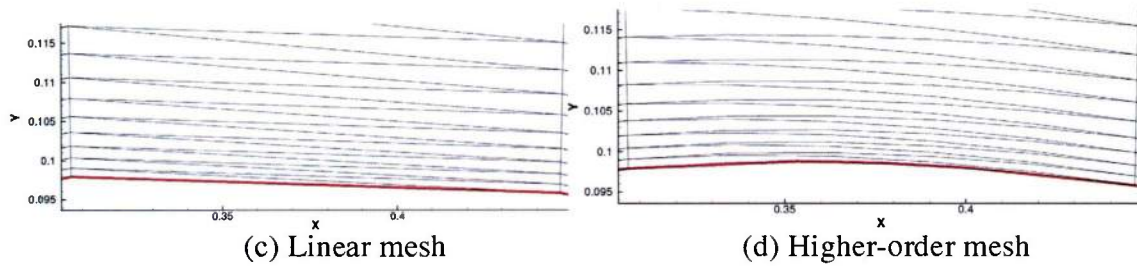
(c) Linear mesh   (d) Higher-order mesh

Figure 45. Mesh movement strategy for higher-order grids using CAPRI and linear elasticity solver [81]

5. Conclusions

An in-house solver capable of solving multispecies Navier-Stokes equations has been developed. The solver is implicit, unstructured and implemented in parallel for computational efficiency. Two applications explored in this project include planar SOFC and catalytic reactor. Results obtained using numerical models of SOFC as well as catalytic combustion of methane are validated by performing comparisons with the experimental results from the literature. Effects of inlet mass flow rate conditions on performance of both SOFC and reformer are investigated. The surface chemistry, heterogeneous combustion and coverages are computed by linking the solver with Cantera. Parametric studies are carried out for several design parameters affecting reactor efficiency for fuel reforming. The code is linked to DAKOTA for computational design and optimization purposes. Based on the presented results, the following conclusions may be drawn.

- The parameter study shows that
  - o Rhodium shows better performance for partial oxidation of methane (conversion of 90%) than platinum (conversion of 77%).
  - o Conversion of methane is predicted to decrease with increasing inlet velocity and Reynolds number.
  - o Conversion of methane and hydrogen production increase with increase in catalytic wall temperature.
- Sensitivity analysis for the methane reformer shows that the methane concentration is an important parameter affecting reformer performance.
- Sensitivity derivatives are used for computational design based on gradient-based optimization algorithm. Computation of sensitivity derivatives using direct differentiation and adjoint method reduced the run time of the optimization process up to 38% for the Fletcher-Reeves conjugate gradient method and 54% for the quasi-Newton algorithm.

A capability to perform thermo-mechanical analysis of different components of SOFCs has been developed by coupling the multispecies solver with the structures code. Results obtained using this capability indicate that the main factors affecting the stress distribution are temperature gradients and mismatch of coefficients of thermal expansion between different components of the cell. Also, capability to perform thermo-mechanical sensitivity analysis has been developed using direct differentiation method. Using this capability, sensitivity derivatives of stress has been computed for planar SOFC.

67

Capability to perform shape design and create curved higher order elements using original definition of CAD model is developed using CAPRI (developed at MIT) and high-fidelity mesh deformation algorithms. This method is successfully applied to create higher order curved elements for viscous grid of NACA 4412.

Acknowledgements

Nomenclature

Symbols	Name	Unit
B	Permeability	m^2
E_t	Total energy	$J\,m^{-3}$
f	Cost function	cost function depended
H	Enthalpy	$J\,kg^{-1}$
i	Current density	$A\,m^{-2}$
i_0	Exchange current density	$A\,m^{-2}$
J	Mass flux vector	$kg\,m^{-2}\,s^{-1}$
$\dot{m}$	Mass flow rate	$kg\,s^{-1}$
M	Molecular weight	$kg\,kmol^{-1}$
ns	Number of species	-
P	Pressure	$N\,m^{-2}$
Q	Solution vector	solution variable dependent
q	Heat flux	$J\,m^{-2}\,s^{-1}$
T	Temperature	K
u	x-velocity component	$m\,s^{-1}$
v	y-velocity component	$m\,s^{-1}$
w	z-velocity component	$m\,s^{-1}$
X_i	Mole fraction of ith species	-

Greek Symbols

β	Design variable vector	design variable dependent

χ	Grid vector	m
ρ	Mass concentration	kg m^{-3}
μ	Molecular viscosity	kg m s^{-1}
ϕ	Electric potential	volt
η	Activation polarization	volt
ε	Porosity	-
κ	Totruosity	-
$\forall$	Control volume	m^3
τ	Viscous flux	kg m^{-1} s^{-2}

Constants

| F | Faraday constant | 96484.56 A s mol^{-1} |
| R_u | Universal gas Constant | 8314.4 J kmol^{-1} K^{-1} |

Indices

a	Anode
c	Cathode
eff	Effective
i,j	Chemical species

References

[1] R.E. Hayes, S. T. Kolaczkowski, "Introduction to Catalytic Combustion", Gordon and Breach Science Publishers, 1997.

[2] Ferguson, J. R., Fiard, J. M., Herbin, R., "Three-Dimensional Numerical Simulations for Various Geometries of Solid Oxide Fuel Cells", J. Power Sources, 58 (1996) 109-122.

[3] Fiard, J. M., Herbin, R., "Comparison Between Finite Volume and Finite Element Methods for an Elliptic System Arising in Electrochemical Engineering", Comp. Methods in App. Mech. and Eng., 115, (1994) 315-338.

[4] Haberman, B. A., Young, J. B., "Three-Dimensional Simulation of Chemically Reacting Gas Flows in the Porous Support Structure of an Integrated-Planar Solid Oxide Fuel Cell", Int. J. of Heat and Mass Transfer, 47, (2004) 3617-3629.

[5] Khaleel, M. A., Lin, Z., Singh, P., Surdoval, W., Collin, D., "A finite element analysis modeling tool for solid oxide fuel cell development: coupled electrochemistry, thermal and flow analysis in MARC", J. of Power Sources, 130, (2004) 136-148.

[6] Lehnert W., Meusinger J., Thom F., "Modelling of gas transport phenomena in SOFC anodes", J. Power Sources, 87, (2000) 57-63.

[7] Li P. W., Chyu. M. K., "Simulation of the Chemical/Electrochemical Reaction and Heat/Mass Transfer for a Tubular SOFC Working in a Stack", J. Power Sources, 124, (2003) 487-498.

[8] Chan, S. H., Khor, K. A., Xia, Z. T., "A complete polarization model of a solid oxide fuel cell and its sensitivity to the change of cell component thickness", J. Power Sources, 93, (2001) 130-140.

[9] Campanari, S., Iora, P., J. Power Sources, "Definition and sensitivity analysis of a finite volume SOFC model for a tubular cell geometry", 132 (2004) 113-126.

[10] Grujicic, M., Chittajallu, K. M., "Design and optimization of polymer electrolyte membrane (PEM) fuel cells", Applied Surface Sci., 227 (2004) 56-72.

[11] Grujicic, M., and Chittajallu, K. M., "Optimization of the cathode geometry in polymer electrolyte membrane (PEM) fuel cells", Chem. Eng. Sci., 59 (2004) 5883-5895.

[12] Anderson, W.K., Newman, J.C., Whitfield, D.L., Eric Nielsen, E.J., "Sensitivity Analysis for the Navier-Stokes Equations on Unstructured Meshes Using Complex Variables", AIAA Journal,39, 1, (2001) 56-63.

[13] Burden, R. L., Faires, D. J., "Numerical Analysis", Sixth Edition, Brooks/Cole Publishing Company, 1997, 16-26.

[14] Anderson, W. K., Venkatakrishnan, V., "Aerodynamic Design Optimization on Unstructured Grids with a Continuous Adjoint Formulation", Computers and Fluids, 28, 4-5, (1999) 443-480.

[15] Anderson, W. K., Bonhaus, D. L., "Airfoil Design on Unstructured Grids for Turbulent Flows", AIAA Journal, 37, 2, (1999) 185-191.

[16] Burdyshaw, C. E., Anderson, W. K., "A General and Extensible Unstructured Mesh Adjoint Method", AIAA J. of Aerospace, Computing, Information, and Communication, 2, 10, 401-413 (2005).

[17] Burdyshaw, C. E., "Achieving Automatic Concurrency Between Computational Field Solvers and Adjoint Sensitivity Codes," Ph.D. Thesis, University of Tennessee, Chattanooga, May, 2006.

[18] Jameson, A., "Aerodynamic Design Via Control Theory", J. Scientific Computing, 3, (1998) 233-260.

[19] Jameson, A., Alonso, J. J., Reuther, J., Martinelli, L., Vassberg, J. C., "Aerodynamic Shape Optimization Techniques Based on Control Theory", AIAA Paper No. 98-2538, (1998).

[20] Mohammadi, B., "Optimal Shape Design, Reverse Mode of Automatic Differentiation and Turbulence", AIAA Paper No. 97-0099, (1997).

[21] Nielsen, E. J., Anderson, W. K., "Recent Improvements in Aerodynamic Optimization on Unstructured Meshes", AIAA J., 40, 6, (2002) 1155-1163.

[22] Nielsen, E. J., Anderson, W. K., "Aerodynamic Design Optimization On Unstructured Meshes Using the Navier-Stokes Equations", AIAA J., 37, 11, (1999) 1411-1419.

[23] Nielsen, E. J., "Aerodynamic Design Sensitivities on an Unstructured Mesh Using the Navier-Stokes Equations and a Discrete Adjoint Formulation", Ph.D. Dissertation, Virginia Polytechnic Institute and State University, (1998).

[24] Nielsen, E. J., Kleb, W. L., "Efficient Construction of Discrete Adjoint Operators on Unstructured Grids by Using Complex Variables", AIAA J., 44, 4 (2005) 827-836.

[25] Park, M., "Adjoint-Based, Three-Dimensional Error Prediction and Grid Adaptation", AIAA Paper No. 2002-3286, (2002).

[26] Kapadia S., Anderson W. K., Elliott L., Burdyshaw C., "Adjoint method for solid-oxide fuel cell simulations", J. Power Sources, 166 (2007) 376-385.

[27] Kapadia S., Anderson W. K., Burdyshaw, C., "Channel shape optimization of solid oxide fuel cells using advanced numerical techniques", Computers and Fluids, 41, 1 (2011) 41-50.

[28] Kapadia S., Anderson W. K., Elliott L., Burdyshaw C., "Adjoint based Sensitivity Analysis and Error Correction Methods applied to Solid Oxide Fuel Cells", ASME J. Fuel Cell Sci. Tech., 6, 2, (2009).

[29] Lin C., Huang L., Chiang L., Chyou Y., "Effects of clamping load on the thermal stress distribution in a planar SOFC with compressive sealing", ECS Transactions, 25, 2 (2009) 349-358.

[30] Lin C., Huang L, Chiang L., Chyou Y., "Thermal stress analysis of planar solid oxide fuel cell stacks: Effects of sealing design", J. Power Sources 192 (2009) 515-524.

[31] Chiang L, Liu H., Shiu Y., Lee C., Lee R., "Thermo-electrochemical and thermal stress analysis for an anode-supported SOFC cell", Renewable Energy 33 (2008) 2580-2588.

[32] Iqbal G., Pakalapati S., Blancas F., Guo H., Celik I., Kang B., "PEN structure thermal stress analysis for planar-SOFC configurations under practical temperature field", Advances in Materials Science for Environmental and Nuclear Technology II, Ceramic Transactions 227 (2011) 61-68.

[33] Jiang T., Chen T., "Thermal-stress analyses of an operating planar solid oxide fuel cell with the bonded compliant seal design", Int. J. Hydrogen Energy 34 (2009) 8223-8234.

[34] Weil K., Koeppel B., "Comparative finite element analysis of the stress-strain states in three different bonded solid oxide fuel cell seal designs", J. Power Sources 180 (2008) 343-353.

[35] Chiang L., Liu H, Shiu Y., Lee C., Lee R., "Thermal stress and thermo-electrochemical analysis of planar anode-supported solid oxide fuel cell: Effect of anode porosity", J. Power Sources 195 (2010) 1895-1904.

[36] ABAQUS webpage: http://www.3ds.com/products/simulia/portfolio/abaqus/abaqus-portfolio/

[37] FLUENT webpage: http://www.ansys.com/Products/Simulation+Technology/Fluid+Dynamics/Fluid+Dynamics+Products/ANSYS+Fluent

[38] ANSYS webpage: http://www.ansys.com

[39] STAR-CD webpage: http://www.cd-adapco.com/products/star_cd/

[40] MARC webpage: http://www.mscsoftware.com/product/marc

[41] A. Kumar, "Physical Models and Computational Algorithms for Simulation of Catalytic Monolithic Reactors", PhD Thesis, Ohio State University, (2009).

[42] A.E. Cerkanowicz, R.B. Cole, J.G. Stevens., "Catalytic Combustion Modeling; Comparisons With Experimental Data", ASME. J. Eng. Power, 99, 4, (1977), 593-600.

[43] Kramer, J.F., Reihani, S.A., Jackson, G.S., "Low Temperature Combustion of Hydrogen on Supported Pd Catalysis", 29th International Symposium on Combustion, Japan, 2002.

[44] L. L. Raja, R. J. Kee, O. Deutschmann, J. Warnatz, L. D. Schmidt, "A critical evaluation of Navier–Stokes, boundary-layer, and plug-flow models of the flow and chemistry in a catalytic-combustion monolith", Catalysis Today, 59, Issues 1–2, (2000), 47-60.

[45] O Deutschmann, L.I Maier, U Riedel, A.H Stroemman, R.W Dibble, "Hydrogen assisted catalytic combustion of methane on platinum", Catalysis Today, 59, Issues 1–2, (2000), 141-150.

[46] U. Dogwiler, P. Benz and J. Mantzaras, "Two-Dimensional Modelling for Catalytically Stabilized Combustion of a Lean Methane-Air Mixture with Elementary Homogeneous and Heterogeneous Chemical Reactions", Combustion and Flame, 116, (1999), 243-258.

[47] P. Markatou, L. D. Pfefferle, M. D. Smooke, "A computational study of methane-air combustion over heated catalytic and non-catalytic surfaces", Combustion and Flame, 93, 1–2, April 1993, 185-201.

[48] M. Hartmann, L. Maier, H.D. Minh, O. Deutschmann, "Catalytic partial oxidation of iso-octane over rhodium catalysts: An experimental, modeling, and simulation study", Combustion and Flame, 157, 9, September 2010, 1771-1782.

[49] Matteo Maestri, Alberto Cuoci, "Coupling CFD with detailed microkinetic modeling in heterogeneous catalysis", Chemical Engineering Science, 96, 7 June 2013, 106-117.

[50] M. Hettel, C. Diehm, H. Bonart, Olaf Deutschmann, "Numerical simulation of a structured catalytic methane reformer by DUO: The new computational interface for OpenFOAM® and DETCHEM™", Catalysis Today, Available online 26 February 2015.

[51] OpenFOAM, The Open Source CFD Toolbox, www.openfoam.org.

[52] O. Deutschmann, S. Tischer, C. Correa, D. Chatterjee, S. Kleditzsch, V.M. Janardhanan, N. Mladenov, H.D. Minh, H. Karadeniz, M. Hettel, DETCHEM Software Package, www.detchem.com.

[53] H. D. Minh, H. G. Bock, S. Tischer, O. Deutschmann, "Optimization of Two-Dimensional Flows with Homogeneous and Hetergeneously Catalyzed Gas-Phase Reactions", AIChE journal, 54, 9, (2008), 2432-2440.

[54] H.D. Minh, "Numerical Methods for Simulation and Optimization of Chemically Reacting Flows in Catalytic Monoliths", PhD Thesis, University of Heidelberg, 2005.

[55] David G. Goodwin, Harry K. Moffat, and Raymond L. Speth, "Cantera: An object-oriented software toolkit for chemical kinetics, thermodynamics, and transport processes", http://www.cantera.org, (2015), Version 2.2.0.

[56] Adams, B.M., Bauman, L.E., Bohnhoff, W.J., Dalbey, K.R., Ebeida, M.S., Eddy, J.P., Eldred, M.S., Hough, P.D., Hu, K.T., Jakeman, J.D., Swiler, L.P., and Vigil, D.M., "DAKOTA, A Multilevel Parallel Object-Oriented Framework for Design Optimization, Parameter Estimation, Uncertainty Quantification, and Sensitivity Analysis: Version 5.2

User's Manual," Sandia Technical Report SAND2010-2183, December 2009. Updated November 2011.

[57] Wang, Y., Yoshiba, F., Watanbe, T., Weng, S., "Numerical analysis of electrochemical characteristics and heat/species transport for planar porous-electrode-supported SOFC", J. Power Sources, 170, (2007) 101-110.

[58] Hwang, J. J., Chen, C. K., Lai, D. Y., "Computational analysis of species transport and electrochemical characteristics of a MOLB-type SOFC", J. Power. Sources, 140, (2005) 235-242.

[59] Noren, D. A., Hoffman, M. A., "Clarifying the Butler-Volmer equation and related approximation for calculating activation losses in solid oxide fuel cell models", J. Power Sources, 152, (2005) 175-181.

[60] Costamagna, P., Selimovic, A., Borghi, M., Agnew, G., "Electrochemical model of the integrated planar solid oxide fuel cell (IP-SOFC)", Chem. Eng. J., 102, (2004) 61-69.

[61] O. Deutschmann, "Modeling and Simulation of Heterogeneous Catalytic Reactions", Wiley-VCH, (2012).

[62] R. J. Kee, M. Coltrin, P. Glarborg, "Chemically Reacting Flow: Theory & Practice", John Wiley & Sons, 2003.

[63] Anthony G. Dixon, "Advances in Chemical Engineering- Modeling and simulation of heterogeneous catalytic processes", 45, Academic Press, (2014).

[64] Karman, S. L Jr., Anderson, W. K., Sahasrabudhe M.,"Mesh Generation Using Unstructured Computational Meshes and Elliptic Partial Differential Equation Smoothing", AIAA J., 44, 6, June 2006.

[65] Nielsen, E. J., Park, M. A., "Using An Adjoint Approach to Eliminate Mesh Sensitivities in Computational Design", AIAA J., 44, 5, (2006) 948-953.

[66] Anderson, W. K., Karman, S. L., Burdyshaw, C., "Geometry Parameterization Using Control Grids," Presented at the 12th AIAA/ISSMO Multidisciplinary Analysis, 2008.

[67] Haimes, R, Follen, G., "Computational Analysis Programming Interface", Proceedings of the 6th International Conference on Numerical Grid Generation in Computational Field Simulations, Editors: Cross, Eiseman, Hauser, Soni and Thompson, July 1998.

[68] J. C. Meza, R. A. Oliva, P. D. Hough, and P. J. Williams. OPT++: An object oriented toolkit for nonlinear optimization. ACM Transactions on Mathematical Software, 33, 2, (2007).

[69] Vanderplaats Research and Development, Inc., Colorado Springs, CO. DOT Users Manual, Version 4.20, (1995).

[70] Grama A., Gupta, A., Karypis, G., Kumar, V., "Introduction to Parallel Computing", Second Edition, Addison Wesley, Jan. 16, 2003.

[71] METIS webpage: http://glaros.dtc.umn.edu/gkhome/views/metis

[72] POINTWISE webpage: http://www.pointwise.com

[73] Roe, P. L., "Characteristic-based schemes for the Euler equations", Ann. Rev. Fluid Mech., 18, (1986) 337-365.

[74] Busby M., "Steps Toward More Accurate and Efficient Simulations of Reactive Flows", Ph.D. Thesis, Mississippi State University, August 1997.

[75] Olaf Deutschmann, Renate Schwiedemoch, Luba I. Maier, Daniel Chatterjee, "Natural Gas Conversion in Monolithic Catalysts: Interaction of Chemical Reactions and Transport Phenomena", In: E. Iglesia, J.J Spivey and T.H. Fleisch, Editor(s), Studies in Surface Science and Catalysis, Elsevier, 136, (2001), 251-258.

[76] O. Deutschmann, L. D. Schmidt, "Modeling the Partial Oxidation of Methane in a Short-Contact-Time Reactor", AIChE Journal, 44, 11, (1998), 2465-2477.

[77] O. Deutschmann, R. Schmidt, F. Behrendt, J. Warnatz, "Numerical Modeling of Catalytic Ignition", Proc. Combust. Inst., 26, (1996), 1747-1754.

[78] Shi L., Bayless D., Prudich M., "A CFD model of autothermal reforming", International Journal of Hydrogen Energy, 34, (2009), 7666-7675.

[79] Thormann J., Maier L., Pfeifer P., Kunz U., Deutschmann O., Schubert K., "Steam reforming of hexadecane over a Rh/CeO_2 catalyst in microchannels: Experimental and numerical investigation", International Journal of Hydrogen Energy, 34, (2009), 5108-5120.

[80] Tee L., Gotoh S., Stewart W., "Molecular Parameters For Normal Fluids", I & EC Fundamentals, 5, 3, August 1996.

[81] Wang L., Anderson W. K., Erwin T. J., Kapadia S., "Discontinuous Galerkin and Petrov Galerkin methods for compressible viscous flows", Comp. & Fluids, 100, (2014), 13-29.

[82] http://zjwang.com/hiocfd.html

JP-8 Fuel Desulfurization and Reforming/Shifting
—Making Hydrogen Rich Fuels for Solid Oxide Fuel Cells

Presented by:

Peiwen (Perry) Li
Energy and Fuel Cell laboratory
Department of Aerospace and Mechanical Engineering
The University of Arizona
Tucson, AZ 85721
peiwen@email.arizona.edu

Submit to:

Sagar Kapadia
SimCenter
University of Tennessee at Chattanooga
701 E. ML King Blvd.
Chattanooga, TN 37403
Sagar-kapadia@utc.edu

TABLE OF CONTENTS

1. Executive summary

In order to supply hydrogen or syngas for fuel cell-based auxiliary power units, onboard fuel processing technology has been paid significant attention in energy and fuel cell society. For providing hydrogen rich fuels to fuel cells, converting hydrocarbon fuels into syngas through reforming/shift reactions has relatively less technical obstacles regarding the storage of hydrocarbon fuels compared to hydrogen gas fuel.

This project focused on onboard fuel processing of commercial Jet-A (equivalent to JP-8 regarding sulfur and hydrocarbon content) fuel to produce hydrogen and syngas for fuel cell auxiliary power units. Jet-A fuel was studied because it is the logistic fuel (equivalent to JP-8) commonly used for civilian airplanes and military heavy duty trucks. The research team developed a new catalyst, using low cost materials, for desulfurization from Jet-A fuel at room temperature and ambient pressure, which is innovative and cost-effective. Ultra-deep adsorptive desulfurization has been achieved for Jet-A fuel from over 1,000 ppmw to below 50 ppmw. The second part of this work focused on autothermal reforming of desulfurized jet-A fuel. Autothermal reforming catalyst and monolith reaction section have been developed. The experimental tests for syngas production were conducted firstly using n-dodecane (as a surrogate of Jet-A fuel), and then using desulfurized Jet-A fuel. A reactor accommodating both reformer and water-shift reactions for desulfurized Jet-A fuel has been designed and operated.

For the adsorptive desulfurization of Jet-A fuel, a novel cost-effective $NiO-CeO_2/Al_2O_3-SiO_2$ adsorbent was proposed and prepared in-house for experimental tests. Details of the compositions of catalyst and procedures of making and processing the catalyst are provided in this report. The sulfur adsorption kinetic characteristic and isotherm at equilibrium were studied in batch tests. The maximum desulfurization efficiency could reach up to 98%. For Jet-A fuel in a total sulfur concentration of 1037 ppmw, the lowest achieved sulfur concentration at room temperature in the treated fuel was 22.13 ppmw. This is a significant achievement regarding the desulfurization efficiency, especially at room temperature and using commercial Jet-A fuel with no pretreatment. The dynamic desulfurization performance of the adsorbent was investigated in fixed-bed reactor tests. The flow rate of fuel, size of adsorbent particles, and dimensions of an adsorbent-packed fixed-bed were optimized to obtain a high sulfur adsorption capacity per unit mass of adsorbent. At a breakthrough sulfur concentration of 10 ppmw a very high sulfur adsorption capacity of 0.633 mg S/g adsorbent was achieved. At a mean sulfur concentration of 30 ppmw in the treated accumulated fuel, the best capacity achieved is 1.98 mg S/g adsorbent. The scaling-up strategies for the fixed-bed reactor and the method for adsorbent regeneration are also investigated. Finally, preliminary tests of adsorbent regeneration showed that the first-time regenerated adsorbent could recover 83% of the sulfur removal capacity compared to a fresh adsorbent, and a second time regeneration could recover 50.4% of that of fresh adsorbent.

For the reforming of Jet-A fuel, autothermal reforming (ATR) method was employed and a bimetallic NiO-Rh catalyst with promoters of Ce, K, and La were synthesized for the ATR reactions. A lab-scale 2.5 kW_t autothermal reforming system including the reformer and balance-of-plant was designed, fabricated, integrated and tested. The reforming system performance at various operation conditions was compared. Reformer operation temperature, steam to carbon ratio and oxygen to carbon ratio, as well as pre-heating temperatures for fuel, air, and steam were optimized for better system energy conversion efficiency, H_2 selectivity, and COx selectivity. For n-dodecane the energy conversion efficiency was 83.5% while for desulfurized commercial Jet-A fuel the efficiency reduced to 77.0%.

2. Introduction

High energy efficiency and energy density, together with rapid refuel capability, render fuel cells being highly attractive for portable power generation, serving as auxiliary/backup power units (APUs). Fuel cell APUs need hydrogen or syngas as the energy source to produce electrical power, however, there is no existing infrastructure for hydrogen production and storage. To provide hydrogen for fuel cells in military and civilian APUs, jet fuels are widely considered as an excellent choice since they are logistic fuels for both civilian and military transportation vehicles. Integrated micro fuel processors in combination with solid oxide fuel cell (SOFC) stacks using jet fuels have been viewed as achievable technologies for power generation.

There are various organic sulfur compounds contained in jet fuels. As regulated by the US Environmental Protection Agency (EPA) in 2010, the highest sulfur concentration allowed in jet fuels is 3000 ppmw. The major sulfur compounds in jet fuels are 2,3-DMBT (2,3-dimethylbenzothiophene), 2,3,7-TMBT (2,3,7-trimethylbenzothiophene), 2,3,5-TMBT (2,3,5-trimethylbenzothiophene), and 2,3,6-TMBT (2,3,6-trimethylbenzothiophene). The sulfur contents must be removed before jet fuels can be reformed to produce hydrogen or syngas for fuel cells. This is because the presence of high level sulfur compounds is harmful to the catalyst for the reforming reaction, and also because sulfur is poisonous to the electrodes and catalysts in fuel cells. Therefore, for jet fuels being supplied to reforming and water-shift for producing hydrogen rich fuels, there are three critical research subjects to be addressed: 1) catalytic desulfurization of the fuel; 2) autothermal catalytic reforming with precisely controlled oxygen, steam, and fuel at a temperature; 3) system integration and thermal management for reforming and water-shift to be included in one reactor.

Conventional desulfurization technology employed in refineries is the hydrodesulfurization (HDS) method. This technology, working at 300–400 °C and 40–50 bars, requires heavy expenditure in both capital and operation. It also needs large volume reactors, making it inconvenient for portable fuel cell applications. Another drawback of HDS is that the octane number is significantly reduced, due to the saturation of alkenes and arenes by hydrogen at high temperatures and pressures. Desulfurization of commercial jet fuel at room temperature and atmospheric pressure is desirable for practicality and simplicity of the system. Selective adsorptive desulfurization or (selective adsorption for removing sulfur—SARS) of real Jet-A fuel with an initial total sulfur concentration of over 1000 ppmw at room temperature and atmospheric pressure is the objective of our present study. Using commercial Jet-A fuel instead of model fuel is a big challenge in the adsorptive desulfurization study, because aromatics and olefins in the real fuel have a strong inhibiting effect on the adsorptive desulfurization performance, especially at low temperatures [1].

Desulfurization methods suitable for portable applications without reducing the fuel octane number have been studied in recent years, and two of the promising processes were pervaporation [2-4] and selective adsorption [5-8]. The latter is considered the most promising method [1]. Various adsorbents, based on transition metals and supported materials including metals, carbon, and zeolites, have been proposed for sulfur adsorption performances [9-13]. Nickel and copper supported on activated carbon and zeolite exhibited effective desulfurization effects for jet fuels [14,15]. Muzic et al. [16] examined the adsorptive desulfurization of three commercial activated carbon adsorbents on diesel fuel. Dastanian and his coworkers [17] studied the desulfurization of gasoline containing 140 ppmw total sulfur by using a nanoporous Ni loaded, Y-type zeolite at ambient conditions. The adsorption capacity of Ni-Y zeolite was 0.84 and 2.31 mg S/g adsorbent, corresponding to the fuel residual sulfur concentrations of 10 and 30

ppmw, respectively, in a batch test. Montazerolghaem et al. [18] investigated the adsorptive sulfur removal from a modeled gasoline by Na-Y zeolite and Ce-Y zeolite at room temperature. Their sulfur model solution consisted of iso-octane and thiophene that contained about 116 ppmw total sulfur compounds initially, and after the desulfurization, the total sulfur concentration was about 20 ppmw. The Ce-Y zeolite was reported to have a better desulfurization performance than the Na-Y zeolite, and the capacity of Ce-Y zeolite was around 0.68 mg S/g adsorbent at the adsorbent to modeled gasoline ratio of 1 g/10 ml fuel. Nevertheless, these mentioned catalysts and supporter materials (such as activated carbon and zeolite) are generally expensive, and search for low cost catalyst for practical application is focused in this project.

The ideal adsorbent for the SARS process at room temperature and atmospheric pressure must simultaneously satisfy merits of strong Lewis surface acidity, big specific surface area, strong ionic polarity, perfect redox properties, and chemical and thermal stabilities. In our works [12], using the advantages of the SARS mechanisms of p-complexation, direct S–M interaction, active sites for adsorption, and the promotional effect of adsorbent material structure corresponding to the novel geometric effect and the meso-porous structure, we developed a promising adsorbent, $Ni–Ce/Al_2O_3–SiO_2$, for the ultra-deep desulfurization of jet fuels with a high sulfur content at room temperature. The adsorbent to be investigated in this work has been proven to have good sulfur compounds selectivity, reasonable adsorptive capacity, and the ability to decrease the total sulfur concentration to below 50 ppmw. Very importantly, the cost of the catalyst materials is low which important for large scale application.

The three main approaches for reforming of hydrocarbon fuels are steam reforming (SR), partial oxidation (POX), and autothermal reforming (ATR). There has been a number of research works studied the reforming of different fuels, such as ethanol, gasoline, diesel, and jet fuels employing one of the above-mentioned approaches. It is understood from the literature that SR has high H_2 concentration in reformate, but it requires lots of external heat and the system is usually bulky and heavy. POX has a compact system and the reaction is exothermic, however, the H_2/CO ratio in reformate is relatively low. ATR is a combination of POX followed by SR and it has the most suitable characteristics for onboard fuel reforming. An ATR system has favorable H_2/CO ratio in reformate, less coke formation tendency, no requirement of external heat source, relatively compact system size and weight, and rapid startup and dynamic responses. Because of the advantages of ATR, it was selected as the approach of reforming in the present study. Both reforming catalyst and operation conditions can significantly influence the ATR reaction in respect to H_2 and CO concentrations, hydrogen and COx selectivity, as well as system energy conversion efficiency [19]. Ni-based catalysts for fuel reforming have been widely used because of the high activity and low cost. However, Ni catalysts have inherent challenges such as sulfur poisoning and coke formation [20]. Noble metals were proven to be effective in fuel reforming reactions, but the high price of noble metals is a disadvantage [21,22]. Thus bimetallic catalysts (including nickel and noble metal) have been proposed and investigated in some works for fuel reforming. Effects of ATR operating conditions such as steam to carbon ratio (S/C) and oxygen to carbon ratio (O_2/C) were investigated both numerically and experimentally for different reformers, and it is believed that the reasonable working ranges of S/C and O_2/C are 1.25-2.5 and 0.35-0.5, respectively. A lab-scale 2.5 kW$_t$ autothermal reforming system with a new reformer design and novel catalyst was experimentally studied. The used bimetallic catalyst is NiO-Rh which is mixed with promoters of CeO_2, K_2O, and La_2O_3, and was prepared in-house for experimental test. Using n-dodecane as a surrogate of Jet-A fuel, the effects of operating

conditions such as reformer temperature, S/C, and O_2/C were experimentally investigated in respect to hydrogen selectivity, COx selectivity, and the energy conversion efficiency. Coke formation was suppressed by reducing the pre-heating temperature of the fuel. After the optimized operating conditions were determined, desulfurized commercial Jet-A fuel was tested in the ATR system.

Because of the complexity of carbon content in jet-A fuel, surrogate of Jet-A fuel, *n*-dodecane, was firstly used in laboratory experiments to investigate the reforming characteristics. Real desulfurized commercial Jet-A fuel was thereafter tested at the optimized reforming operation conditions.

3. A new selective adsorption catalyst for Jet fuel desulfurization at room temperatures

The main objectives of the present work include: 1) addressing the challenges of removing sulfur compounds in commercial jet fuels to an acceptable level using low cost catalyst; 2) reforming the low-sulfur jet fuels into hydrogen rich syngas for use in SOFC APUs. Jet-A and JP-8 are the two most commonly used jet fuels in civilian and military applications. Since JP-8 fuel is for military use and restricted for public to purchase, Jet-A fuel was selected as the test fuel in this study. The hydrocarbon and sulfur content of jet-A and JP-8 are believed the same.

3.1 Jet fuel analysis

Jet fuels are commonly used in heavy-duty trucks, aircraft, and ships, and they are also the preferred logistic fuels in military applications because of their higher efficiency and power density as well as lower flammability than gasoline. JP-8 was selected as the exclusive battlefield fuel by the Department of Defense and North Atlantic Treaty Organization [23] due to its high flash point of 38 °C and good low-temperature operations [24]. The specifications for JP-8 are similar to Jet-A except that JP-8 has required additives for anti-icing, a corrosion inhibitor, lubricity improver, and anti-static, as well as antioxidant and metal deactivators [25]. Jet-A is a kerosene type of fuel and is widely used as fuel for civilian airliners [26]. A better understanding of diesel and jet fuel properties will be helpful to the development of an onboard fuel processing system for the fuel cell APUs.

Jet fuels consist of thousands of chemicals, mainly hydrocarbons, as well as functional additives. Kerosene types Jet-A and JP-8 fuels have approximate carbon number distributions between 8 and 16, and H/C molar ratios from 1.6 to 2.0. The average molecular formula of JP-8 fuel is $C_{11}H_{21}$ [27], and the average molecular formula of Jet-A fuel is $C_{11.6}H_{22.3}$ [28]. Aromatics in jet fuels are limited to no more than 25% by volume [29]. As listed in reference [20], typical jet fuels in the U.S. has an average 71% volume of paraffins, 19% volume of aromatics, 6.2% volume of naphthalenes and 3.5% volume of olefins.

Various sulfur compounds are contained in commercial jet fuels. The major sulfur compounds in jet fuels are 2,3-DMBT (2,3-dimethylbenzothiophene), 2,3,7-TMBT (2,3,7-trimethylbenzothiophene), 2,3,5-TMBT (2,3,5-trimethylbenzothiophene), and 2,3,6-TMBT (2,3,6-trimethylbenzothiophene). Desulfurization will remove these compounds as much as possible.

Sulfur compounds contained in both diesel and jet fuels are unwanted because they are poisonous to catalysts and electrodes in fuel cells. In the U.S., the regulations for sulfur content in diesel and jet fuels set by the Environmental Protection Agency (EPA) have become more and more strict. Table 1 shows the regulations for sulfur content from 1993 to 2010 [30]. Although the sulfur concentration regulation set by EPA in 2010 is less than 3,000 ppmw, the average

value of sulfur concentration for jet fuel reported in the literature is 714 ppmw. However, there is a standard deviation of 414 ppmw, which reflects that the variations of sulfur concentrations in different fuel sources are quite large [31-36]. The jet-A fuel in this work was purchased from Million Air, Tucson—a local fuel supplier at the airport. The total sulfur concentration in the fuel was measured by a Thermo TS 3000 total sulfur analyzer, which has a working range of 0.02–5000 ppmw and an uncertainty of less than 5% of the measured value. Our measurement to the commercial jet-A fuel showed a content of 1140 ppmw of sulfur.

Table 1 U.S. EPA's sulfur regulations for diesel and jet fuels [30]

Category	Year		
	1993	2006	2010
Highway diesel (ppmw)	500	15	15
Non-road diesel (ppmw)	5000	500	15
Jet fuel (ppmw)	3000	3000 max	<3000

Surrogates of diesel and jet fuels are usually used in laboratory research and experiments to better calculate and control the reforming processes for optimization. Surrogates are typically divided into two types. Physical surrogates are mixtures that have similar physical properties (e.g., heating value, density, viscosity, specific heat capacity, flash point, etc.) to real fuels. Chemical surrogates are mixtures that have generally the same chemical-class compositions (e.g., aromatics, naphthenes, olefins, alkanes, etc.) and average molecular weight as real fuels [37,38]. In the fuel reforming process, surrogates are expected to reproduce most of the fuel chemical characteristics, as well as some important physical properties in heat and mass transfer [39]. The lower heating value (LHV) is one most important property of fuels since it determines the reforming efficiency. The quantity of LHV is determined by subtracting the heat of water vaporization from the higher heating value (HHV), which is the thermodynamic heat of combustion. A number of recent studies on surrogates of diesel and kerosene type jet fuels for autothermal reforming have been reported [40-45]. n-dodecane ($\geq$99%) was proved to be a good surrogate of Jet-A [39] to study the autothermal reforming in terms of fuel conversion, hydrogen yield, reactor temperature profile and reforming efficiency. As a surrogate fuel, n-dodecane has the chemical formula of $C_{12}H_{26}$ with hydrogen content 15.28 wt.%. And the molecular weight was 170.3 g/mol, and LHV was 44.14 MJ/kg (LHV of Jet-A fuel is 43.26 MJ/kg).

3.2 Proposed catalyst and the procedures of preparation

3.2.1 Design of catalyst

Two most popular types of adsorptive desulfurization mechanisms are π-complexation [46-48] and direct Sulfur-Metal (S-M) interaction. The π-complexation adsorbents particularly the Y-zeolites exhibit high sulfur-adsorption capacity, but show low selectivity for sulfur compounds as the result of competitive adsorption of aromatic compounds. Meanwhile, according to the adsorption mechanism of direct S-M interaction, the adsorbents possess high selectivity for sulfur compounds, but the steric hindrance make them difficult to remove sulfur from DMDBT (dimethyl dibenzothiophene) etc. In this project, the investigators believe that both of the positive effects of the above two mechanisms may be utilized by selecting a proper adsorbent. Thiophene has two lone pairs of electrons on the sulfur atom: one pair lies on the six-electron π system and the other lies in the plane of the ring. Thiophene can act either as an n-type donor by

donating the lone pairs of electrons that lie in the plane of the ring to the adsorbent (direct S-M σ bond) or as a π-type donor by utilizing the delocalized π electrons of the aromatic ring (π bond) to form a π-type complex with the metal ions [15]. On the other hand, the sulfur-adsorption capacity and selectivity of adsorbents can be further improved by modifying various types of surface active sites for sulfur adsorption, such as Lewis acid sites, useful functional groups, electronic defect centers, micro-structural defects and so on. According to Lewis acid-base theory, most thiophene sulfur compounds in jet fuels are Lewis base [49], which are easy to be adsorbed at Lewis acid sites. Hence, we can design and select materials that possess strong Lewis acid sites to selectively adsorb thiophene sulfur compounds with the lone pair electrons in jet fuels. The Lewis acid-base adsorption mechanism is the interaction between the acid sites on the surface of adsorbents and thiophene derivatives. Additionally, it is known that sulfur compounds have more affinity to oxidation than their analogue hydrocarbons in jet fuels [35], therefore, perfect redox properties of adsorbents can improve oxidization of sulfur compounds into sulfones and sulfoxides. High conversions of sulfides to sulfones and sulfoxides provide stronger polarities that enhanced selective removal of organic sulfur compounds with solid adsorbents at ambient temperature and atmospheric pressure. As a consequence, perfect redox properties of adsorbents can indirectly increase the sulfur-adsorption capacity and selectivity. Therefore, in the present study we developed a novel hybrid meso-porous material of Ni^{2+} and Ce^{4+} modified Al_2O_3-SiO_2 binary oxide, with Al_2O_3 being the main component, for selectively removing sulfur from real jet-A fuel with high sulfur content. The ideal adsorbent model is shown in Fig.1.

Figure 1.   Ideal adsorbent model for desulfurization of Jet-A fuel

In the adsorbent of Al_2O_3-SiO_2 with Al_2O_3 being the main component oxide, the charge difference for each bond is 1/2, and for all the bonds the valence unit is 2 according to Tanabe's hypothesis on the surface acidity of binary oxide [50]. In this case, the Lewis acidity appears upon the presence of the positive charge. Therefore, the big specific surface and the Lewis acidity of the mesoporous Al_2O_3-SiO_2 binary oxide will greatly enhance adsorption capacity of thiophene sulfurs in jet fuels at low temperatures. Compared to conventional adsorbent using

SiO_2-Al_2O_3 as support material with SiO_2 being the major component oxide, the advantage of novel adsorbent NiO-CeO_2/Al_2O_3-SiO_2 with Al_2O_3 being the major component oxide for desulfurization at ambient temperature and pressure has been reported in the previous work.

3.2.2 Catalyst preparation procedures (information with patent pending)

In our preliminary work [12], adsorbent preparation methods—extrusion, sol-gel, and wet impregnation, as shown in Fig. 2—were evaluated, and the extrusion method was recommended due to its relatively high desulfurization efficiency of the thereby prepared adsorbent. In the preparation of the proposed NiO-CeO_2/Al_2O_3-SiO_2 adsorbent, low cost raw materials, large pore Pseudo-boehmite (68~72% Al_2O_3, surface area > 300 m^2/g, pore volume 0.8~1.0 cm^3/g) and diatomite (>95% SiO_2), were respectively used as the source of alumina and silica, and analytical reagent grade nickel acetate hydrate ($Ni(CH_2COOH)_2.4H_2O$) and cerium acetate hydrate ($Ce(CH_2COOH)_3.5H_2O$) were employed as precursors. The mass composition of Ni–Ce/Al_2O_3–SiO_2 satisfies that Ni/Ce = 10 in mol, Al/Si = 15 in mol, and then Al–Si–Ox/Ni–Ce–Oy = 9 in mass (refer to publication #2 under this project). First, Ni-Ce solution was synthesized by dissolving nickel acetate hydrate and cerium acetate hydrate in distilled water under constant stirring at 60 °C. Then pseudo-boehmite and diatomite were mixed with distilled water and a certain amount of nitric acid in another container. The next step was to add the Ni-Ce solution to the pseudo-boehmite and diatomite mixture and stir them vigorously for 10 min to get the adsorbent slurry ready. The prepared adsorbent slurry was then extruded by using a catalyst extruder machine. After drying the extrudates at 50 °C in a forced air oven overnight, the dried extrudates were then calcined in helium gas in a tube furnace (MTI OTF-1200X-80) at 650 °C for 2 h. After cooling down to the room temperature, the calcined adsorbents were pelletized and sieved to the required particle size. Before using for desulfurization, the prepared adsorbents need to be dried in helium gas in tube furnace at 500 °C for 2 h for dehydration. The BET surface area and pore size distribution of the prepared adsorbent were measured/characterized by a Micromeritics TriStar II 3020 equipment using the N_2 adsorption-desorption method at liquid N_2 temperature. Characterization of the adsorbents helped us to analyze and optimize the procedures and conditions for fabrication of the catalyst.

*Figure 2   Ni–Ce/Al₂O₃–SiO₂ adsorbents prepared by three different methods. (a) Extrusion molding—**the best method adopted**; (b) wet impregnation; (c) sol–gel.*

3.3   Desulfurization results from batch test

Batch tests were designed to study the equilibrium and kinetics of Jet-A fuel desulfurization process based on the NiO-CeO_2/Al_2O_3-SiO_2 adsorbent. For each test run, 5 g of Jet-A fuel with a measured sulfur concentration of 1037 ppmw was put in a flask containing pre-weighted adsorbent. The flasks were sealed by plastic films and agitated at a constant rate of 250 rpm in an orbital shaker (Scilogex SK-O330-Pro) at room temperature and atmospheric pressure for 24 h.

The desulfurization performances of adsorbents were characterized by measuring the residual sulfur concentration in supernatant fuel liquid after a sufficiently long time was taken to reach the adsorption equilibrium. Figure 3 shows a visual comparison of the commercial Jet-A fuel and the treated fuel in our preliminary study. The color of the fuel changed from a straw color to colorless, which proves that the developed adsorbent has an impressive selectivity of organosulfur compound. The total sulfur concentration was measured by a Thermo TS3000 total sulfur analyzer, which has a working range of 0.02-5000 ppmw, and an uncertainty of less than 5% of the measured value. The desulfurization efficiency (%) and equilibrium adsorption loading q in the adsorbent (mg/g) were calculated as follows:

$$\text{Desulfurization efficiency (\%)} = (C_0 - C_s)/C_0 \times 100 \tag{1}$$

$$\text{Loading } q \text{ (mg-S/g-ads)} = m_{fuel}(C_0 - C_s)/m_{ads} \tag{2}$$

where C_0 is the initial sulfur concentration (ppmw), C_s is the residual sulfur concentration (ppmw), m_{fuel} (g) is the mass of fuel sample, and m_{ads} (g) is the mass of the adsorbent, which includes the catalyst and support material.

Figure 3 Left: original Jet-A fuel; Right: treated Jet-A fuel

3.3.1 Effects of adsorbent calcination temperature and time

To prepare the adsorbent, any dried adsorbent extrudate was calcined at a constant temperature for 3 hours in a helium gas atmosphere. In our preliminary study helium was proved to be a better calcination gas than nitrogen, argon and air. Different temperatures ranging from 400– 800 °C were chosen for the calcination process, and the prepared adsorbent was tested for desulfurization efficiency in order to optimize the calcination temperature. For each test, sufficient mass of 4 g adsorbent was put into 5g Jet-A fuel, and the sulfur concentration in the Jet-A fuel sample was measured after 24 h adsorption.

The desulfurization efficiencies of each adsorbent calcined at different temperatures are shown in Fig. 4. It is evident that the desulfurization performance of the adsorbent significantly improves as the calcination temperature increases from 400 °C to 650 °C. From 650 °C to 800 °C the desulfurization performance slightly decreases with the increase of calcination temperature. The increase of calcination temperature accelerates adsorbent sintering, promoting the combustion of organic matters and the volatilization of physically and chemically combined

water, which enhances the surface activation energy of the adsorbents. However, extremely high temperatures can induce over-sintered adsorbents, thus lowering the adsorption activity. In conclusion, the adsorbent calcined at 650 °C has the best desulfurization efficiency of 96.5% on Jet-A fuel with a 1,037 ppmw initial sulfur concentration.
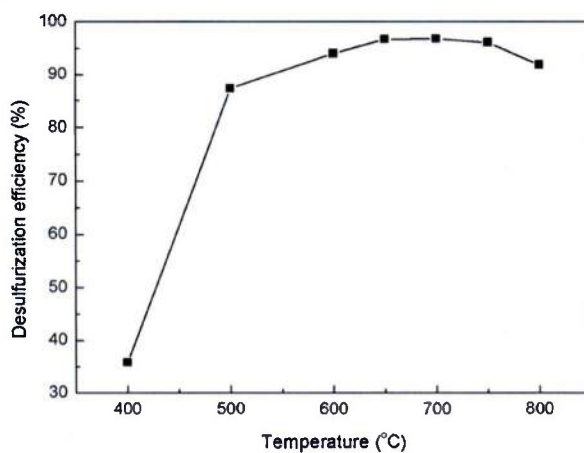

Figure 4 Effect of calcination temperature on adsorbent desulfurization performance

Besides the calcination temperature, the calcination time can also influence the adsorbent desulfurization performance. Figure 5 presents the effect of calcination time on adsorbent desulfurization efficiency for Jet-A fuel. All adsorbents were calcined at 650 °C in a helium gas atmosphere. Again, for each of the tests, sufficient adsorbent and time were used and sulfur concentration could no longer be reduced by adding more adsorbent. It shows that the variation of calcination time in 0.5 to 4 hours affects the desulfurization efficiency about 3%, which is less significant compared to the effect of the calcination temperatures. Nevertheless, the experimental results showed that 2 hours is the optimal calcination time, which is used to prepare the adsorbent samples in our study. The maximum desulfurization efficiency could reach up to 98%.
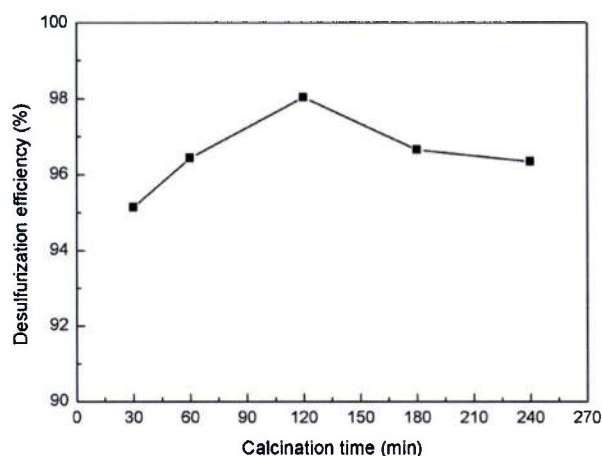

Figure 5   Effect of calcination time on adsorbent's desulfurization performance

3.3.2 Preliminary adsorbent screening

The adsorbents with different proportions of metal catalysts and support materials were prepared under the same procedure, followed by calcination at 650 °C for 2 h in helium gas. There were 10 samples prepared in this study. Their molar ratios of Al to Si for the support, Ni to

Ce for the catalyst, and mass ratio of Al-Si-Ox to Ni-Ce-Oy, varied in the ranges of 10-20, 5-15, and 4-11, respectively. For each test, sufficient mass of 4 g adsorbent was put into 5g Jet-A fuel, and the sulfur concentration in the Jet-A fuel sample was measured after 24 h adsorption. The desulfurization efficiencies of the samples are compared in Figure 6. Sufficient adsorbent and time was used and sulfur concentration could no longer be reduced by adding more adsorbent. The curves in Fig. 6 indicate that the performance of the 10 samples varies significantly. It is understood that the disparate loading of metal catalysts on support materials results in different specific surface areas, as well as different pore diameters and volumes on the adsorbent, which drastically affects the sulfur adsorption [51,52]. The highest desulfurization efficiency reaches 98%. The composition of the metal catalyst and support materials from this sample with the best performance was used in the following further study. The adsorbent sample with the best desulfurization performance had Ni/Ce=10 in mole, Al/Si=15 in mole, and Ni-Ce-Ox/Al-Si-Oy=9 in mass.
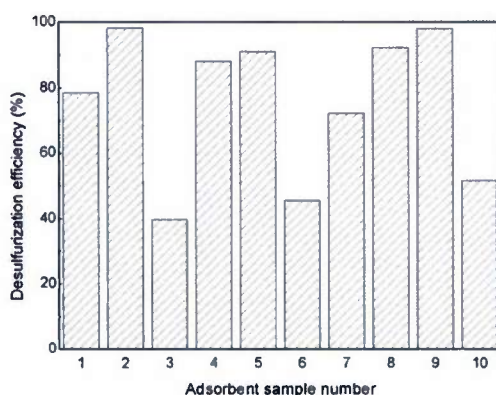

Figure 6 Effect of composition on adsorbent desulfurization performance

3.3.3 Effect of adsorbent-to-fuel mass ratio

The effect of the adsorbent mass in a certain amount of fuel was investigated by varying the adsorbent from 0 to 8 g for 5 g Jet-A fuel in the desulfurization tests. After shaking the test samples with the fuel on a vibration plat with 250 rpm for 24 h, the sulfur concentrations in the fuel were measured, and the results are shown in Fig. 7. Obviously, with the increase of the mass of adsorbent from 0 to 4 g, less and less sulfur compounds were left in the fuel, which is reflected as a significant increase of the desulfurization efficiency. When the mass of the adsorbent is more than 4 g, the sulfur concentrations of the after-treated fuel does not decrease any more, which means there is no increase of the desulfurization efficiency.
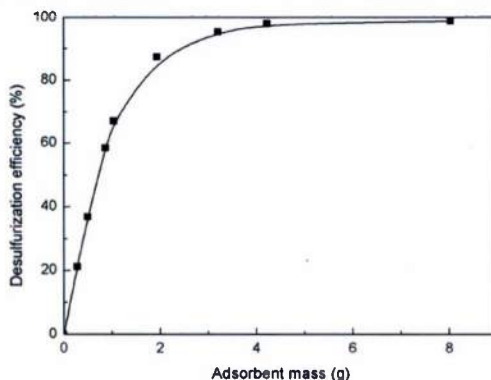
Figure 7 Effect of adsorbent mass on adsorbent desulfurization performance (at room temperature)

The increase of sulfur adsorption shown in the curve is due to the increase of the mass of the absorbent from 0 to 4 g, which actually increases the active surface area, or sites for sulfur adsorption. When the mass of the adsorbent is more than 4 g, the adsorption equilibrium between adsorbate and adsorbent is reached so that the desulfurization efficiency is almost constant. This effect is the so called overcrowding of particles as elaborated in the reference [9].

3.3.4 Kinetic models and equations

In order to better understand the adsorption process, the commonly used kinetic models including the pseudo-first order model, the pseudo-second order model, and the intraparticle diffusion model were examined to best describe the sulfur adsorption kinetics of the new developed adsorbents.

The pseudo-first order Lagergren model is expressed as

$$r_q = k_f \left(q_e - q_t \right) = dq_t / dt \tag{3}$$

where q_t is the load or uptake of sulfur per unit mass of adsorbent in a time period of t, r_q is the sulfur adsorption rate in mg.g^{-1}min^{-1}, k_f is the pseudo-first order model rate constant (min^{-1}), and q_e is the equilibrium sorption uptake (mg.g^{-1}). From kinetic batch test of sulfur loading versus adsorption time, the experimental equilibrium sorption uptake q_e was determined at the adsorption time that is long enough to reach the equilibrium state. And the calculated value of q_e can be used to compare with the experimental value to validate the kinetic model. In this test a sufficient mass of 4 g adsorbent was put into 5 g Jet-A fuel to study the sulfur adsorption kinetics. The experimental equilibrium sorption uptake q_e was 1.321 mg/g at the adsorption time of 22 h. The integrated form of Eq. (3) is given as

$$\ln(q_e - q_t) = \ln q_e - k_f t \tag{4}$$

The pseudo-first order model inherently assumes the sulfur concentration in the ambient (which refers to the 5 g Jet-A fuel in this test) doesn't change with time, and $1/k_f$ is a time constant in the above equation. However, in this test the sulfur concentration Cs in the Jet-A fuel sample reduced significantly as the adsorption time increased, because the mass of the Jet-A fuel was limited and sufficient mass of adsorbent was added into the fuel. At time t, the mass balance of sulfur is expressed as,

$$m_f \left(C_0 - C_s \right) = m_{s,0} - m_f C_s = q_t \cdot m_{ads} \tag{5}$$

where C_0 is the initial sulfur concentration (ppmw), Cs is the residual sulfur concentration (ppmw), m_{fuel} (g) is the mass of fuel sample, m_{ads} (g) is the mass of the adsorbent, and $m_{s,0}$ (g) is the total mass of the sulfur. At equilibrium state, there was still sulfur left in the fuel because of the balance of adsorption and desorption.

$$m_{s,0} = m_f C_e + q_e m_{ads} \tag{6}$$

where C_e is the sulfur concentration in the Jet-A fuel at equilibrium state. By substituting Eq. (6) to Eq. (5), the following equation is obtained as:

$$q_e - q_t = \frac{m_f}{m_{ads}}(C_s - C_e) \tag{7}$$

The pseudo-second order model is obtained by combining Eq. (3) and Eq. (7):

$$r_q = k_s (q_e - q_t)^2 = dq_t / dt \tag{8}$$

where k_s is the pseudo-second order model rate constant (g.mg^{-1}min^{-1}),

$$k_s = k_f \frac{m_{ads}}{m_f} \frac{1}{C_s - C_e} \tag{9}$$

The integrated form of Eq. (8) is:

$$\frac{t}{q_t} = \frac{1}{k_s q_e^2} + \frac{t}{q_e} \tag{10}$$

The intraparticle diffusion model is presented in the form of

$$q_t = k_i t^{1/2} + C \tag{11}$$

where k_i is the intraparticle diffusion model rate constant (mg.g^{-1}min$^{-0.5}$) and C is a constant (mg.g^{-1}).

From the experimentally measured data of q_t versus time t, linear regression of Eqs. (4), (10) and (11) can be conducted, and thus the q_e, k_f, k_s and C in the equations have been found as given in Table 2.

Table 2 Kinetic analysis results of three different models	
Pseudo-first order model	*Correlation coefficient* R^2
$q_{e,cal}$ =0.1078 (mg/g)　　k_f =0.00232 (min^{-1})	0.9584
Pseudo-second order model	
$q_{e,cal}$ =1.321 (mg/g)　　k_s =0.7569 (g.mg^{-1}min^{-1})	0.9999
Introparticle diffusion model	
C = 1.1467 (mg/g)　　k_i =0.0058 (mg.g^{-1}min$^{-0.5}$)	0.5851

The kinetic analysis results following the above-mentioned three different models are shown in Fig. 8 to Fig. 10. It was found that the pseudo-second order model can best fit the current experimental data. Table 2 lists the data-fitted q_e and the correlation coefficient R^2 for all three models. Because of the excellent fit of the experimental data to the equation from the pseudo-second order model, the thus obtained equilibrium loading q_e agrees with the experimental data in Fig. 7 very well. This leads to the conclusion that the kinetics of the desulfurization of Jet-A fuel using the currently developed adsorbent can be well described by the pseudo-second order model.

The intraparticle diffusion model has a poor fitting with the experimental data, which indicates that the diffusion process may have more than one rate-controlled stage, which needs two piecewise data regressions. This is clearly illustrated by plotting the adsorbent loading versus t$^{1/2}$ as shown in Fig. 8. Kumar et al. [9] also proposed that the adsorption rate is controlled by both chemical adsorption and intraparticle transport at the beginning, and then followed by
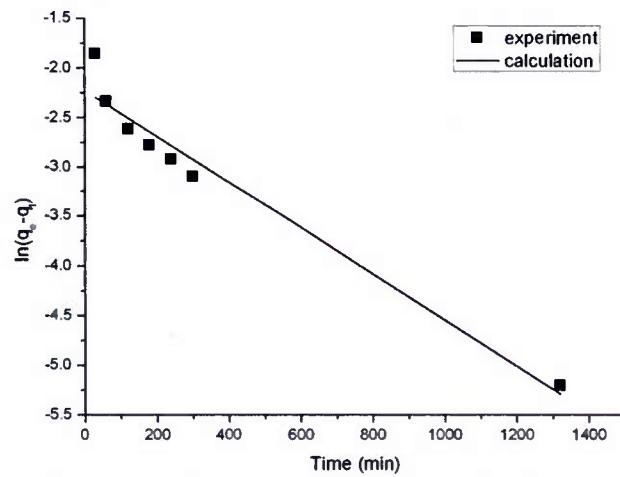
meso-pore diffusion and micro-pore diffusion.

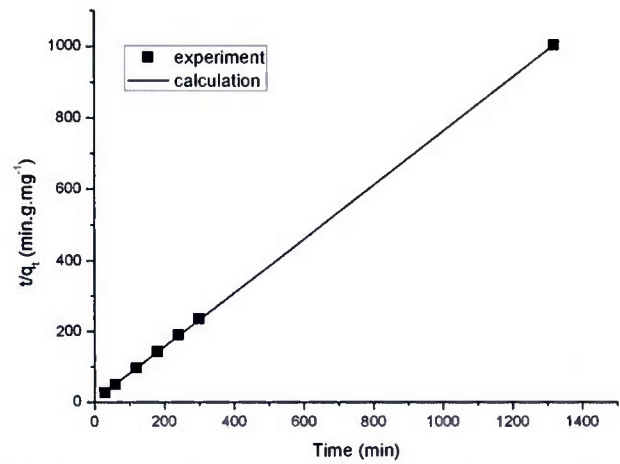*Figure 8 Kinetic modeling analysis of pseudo-first order model*

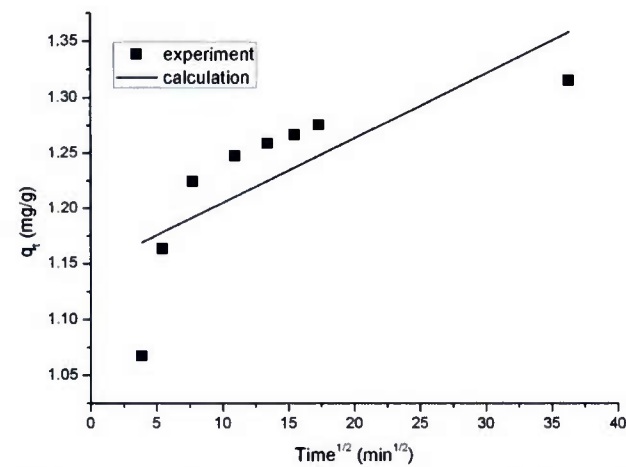*Figure 9 Kinetic modeling analysis of pseudo-second order model*

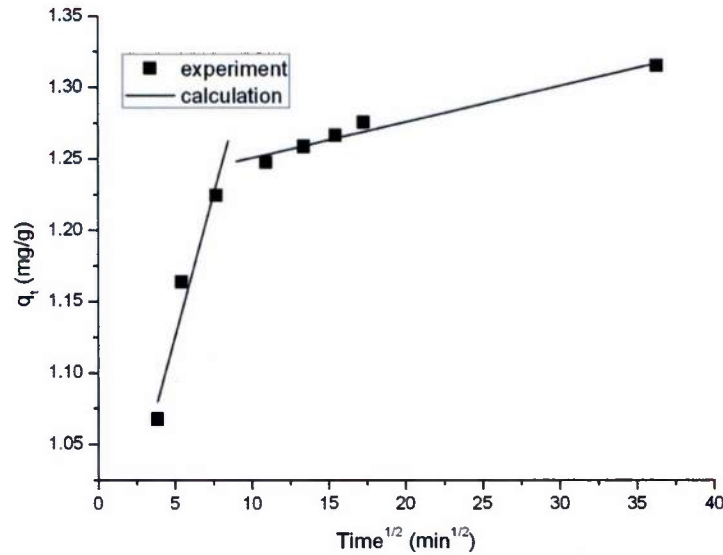*Figure 10 Kinetic modeling analysis of intraparticle diffusion model*

Figure 11 Plot of loading versus $t^{1/2}$

3.3.5 Equilibrium isotherm

The equilibrium adsorption loads of sulfur on the adsorbent from the present experimental data are shown in Fig. 12 in respect of the loading, q, against the residual sulfur concentration, Cs. The curves are also called isotherm. Two-parameter Freundlich and Langmuir isotherm equations and three-parameter Redlich-Peterson and Brunauer-Emmett-Teller (BET) isotherm equations were used to analyze the adsorption data. The linear forms of the four equations are given as

Freundlich:
$$\ln q = \ln K_F + \frac{1}{n} \ln C_s \tag{12}$$

Langmuir:
$$\frac{1}{q} = \frac{1}{q_m} + \frac{1}{K_L q_m} \frac{1}{C_s} \tag{13}$$

Redlich-Peterson:
$$\ln\left(K_R \frac{C_s}{q} - 1 \right) = \beta \ln C_s + \ln a_R \tag{14}$$

BET:
$$\frac{C_s}{q(C_m - C_s)} = \frac{K_B - 1}{q_m K_B} \frac{C_s}{C_m} + \frac{1}{q_m K_B} \tag{15}$$

The regression of the experimental data in Fig. 12 following Eq. (12) allowed us to find K_F and $1/n$., and similarly we can find K_L and q_m for Eq. (13). The data regression for Eq. (14) requires us to guess a K_R and find β and a_R for the best fit of the data. Through trail-and-error analysis, the current analysis found the best fit at a correlation coefficient $R^2 = 0.9789$. The data regression for Eq. (15) requires us to guess a value for C_m and then find q_m and K_B for the best fit to the data. Through trail-and-error analysis, the current analysis found the best fit at a correlation coefficient $R^2 = 0.9986$.

In order to better estimate the deviation of the calculated values from data-fitted equations and experimental data, the sum of the square of errors (SSE) is calculated,

$$SSE = \sum_i \left(q_{i,cal} - q_{i,exp} \right)^2 \tag{16}$$

The Marquardt's percent standard deviation (MPSD) error function is also calculated from the equation

$$MPSD = 100 \sqrt{\frac{1}{n_m - n_p} \sum_i \left(\frac{q_{i,cal} - q_{i,exp}}{q_{i,exp}} \right)^2} \tag{17}$$

where the subscript 'exp' and 'cal' represent the experimental data and calculated value from the data-fitted equation, respectively, n_m is the total number of measurement points and n_p is the number of to-be-determined parameters in the model equations.

The curves from the data-fitted equations for the Freundlich, Langmuir, Redlich-Peterson, and BET models are also shown in Fig. 12. The obtained parameters from data regression, the correlation coefficient R^2, SSE, and MPSD values of each model are given in Table 3. It is seen that all four models can more or less fit the experimental data in the investigated range of residual concentration. A very good fit is seen for the BET model, which has the highest correlation coefficient R^2, and the lowest SSE and MPSD, which indicates that the BET model is the most suitable one. The BET model was believed most suitable for the case of multi-layer adsorption and thus high desulfurization efficiency. The good fit of the BET model to the current data indicates that the adsorbent developed offers multi-layer adsorption. The satisfactory fitting of the equations with the experimental data also indicates that the organosulfur compounds in Jet-A fuel can be well represented by the total sulfur amount in the fuel.
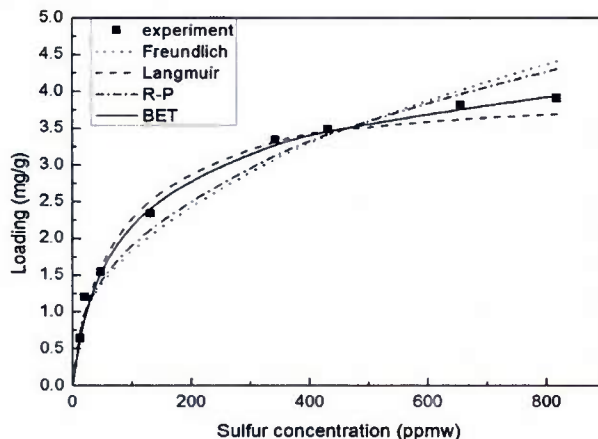

Figure 12   Adsorption equilibrium isotherm at room temperature

Table 3 Isotherm parameters for sulfur adsorption

Freundlich Equation				
K_F [(mg/g)/(mg/kg)$^{1/n}$] 0.2998	1/n 0.4007	R^2 0.9513	SSE 0.5001	MPSD 16.747

Langmuir Equation				
K_L (kg/mg) 0.0158	q_m (mg/g) 3.9736	R^2 0.9609	SSE 0.2897	MPSD 11.682

Redlich-Peterson Equation

K_R (kg/g)	a_R (kg/mg)	β	R^2	SSE	MPSD
0.219	0.4684	0.6657	0.9789	0.3074	14.985
		BET Equation			
C_m (mg/kg)	q_m (mg/g)	K_B	R^2	SSE	MPSD
6250	3.6426	103.4261	0.9986	0.1435	11.5193

3.4 Desulfurization results from fixed bed reactor

Fixed bed tests were conducted for dynamic sulfur adsorption measurements and investigated effects of fuel flow rate, adsorbent particle size, fixed bed dimensions, etc. [48]. A vertically-oriented stainless steel column fully packed with adsorbents was used as the fixed bed reactor. The experimental system consisted of a HPLC pump (high performance liquid chromatography pump), a fuel tank, and the fixed bed column. Nitrogen was used to flush out the residual fuel after each test. Figure 13 shows schematically the test rig of the fixed bed adsorption system. After the tubing was rinsed with distilled water and dried, pre-weighted adsorbent was packed into the fixed bed column. The HPLC pump (SSI B2300) was used to feed the Jet-A fuel to the adsorption bed at the desired flow rate. The effluent fuel from the adsorption bed was sampled every 15 min. and the sulfur concentration, $C(t)$, of every sample at a time was measured by the Thermo TS 3000 total sulfur analyzer. The treated accumulated fuel after desulfurization was collected in a beaker. The sulfur adsorption capacity of the adsorbent was calculated as follows:

$$\text{Sulfur adsorption capacity} \quad q_c = \frac{\rho_f V_f}{1000 \cdot m_{ads}} \int_0^t \left(C_0 - C(t) \right) dt \tag{18}$$

where q_c has a unit of mg-S/g-adsorbent, ρ_f(g/ml) is the density of fuel, V_f (ml/min) is the fuel flow rate, m_{ads} (g) is the mass of packed adsorbent, and C_0 (ppmw) is the initial sulfur concentration in the Jet-A fuel.
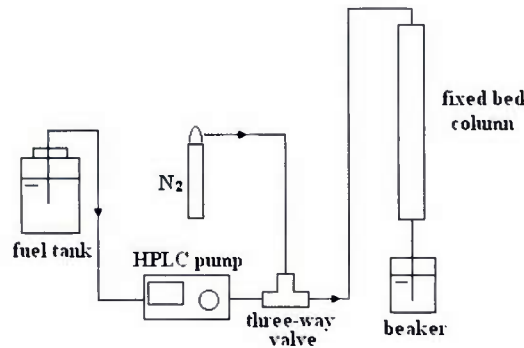

Figure 13 Schematic of the fixed-bed sulfur adsorption system

All the results were obtained with repeatability validation. We repeated and prepared the absorbent in two times. Also, each test was run twice in the data collection stage in order to confirm the repeatability of experiments.

3.4.1 Effect of LHSV (liquid hourly space velocity)

The desulfurization performance of adsorbent strongly depends on the LHSV (liquid hourly space velocity), which can be changed by using different flow rate of fuel. In order to demonstrate this effect for the current adsorbent, adsorptive desulfurization experiments were

carried out under flow rates of 0.1, 0.2, 0.3, and 0.4 ml/min (in corresponding LHSVs of 0.168, 0.336, 0.504, and 0.672 h^{-1}, respectively) while keeping other parameters unchanged. Adsorbents with particle size between 0.5 and 3 mm were used in each test. The adsorption capacities versus the mean sulfur concentration of the treated (accumulated) fuel at different flow rates are shown in Fig. 14. It is seen that as the flow rate decreases from 0.4 to 0.1 ml/min, the adsorbent capacity increases significantly. When the accumulated treated fuel sulfur concentration reached 30 ppmw, the capacity of sulfur adsorption at the flow rate of 0.1 ml/min is about two times of that of the 0.4 ml/min flow rate. This is because that at the high flow rate, the per unit volume of fuel contacts the adsorbent bed in a shorter time, therefore the sulfur compounds do not have sufficienct time to diffuse into the pores of the adsorbent. After all, although setting a low flow rate increases the desulfurization performance of the adsorbent, the fuel desulfurization rate can be too small, particularly when the flow rate is less than 0.1ml /min. Therefore, in the tests hereafter, the fuel flow rate was selected to be no less than 0.1 ml/min.
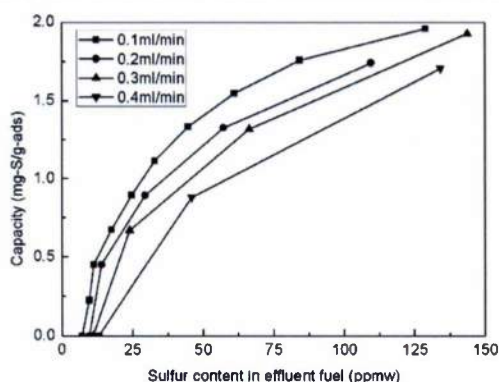
Figure 14 Effect of flow rate on sulfur removal performance

3.4.2 Effect of adsorbent particle size

To study the effect of particle size on the sulfur adsorption capacity, three experiments were carried out under the same conditions except for the particle size. The test results are shown in Figure 15. Since the total mass of the adsorbent is the same, the packed bed has different porosities due to the difference of the particle sizes. Figure 15 shows that with smaller particle size a higher sulfur adsorption capacity was obtained. Because of this, the lifetime of adsorbent is also significantly increased. This is understandable because with a smaller particle size for the adsorbent the sulfur mass diffusion can reach the center of the particles easier and thus increase the utilization of the adsorbent material.
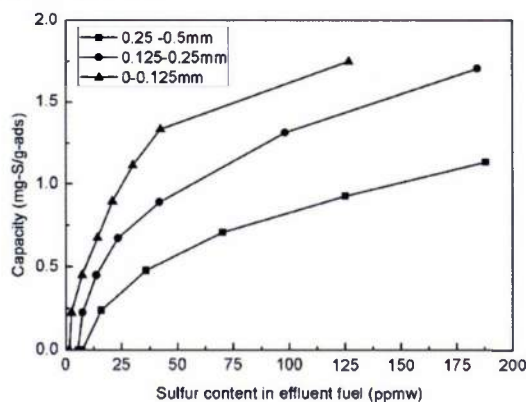
Figure 15   Effect of adsorbent particle size on sulfur removal performance

3.4.3 Effect of fixed bed dimensions

While keeping the same volume of adsorbent, the tube diameter and the length of the packed bed can be varied. To investigate the effect of the packed bed dimensions on the desulfurization capacity of the adsorbent, three different diameters and lengths of the packed bed were chosen and filled with adsorbent of particle sizes 0-125 µm. The fuel feeding flow rate and the mass of packed adsorbent were identical in these tests. Figure 16 shows the results of sulfur adsorption capacity versus the total sulfur concentration of the accumulated fuel after desulfurization.

The test results show an optimal diameter for the fixed volume of the reactor. Of the tested three diameters, the packed bed with a diameter of 7.75 mm gave the highest adsorption capacity of 1.55 mg S/g adsorbent at 50 ppmw S in effluent fuel. When the volume of the adsorbent bed and the fuel flow rate were both unchanged in the tests, the difference of the packed bed diameter only causes different velocities of the fuel when it flows through the packed bed. On the other hand, the time of the fuel passing through the packed bed is the same for all the cases. Therefore, the different adsorption capacity in the three cases is only due to the difference of flow velocities. A very low velocity does not contribute to a relatively good mass diffusion/adsorption and, therefore, we see that the highest sulfur adsorption capacity is from the case of a packed bed diameter of 7.75 mm.
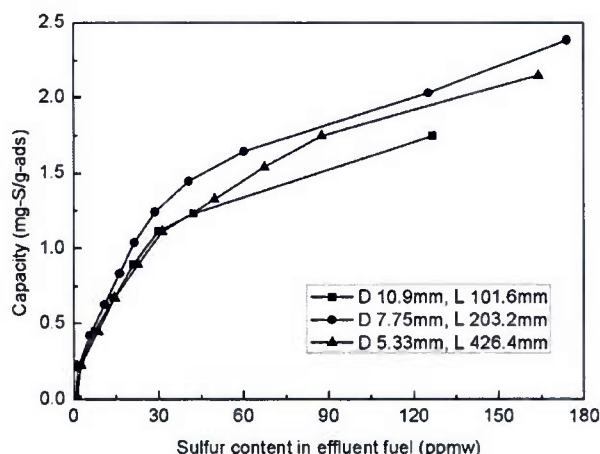

Figure 16 Effect of fixed bed dimensions on sulfur removal performance

A complete adsorption curve, effluent sulfur concentration versus adsorption capacity is shown in Fig. 17, which was obtained at conditions of L=203.2 mm, D=7.747 mm, fuel flow rate=0.1 ml/min, LHSV=0.63, adsorbent particle size=0~0.125 mm, fuel initial sulfur concentration=1,037 ppmw, mass of adsorbent=4.88 g. At a breakthrough sulfur concentration of 10 ppmw a very high sulfur adsorption capacity of 0.633 mg S/g adsorbent was achieved, which is significantly higher than the value of 0.12 mg S/g adsorbent reported in literature [53]. The sulfur adsorption capacity reached 1.98 mg S/g adsorbent at the point of 30 ppmw of mean sulfur concentration in the treated accumulated fuel.
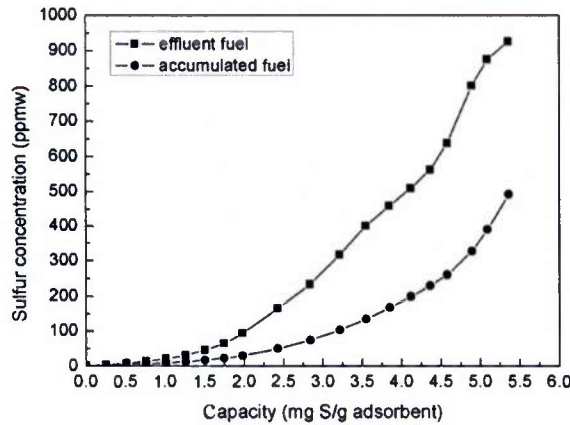
Figure 17   A complete adsorption curve
(L=203.2 mm; D=7.747 mm; fuel flow rate=0.1 ml/min; LHSV=0.63; adsorbent particle size=0~0.125 mm; fuel initial sulfur concentration=1037 ppmw; adsorbent mass=4.88 g)

3.4.3 Effect of the amount of nitric acid used for absorbent

In the adsorbent preparation process, a small amount of nitric acid was added in order to help the alumina sol formation when preparing the adsorbent support. However, it was observed that the amount of nitric acid had some effect in the adsorbent desulfurization performance. In this study, the total 128.25 gram of prepared mixture of pseudo-boehmite, diatomite, cerium acetate hydrate, nickel acetate hydrate, and distilled water, was added with different amount of nitric acid from 0 to 5 g, and the desulfurization performance of the processed adsorbent was tested. Sulfur adsorption capacities of the five adsorbents with 0 g, 1.5 g, 3 g, 4 g and 5 g nitric acid versus total sulfur concentration in effluent fuel are shown in Fig. 18. Breakthrough points for all five adsorbents occurred at around 50 ppmw S in effluent fuel, and it indicated that the less the nitric acid was added in the adsorbent preparation stage, the better desulfurization performance the adsorbent had. At 50 ppmw S breakthrough point, the sulfur adsorption capacity for adsorbent with no use of nitric acid was 2.95 mg-S/g-ads, while the obtained adsorption capacity was 2.5 mg-S/g-ads for adsorbent with 1.5 g nitric acid, 2.2 mg-S/g-ads for adsorbent with 3 g nitric acid, 2.16 mg-S/g-ads for adsorbent with 4 g nitric acid and 2.1 mg-S/g-ads for adsorbent with 5 g nitric acid. Although the difference of capacities for the five adsorbents was not significant at 50 ppmw S in the effluent fuel, the gap became larger as the sulfur concentration in the effluent fuel increases.
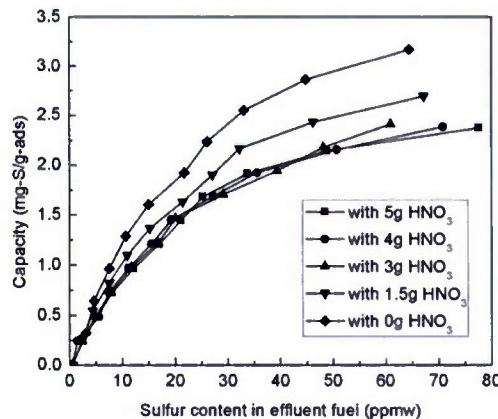

Figure 18   Effect of acid on sulfur removal performance

Whereas the mechanism of desulfurization by using the selected metal and support materials from the chemistry point of view has been discussed, some physical details of the adsorbent should be interesting to examine. The BET surface areas were 256, 253, 252, 249 and 249 m^2/g for adsorbents containing 0, 1.5, 3, 4 and 5 g nitric acid, respectively. The pore size distributions of the five adsorbents are shown in Fig. 19. The surface areas slightly decrease with the increased addition of nitric acid. Also, the addition of nitric acid in adsorbent preparation reduces the pore size of the adsorbent. The BJH average pore diameter (4V/A) were 92, 74, 72, 70 and 65 Å for adsorbents with 0 g, 1.5 g, 3 g, 4 g and 5 g nitric acid, respectively. The result of reduction of both surface area and pore size is correlated to the reduction of desulfurization performance of the adsorbent. It is understood that the increase of surface area of the adsorbent has positive effect to the amount of adsorption of sulfur compound, whereas the large pore size in the adsorbent is favorable for the mass transfer resistance in the adsorbent, which can be even more important. Sulfur compound with large molecules may not able to pass through the small pores and thus the adsorption efficiency can be low. The reduction of BET surface area and BJH average pore diameter caused by addition of acid might be due to the fact that nitric acid could dissolve pseudo-boehmite to prepare alumina sol. More pseudo-boehmite was dissolved as more nitric acid was added in the adsorbent preparation. Because the structure of alumnia sol is different to that of pseudo-boehmite, the addition of nitric acid caused structure change of the prepared adsorbents and so as the desulfurization performance of the adsorbents in fixed bed tests.
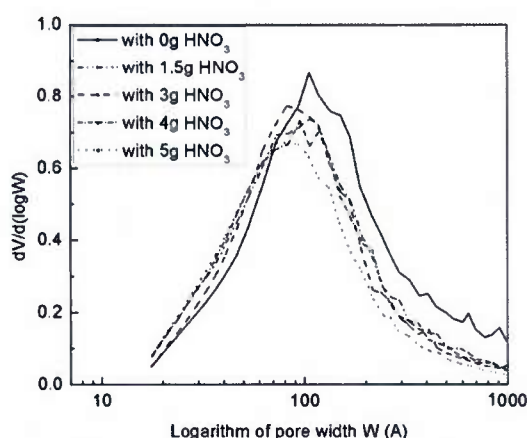

Figure 19   Pore size distribution of adsorbents with various acid amounts
(Unit of pore size W: Å)

3.4.4 Effect of compositions of materials in adsorbent

The loading ratio of the two metal oxides and the ratio of alumina to silica affect the dispersion of active sites and interactions of metals with support materials. As the result, the ratios of Ni/Ce and Al/Si could significantly influence the desulfurization performance. Obviously, the desulfurization mechanism includes both chemical and physical aspects. The following measured physical properties of the adsorbent will help for better understanding of the desulfurization performance of different adsorbent samples from mass transfer and surface adsorption point of view.

Table 4   Molar ratios in metal oxide materials and properties of adsorbent

Adsorbent	Ni/Ce in mole	Al/Si in	Al-Si-Ox/Ni-Ce-Oy	Total wt.% of	Surface area	Average pore size

		mole	in mass	metal oxide	(m^2/g)	(Å)
Support	n/a	15	9	0	288	105
Ads-1	10	15	10	6.6	277	93
Ads-2	10	15	9	7.4	256	92
Ads-3	8	15	9	7.3	242	96
Ads-4	12	15	9	8.2	235	91
Ads-5	10	15	8	8.0	266	86
Ads-6	10	12	9	7.4	245	94

In order to observe the optimized adsorbent performance in fixed bed reactor test, six adsorbents labeled as Ads-1 to Ads-6 were studied under the same fixed bed operation condition. And the performance of pure support material was also tested as a baseline sample. For Ads-1 to Ads-5, the support materials were the same, meaning the ratio of pseudo-boehmite versus diatomite are the same; whereas the loading of NiO varies from 5 wt.% to 7 wt.%, and the loading of CeO_2 varies from 1.2 wt.% to 1.6 wt.%. The total metal oxide loading is given in Table 4. The samples Ads-6 and Ads-2 had the same metal oxide loadings for both the ratios of NiO/CeO2 and metal materials versus support materials. But, in the support material of Ads-6 the ratio of pseudo-boehmite versus diatomite was different from that of sample of Ads-2. Table 4 also gives the mole ratios of Ni versus Ce, the total weight percentage of metal oxide in the adsorbent, as well as the measured surface area and pore size.

The BET measurement showed that the surface area of Ads-1 to Ads-4 decreases from 277 m^2/g to 235 m^2/g as the metal oxide loading increases. If only consider support materials with no metal oxide loading, the surface area was measured to be 288 m^2/g. This means that the loading of metal oxide actually slightly reduces the surface area of the adsorbent. The pore size distribution curves of Ads-1 to Ads-6 didn't vary significantly as shown in Fig. 20. The BJH average pore diameter for only support material and Ads-1 to Ads-6 were 105, 93, 92, 96, 91, 86 and 94 Å, respectively. The diffusion limitation of large sulfur compound molecule was the key factor in the sulfur adsorption, and adsorbent with large pores can have minimized diffusion limitation and thus increase sulfur adsorption performance. The pore size increase is more effective on adsorbent sulfur adsorption capacity than the BET surface area increase. For the currently developed $NiO-CeO_2/Al_2O_3-SiO_2$ adsorbent, the measured pores were mainly mesopores (pore width between 2-50 nm), and the BJH average pore diameter 4V/A (~90 Å) of the new adsorbents are much larger than the BJH average pore size of adsorbents made of Y-zeolite (~20 Å) [14], MCM-41 (~30 Å), and SBA-15 (~60 Å).
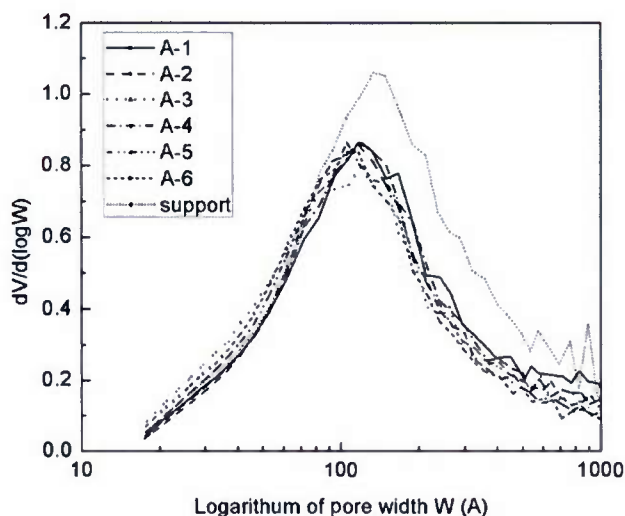
Figure 20 Pore size distribution of Ads-1 to Ads-6 and pure support
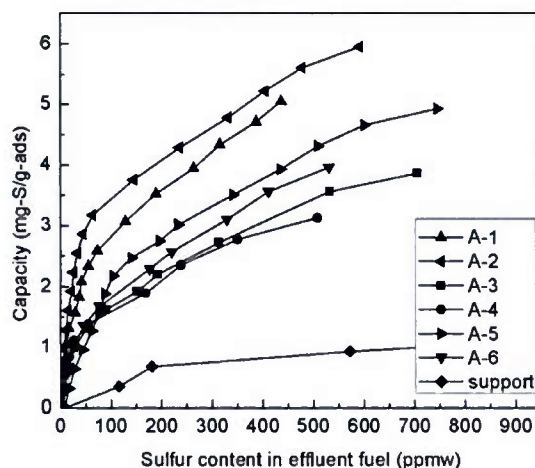*(Unit of pore size W: Å)*

Figure 21 Capacity versus sulfur content in effluent fuel for various adsorbents
(C_0: 1140 ppmw; LHSV: 0.63 h^{-1}; particle size: 0-125 μm)

The pore size, surface area, and the total weight percentage of metal oxide in the adsorbent work together to influence the desulfurization performance. The adsorption capacities of Ads-1 to Ads-6 against the sulfur content in effluent fuel are shown in Figure 21. While larger surface area is favorable; the total weight concentration of metal oxide and the pore size also play significant roles. Overall, <u>Ads-2 had the best desulfurization performance than other adsorbents.</u> Its sulfur adsorption capacities were 1.22 and 2.95 mg-S/g-ads at 10 and 50 ppmw S in effluent fuel, respectively. The treated fuel volumes were 1.36 and 3.3 ml/g-ads at 10 and 50 ppmw S in effluent fuel, respectively. The sample Ads-2 has a good level of surface area, total metal oxide, as well as large pore size. The sample Ads-1 has lower total weight percentage of metal oxide, although its surface area is slightly higher than that of Ads-2. The sample Ads-3 has both lower total weight percentage of metal oxide and surface area than that of Ads-2. The sample Ads-4 has the lowest surface area even if its metal oxide weight percentage is high. The sample Ads-5 has the smallest pore size even if there is a sufficiently high surface area. Sample 6 has similar weight percentage of metal oxide and a slightly lower surface area, and its support material has

different components ratio; therefore, its desulfurization performance is also lower than that of sample Ads-2. Obviously the significant low surface area contributes to the low desulfurization capacity of sample Ads-4. As a conclusion, with metal oxide weight percentage, surface area, and pore size being all high, the desulfurization performance could reach the best, as see for sample Ads-2. The XRD of Ads-2 is shown in Figure 22. The XRD graph was amorphous with broad peaks.
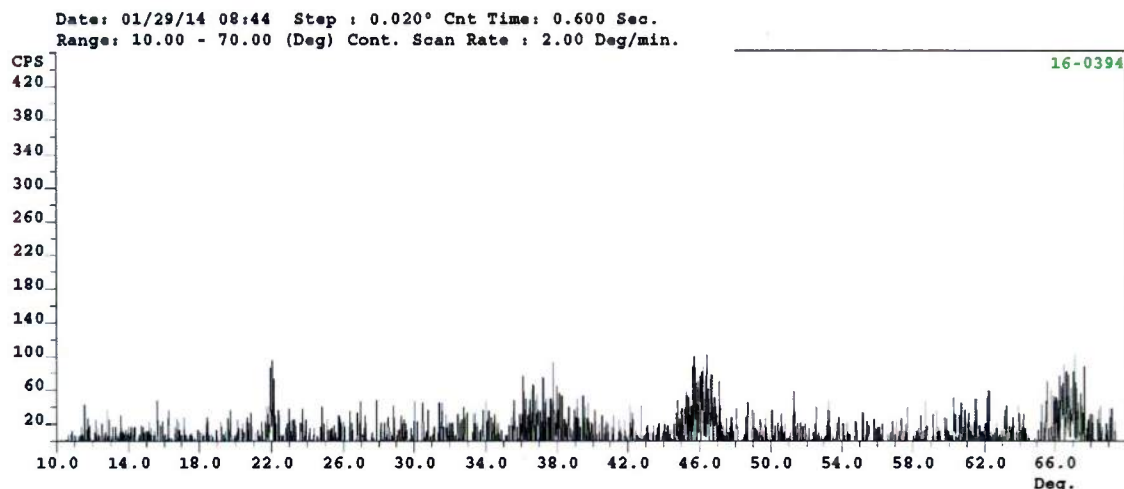

Date: 01/29/14 08:44   Step : 0.020° Cnt Time: 0.600 Sec.
Range: 10.00 - 70.00 (Deg) Cont. Scan Rate : 2.00 Deg/min.

Figure 22 XRD results of NiO-CeO$_2$/Al$_2$O$_3$-SiO$_2$ adsorbent

3.4.5 Adsorbent regeneration and capacity recovery

Regeneration of used adsorbents is an important practical issue, since the sulfur adsorption capacity is not very high due to the fact that the sulfur concentration in jet fuel is high and also the required sulfur concentration in treated fuel is very low. For regeneration study to the currently optimized adsorbent, sulfur saturated adsorbent (used previously) was heated at 250 °C for 30 min in flowing helium for removing/evaporating fuel held in pores, and then heated at a raised temperature for 2 h in helium to regenerate. The four different raised regeneration temperatures were 300, 400, 500 and 600 °C. The desulfurization performances of regenerated adsorbents due to different regeneration temperatures are shown in Fig. 23. Adsorbent regenerated at 500 and 600 °C had better desulfurization performance than those regenerated at 300 and 400 °C, and at low sulfur concentration level in effluent fuel the adsorbent regenerated at 500 °C had the best performance with the high volume of fuel treatment per gram of adsorbent.
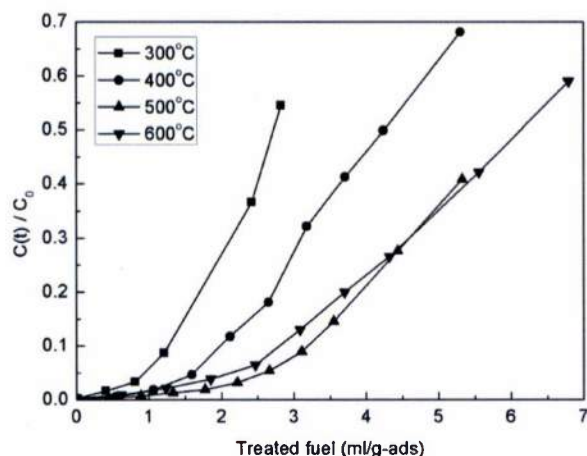
Figure 23 Adsorbent regeneration at different temperatures
(C_0: 1140 ppmw; LHSV: 0.63 h^{-1}; particle size: 0-125 μm)

After the first regeneration test, multiple cycles of regeneration tests were performed by the repeated treatment of the saturated adsorbent at 500 °C after each test in a cycle. The four-cycle breakthrough curves and the adsorption capacities corresponding to sulfur content in effluent fuel are shown in Fig. 24 and Fig. 25. The sulfur adsorption capacity of the regenerated adsorbent decreased with the increase of regeneration cycles. At a breakpoint of 50 ppmw S in effluent fuel, the sulfur adsorption capacity was 2.95 mg-S/g-ads for fresh adsorbent, and was 2.21, 1.95, 1.76 and 1.49 mg-S/g-ads for cycles 1 through 4. In cycle 1 through 4, about 75%, 66%, 59% and 51% sulfur adsorption capability was recovered in the regenerated adsorbent. The measured BET surface areas are 256, 253, 250, 222 and 219 m^2/g respectively for the fresh and regenerated adsorbents through cycles 1 to 4. The BJH average pore diameter was around 91±1 Å for all adsorbents. The pore size distributions are shown in Fig. 26. The reduction of adsorption capacity is strongly correlated to the decrease of the surface area, which reflects the decrease of the active sites in the adsorbent for sulfur adsorption [54].
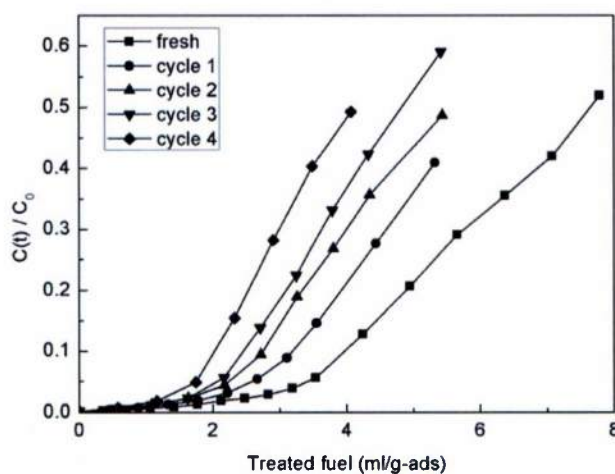

Figure 24 Four-cycle breakthrough curves
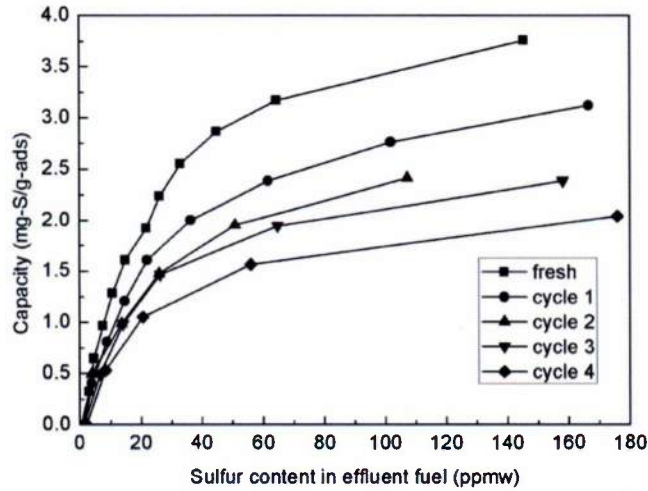*(C_0: 1140 ppmw; LHSV: 0.63 h^{-1}; particle size: 0-125 μm)*

Figure 25 Capacity versus sulfur content in effluent fuel for four-cycle tests
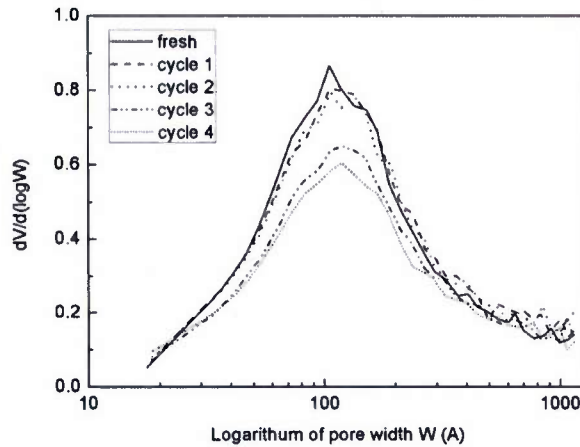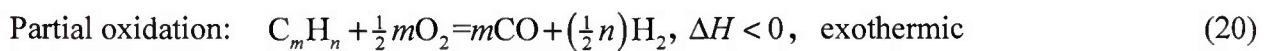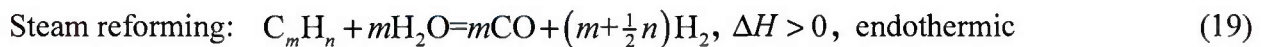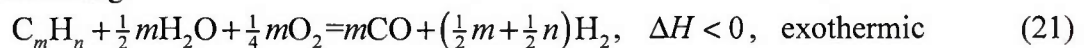*(C$_0$: 1140 ppmw; LHSV: 0.63 h^{-1}; particle size: 0-125 μm)*

Figure 26 Pore size distribution of regenerated adsorbent
(Unit of pore size W: Å)

4.0   Autothermal reforming of n-dodecane (surrogate of JP-8) and Jet-A fuels

The conversion of hydrocarbon fuel to hydrogen or syngas can be made based on three main mechanisms. These are steam reforming (SR), partial oxidation (POX), and autothermal reforming (ATR) [55]. These technologies are distinguished by whether steam or oxygen, or a mixture of steam and oxygen, is used. Production of syngas in the current industry is dominated by a steam reforming method [56,57]. The three fuel reforming reactions are expressed through Eqs. (19)-(20).

Steam reforming: $C_mH_n + mH_2O = mCO + \left(m + \tfrac{1}{2}n\right)H_2$, $\Delta H > 0$, endothermic   (19)

Partial oxidation: $C_mH_n + \tfrac{1}{2}mO_2 = mCO + \left(\tfrac{1}{2}n\right)H_2$, $\Delta H < 0$, exothermic   (20)

Autothermal reforming:
$$C_mH_n + \tfrac{1}{2}mH_2O + \tfrac{1}{4}mO_2 = mCO + \left(\tfrac{1}{2}m + \tfrac{1}{2}n\right)H_2, \quad \Delta H < 0, \text{ exothermic}$$ (21)

Steam reforming (SR) is a high endothermic reaction and requires a lot of heat from an external source. It is an approach with high hydrogen concentrations and higher system efficiencies, except the startup time is typically long [58]. The processing system tends to be heavy for steam reforming and is more suitable for continuous operation under a steady state, rather than for onboard fuel cell stacks with frequent load variations [59]. In a partial oxidation (POX) process, hydrocarbon fuels are converted to syngas by partially oxidizing with oxygen. This is a high exothermic reaction process, and generally the operating temperature ranges from 1100 $^{\circ}$C to 1200 $^{\circ}$C in order to prevent coking in the reactor. Compared with steam reforming, partial oxidation has the advantages of compactness, fast start-up, and rapid responses [58, 60, 61]. Depending on the presence or absence of a catalyst, POX has two types: homogeneous POX or heterogeneous catalytic POX. Homogeneous POX is the reactions of fuels with the oxygen in air at high temperature and high pressure in the absence of any catalyst for producing syngas [1]. The main advantage is its compatibility with various fuels from natural gas to gasified coal, which may have low hazard emissions such as NOx or SOx. However, the hydrogen production efficiency of homogeneous POX is relatively low due to the very high temperature required to partially oxidize fuels [62]. For instance, the noncatalytic process for gasoline reforming requires temperatures in excess of 1000 $^{\circ}$C [63]. The presence of a suitable catalyst can reduce the operating temperature to 800-900 $^{\circ}$C, which enables the application of common materials such as stainless steel to construct a reactor and also increases system efficiency [64]. Regularly, the catalyst can only be employed if the sulfur content in the fuel is below 50 ppm in order to avoid catalyst poisoning [65,66]. But some recent studies also show POX catalysts can tolerate sulfur of a content of up to a couple of hundreds ppm [67-69], Autothermal reforming (ATR) is a combination of exothermic partial oxidation sequentially followed by endothermic steam reforming. The heat released by POX can sustain SR and the overall ATR reaction is thermally neutral or slightly exothermic. The operating temperature is usually in the range of 900 $^{\circ}$C to 1150 $^{\circ}$C in reactors with a lower pressure compared to POX. So far, reformers with pressure between 1 and 80 bar have been designed and built [1]. The H_2 to CO molar ratio in ATR reformate is about 2, which is more favorable than the ratio in POX. An external heat source is not required for a steady-state ATR process. However, startup of the oxidation does not occur at ambient conditions and requires some energy. The startup phase of ATR is called light-off, which is correspond to about 10% total oxidation conversion of the fuel in a typical case and is characterized by the light-off temperature. The light-off temperature is affected by fuel type, O_2/C ratio, and types of catalyst. For all fuels, noble metal has higher activities than Ni and leads to relatively lower light-off temperatures [70]. The light off temperature of diesel was reported by Kang et al. [71] as 250 $^{\circ}$C and by Borup et al. [72] as 270 $^{\circ}$C. The light off temperature of Jet A-1 fuel was reported by Karatzas et al. [19] as 300 $^{\circ}$C. The advantages and disadvantages of these three reforming technologies are summarized and compared in Table.

Table 5 Comparison of reforming technologies

Technologies	Advantages	Disadvantages
Steam reforming	Most industrial experience	Highest air emissions
	Oxygen not required	Heavy system
	Lowest temperature	Heat source required
	Highest H_2/CO ratio	
	Slow startup	

Partial oxidation	Higher sulfur tolerance No heat source required Compact system Fast startup	Low H_2/CO ratio Highest temperature coke formation Oxygen or air required Too much heat produced
Autothermal reforming	Medium temperature No heat source required Favorable H_2/CO ratio Least coke formation Relatively compactness	Limited experience Oxygen or air required

Considering the requirements of size and weight of a fuel processing system, rapid startup and dynamic responses [73], and the converting ability of complex fuels such as diesel and jet fuels, the ATR approach has been chosen to be the best solution for onboard reforming applications [74,75]. Also, because high-temperature SOFC is selected to be the end-user unit, which can directly consume carbon monoxide the same as hydrogen, no post-processing reactors such as a water gas shift (WGS) reactor and preferential oxidation (Prox) reactor is required. This reduces the system complexity and the difficulty of maintenance. The purpose of both WGS and Prox is to selectively decrease carbon monoxide concentration in the syngas reformate to a very low level of 1% or below for a high temperature PEFC, and less than 50 ppm for a regular PEFC [76,77].

Ni-based catalysts for reforming have been widely used for many years because of their activity and low cost. The first catalyst with Ni as the active metal for reforming was reported by Prettre and his coworkers [78]. Then a lot of research works on Ni based catalyst for reforming were carried out. However, Ni catalysts have inherent challenges such as sulfur poisoning, carbon formation and sintering [20]. Thus noble metals were introduced in catalysts for reforming reactions [79,80] but the high price of noble metals is a challenge. Recently, the study of bimetallic metal catalysts by introducing noble metals into Ni-based catalysts has become a popular approach. It is believed that the bimetallic metal catalyst attains both benefits of nickel and noble metal [81], and improves catalyst performance in sintering resistance and even distribution of temperatures [82,83]. In noble metals, Pt has a high activity for oxidation but low activity for steam reforming. Pd has a better steam reforming activity than Pt but is sensitive to coke formation. Rh and Ru are very good catalyst candidates because of their good activity for both oxidation and steam reforming reactions. The price of Rh is relatively high for noble metals, and Ru is relatively cheaper.

Autothermal reforming of jet fuels has been investigated by several research teams. Lenz et al. [84] studied autothermal reforming of desulfurized Jet A-1 with a 15 kW_t test rig and the best energy conversion efficiency of 78.5% was obtained at air to fuel ratio of 0.28 and steam to carbon ratio of 1.5. Pasel et al. [85, 86] studied autothermal reforming of commercial Jet A-1 on a 5 kW_e scale. For a C_{13}-C_{15} alkane mixture surrogate fuel they reported an optimized energy conversion efficiency of 80% at oxygen to carbon molar ratio $O_2/C = 0.43$ and steam to carbon molar ratio $S/C = 1.9$. Karatzas et al. [19] tested autothermal reforming of commercial Jet A-1 and the optimized energy conversion efficiency was only 42%, which led to the conclusion that the high sulfur content in the fuel had a detrimental effect on the reformer performance.

There are several issues to be addressed for the design and operation of a reforming system for heavy hydrocarbon fuels [87]. First, local hot-spots may exist in the reforming catalyst due to the non-uniform temperature distribution, and local catalyst deactivation can be caused by the local high temperature. Second, the large carbon contents may cause coking, which can significantly decrease the effectiveness of the catalyst and thus reforming efficiency [88]. Hard coke such as graphitic is unreactive with hydrogen and can block active sites of the catalyst. Third, inhomogeneous mixing of reactants, air, fuel and steam, can cause both local hot-spots and coke formation in the catalyst surface. Fourth, as discussed in the previous section, sulfur components could deactivate the reforming catalyst and poison electrodes in fuel cells. The catalyst deactivation can be caused by the formation of strong metal-S bonds which modify the surface chemistry. The chemisorbed sulfur onto the active catalyst sites also prevents reactant access [89,90]. Generally, coke formation can be suppressed by controlling the fuel evaporation temperature [91] and optimizing the mixing ratio of fuel, water steam, and air. The catalyst poisoning problem due to sulfur can be solved by fuel desulfurization technology [92-94].

The autothermal reforming reactor consists of a thermal zone where partial oxidation happens, which generates heat to drive the steam reforming reactions in a downstream catalytic zone [95,96]. The thermal zone may take 20% of the top catalyst bed for catalytic POX. Therefore, the temperature distribution in the axial direction of the reformer is non-uniform. The temperature profile has a sharp rise to the peak in the POX zone and then a decrease due to the endothermic reactions to a relatively low and flat level in the SR zone [97,98]. The non-uniform axial temperature distribution could cause the problem of so called "hot-spots", which induce the potential risk of local catalyst deactivation due to thermal-induced mechanisms such as sintering. Sintering is defined as a thermal process that produces a decline in surface area of the active ingredient or the support of the catalyst, which results in a decline in the observed rate of reactions [99]. As Qi [21] reported in the ATR of gasoline, due to the temperature gradient greater than 150 °C in the axial direction, the catalyst rapidly deactivated and the gasoline conversion decreased from 100% to 95% after 40 hr operation.

The primary measure to minimize hot-spots is to employ proper reactor materials, catalyst support structures, and flow configurations, which favor effective heat transfer and more uniform axial temperature distribution. Stainless steel can be used to construct the reactor because of its relatively good thermal conductivity and high temperature tolerance. A traditional pellet catalyst with a packed-bed configuration has poor heat transfer performance [100] and it has been suggested that it be replaced by metallic monoliths, foams, wire-gauzes, or microchannel reactors [101,102]. Flow with high turbulence can improve hot-spots since the turbulent flow enhances the heat transfer coefficient between the flow and solid walls. Therefore, structured flow paths allowing high flow rates are preferred. The selection of appropriate channel diameters and geometries of the catalyst monolith is to achieve effective mixing, and high Sherwood and Nusselt numbers, which are equivalent to high mass and heat transfer coefficients. Other issues, such as pressure drops, also need to be considered to be within acceptable limits.

Coke is a high-molecular-weight polymer with low hydrogen content. Formation of coke on the catalyst surface is thought to occur in many instances by polymerization of aromatic compounds originally present or formed in reactions [99]. Olefin and aromatic contents in diesel and jet fuels are precursors of coke formation [98,103]. Coke formation could cause degradation of the reformer performance and reduces its life time significantly [104-106]. Souza et al. [107] reported that in the ATR of methane over Pt/ZrO_2 catalyst, the fuel conversion decreased from 80% to 65% after 30 h of operation in the existence of coke formation. Yoon et al. [108] reported

that in the ATR of synthetic diesel, due to coke formation the fuel conversion decreased from 100% to 90% and the reformer efficiency decreased from 65% to 45% after 40 h of operation. High temperature is required to minimize coke formation. Holladay [109] summarized the minimum reaction temperatures required for avoiding coke formation during isooctane reforming at thermodynamic equilibrium. For $O_2/C=0.5$ and $H_2O/C=1$, the minimum required temperature is 1030 °C and for $O_2/C=1$ and $H_2O/C=2$, the temperature is drastically reduced to 575 °C. The required temperature for ATR is higher than that for SR [97,109,110], but it was proved that ATR produces less coke compared with SR and POX [111,112]. Promoted catalysts have a positive effect in coking resistance, and generally, Rh-based catalysts give better performance than Ni-based catalysts in coking prevention.

Ethylene (C_2H_4) is reported to be the main reason for rapid carbon formation in the reforming process [98]. A large quantity of ethylene can be produced by pyrolysis of heavier hydrocarbons at the local fuel-rich zones if the mixing of fuel, air, and steam is not homogeneous. Ethylene can be decomposed into carbon in the absence of oxygen and water. In order to investigate the mechanism of carbon formation caused by ethylene pyrolysis, Yoon et al. [108] designed a diesel ATR processing system to study the correlation between carbon formation and O_2/C and H_2O/C ratios under the reforming conditions of SR, POX, and ATR. A blank reactor and a catalyst-loaded reactor were used to distinguish the carbon formation performance between homogeneous (in a blank reactor) and heterogeneous (in a catalyst-loaded reactor) reactions. Their testing results for two reactors under the ATR condition show that the homogeneous reaction produced much more ethylene than the heterogeneous reaction, and therefore they concluded that almost all the ethylene is produced in a homogeneous reaction at the reactor entrance for ATR reactors. The comparison of CO level in the reformate shows that both POX and SR have more carbon deposition than ATR. Figure 27 shows the detected carbon by TPO (temperature programmed oxidation method) analysis for three reforming approaches, and the two SR lines represent SR with different H_2O/C ratios. Apparently, insufficient steam resulted in reforming performance degradation, and carbon formation is prone to happen in the absence of oxygen. In the real fuel ATR process, most oxygen is consumed by fuel decomposition in the homogeneous reaction at the entrance. A lack of oxygen in the downstream section causes formation of ethylene. Because ethylene is practically exposed to SR in the catalyst zone, it causes carbon deposition. As a conclusion, the control of H_2O/C and O_2/C ratios of the feeding gases plays an essential role in suppression of carbon formation.
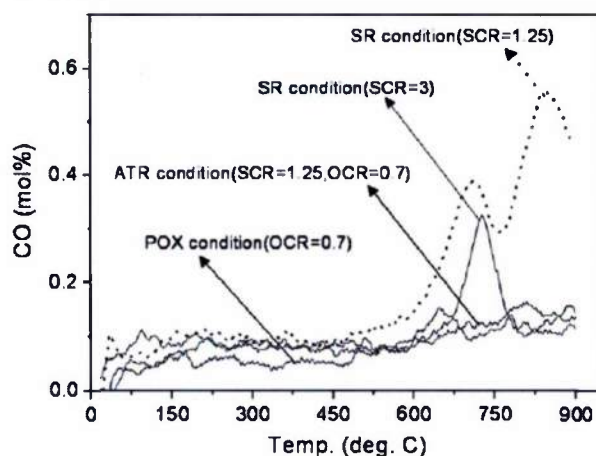

Figure 27 Carbon detected by TPO for C_2H_4 reforming
(TPO: air 500ml/min, 18-900 °C, 10 °C /min) [108]

Complete fuel evaporation and homogeneous mixing with air and steam are a big challenge in the ATR reactor design for long-chain hydrocarbon fuels. Many undesired problems can result in insufficient fuel evaporation or inhomogeneous mixing [113]. First, coke formation can be formed immediately if liquid fuel contacts the catalyst due to the presence of aromatics in diesel and jet fuels. Second, unexpected hot-spots can be caused by the local occurrence of insufficient steam or excess oxygen if the mixing of fuel, oxygen, and steam is not homogeneous [114]. Stable and sustainable hydrogen throughput also requires homogeneous and constant mixing. Lindstrom [115] compared the performances of three reactors with different mixing chamber designs. In the M2 reactor the diesel-slip (diesel not converted) in the reformate was 1,500 ppm, and the H_2 volumetric percentage in the production suddenly decreased from 35% to 25% after 200 min of operation. In the M4 reactor the diesel-slip was less than 15 ppm, and the H_2 was stable at 35% level after 450 min of operation. In the M5 reactor with an improved fuel injection system, the diesel-slip was controlled less than 10 ppm and the H_2 was stable at 40% level. Another issue related to complete fuel evaporation and homogeneous mixing is a safety concern. Since the boiling temperature for diesel and jet fuels is higher than the auto-ignition temperature, if the evaporation and mixing do not complete rapidly and uniformly, the formation of local oxygen-rich zones is possible. In these zones, the volume ratio of fuel and oxygen can be lower than the critical values and may end up in an explosion, which is quite dangerous in a well-sealed space.

4.1 Theory and thermodynamics analysis of autothermal reforming

The following thermodynamics analysis for a reforming process will make clear of the required proper oxygen to carbon ratio and the range of reaction temperature that an autothermal reaction can sustain without external heating and cooling. For a general hydrocarbon or oxygenate fuel, $C_mH_nO_z$, the autothermal reforming reaction stoichiometry can be expressed as

$$C_mH_nO_z + aO_2 + bH_2O = cCH_4 + dCO + eCO_2 + fH_2 \qquad (22)$$

where CO_2 comes from the water-gas-shift reaction and CH_4 from methanation reaction as follows:

$$CO + H_2O = CO_2 + H_2 \qquad (23)$$
$$CO + 3H_2 = CH_4 + H_2O \qquad (24)$$
$$CO_2 + 4H_2 = CH_4 + 2H_2O \qquad (25)$$

Based on atomic balance, the stoichiometric coefficients can be expressed as follows:

$$d = 2m - z - 2a - b - 2c \qquad (26)$$
$$e = -m + z + 2a + b + c \qquad (27)$$
$$f = \frac{n}{2} + b - 2c \qquad (28)$$

Since both hydrogen and carbon monoxide are fuels for SOFC, the total yield is

$$d + f = 2m + \frac{n}{2} - z - 2a - 4c \qquad (29)$$

which implies that the theoretical maximum yield can be achieved when no methane is produced. For each of the WGS and methanation reactions, at equilibrium state the system Gibbs energy is zero and the equilibrium equation is satisfied,

$$-\Delta G^0 = RT \ln K \qquad (30)$$

The relation of equilibrium constant K and temperature can be plotted as shown in Fig. 28. Commonly the working temperature of the ATR processor is in the range of 650 °C to 900 °C [116]. In this temperature range the equilibrium constant K for reactions by Eq. (24) and (25) are almost zero, which indicates that production of methane due to methanation reactions is ignorable. Nevertheless, both CO and CO_2 exist in the products of autothermal reforming.
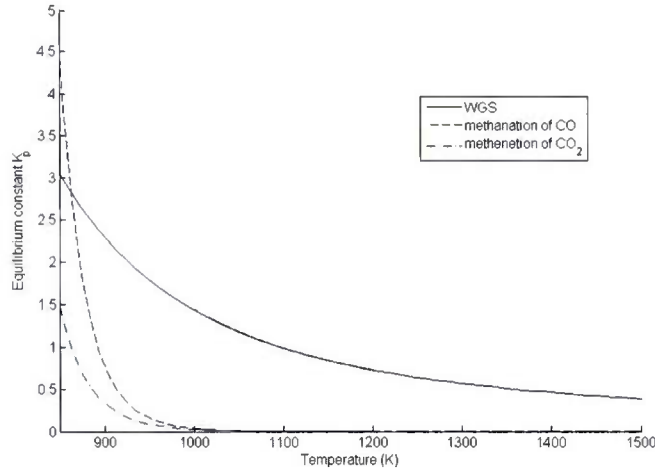

Figure 28   Relation of equilibrium constant K and temperature

Rase [99] proposed a simple method to estimate the equilibrium constant value for ideal gases in a reaction. Since the standard free energy can be expressed by standard enthalpy and entropy,

$$\Delta G^0 = \Delta H - T\Delta S^0 \tag{31}$$

Dividing both sides by T, the differential term can be obtained as

$$\frac{d\left(\Delta G^0 / T\right)}{dT} = \frac{1}{T}\left(\frac{d\Delta H}{dT}\right) - \frac{\Delta H}{T^2} - \frac{d\Delta S^0}{dT} \tag{32}$$

Since $dH_j = TdS_j + VdP$, differentiating the equation with dT and putting the result back into Eq. (32), the following equation is obtained:

$$\frac{d\left(\Delta G^0 / T\right)}{dT} = -\frac{\Delta H}{T^2} \tag{33}$$

Combining Eqs. (30) and (33) gives

$$\frac{d\ln K}{dT} = \frac{\Delta H}{RT^2} \tag{34}$$

The ΔH can be obtained through integrating the standard empirical heat capacity as shown in Eq. (35).

$$\frac{d\Delta H}{dT} = \sum_P^j v_j C_{P,j}(T) - \sum_R^j v_j C_{P,j}(T) \tag{35}$$

where P represents for products and R represents for reactants and v is the stoichiometric coefficient. $C_{P,j}(T)$ is the heat capacity of species j as a function of temperature. Çengel [117] and Chase [118] summarized the empirical expression of $C_{P,j}(T)$ as follows,

$$C_{P,j}(T) = A_j + B_j T + C_j T^2 + D_j T^3 \tag{36}$$

A through *D* are empirical coefficients for heat capacity. For the substances the empirical expression of which are not given, $C_{P,j}(T)$ can be calculated by Method of Joback [119] based on group contributions analysis. By integrating Eq. (36), the system enthalpy change is given as,

$$\Delta H = I_H + \sum_P^j v_j H_j - \sum_R^j v_j H_j \tag{37}$$

$$H_j = A_j T + \frac{B_j T^2}{2} + \frac{C_j T^3}{3} + \frac{D_j T^4}{4} \tag{38}$$

The right-hand-side term of Eq. (34) can be substituted, and after integration, Eq. (34) is expressed in a new form as given by Eq. (39):

$$\ln K = \frac{1}{R} \left(-\frac{I_H}{T} + I_K + \sum_P^j v_j K_j - \sum_R^j v_j K_j \right) \tag{39}$$

$$K_j = A_j \ln T + \frac{B_j T}{2} + \frac{C_j T^2}{6} + \frac{D_j T^3}{12} \tag{40}$$

where I_H and I_K are integration constants that can be evaluated based on the substance information at 298K. Using this equation, the equilibrium constant K can be estimated for different reaction temperatures if the reaction stoichiometries are determined. Take the following reforming reaction of dodecane, for example,

$$C_{12}H_{26} + xO_2 + (24-2x)H_2O = 12CO_2 + (37-2x)H_2 \tag{41}$$
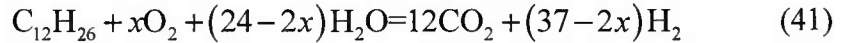
The effects of temperature on the system enthalpy change, system Gibbs free energy change and equilibrium constant K at various O_2 to carbon ratios at the operation temperature between 800 and 1500 K are shown in Fig. 29 to Fig. 31. Figure 29 indicates that the O_2/C ratio has to be greater than 0.3 to meet the exothermic reaction requirement. If O_2/C ratio is less than 0.3 the reaction becomes endothermic, which cannot self-sustain. Figure 30 shows that the reaction can go forward when the O_2/C ratio is above 0.20. Figure 31 shows the operation temperature doesn't influence the equilibrium constant much. In contrast, high oxygen to carbon ratio can increase the value of the equilibrium constant.
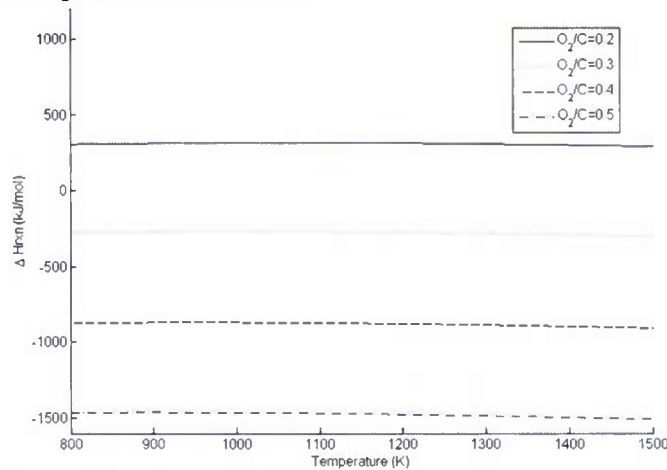

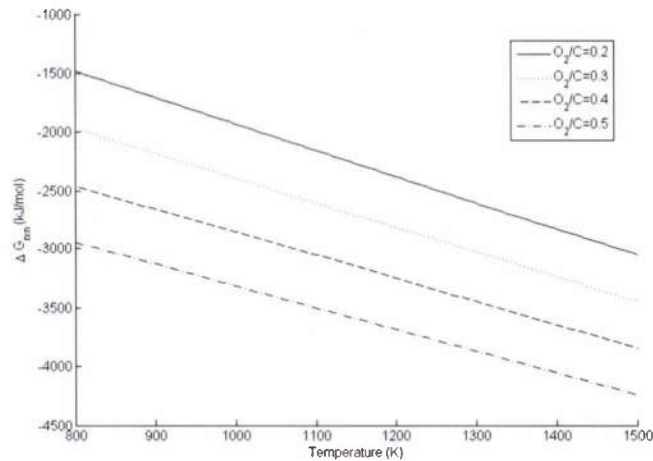*Figure 29   System enthalpy change versus temperature*

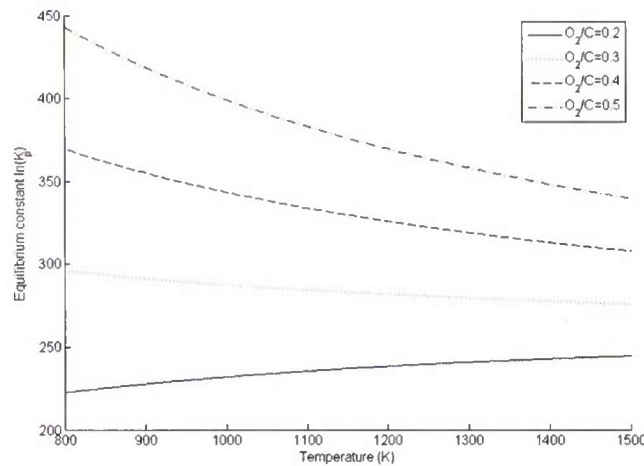*Figure 30 System Gibbs free energy change versus temperature*

Figure 31 Equilibrium constant lnK_p versus temperature

4.2 Monolithic reformer

Monolithic reactor is one popular type of reactor in reforming systems. Monoliths are continuous structures with well-defined geometries involving parallel and identical channels with small diameters. The shape of the cross-section of the channels can be square, sinusoidal, triangular, hex, round, and so on [120]. Fig. 32 illustrates three monoliths with different cell geometries [121]. Compared with a packed bed, a monolithic or honeycomb structure has the advantages of low pressure drop and high surface area/volume ratio. The large open front area (OFA) and straight parallel channels in monoliths ensure small flow resistance, even at high flow rates. The large surface area is usually achieved by depositing a high-surface-area carrier, a catalyst that can be impregnated into the channel walls. The deposited catalyst carrier is called washcoat, and its thickness is determined by the geometry of the channel and coating method. Too thick a washcoat could result in an increase of pressure drop to an unacceptable level. Besides, the increase in cell density could cause a significant increase in both surface area and pressure drop [120].
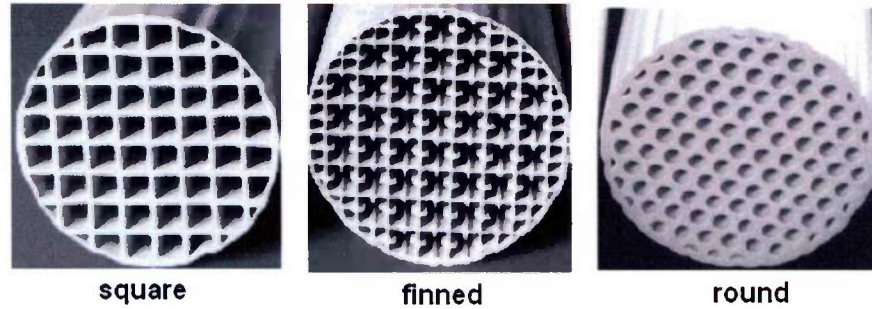
Figure 32 Monoliths with different cell geometries [121]

Synthetic cordierite is the most commonly used ceramic for monolithic catalyst support. Its characteristics of low thermal expansion coefficient in the magnitude of 10^{-6} K^{-1}, high mechanical strength of 3,000 pounds per square inch, and high melting point over 1,300 °C make it the preferred material to apply to an exothermic reaction. However, the thermal shock resistance of the monolith can be influenced by the washcoat, which usually has a larger thermal expansion coefficient. More attention needs to be paid to this thermal shock resistance difference in rapid temperature change situations such as startup and shutdown. Particle size of the carrier and thickness of the washcoat are two key parameters that can be optimized to decrease an undesired impact. One drawback of a cordierite monolith is it is less suitable for isothermal operations due to its low thermal conductivity. High temperature resistant aluminum-containing-steel is another popular material for monoliths. Its main advantage compared to cordierite is its potential to be manufactured with thinner walls, which leads to higher cell densities and lower pressure drop. The 15-20 times higher thermal conductivity than ceramic is another advantage that makes the isothermal operation possible, which favors fast startup. However, its application is limited to electrically heated catalytic converters as it is electrically conductive [120].

The most important characteristics to justify the performance of monoliths are cell density (n), geometric surface area (GSA), open frontal area, hydraulic diameter (D_h), bulk density, the thermal integrity factor (TIF), the mechanical integrity factor (MIF), resistance to flow (R_f), bulk heat transfer (H_s), and light-off (LOF) [120]. The asymptotic Sherwood (Sh) number and Nusselt (Nu) number are two dimensionless numbers that are used to characterize heat and mass transfer coefficients. Both numbers have constant values for fully developed laminar flow away from the entrance in channels with fixed diameter and shape. Also, the flow in monolithic channels is always laminar since the diameter is quite small and the Reynolds number is low. Pressure drop across the substrate depends linearly on flow velocity and length but inversely on the square of the hydraulic diameter. Sherwood number, Nusselt number, and pressure drop are defined as follows, respectively:

$$Sh = K \cdot D_h / d_{AB} \tag{42}$$

$$Nu = h \cdot D_h / k_f \tag{43}$$

$$\Delta p = \frac{C_f V_e L}{A D_h^2 (\text{OFA})} \tag{44}$$

where K is the mass transfer coefficient, d_{AB} is the mass diffusivity, h is the heat transfer coefficient, k_f is the thermal conductivity of fluid, C_f is the friction coefficient, A is the cross section area of the substrate, L is the length of the substrate, and V_e is volumetric flow rate.

For cordierite monoliths, thin and ultrathin wall structures with high cell density have been investigated to minimize thermal mass and maximize surface area [122, 123]. It has been found that the thin wall substrates have 40% lower heat capacity, 50% lower mass, and 60% higher GSA than standard substrates. However, higher pressure loss is also observed because of denser cells and increased flow resistance. The performances of square, triangular, and hexagonal (hex) cells have also been compared to study the effect of different cell shapes. The square and triangular cells have been proven to be the most cost effective in terms of extrusion die cost [124]. Experimental results show that a hex cell has 7% lower thermal mass than a square cell, and the triangular cell has a 13% higher thermal mass than a square cell. However, by including the effects of the heat transfer factor and GSA on a light-off factor (LOF) and conversion efficiency factor (CEF), the square cell offers an equivalent or even slightly better performance than that of hex cells because of the inherent high GSA of a square cell, although the thermal mass for a square cell is higher. On the other hand, the LOF and CEF values of a triangular cell appear to be even higher than those of a square cell. Considering that in real cases there is little or no flow in the acute corner regions, the effective performance of a triangular cell is not as good as a square cell. Furthermore, the pressure drop of a triangular cell substrate is nearly 30% higher than that of a square cell substrate, which makes a square cell structure the preferred choice in terms of overall performance. A hex cell substrate has approximately 10-12% less pressure loss than a square cell substrate, which is the only advantage of a hex cell over a square cell [120].

The challenges of monolith reactors are mainly related to even flow distribution and replacement of the catalyst [113]. A uniform distribution is essential for keeping a narrow RTD, which is important in the ATR process to make sure that a partial oxidation reaction does not transform into a total oxidation reaction. A supplemental device for distributing reactant flow is required, and the system becomes more complex. Catalyst deactivation is also a serious problem, which a monolith reactor cannot avoid. Theoretically, the replacement can be done by disintegration of the washcoat from the monolithic support, but it is obviously difficult to execute and the capital cost is also significant. One additional problem monolith reactors may encounter is washcoat loss. The high flow velocities and rapid temperature changes could lead to the loss of bonding between the washcoat and monolith walls. Research teams in Argonne National Laboratory [73], Royal Military College of Canada [21,125,126], Forschungszentrum Juelich GmbH in Germany [86,114,127], and KTH-RIT in Sweden [19] have done a significant amount of research of ATR in monolithic reactors. For diesel ATR in monolithic reactor, Shigarov et al. [128] tested several catalyst composites and the optimum operating conditions were specified as O_2/C ratio of 0.5-0.6, S/C ratio of 1.5-1.7 and inlet mixture temperature of 300-400 °C. At these conditions the yield of H_2+CO was 2.88 L/g fuel, the hydrogen yield was 18 mol/mol fuel, and the H_2/CO ratio was 3.5 in the products. Karatzas [19] studied a monolithic ATR reformer of 5 kW_e for diesel (~10 ppm S) and jet fuel (~200 ppm S) reforming. At optimized conditions of O_2/C ratio of 0.49, S/C ratio of 2.5 and fuel inlet temperature of 60 °C, reformer efficiency of 81% and H_2 selectivity of 96% were established for diesel. And at the same operating conditions, the reforming efficiency of jet fuel was only 42%. Lenz et al. [84] investigated the ATR of desulfurized jet fuel in a monolithic reactor. At S/C ratio of 1.5, air to fuel ratio of 0.28, and GHSV (Gas hourly space velocity) of 50000 h^{-1}, the best efficiency of 78.5% was reached.

Besides the traditional honeycomb monoliths carriers, foam monoliths have been considered as an alternative catalyst carrier for their advantages of better heat and mass transfer properties.

Their mass transfer coefficients are between those of packing particles and honeycomb monoliths, and their heat transfer coefficients are efficient compared to particle beds. The flow through the foam structure follows the same convective fluid mechanics as in packed beds and better turbulence is obtained compared to honeycomb monoliths. The pressure drop in a foam structure is reduced by a factor of 10 compared to a packed bed since porosities are almost twice as large. But the pressure loss is higher than that through honeycomb monoliths [129,130].

4.3 Catalyst preparation for the reformer

The NiO-Rh bimetallic catalysts were prepared by the washcoating method [21,131,132]. Support substrates were cordierite monoliths with 400 cpsi and a wall thickness of 0.25 mm, length of 60 mm and diameter of 40 mm. Picture and XRD graph of the used cordierite monolith are shown in Fig. 33. Pseudo-boehmite (70 wt.% Al_2O_3) was coated as the first layer in the monoliths to increase the total surface area. Cerium was added to increase the sulfur resilience capability of the catalyst, as explained by Argonne National Laboratory that Ce could form a stable sulfide in the temperature range of ATR to serve as a sulfur sink [21]. Potassium was proved to be the most effective promoter in suppressing coke formation in ATR. The addition of K not only lowers the coking tendencies of alumina supports, but also prevents nickel from catalyzing the decomposition reactions [133]. Lanthanum was added as a promoter to improve the catalytic activity of nickel. In reforming reactions, the addition of a small amount of La could possibly increase the nickel catalyst activity significantly [134]. Nickel oxide and rhodium were the major catalytic components in the proposed catalysts.
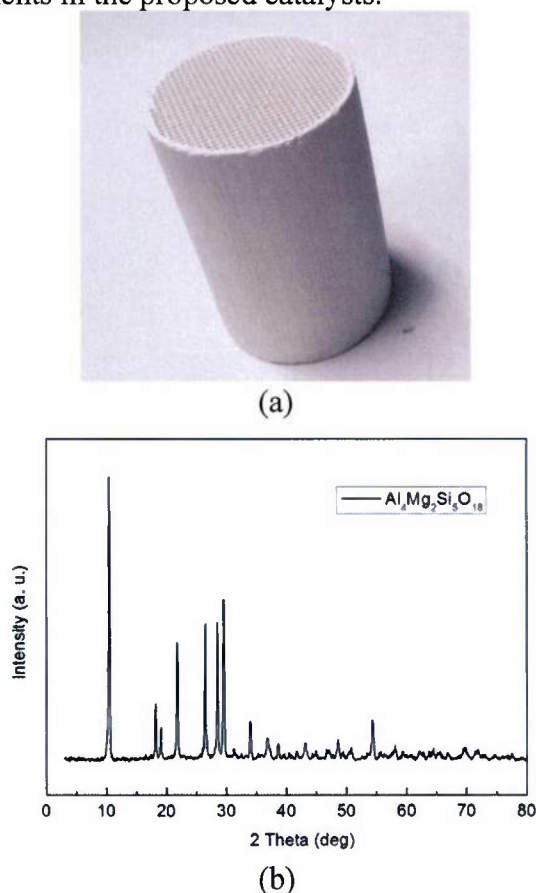

(a)

(b)

Figure 33 (a) Picture of the used cordierite monolith (b) XRD graph of the cordierite monolith

Regent grade rhodium chloride hydrate $RhCl_3.3H_2O$ ($Rh \geq 39.5$ wt.%), cerium acetate hydrate $Ce(CH_2COOH)_{3.5}H_2O$ and lanthanum acetate hydrate $La(CH_2COOH)_{3.5}H_2O$ (from Hangzhou Ocean Chemical Co., Ltd., China), nickel acetate hydrate $Ni(CH_2COOH)_{2.4}H_2O$ (from Sinopharm Chemical Reagent Co., Ltd., China), and potassium nitrate KNO_3 (from Sigma-Aldrich) were used as sources of metals in the catalysts. Before coating the cordierite monoliths were cleaned in 10% nitric acid and then washed by distilled water. Followed by drying at 60 °C overnight the clean monoliths were calcined in air at 815 °C for 2 h. After cooling the monoliths were ready for washcoating. The first step was to impregnate the cordierite monoliths into prepared Al-Ce sol solution for 20 min. The surplus solution remaining in the monolithic channels was evacuated by N_2 flow. After drying at 60 °C overnight the monoliths were then calcined in air at 815 °C for 2 h. The process was repeated until the desired amount of Al_2O_3-CeO_2 was coated in the monoliths. The same procedure was then applied to the monoliths repeatedly with La-K solution, Ni solution and Rh solution.
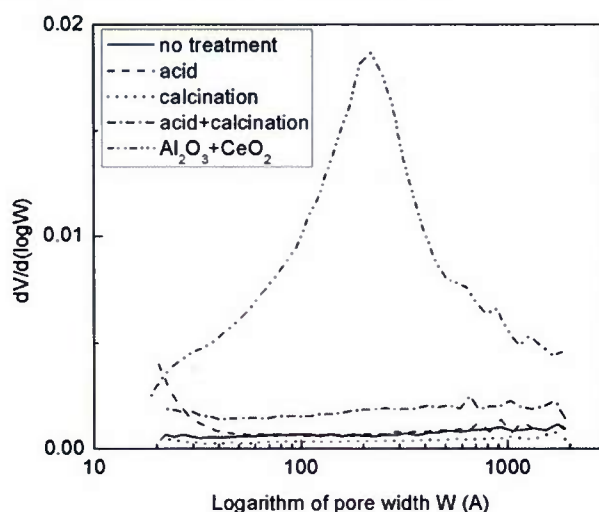

Figure 34 Pore size distribution of monoliths with different treatments
(Unit of pore size W: Å)

Micromeritics TriStar II 3020 was used to measure the surface area and pore size distribution of the cordierite monoliths. Figure 34 shows the pore size distribution of monolith without any treatment, monolith treated with acid cleaning, monolith treated with calcination, monolith treated with both acid cleaning and calcination, and monolith coated by 7 wt.% Al_2O_3 and 2 wt.% CeO_2. The corresponding surface areas were 0.525, 6.273, 0.285, 1.417 and 5.332 m^2/g respectively. It is clear that the acid cleaning can remove undesired matters from the monolith, and the alumina coating layer can significantly increase the surface area of the monolith, as well as increase the number of pores in the size range between 10 and 100 nm. Since structured monolith support with large surface area and small pores is desired in the catalyst preparation process, in further tests all cordierite monolith supports were firstly washed with 10% nitric acid followed by calcination in air at 815 °C for 2 h. And before the promoters and active components were added, several layers of alumnia were washcoated onto the monolith.

4.4 Autothermal reforming system design

Figure 35 indicates the lab scale experimental set-up of the 2.5 kW_t ATR system [135]. The liquid fuel and water were delivered to the reactor by Flash 100 HPLC (High-performance liquid

chromatography) pumps at constant flow rates. Water was heated to superheated steam in a Paragon kiln before entering the reactor. Liquid fuel and compressed air were firstly pre-heated in a kiln through separate tubing paths and then heated in heating hoses to preset temperatures. The H900 series heating hoses are made by Hillesheim, with diameter of 80 mm, length of 50 cm, and maximum temperature of 450 °C. The heating hoses temperatures were controlled by HT 43 PID controllers.
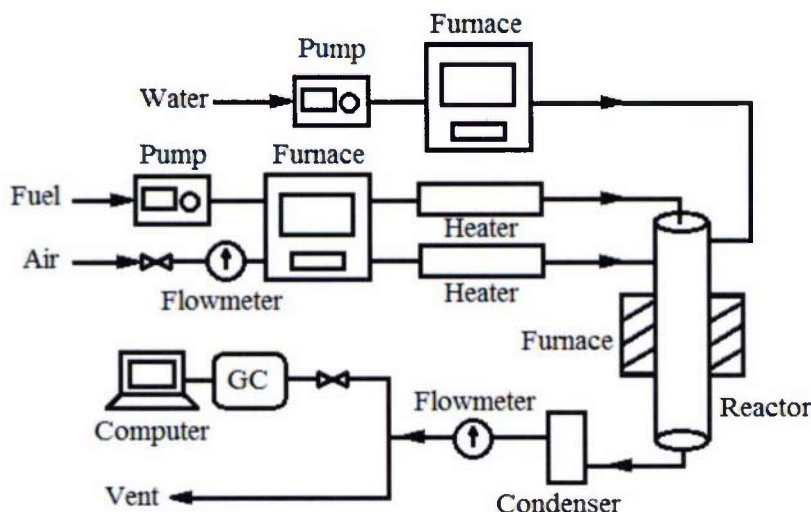

Figure 35 Experimental set-up of the lab-scale ATR system

The preheated liquid fuel was injected into the reactor through a stainless steel Steinen mist-jet misting nozzle. The misting nozzle generated hollow cone fuel spray with a spray angle of 90°. The preheating of fuel could lower the fuel viscosity and surface tension and therefore benefit the fuel transportation and injection through the nozzle [19]. Superheated steam and air were evenly distributed in the tubing system as shown in Fig. 36 before entering the ATR reformer. Both steam and air were injected into the reactor through four holes in the wall. The steam injection was positioned upstream and the air injection was positioned downstream to prevent possible fuel ignition [85]. All the tubing was wrapped with heat insulation materials to reduce heat loss. Followed by injection the fuel spray was firstly evaporated by the heat from superheated steam and then mixed with air to form the fuel/steam/air reactants mixture.

Figure 36 ATR reactor with steam and air distribution tubing

Figure 37 shows the detailed design of the ATR reformer. Because catalyst screening was planned, the reformer was designed for ease catalyst replacement. The reformer was a stainless steel pipe with diameter of 48.26 mm and length of 47 cm. The reformer was placed in a tubular furnace in order to keep the constant operation temperature of the catalytic zone. Two pieces stainless steel mesh (mesh size 20×20, open area 46%) were mounted in front of the catalytic zone aiming to distribute the mixing flow of reactants. Cordierite monolithic catalyst was placed in the catalytic zone and its length was 60 mm. After reaction, the reformate was cooled in the copper coils as shown in Fig. 35 and the residual liquid water was collected in a condenser. Then the dry reformate was analyzed in a GC system. Agilent GC6890 equipped with TCD (thermal conductivity detector) was employed to quantitatively analyze the dry reformate. Molecular Sieve 5A column (Supelco, 60/80 mesh, 6FT×1/8 IN) and Hayesep Q column (Agilent, 80/100 mesh, 10FT×1/8 IN) were used to detect molar fractions of H_2, N_2, $O2$, CO and CO_2. The total dry reformate volumetric flow rate was measured by Dwyer flowmeter. The hydrogen selectivity, carbon selectivity and total energy conversion efficiency [136] in tests were defined as follows,

$$\text{Hydrogen selectivity (\%)} = \frac{\dot{n}_{H_2} + \dot{n}_{CO}}{(m+n/2) \times \dot{n}_{C_m H_n}} \times 100 \tag{45}$$

$$\text{Carbon selectivity (\%)} = \frac{\dot{n}_{CO} + \dot{n}_{CO_2}}{m \times \dot{n}_{C_m H_n}} \times 100 \tag{46}$$

$$\text{Efficiency } \eta \text{ (\%)} = \frac{\dot{n}_{H_2} LHV_{H_2} + \dot{n}_{CO} LHV_{CO}}{\dot{n}_{C_m H_n} LHV_{C_m H_n}} \times 100 \tag{47}$$

For n-dodecane, in the above equations $m = 12$ and $n = 26$; and for desulfurized Jet-A fuel, $m = 11.3$ and $n = 22.6$.
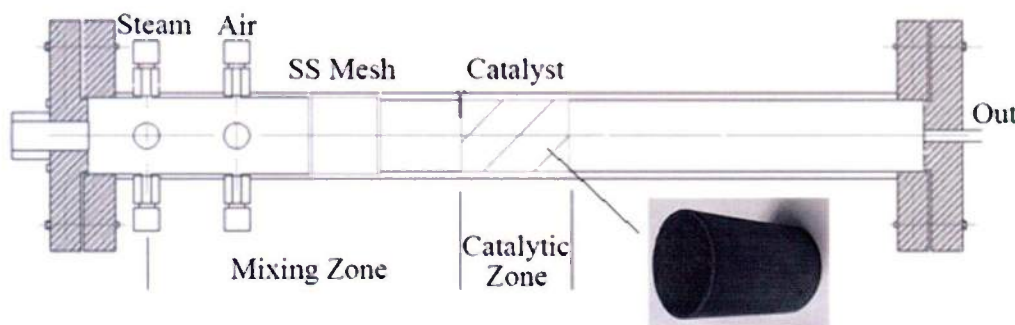

Figure 37 Detailed ATR reactor design

4.5 Autothermal reforming experimental tests and results

In the ATR tests presented in section 4.5.1 to 4.5.4, n-dodecane (≥99%) was used as the surrogate fuel of Jet-A to study the autothermal reforming characteristics of the reformer and the proposed catalyst. Rachner [28] reported an empirical formula for Jet-A to be $C_{11.6}H_{22.3}$ with molecular weight about 161.9 g/mol and LHV of 43.26 MJ/kg. As a surrogate fuel, n-dodecane has the chemical formula of $C_{12}H_{26}$ with hydrogen content 15.28 wt.%. And the molecular weight was 170.3 g/mol, and LHV was 44.14 MJ/kg.

4.5.1 Catalyst screening based on test results of surrogate fuel (n-dodecane)

The major advantage of using monolith as the catalyst support is that monolith has high open frontal area so that the flow pressure drop is low. But the monolith also has drawbacks compared

to fixed bed. The mass and heat transfer rates are not strong due to low Reynolds number, and the mass transfer in radial direction doesn't exist in monolith. Therefore the high loading of catalyst and uniform distribution of active components on the wall of the monolith are crucial for the catalyst preparation. Six catalyst combinations were tested and compared in the present study. The catalyst samples details are listed in Table 6. Catalyst 1 to 3 had higher loading of alumina and cerium oxide compared to the rest. Catalyst 4 to 6 have different loading of potassium oxide and nickel oxide. The six catalysts were tested separately in the ATR reformer at identical operation conditions: flow rate of n-dodecane = 6 ml/min, O_2/C = 0.45, S/C = 1.8, steam was pre-heated to 210 ^{o}C, air was pre-heated to 165 ^{o}C, n-dodecane was pre-heated to 180 ^{o}C, and the operation temperature of the reformer catalytic zone was kept at 700 ^{o}C. Figure 38 compares the mole fraction of H_2, CO and CO_2 in dry reformates. Figure 39 indicates the percentages of hydrogen selectivity, carbon selectivity, and energy conversion efficiency.

Figure 38 shows that catalyst 5 produced the highest hydrogen concentration of 43.6% as well as the highest carbon monoxide concentration of 12.9%. Since both hydrogen and carbon monoxide are fuel sources for SOFC, the addition of hydrogen and carbon monoxide is used to compare the performance of different catalysts. Catalyst 5 had the highest H_2+CO concentration of 56.5%, followed by catalyst 4 with 52.8% H_2+CO concentration and catalyst 6 with 48.6% H_2+CO concentration. Figure 39 shows the same tendency of hydrogen selectivity, carbon selectivity and energy conversion efficiency. Catalyst 5 had the best hydrogen and carbon selectivity of 99% and 88% respectively. The efficiency achieved 84.5%, and the output power was 2.8 kW$_t$. Catalyst 5 was then used in further study to characterize the reforming system.

Table 6   Catalyst screening test samples

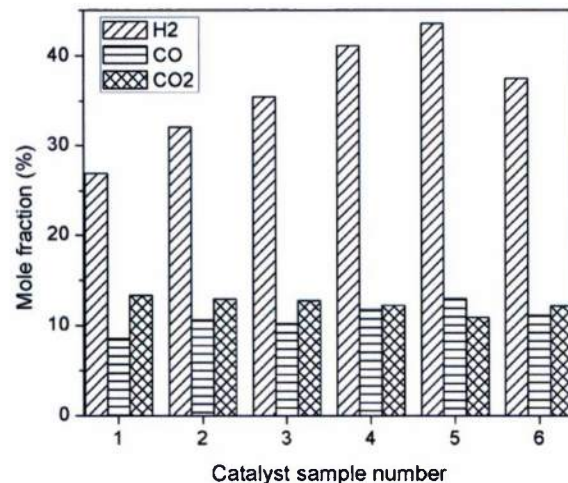| Catalyst number	Composition weight ratio (wt. %)					
	Al_2O_3	CeO_2	La_2O_3	K_2O	NiO	Rh
1	7	3	2.5	2.5	5	0.3
2	7	2	0.4	0.8	5	0.3
3	7	4	0.4	0.8	5	0.3
4	3.5	1	0.4	0.8	5	0.3
5	3.5	1	0.4	1.6	5	0.3
6	3.5	1	0.4	0.8	10	0.3

Figure 38   Mole fraction of H_2, CO and CO_2 in dry reformates
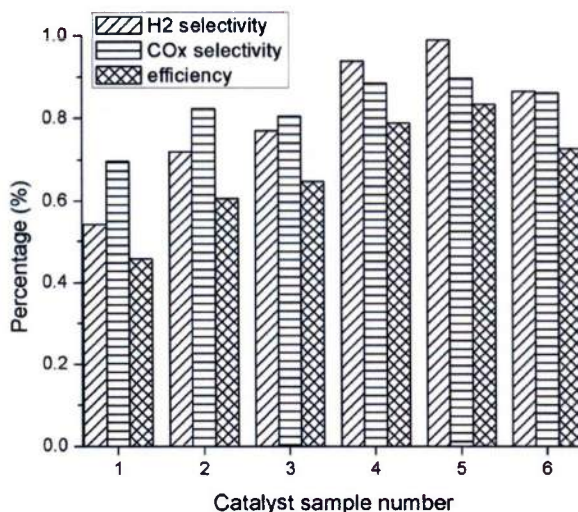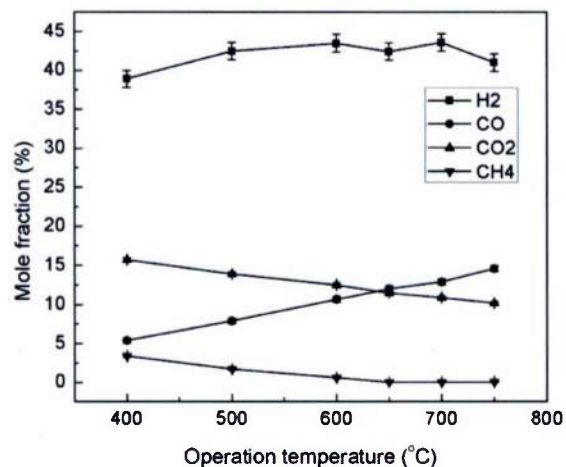
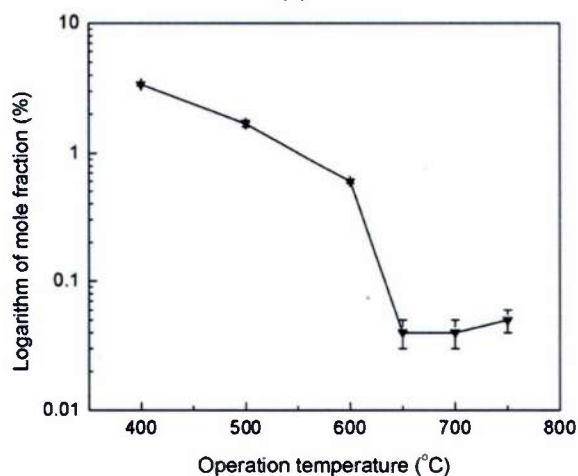*Figure 39 H₂ selectivity, carbon selectivity and reaction efficiency comparison*

4.5.2 Effect of reformer operating temperature

The ATR reaction is a combination of exothermic partial oxidation reaction (POX) occuring in the upstream of the catalyst sequentially followed by endothermic steam reforming reaction (SR). Ideally the heat released by POX can sustain SR if the reformer wall is adiabatic, and overall the ATR reaction is thermally neutral or slightly exothermic. However, in the present study the ATR reformer was not thermally insulated, so that external heat source was needed to sustain the catalytic zone at constant operation temperature. The tubular furnace was also used to heat the catalytic zone to light-off temperature before reactants entering the reformer since POX reaction does not occur at ambient temperature.

The temperature was programmed to increase from 400 °C to 750 °C. Seven different temperature points were tested and at each point the temperature were kept for 40 min. Temperature higher than 750 °C cannot be reached due to the endothermic SR reaction and the cooling effect of the reactants flow and reformate flow. All the other operation conditions were identical: flow rate of *n*-dodecane = 6 ml/min, O_2/C = 0.45, S/C = 1.8, steam was pre-heated to 210 °C, air was pre-heated to 165 °C, *n*-dodecane was pre-heated to 180 °C. Figure 40 shows the product molar fractions in dry reformate at different temperatures, and Fig. 41 shows the hydrogen selectivity, carbon selectivity, and efficiency at different temperatures. It can be observed from Fig. 40 that the H_2 molar fraction is at a relative stable level between 39% and 43.5% at different temperatures, whereas CO fraction increases from 5% to 15%, and CO_2 decreases from 15% to 10% as the temperature increases from 400 °C to 750 °C. CH_4 has a high concentration of 3.4% at 400 oC and decreases gradually as the temperature increases. At 650 °C the CH_4 concentration reduced to 0.04%. Hydrogen selectivity, carbon selectivity, and efficiency are all quite low at 400 °C as shown in Fig. 41, and they all increase gradually as the temperature increases. At 700 °C the hydrogen selectivity and efficiency are slight higher than that at 750 °C, which indicates the best performance of the ATR reformer can be obtained at 700 °C operation temperature.

(a)

(b)

Figure 40   (a) H₂, CO, CO₂ and CH₄ fractions in dry reformate at different operation temperatures; (b) CH₄ fraction in dry reformate at different operation temperatures
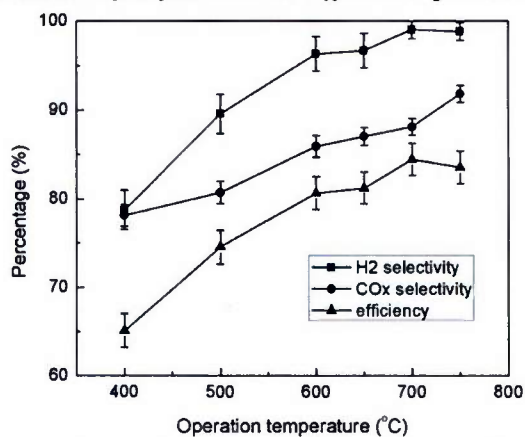

Figure 41   H₂ selectivity, carbon selectivity and reaction efficiency at different operation temperatures

4.5.3 Effects of S/C (steam/carbon) and O₂/C (oxygen carbon) ratios

Steam to carbon ratio and oxygen to carbon ratio are crucial variables to the reformer syngas compositions. Qi et al. [126] reported the optimal S/C and O_2/C for ATR were in the range of 1.5-2.0 and 0.35-0.5, respectively. By keeping other parameters as constants (flow rate of *n*-dodecane = 6 ml/min, steam was pre-heated to 210 °C, air was pre-heated to 165 °C, *n*-dodecane was pre-heated to 180 °C, and the operation temperature of the reformer catalytic zone was kept at 700 °C), nine different S/C and O_2/C combinations were tested in the reformer. S/C ratio was controlled by water flow rate and O_2/C was controlled by compressed air flow rate. Figure 42 shows the H_2 concentration in dry reformates at various S/C and O_2/C. Figure 43 shows the CO concentration at the same operation conditions. Both H_2 and CO concentrations were significantly influenced by S/C and O_2/C. Figure 42 shows that O_2/C has relatively stronger effect on H_2 production compared with S/C. As O_2/C increases from 0.45 to 0.48, H_2 concentration has a tendency to decrease. This could be caused by the combustion of H_2 with excessive O_2. As seen from Fig. 43, S/C influences CO production more than O_2/C. CO concentration varies at a range of 1% at different O_2/C conditions, yet it can change at a range of 4% at different S/C operations. The potential causes could be combinations of CO combustion and water gas shift reaction. The energy conversion efficiency was determined by both the H_2 and CO productions and the total production flow rate. Figure 44 shows the efficiency comparison at different operation ratios. It can be concluded that the efficiency decreases as the S/C increases, and at S/C = 1.5, O_2/C =0.45 the highest efficiency of 85.7% is achieved. At S/C = 1.5, O_2/C =0.42 and O_2/C =0.48 the efficiencies of 85.5% and 85.1% are slightly lower than the highest value.
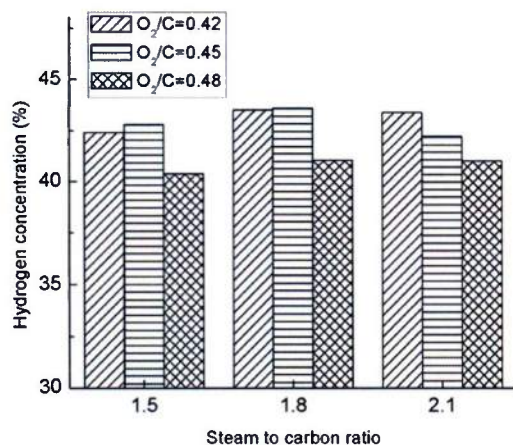

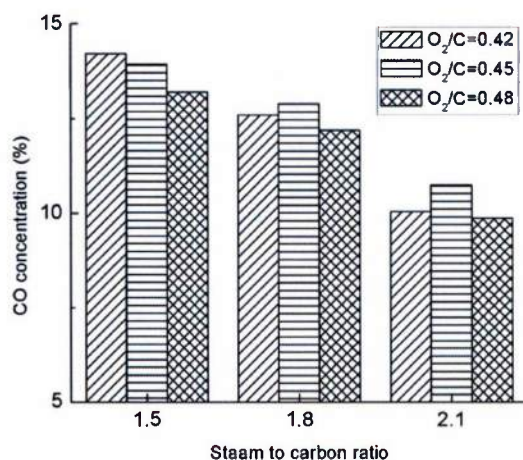*Figure 42 H_2 concentration in dry reformate at various S/C and O_2/C*

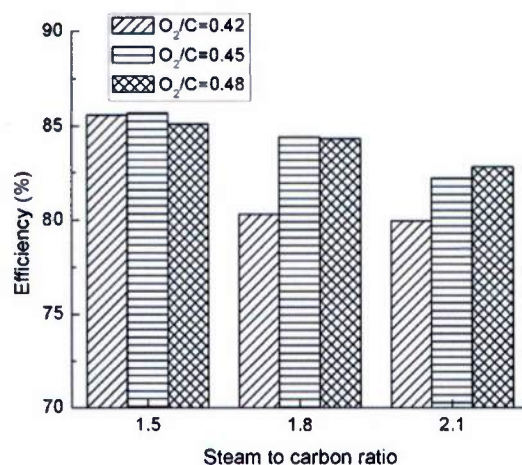*Figure 43 CO concentration in dry reformate at various S/C and O$_2$/C*

Figure 44 Energy conversion efficiency at various S/C and O$_2$/C

4.5.4 Coke formation

Figure 45 compares the carbon selectivity of CO and CO_2 at various S/C and O$_2$/C. It is noticed that in the high energy conversion efficiency operation conditions, the carbon selectivity is relatively low in the range of 82% to 87%. Since the detectable CH_4 was below 0.5% for all tests, it was believed there was high possibility that the unconverted carbon in the fuel was transferred to coke. After about 80 hours running of the ATR system, the fuel heating hose was dissembled and it was found that coke formation in the tube fittings as well as inside the heating hose was quite severe at both ends of the heating hose. Figure 46 shows pictures of coke formation in the two fittings. The fitting at the front end had more serious coke problem than the one at the rear end. The downstream path of the heating hose was tested with N_2 flow and no apparent coking was detected. The front cap of the ATR reformer was dissembled to check for coke formation and both the flange cap and fuel pressurized nozzle were free of coke as shown in Fig. 47. It draws the conclusion that the most severe coke formation was caused by the high pre-heat temperature for the liquid fuel.
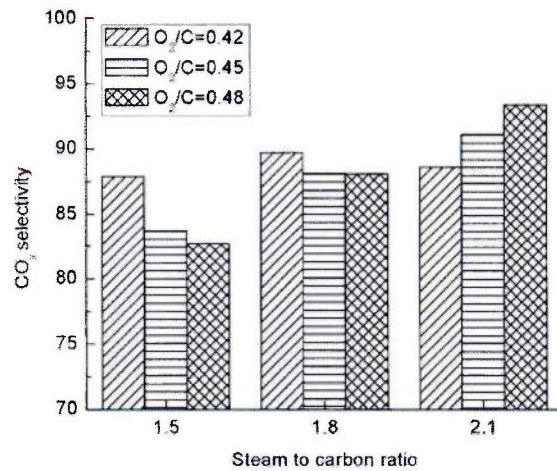
Figure 45 Carbon selectivity at various S/C and O_2/C

fitting at front end   fitting at rear end

Figure 46 Coke formation in heating hose fittings

Figure 47 Flange cap and nozzle are free of coke

In order to control the coke formation in the ATR system, the fuel pre-heat temperature was reduced and the pre-heat temperatures of steam and air were increased to supply more heat for fuel evaporation. Six tests of different pre-heating temperatures were conducted and the details

are listed in Table 7. Test #7 is the test with unacceptable level of coke. Temperatures higher than 250 °C for steam and 175 °C for air were difficult to achieve because of limitation of the heating elements and significant heat loss along the transportation paths. Other operation conditions were identical and at the optimized conditions: flow rate of *n*-dodecane = 6 ml/min, $O_2/C = 0.45$, S/C = 1.5, and the reformer temperature = 700 °C. Details of the temperatures tests as well as the mole fraction of substances in the dry reformates are listed in Table 7. Figure 48 shows the energy conversion efficiency and carbon selectivity at different temperature conditions. It can be seen that the H_2 molar fraction and the energy conversion efficiency increased as the pre-heating temperatures of reactants increased. When the fuel temperature reached 100 °C, the highest carbon selectivity of 98% was achieved and the corresponding efficiency was 79.7%. As the fuel temperature increased to 120 and 140 °C, the carbon selectivity reduced to 96% and 93% respectively, but the energy conversion efficiency increased to 81.7% and 83.5%. Considering both the carbon selectivity and energy conversion efficiency, pre-heating temperatures in test #6 was selected as the best operation conditions. After 20 hours running at this condition, the fuel heating hose was dissembled from the ATR system and no significant coke formation was observed at the fittings in both ends.

Table 7   Tests of different pre-heat temperatures

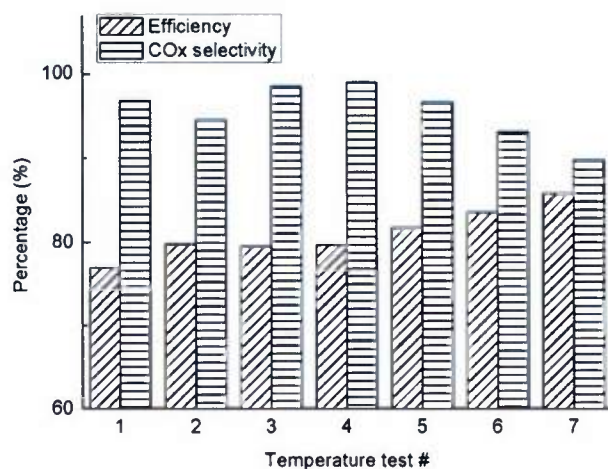| Test #	Fuel temperature (°C)	Steam temperature (°C)	Air temperature (°C)	Mole fraction (%)			
				H_2	CO	CO_2	CH_4
1	80	250	155	33.70	15.80	9.70	0.90
2	80	250	165	35.40	15.98	8.90	0.61
3	80	250	175	35.79	15.48	10.45	0.64
4	100	250	175	35.80	15.60	10.83	0.41
5	120	250	175	37.48	15.30	10.13	0.64
6	140	250	175	38.66	15.35	9.15	0.42
7	180	210	165	42.80	13.94	10.11	0.12

Figure 48   Efficiency and carbon selectivity of temperature tests

4.5.5 Reforming of desulfurized Jet-A fuel

Sulfur clean real commercial Jet-A fuel was tested at the optimized and coke formation reduced ATR conditions. The sulfur concentration in the tested desulfurization Jet-A fuel was about 20 ppmw. Figure 49 shows the mole fraction of H_2, CO, CO_2 and CH_4 in the dry reformate at reforming time of 0, 30, 60 and 90 min. It can be seen that the production of H_2 and CO is relatively stable. The mole fraction of H_2 is around 35% and the mole fraction of CO is about 12.5%. Concentration of CO_2 is in the similar level with CO. ATR of desulfurized commercial Jet-A fuel produces more CH_4 than ATR of n-dodecane. Averagely 2% CH_4 is produced in ATR of real Jet-A fuel while it is usually below 1% in ATR of n-dodecane. Figure 50 shows the average energy conversion efficiency, H_2 selectivity and COx selectivity of ATR of desulfurized commercial Jet-A fuel. The H_2 selectivity is 93% and the COx selectivity is above 96%, so that the coke formation should not be a severe problem. However, the energy conversion efficiency for the ATR of desulfurized commercial Jet-A fuel is lower than that for the ATR of n-dodecane at the same operation conditions. For n-dodecane the energy conversion efficiency is 83.5% while for desulfurized commercial Jet-A fuel the efficiency reduces to 77% with all identical operation conditions.
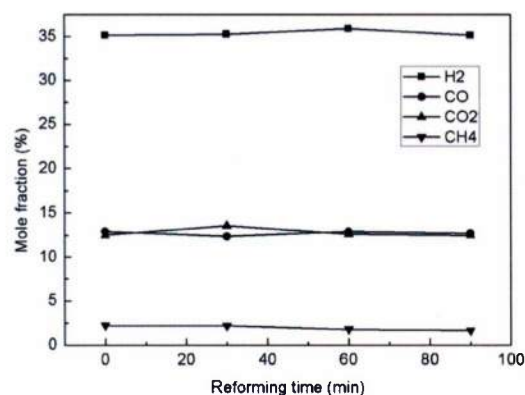
(a)
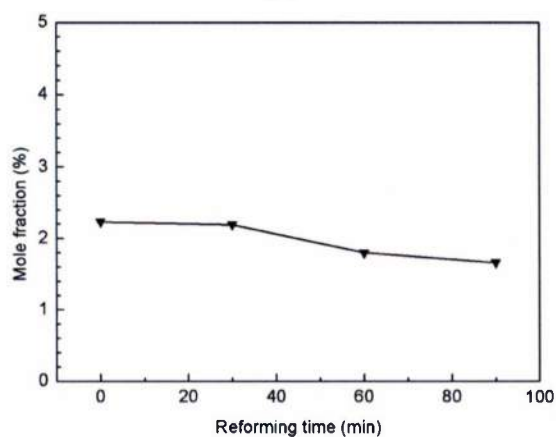
(b)

Figure 49   (a) Mole fraction of products in the dry reformate; (b) Mole fraction of CH_4 in the dry reformate
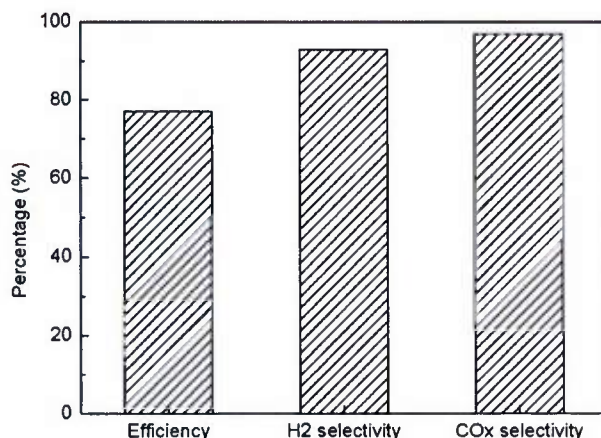
Figure 50   Energy conversion efficiency, H₂ selectivity and COx selectivity

5. Fuel adaptability study of a lab-scale 2.5 kWth autothermal reformer

Fuel adaptability of a lab-scale 2.5 kWth autothermal reforming system was experimentally investigated. Analyses of thermodynamics of autothermal reforming of different fuels at various temperatures were provided to determine the associated flow rates of fuel, air, and steam. The tested reformer has a specifically designed mixing chamber and NiO-Rh based bimetallic catalyst with promoters of Ce, K and La, which were originally designed for autothermal reforming of Jet-A fuel. The adaptability of the reformer to multiple fuels, including diesel, gasoline, ethanol, and methanol was experimentally studied at different operating conditions. Molar fractions of H_2, CO, CO_2, and CH_4 in the dried reformate were measured and the results were compared. The autothermal reforming performance of the reformer for different fuels was evaluated with regard to hydrogen selectivity, COx selectivity, and energy conversion efficiency. It was concluded that the currently developed reformer and the associated catalyst have great fuel adaptability and high potential being used in a fuel-flexible autothermal reforming system.

Logistic fuels of gasoline, diesel, and Jet-A fuel, and potential alternative fuels of methanol and ethanol were tested in the lab-scale ATR system. Gasoline with total sulfur concentration of 9.6 ppmw, and diesel with total sulfur concentration of 5.4 ppmw were purchased from local Shell-Oil gas station. Jet-A fuel with initial total sulfur concentration of 1140 ppmw was purchased from local airport fuel service and was desulfurized to 20 ppmw by homemade NiO-CeO_2/Al_2O_3-SiO_2 adsorbent prior to reforming. Important properties of the fuels in the reforming tests are listed in Table 8.

In Fig. 51 to Fig. 55 the molar fractions of reformate for five different types of fuels are presented. The reforming operating conditions including inflow molar ratios of O_2/C, S/C (steam/carbon), total flow rate, reforming temperature, and GHSV (gas hourly space velocity) are given for each tested case.

Table 8 Properties of the tested fuels (Jet-A desulfurized in-house)

	Gasoline	Diesel	Jet-A	Methanol	Ethanol
Average chemical formula	C_8H_{18}	$C_{14}H_{26}$	$C_{11.6}H_{22.3}$	CH_3OH	C_2H_5OH
Molecular weight (g mol⁻¹)	114	194	161.5	32	46
Boiling point @ 1 atm (°C)	25–205	180–360	176	66	79
Liquid density @ 15 °C (kg m⁻³)	719.7	832	800	791.8	789
Lower heating value (MJ/kg)	44.4	43.4	43.26	19.93	28.86
Sulfur content (ppmw)	9.6	5.4	20	0	0

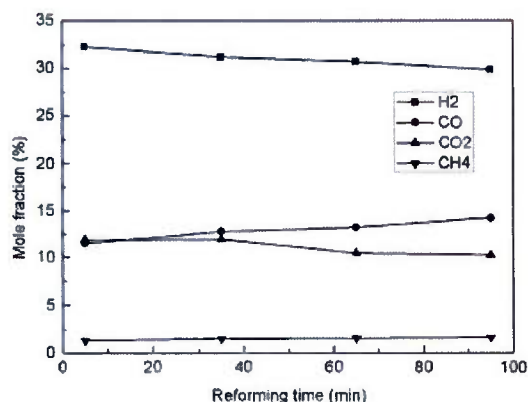*Figure 51 Results of ATR of gasoline (O₂/C=0.4, S/C=2, reformer temperature =700 °C, fuel flow rate=6.1 ml/min, GHSV= 41,370 h⁻¹).*

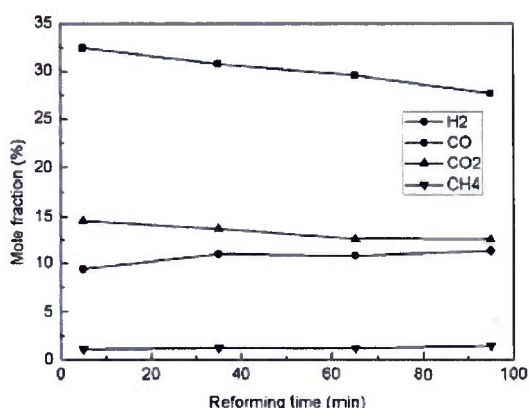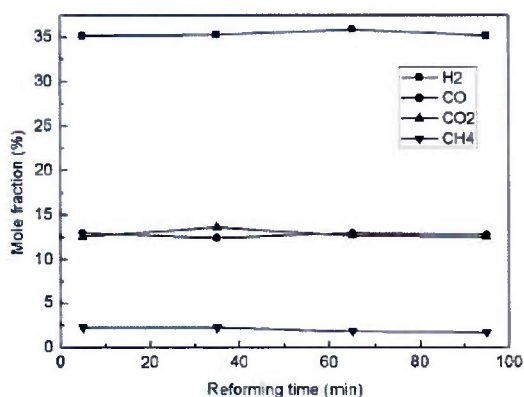*Figure 52 Results of ATR of diesel (O₂/C=0.4, S/C=2, reformer temperature =700 °C, fuel flow rate=5.4 ml/min, GHSV= 42,850 h⁻¹).*

Figure 53 Results of ATR of Jet- A (O₂/C=0.45, S/C=1.5, reformer temperature =700 °C, fuel flow rate=6.0 ml/min, GHSV= 35,980 h⁻¹).

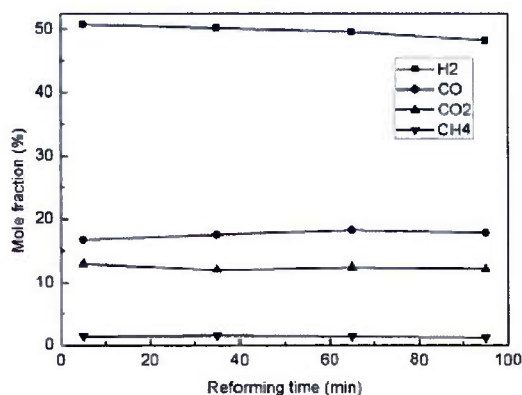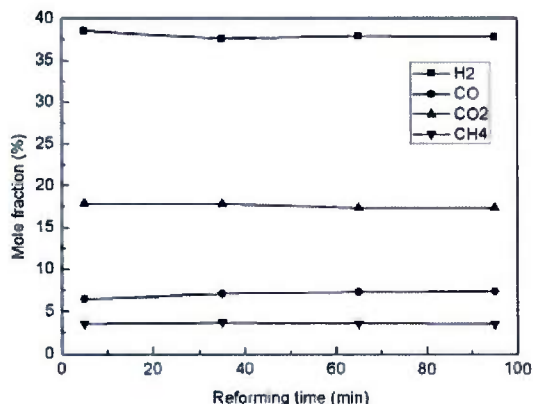*Figure 54 Results of ATR of methanol (O₂/C=0.2, S/C=1.7, reformer temperature =700 °C, fuel flow rate=12.4 ml/min, GHSV=59.250 h⁻¹).*

Figure 55 Results of ATR of ethanol (O₂/C=0.35, S/C=3, reformer temperature =700 °C, fuel flow rate=8.6 ml/min, GHSV=62,630 h⁻¹).
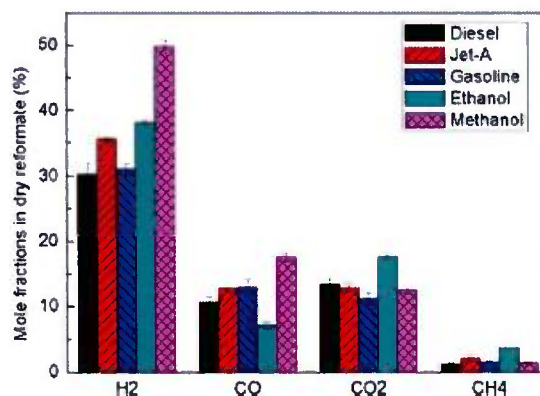

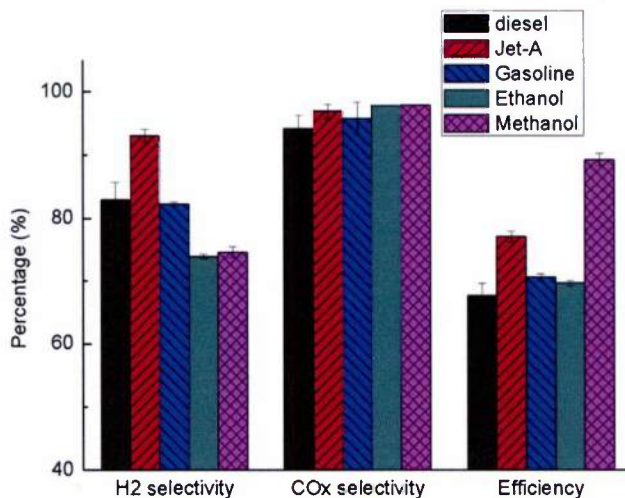*Figure 56 Fractions of H₂, CO, CO₂, and CH₄ in the dry reformate.*

*Figure 57 Comparison of H₂ selectivity, COx
selectivity, and energy conversion efficiency*

Figures 56 and 57 show the comparison of H₂ selectivity, COx selectivity, and energy conversion efficiency of five of the tested fuels. Since the reformer is particularly developed for Jet-A fuel, better reforming performance is seen for Jet-A. However, in general, the reformer can also be adaptable to other four types of fuels.

6. Integrated system of autothermal reforming and shifting with heat recovery

The integration of a hydrocarbon fuel auto-thermal reformer with a water-shift reactor as one compact reactor has been designed and fabricated, as schematically shown in Fig. 58. The reactor include three sections—reforming, heat exchange for giving heat for fuel, air, and steam, and water shifting. The entire unit allows accomplishment of thermal management to have favorable high temperatures for autothermal reforming and low temperatures for water-shift reaction, while heat from reformate is recovered. In overall, high hydrogen conversion rate from hydrocarbon fuels is achievable through the reactor.
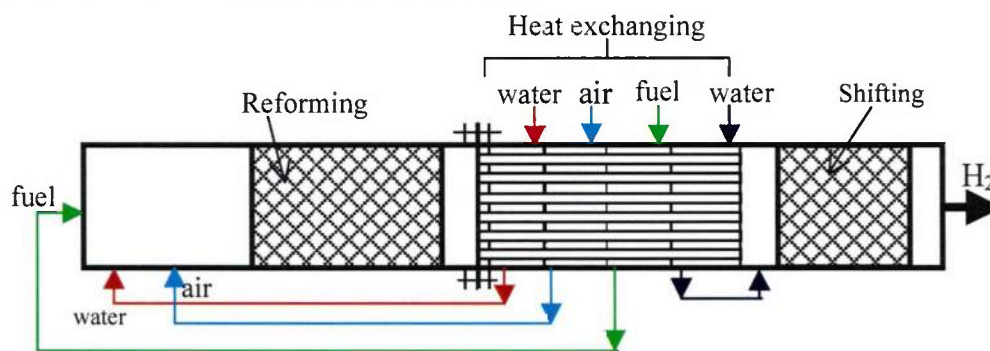

Figure 58 Schematic of integrated unit of reformer and water-gas-shift

The auto-thermal reforming works at temperatures from 500 °C to 700 °C. The reformed gas temperature is then lowered to 350 °C in four sections of heat exchange, which at the same time heats up the fuel, air, and water going into the front of the reformer. The water shift section

performs at temperatures of around 350 °C. Test results are expected to be available in two months. Supplemental report will then be provide to UTC and NOR.

Reference

[1] Liu K, Song C, Subramani V. Hydrogen and syngas production and purification technologies. 1st ed. New Jersey: Wiley; 2010.

[2] Lin L, Zhang Y, Kong Y. Recent advances in sulfur removal from gasoline by pervaporation. Fuel 2009;88:1799–809.

[3] Lin L, Kong Y, Xie K. Polyethyleneglycol/polyurethane blend membranes for gasoline desulphurization by pervaporation technique. Sep Purif Technol 2008;61:293–300.

[4] Bettermann I, Staudt C. Desulphurization of kerosene: pervaporation of benzothiophene/n-dodecane mixtures. J Membr Sci 2009;343:119–27.

[5] Wang Y, Geder J, Schubert JM, Dahl R, Pasel J, Peters R. Optimization of adsorptive desulfurization process of jet fuels for application in fuel cell systems. Fuel Proces Technol 2012;95:144–53.

[6] Aicher T, Lenz B, Gschnell F, Groos U, Federici F, Caprile L, et al. Fuel processors for fuel cell APU applications. J Power Sources 2006;154:503–8.

[7] Hernandez SP, Fino D, Russo N. High performance sorbents for diesel oil desulfurization. Chem Eng Sci 2010;65:603–9.

[8] Velu S, Ma X, Song C, Namazian M, Sethuraman S, Venkataraman G. Desulfurization of JP-8 jet fuel by selective adsorption over a Ni-based adsorbent for micro solid oxide fuel cells. Energy Fuels 2005;19:1116–25.

[9] Kumar S, Srivastava VC, Badoni RP. Studies on adsorptive desulfurization by zirconia based adsorbents. Fuel 2011;9:3209–16.

[10] Kim JH, Ma X, Zhou A, Song C. Ultra-deep desulfurization and denitrogenation of diesel fuel by selective adsorption over three adsorbents: a study on adsorptive selectivity and mechanism. Catal Today 2006;111:74–83.

[11] Jeevanandam P, Klabunde KJ, Tetzler SH. Adsorption of thiophenes out of hydrocarbons using metal impregnated nanocrystalline aluminum oxide. Microporous Mesoporous Mater 2005;79:101–10.

[12] Shen Y, Xu X, Li P. A novel potential adsorbent for ultradeep desulfurization of jet fuels at room temperatures. RSC Adv 2012;2:6155–60.

[13] Zhang ZY, Shi TB, Jia CZ, Ji WJ, Chen Y, He MY. Adsorptive removal of aromatic organosulfur compounds over the modified Na-Y zeolites. Appl Catal B: Environ 2008;82:1–10.

[14] Sarda KK, Bhandari A, Pant KK, Jain S. Deep desulfurization of diesel fuel by selective adsorption over Ni/Ai2O3 and Ni/ZSM-5 extrudates. Fuel 2012;93:86–91.

[15] Velu S, Ma X, Song C. Selective adsorption for removing sulphur from jet fuel over zeolite-based adsorbents. Ind Eng Chem Res 2003;42:5293–304.

[16] Muzic M, Sertic-Bionda K, Gomzi Z. Kinetic and statistical studies of adsorptive desulfurization of diesel fuel on commercial activated carbons. Chem EngTechnol 2008;31:355–64.

[17] Dastanian M, Seyedeyn-Azad F. Desulfurization of gasoline over nanoporous nickel-loaded Y-type zeolite at ambient conditions. Ind Eng Chem Res 2010;49:11254–9.

[18] Montazerolghaem M, Rahimi A, Seyedeyn-Azad F. Equilibrium and kinetic modeling of adsorptive sulfur removal from gasoline by synthesized Ce-Y zeolite. Appl Surf Sci 2010;257:603–9.

[19] Karatzas X, Nilsson M, Dawody J, Lindstr€om B, Pettersson LJ. Characterization and optimization of an autothermal diesel and jet fuel reformer for 5kWe mobile fuel cell applications. Chem Eng J 2010; 156:366-79.

[20] Sehested J. Four challenges for nickel steam-reforming catalysts. Catal Today 2006;111:103-10.

[21] Qi A, Wang S, Ni C, Wu D. Autothermal reforming of gasoline on Rh-based monolithic catalysts. Int J Hydrogen Energy 2007;32:981-91.

[22] Dinka P, Mukasyan AS. Perovskite catalysts for the autoreforming of sulfur containing fuels. J Power Sources 2007;167:472-81.

[23] NATO Logistics Handbook. http://www.nato.int/docu/logi-en/logist97.htm, accessed on April 2014

[24] J. P. Stucker, J. F. Schank, B. Dombey-Moore, *Assessment of DoD fuel standardization policies*, firest ed., National Defense Research Institute, Santa Monica, **1994**

[25] Exxon-mobil aviation: World jet fuel specifications with avgas supplement, http://www.exxonmobilaviation.com/AviationGlobal/Files/WorldJetFuelSpec2008_1.pdf, accessed on April 2014

[26] B. K. Lavine, A. J. Moores, H. Mayfield, A. Faruque. Genetic algorithms applied to pattern recognition analysis of high-Speed gas chromatograms of aviation turbine fuels using an integrated Jet-A/JP-8 Database. *Microchemical Journal.* **1999**, 61, 69-78

[27] T. Edwards, L. Maurice. Surrogate mixtures to represent complex aviation and rocket fuels. *Journal of Propulsion and Power.* **2001**, 17, 461-466

[28] M. Rachner. The properties of kerosene Jet A-1. DLR Mitteilung 98-01, Koeln, **1998**

[29] M. L. Witten, E. Xeiger, G. D. Ritchie, *Jet Fuel Toxicology*, first ed., CRC Press, New York, **2010**

[30] EPA. Reducing non-road diesel emissions. U.E.P. Agency, **2003**

[31] I. C. Lee. Rhodium supported on thermally enhanced zeolite as catalysts for fuel reformation of jet fuels. *Catalyst Today.* **2008**, 136, 258-265

[32] B. Dreyer, I. C. Lee, J. Krummenacher, L. D. Schmidt. Autothermal steam reforming of higher hydrocarbons: n-decane, n-hexadecane, and JP-8. *Applied Catalysis A: General.* **2006**, 307, 184-194

[33] J. Strohm, J. Zheng, C. Song. Low temperature steam reforming of jet fuel in the absence and presence of sulfur over Rh and Rh-Ni catalysts for fuel cells. *Journal of Catalysis.* **2006**, 238, 309-320

[34] I. C. Lee, H. C. Ubanylonwu. Determination of sulfur contaminants in military jet fuels. *Fuel.* **2008**, 87, 312-318

[35] O. Etemadi, T. F. Yen. Selective adsorption in ultrasound-assisted oxidative desulfurization process for fuel cell reformer applications. *Energy Fuels.* **2007**, 21, 2250-2257

[36] F. Barrai, M. J. Castaldi. Experimental investigation of a JP8 fuel processor: autothermal reformer and CO-cleanup train. *Industrial&Engineering Chemistry Research.* **2010**, 49, 1577-1587.

[37] C. P. Wood, V. G. McDonell, R. A. Smith, G. S. Samuelsen. Development and application of a surrogate distillate fuel. *Journal of Propulsion and Power.* **1989**, 5, 399-405

[38] C. R. Martel. Molecular weight and average composition of JP-4, JP-5, JP-8 and Jet A. Chemical Propulsion Information Agency Airbreathing Propulsion Manual CPIA/M6, Units 8(JP-7) and 11 (JP-8), Columbia, MD, Sep. **2000**

[39] T. G. DuBois, S. Nieh. Selection and performance comparison of jet fuel surrogates for autothermal reforming. *Fuel.* **2011**, 90, 1439-1448

[40] A. Agosta, N. P. Cernansky, D. L. Miller, T. Faravelli, E. Ranzi. Reference components of jet fuel: kinetic modeling and experimental results. *Experimental Thermal and Fluid Science.* **2004**, 23, 701-708

[41] A. Violi, S. Yan, E. G. Eddings, A. F. Sarofim, S. Granata, T. Faravelli, E. Ranzi. Experimental formulation and kinetic model for JP-8 surrogate mixtures. *Combustion Science and Technology.* **2002**, 174, 383-401

[42] D. Shekawat, D. A. Berry, D. I. Haynes, J. J. Spivey. Fuel constituent effects on fuel reforming properties for fuel cell applications. *Fuel.* **2009**, 88, 817-825

[43] R. K. Kaila, A. O. I. Krause. Autothermal reforming of simulated gasoline and dieselfuels. *International Journal of Hydrogen Energy.* **2006**, 31, 1934-1941

[44] B. D. Gould, A. R. Tadd, W. Schwank. Nickel catalyzed autothermal reforming of jet fuel surrogates: *n*-dodecane, tetralin, and their mixture. *Journal of Power Sources.* **2007**, 164, 344-350

[45] J. Kopaz, D. Applegate, L. Miller, H. K. Liao, S. Ahmed. Unraveling the maze: understanding of diesel reforming through the use of simplified fuel blends. *International Journal of Hydrogen Energy.* **2005**, 30, 1243-1250

[46] A. Takahashi, F. H. Yang, R. T. Yang. New sorbents for desulfurization byπ-Complexation: thiophene/benzene adsorption. *Industrial & Engineering Chemistry Research.* **2002**, 41, 2487-2496

[47] A. J. Hernandez-Maldonado, F. H. Yang, G. Qi, R. T. Yang. Desulfurization of transportation fuels by π-complexation sorbents: Cu(I)-, Ni(II)-, and Zn(II)-zeolites. *Applied Catalysis B: Environmental.* **2005**, 56, 111-126

[48] A. J. Hernandez-Maldonado, G. Qi, R. T. Yang. Desulfurization of commercial fuels byπ-complexation: Monolayer CuCl/γ-Al2O3. *Applied Catalysis B: Environmental.* **2005**, 61, 212-218

[49] M. Xue, R. Chitrakar, K. Sakane, T. Hirotsu, K. Ooi, Y. Yoshimura, Q. Feng, N. Sumida. Selective adsorption of thiophene and 1-benzothiophene on metal-ion-exchanged zeolites in organic medium. *Journal of Colloid and Interface Science.* **2005**, 285, 487-492

[50] K. Tanabe, T. Sumiyoshi, K. Shibata, T. Kiyoura, J. Kitagawa. A new hypothesis regarding the surface acidity of binary metal oxides. *Bulletin of the Chemical Society of Japan.* **1974**, 47, 1064-1066

[51] S. Hernandez, L. Solarino, G. Orsello, et al. Desulfurization processes for fuel cells systems. *International Journal of Hydrogen Energy.* **2008**, 33, 3209-3214

[52] J. G. Park, C. H. Ko, K. B. Yi, et al. Reactive adsorption of sulfur compounds in diesel on nickel supported on mesoporous silica. *Applied Catalysis B: Environmental.* **2008**, 81, 244-250

[53] A.H.M. S. Hussain, B. J. Tatarchuk. Adsorptive desulfurization of jet and diesel fuels using Ag/TiOx-Al2O3 and Ag/TiOx-SiO2 adsorbents. *Fuel.* **2013**, 107, 465-473

[54] X. Xu, S. Zhang, P. Li, Y. Shen. Adsorptive desulfurization of liquid Jet-A fuel at ambient conditions with an improved adsorbent for on-board fuel treatment for SOFC applications. *Fuel Processing Technology*. **2014**, 124, 140-146

[55] S. Ahmed, K. Krumpelt. Hydrogen from hydrocarbon fuels for fuel cells. *International Journal of Hydrogen Energy*. **2001**, 26, 291-301

[56] D. L. King, K. P. Brooks, C. M. Fischer, L. R. Pederson, G. C. Rawlings, V. S. Stenkamp, W. E. Tegrotenhuis, R. S. Wegeng, G. A. Whyatt in :Y. Wang, J. Holladay (Eds.), *Microreactor Technology and Process Intensification*. ACS, Washington DC, 2005, pp. 119-128

[57] W. I. Baade, N. P. Uday, S. R. Venkat. Hydrogen. *Kirk-Othmer Encyclopedia of Chemical Technology*. New York: John Wiley & Sons, 2001

[58] N. Edwards, S. R. Ellis, J. C. Frost, S. E. Golunski, A. N. J Van Keulen, N. G. Lindewald, J. G. Reinkingh. On-board hydrogen generation for transport applications: the HotSpot™ methanol processor. *Journal of Power Sources*. **1998**, 71, 123-128

[59] S. Ahmed, S. H. D. Lee, J. D. Carter, M. Drumpelt. Method for generating hydrogen for fuel cells. US6713040B2, March **2004**

[60] S. Roychoudhury, M. Lyubovsky, D. Walsh, D. Chu, E. Kallio. Design and development of a diesel and JP-8 logistic fuel processor. *Journal of Power Sources*, **2006**, 160, 510-513

[61] M. Lyubovsky, S. Roychoudhury, R. Lapierre. Catalytic partial oxidation of methane to syngas at elevated pressure. *Catalytic Letter*, **2005**, 99, 113-117

[62] J. M. Ogden, M. Steinbugler, T. G. Kreutz. Hydrogen energy systems studies. Proceedings of the 1998 U.S. DOE Hydrogen Program Review. Alexandria, VA, April **1998**

[63] S. Ahmed, M. Krumpelt, R. Kumar, S. H. D. Lee, J. D. Carter, R. Wilkenhoener, C. Marshall. Catalytic partial oxidation reforming of hydrocarbon fuels. *Fuel Cell Seminar*. Palm Springs, CA, Nov **1998**

[64] R. Kumar, R. Ahluwalia, E. D. Doss, H. K. Geyer, M. Krumpelt. Design, intergration, and trade-off analyses of gasoline-fueled fuel cell systems *Fuel Cell Seminar*. Palm Springs, CA, Nov **1998**

[65] A. Bitsch-Larsen, N. J. Degenstein, L. D. Schmidt. Effect of sulfur in catalytic partial oxidation of methane over Rh–Ce coated foam monoliths. *Applied Catalysis B: Environmental*. **2008**, 78, 364-370

[66] S. Cimino, L. Lisi. Impact of sulfur poisoning on the catalytic partial oxidation of methane on rhodium-based catalysts. *Industrial & Engineering Chemistry Research*. **2012**, 51, 7459-7466

[67] F-P. Nagel. **2008**. Electricity from wood through the combination of gasification and solid oxide fuel cells: systems analysis and proof-of-concept. *Ph.D. thesis*, Swiss Federal Institute of Technology Zurich: Swiss

[68] D. Shekhawat, T. H. Gardner, D. A. Berry, M. Salazar, D. J. Haynes, J. J. Spivey. Catalytic partial oxidation of n-tetradecane in the presence of sulfur or polynuclear aromatics: Effects of support and metal. *Applied Catalysis A: General*. **2006**, 311, 8-16

[69] D. J. Haynes, D. A. Berry, D. Shekhawat, J. J. Spivey. Catalytic partial oxidation of n-tetradecane using Rh and Sr substituted pyrochlores: Effects of sulfur. *Catalysis Today*. **2009**, 145, 121-126

[70] L. Ma, D. L. Trimm, C. Jiang. The design and testing of an autothermal reactor for the conversion of the light hydrocarbons to hydrogen I. The kinetics of the catalytic oxidation of light hydrocarbons. *Applied Catalysis A: General*. **1996**, 138, 275-283

[71] I. Kang, J. Bae, S. Yoon, Y. Yoo. Performance improvement of diesel autothermal reformer by applying ultrasonic injector for effective fuel delivery. *Journal of Power Sources*. **2007**, 172, 845-852

[72] R. L. Borup, M. A. Inbody, T. A. Semelsberger, J. I. Tafoya, D. R. Guidry. Fuel composition effects on transportation fuel cell reforming. *Catalysis Today*. **2005**, 99, 263-270

[73] S. Ahmed, R. Ahluwalia, S. H. D. Lee, S. Lottes. A gasoline fuel processor designed to study quick-start performance. *Journal of Power Sources*. **2006**, 154, 214-222

[74] R. Kumar, S. Ahmed, K. Krumpet, K. M. Myles. Argonne National Laboratory Report ANL-92/31, **1992**

[75] S. Roychoudhury, M. Castaldi, M. Lyubovsky, R. LaPierre, S. Ahmed. Microlith catalytic reactors for reforming iso-octane-based fuels into hydrogen. *Journal of Power Sources*, **2005**, 152, 75-86

[76] C. Song. Fuel processing for low-temperature and high-temperature fuel cells: Challenges, and opportunities for sustainable development in the 21st century. *Catalysis Today*. **2002**, 77, 17-49

[77] G. Hoogers. *Fuel Cell Technology Handbook*. Boca Raton: CRC Press, **2003**

[78] M. Prettre, C. Eichner, M. Perrin. The catalytic oxidation of methane to carbon monoxide and hydrogen. *Transactions of the Faraday Society*. **1946**, 42, 335-339

[79] S. H. Oh, P. J. Mitchell, R. M. Siewert. Methane oxidation over alumina-supported noble metal catalysts with and without cerium additives. *Journal of Catalysis*. **1991**, 132, 287-301

[80] L. Majocchi, G. Groppi, C. Cristiani, P. Forzatti, L. Basini, A. Guarinoni. Partial oxidation of methane to synthesis gas over Rh-hexaaluminate-based catalysts. *Catalysis Letter*. **2000**, 65, 49-56

[81] M. Nurunnabi, Y. Mukainakano, S. Kado, B. Li, K. Kunimori, K. Suzuki, K. Fujimoto, K. Tomishige. Additive effect of noble metals on NiO-MgO solid solution in oxidative steam reforming of methane under atmospheric and pressurized conditions. *Applied Catalysis A: General*. **2006**, 299, 145-156

[82] J. A. C. Dias, J. M. Assaf. Autothermal reforming of methane over Ni/y-Al2O3 catalysts: the enhancement effect of small quantities of noble metals. *Journal of Power Sources*. **2004**, 130, 106-110

[83] W. K. Jozwiak, M. Nowosielska, J. Rynkowski. Reforming of methane with carbon dioxide over supported bimetallic catalysts containing Ni and noble metal: I. Characterization and activity of SiO2 supported Ni-Rh catalysts. *Applied Catalysis A: General*. **2005**, 280, 233-244

[84] B. Lenz, T. Aicher. Catalytic autothermal reforming of jet fuel. *Journal of Power Sources*. **2005**, 149, 44-52

[85] J. Pasel, J. Meißner, Z. Porš, R. C. Samsun, A. Tschauder, R. Peters. Autothermal reforming of commercial Jet A-1 on a 5 kWe scale. *International Journal of Hydrogen Energy*. **2007**, 32, 4847-4858

[86] Z. Porš, J. Pasel, A. Tschauder, R. Dahl, R. Peters, D. Stolten. Optimised mixture formation for diesel fuel processing. *Fuel Cells*, **2008**, 8, 129-137

[87] S. P. Fitzgerald, R. S. Wgeng, A. Y. Tonkovich, Y. Wang, H. D. Freeman, J. L. Marco, G. L. Roberts, D. P. VanderWiel. A compact steam reforming reactor for use in an automotive fuel processor. Proceedings of the 4th International Conference on Microreaction Technology. **2000**

[88] L. Hartmann, K. Lucka, H. Köhne. Mixture preparation by cool flames for diesel-reforming technologies. *Journal of Power Sources*. **2003**, 118, 286-297

[89] J. Dunleavy. Sulfur as a catalyst poison. *Platinum Metals Review*. **2006**, 50, 110

[90] I. Chen, D-W Shiue. Resistivity to sulfur poisoning of nickel-alumina catalysts. *Industrial & Engineering Chemistry Research*. **1988**, 27, 1391-1396

[91] Y. Chen, H. Xu, Y. Wang, X. Jin, G. Xiong. Hydrogen production from liquid hydrocarbon fuels for PEMFC application. *Fuel Processing Technology*. **2006**, 87, 971-978

[92] A. N. Zhou, X. L. Ma, C. S. Song. Liquid-phase adsorption of multi-ring thiophenic sulfur compounds on carbon materials with different surface properties. *Journal of Physical Chemistry B*. **2006**, 110, 4699-4707

[93] S. Satokawa, Y. Kobayashi, H. Fujiki. Adsorptive removal of dimethylsulfide and t-butylmercaptan from pipeline natural gas fuel on Ag zeolites under ambient conditions. *Applied Catalysis B : Environmental*. **2005**, 56, 51-56

[94] Y. Shen, P. Li, X. Xu, H. Liu. Selective adsorption for removing sulfur: a potential ultra-deep desulfurization approach of jet fuels. *RSC Advances*. **2012**, 2, 1700-1711

[95] G. Kolb, T. Baier, J. Schürer, D. Tiemann, A. Ziogas, S. Specchia, C. Galletti, G. Germani, Y. Schuurman. A micro-structured 5kW complete fuel processor for iso-octane as hydrogen supply system for mobile auxiliary power units: Part I. Development of autothermal reforming catalyst and reactor. *Chemical Engineering Journal*. **2008**, 137, 653-663

[96] M. O'Connell, G. Kolb, K. P. Schelhaas, J. Schuerer, D. Tiemann, A. Ziogas, V. Hessel. Development and evaluation of a microreactor for the reforming of diesel fuel in the kW range. *International Journal of Hydrogen Energy*. **2009**, 34, 6290-6303

[97] M. Krumpelt, T. R. Krause, J. D. Carter, J. P. Kopasz, S. Ahmed. Fuel processing for fuel cell systems in transportation and portable power applications. *Catalysis Today*. **2002**, 77, 3-16

[98] F. Joensen, J. R. Rostrup-Nielsen. Conversion of hydrocarbons and alcohols for fuel cells. *Journal of Power Sources*. **2002**, 105, 195-201

[99] H. F. Rase. *Fixed-Bed Reactor Design and Diagnostics*. Stoneham: Butterworth Publishers. **1990**

[100] A. R. Tadd, B. D. Gould, J. W. Schwank. Packed bed versus microreactor performance in autothermal reforming of isooctane. *Catalysis Today*. **2005**, 110, 68-75

[101] L. Kiwi-Minsker, A. Renken. Microstructured reactors for catalytic reactions. *Catalysis Today*. **2005**, 110, 2-14

[102] G. Kolb, V. Hessel. Micro-structured reactors for gas phase reactions. *Chemical Engineering Journal*. **2004**, 98, 1-38

[103] J. R. Rostrup-Nielsen, T. S. Christensen, I. Dybkjaer. Steam reforming of liquid hydrocarbons. *Studies in Surface Science and Catalysis*. **1998**, 113, 81-95

[104] P. K. Cheekatamarla, A. M. Lane. Catalytic autothermal reforming of diesel fuel for hydrogen generation in fuel cells: II. Catalyst poisoning and characterization studies. *Journal of Power Sources*. **2006**, 154, 223-231

[105] P. K. Cheekatamarla, W. J. Thomson. Poisoning effect of thiophene on the catalytic activity of molybdenum carbide during tri-methyl pentane reforming for hydrogen generation. *Applied Catalysis A: General*. **2005**, 287, 176-182

[106] I. Kang, J. Bae, G. Bae. Performance comparison ofautothermal reforming for liquid hydrocarbons, gasoline anddiesel for fuel cell applications. *Journal of Power Sources*. **2006**, 163, 538-546

[107] M. M. V. M. Souza, M. Schmal. Autothermal reforming of methane over Pt/ZrO2/Al2O3 catalysts. *Applied Catalysis A: General*. **2005**, 281, 19-24

[108] S. Yoon, I. Kang, J. Bae. Effects of ethylene on carbon formation in diesel autothermal reforming. *International Journal of Hydrogen Energy*. **2008**, 33, 4780-4788

[109] J. D. Holladay, J. Hu, D. L. King, Y. Wang. An overview of hydrogen production technologies. *Catalysis Today*. **2009**, 139, 244-260

[110] R. Farrauto, S. Hwang, L. Shore, W. Ruettinger, J. Lampert, T. Giroux, Y. Liu, O. Ilinich. New material needs for hydrocarbon fuel processing: generating hydrogen for the PEM fuel cell. *Annual Review of Materials Research*. **2003**, 33, 1-27

[111] A. Shamsi, J. P. Baltrus, J. J. Spivey. Characterization of coke deposited on Pt/alumina catalyst during reforming of liquid hydrocarbons. *Applied Catalysis A: General*. **2005**, 293, 145-152

[112] I. Kang, J. Bae. Autothermal reforming study of diesel forfuel cell application. *Journal of Power Sources*. **2006**, 159, 1283-1290

[113] D. Shekhawat, J. J. Spivey, D. A. Berry. *Fuel Cells: Technologies for Fuel Processing*. Oxford: Elsevier, **2011**

[114] J. Pasel, J. Meissner, Z. Porš, C. Palm, P. Cremer, R. Peters, D. Stolten. Hydrogen production via autothermal reforming of diesel fuel. *Fuel Cells*. **2004**, 4, 225-230

[115] B. Lindstrom, J. A. J. Karlsson, P. Ekdunge, L. D. Verdier, B. Häggendal, J. Dawody, M. Nilsson, L. J. Pettersson. Disel fuel reformer for automotive fuel cell applications. *International Journal of Hydrogen Energy*. **2009**, 34, 3367-3381

[116] L. Shi, D. J. Bayless. Analysis of jet fuel reforming for solid oxide fuel cell applications in auxiliary power units. *International Journal of Hydrogen Energy*. **2008**, 33, 1067-1075

[117] Y. A. Çengel. *Introduction to Thermodynamics and Heat Transfer*. second ed., McGraw-Hill. **2007**

[118]NIST Chemistry WebBook. http://webbook.nist.gov/chemistry/, accessed on April 2014

[119] B. E. Poling, J. M. Prausnitz, J. P. O'Connell. *The Properties of Gases and Liquids*, fifth ed., New York: McGraw-Hill. **2001**

[120] R. M. Heck, R. J. Farrauto, S. T. Gulati. *Catalytic Air Pollution Control: Commercial Technology*. New York: John Wiley, **2002**

[121] T. Boger, A. K. Heibel, C. M. Sorensen. Monolithic catalysts for the chemical industry. *Industrial & Engineering Chemistry Research*. **2004**, 43, 4602-4611

[122] S. Gulati. Performance parameters for advanced ceramic catalyst supports. *SAE Technical Paper 1999-01-3631*, **1999**

[123] S. Gulati. Design considerations for advanced ceramic catalyst supports. *SAE Technical Paper 2000-01-0493*, **2000**

[124] S. Gulati. Design and durability of standard and advanced ceramic substrates. *SAE Technical Paper 2001-26-0011*, **2001**

[125] A. Qi, S. Wang, G. Fu, C. Ni, D. Wu. La–Ce–Ni–O monolithic perovskite catalysts potential for gasoline autothermal reforming system. *Applied Catalysis A: General*. **2005**, 281, 233-246

[126] A. Qi, S. Wang, G. Fu, D. Wu. Autothermal reforming of n-octane on Ru-based catalysts. *Applied Catalysis A: General.* **2005**, 293, 71-82

[127] Z. Porš, A. Tschauder, J. Pasel, R. Peters, D. Stolten. Reformer mixing chamber and method for operating same. US7461618B2, Dec. 9 **2008**

[128] A. B. Shigarov, V. V. Kireenkov, V. A. Kuzmin, N. A. Kuzin, V. A. Kirillov. Autothermal reforming of diesel fuel in a structured porous metal catalyst: Both kinetically and transport controlled reaction. *Catalysis Today.* **2009**, 144, 341-349

[129] F. C. Patcas, G. I .Garrido, B. Kraushaar-Czarnetzki. CO oxidation over structured carriers: A comparison of ceramic foams, honeycombs and beads. *Chemical Engineering Science.* **2007**, 62, 3984-3990

[130] J. T. Richardson, D. Remue, J. K. Hung. Properties of ceramic foam catalyst supports: mass and heat transfer. *Applied Catalysis A: General.* **2003**, 250, 319-329

[131] B. Lindström, J. Agrell, L. J. Pettersson. Combined methanol reforming for hydrogen generation over monolithic catalysts. *Chemical Engineering Journal.* **2002**, 4053, 1-11

[132] B. Lindström, L. J. Pettersson. Steam reforming of methanol over copper based monoliths: the effects of zirconia doping. *Journal of Power Sources.* **2002**, 106, 264-273

[133] J. T. Richardson. *Principles of Catalyst Development*, 1st ed., Plenum Press: New York, **1989**

[134] Y. Chu, S. Li, J. Lin, J. Gu, Y. Yang. Partial oxidation of methane to carbon monoxide and hydrogen over NiO/La2O3/γ-Al2O3 catalyst. *Applied Catalysis A: General.* **1996**, 134, 67-80

[135] X. Xu, S. Zhang, P. Li. Hydrogen production of a heavy hydrocarbon fuel autothermal reformer on NiO-Rh based monolithic catalysts. Proceedings of the ASME 8th International Conference on Energy Sustainability, Boston, MA, **2014**

[136] J. Pasel, R. C. Samsun, R. Peters, D. Stolten. Fuel processing of diesel and kerosene for auxiliary power unit applications. *Energy & Fuels.* **2013**, 27, 4386-4394